



The
University
Of
Sheffield.

Surface Roughness Effects on Thermally Stressed Aviation Fuel

Phil Gadsby

Submitted in accordance with the requirements for the degree of
Doctor of Philosophy.

The University of Sheffield,
Department of Mechanical Engineering
February 25, 2018

Acknowledgements

My sincerest gratitude to everybody who assisted the work described in this thesis...

Simon - for the opportunity, support and editorial guidance.

The technical team at the Low Carbon Combustion Centre;

Del Delorenzi, Dave Dunstan, Andy Hemstock, Tim Haycock and *Dan Price* - for rig life support, machining, brazing, welding, fuel blending, procurement, humour and everything in between.

Members of research staff at the Low Carbon Combustion Centre;

Ehsan Alborzi, Jonathan Knapton, Karim Ansari and *Spiridon Siouris* - for discussions, guidance and assistance.

The centre for Advanced Additive Manufacturing (University of Sheffield);

Neil Harrison and *Kamran Mumtaz* - for the production of ALM components and guidance on additive manufacturing.

My friends, family and most of all, *Hannah* for her unwavering support and astonishing patience.

“Ta!”

Abstract

Thermal instability in aviation fuels has been thoroughly explored over the last 50 years. The problem is complex, with coupling of fuel chemistry, heat transfer and fluid dynamics. Most efforts have been applied to the chemical kinetics of deposit formation and studying physical effects such as temperature, flow rate and Reynolds number in a multitude of small to large scale testing devices. However, much less attention has been paid to the effects of wall surface roughness. This is surprising - since for turbulent flow, wall roughness enhances momentum, heat and mass transfer by disrupting the quiescent viscous layer adjacent to the wall and interfering with structures of turbulence further into the boundary layer. Furthermore, a rough surface increases the wall surface area, presenting more active sites for heterogeneous catalytic reactions.

Additive Layer Manufacturing (ALM) has been touted as 'game changing' technology and is now being proposed as a method to create components for gas turbine engines. The technology results in near net shape parts with reduced weight, number of welds and material waste compared to conventional subtractive machining methods. However, the surface roughness of ALM components can be orders of magnitude greater than machined components and can be highly non-uniform. While reducing external surface roughness is trivial, typical methods of internal roughness reduction (ie. abrasive flow machining) may not be possible for small scale passages. This may result in internal fuel passageways with high relative roughness in components which are subject to high thermal loading - for example, injector feed arms which are exposed to compressor discharge air.

The effect of wall roughness on deposition of thermally stressed aviation fuel was investigated in both laminar and turbulent flow regimes using small to medium scale test devices. Deposition over ALM components was tested in the laminar regime with a modified Jet Fuel Thermal Oxidation Tester (JFTOT) and in the turbulent regime with the Aviation Fuel Thermal Stability Test Unit (AFTSTU).

The High Reynolds Number Thermal Stability Tester (HiReTS) was used to examine deposition in micro-scale tubes with very high relative roughness. As well as microscopy and 3D optical profilometry, momentum and heat transfer experiments were conducted to characterise the roughness as fully as possible. In the laminar regime, the effect of roughness was negligible. For turbulent flow, substantial differences in heat transfer and deposition rate were consistently observed for tubes with the highest relative roughness. The increase in deposition rate is thought to be related to the projection of roughness elements into regions of intense turbulent activity in the boundary layer. The turbulence structures, which are more energetic and have reduced anisotropy over rough walls, increase wall-normal transport - thereby replenishing the near wall region with deposit precursor and providing insoluble particles formed off the wall with inertia with which to deposit.

Contents

Abstract	v
Table of Contents	x
List of Figures	xviii
List of Tables	xx
Nomenclature	xxvi
1 Introduction	1
1.1 Fuel thermal stability; past, present and future	1
1.1.1 Implications for aircraft	4
2 Theoretical Introduction	5
2.1 Fluid viscosity	5
2.2 Reynolds number	7
2.3 Conservation equations for viscous, incompressible, laminar flow .	9
2.3.1 Mass continuity	10
2.3.2 Conservation of momentum	10
2.3.3 Energy conservation	14
2.4 Reynolds Averaged Navier-Stokes Equations	17
2.4.1 Reynolds stresses	18
2.4.2 Reynolds equations for turbulent flow	20
2.4.2.1 Continuity equation	21
2.4.2.2 Momentum equations	21
2.4.2.3 Energy equation	23
2.4.3 Closure of the Reynolds equations	25
2.4.3.1 Boussinesq eddy viscosity hypothesis	25
2.4.3.2 Prandtl mixing length	26
2.4.4 Wall bounded turbulent flow - velocity profiles	27

2.4.4.1	Inner layer : Prandtl law of the wall	27
2.4.4.2	Outer layer: velocity defect law (von Karman)	29
2.4.5	Smooth pipe friction factor	30
2.5	Analogies for momentum, heat and mass transfer for the boundary layer	31
2.5.1	Dimensionless gradients	32
2.5.2	Reynolds analogy	34
3	Literature Review	35
3.1	Physical and Chemical Aspects of Thermal Stability	35
3.1.1	Chemical aspects	35
3.1.2	Physical aspects	42
3.1.3	Gap analysis	52
3.2	Roughness Effects on Momentum, Heat and Mass Transfer	54
3.2.1	Momentum transfer	55
3.2.1.1	3D roughness	55
3.2.1.2	2D roughness	66
3.2.1.3	More advanced studies of higher order turbulence statistics over 2D and 3D roughness	72
3.2.2	Heat transfer	87
3.2.3	Mass transfer	97
4	Experimental Methods	116
4.1	Design Considerations	116
4.1.1	Aims and Objectives	116
4.1.2	Experimental Equipment	117
4.2	Tests with the HiReTS device	122
4.2.1	Repeatability validation	122
4.2.2	Establishing roughness data points	123
4.2.2.1	Capillary tube smoothing	124
4.2.2.2	Effect of tube diameter on test conditions	124
4.2.2.3	Tube selection	127
4.2.3	Roughness characterisation	127
4.2.3.1	Microscopy	128
4.2.3.2	MATLAB image processing	133
4.2.4	Isothermal pressure drop experiments	138
4.2.4.1	Apparatus	138
4.2.4.2	Sources of uncertainty	139

4.2.4.3	Method	140
4.2.4.4	Results	140
4.2.4.5	Discussion	146
4.2.5	Heat transfer experiments	149
4.2.5.1	Apparatus	149
4.2.5.2	Sources of uncertainty	150
4.2.5.3	Method	150
4.2.5.4	Results	151
4.2.5.5	Discussion	160
4.2.6	Deposition experiments	165
4.2.6.1	Apparatus	165
4.2.6.2	Sources of uncertainty	167
4.2.6.3	Fuel selection	167
4.2.6.4	Method	169
4.2.6.5	Results	169
4.2.6.6	Discussion	185
4.3	Tests with the JFTOT	198
4.3.1	Introduction	198
4.3.2	Establishing roughness data points	198
4.3.3	Roughness characterisation	199
4.3.3.1	Profilometry results	200
4.3.4	Deposit quantification	203
4.3.4.1	Image capture	203
4.3.4.2	Image post processing	204
4.3.5	Deposition tests	206
4.3.5.1	Apparatus	206
4.3.5.2	Sources of uncertainty	206
4.3.5.3	Method	207
4.3.5.4	Results	208
4.3.5.5	Discussion	216
4.4	Tests with the AFTSTU	220
4.4.1	Introduction	220
4.4.2	Establishing roughness data points	221
4.4.2.1	ALM SLM build considerations	221
4.4.2.2	SLM build parameter study	222
4.4.2.3	Tube builds	224
4.4.3	Roughness characterisation	225

4.4.3.1	Optical profilometry	225
4.4.3.2	Isothermal pressure drop experiments	226
4.4.3.3	Apparatus	226
4.4.3.4	Sources of uncertainty	227
4.4.3.5	Method	227
4.4.3.6	Results	227
4.4.3.7	Discussion	230
4.4.4	Deposition experiments	231
4.4.4.1	Method / Apparatus	231
4.4.4.2	Results	232
4.4.4.3	Discussion	234
5	General Discussion	235
5.1	Laminar flow	235
5.2	Turbulent flow experiments	236
5.2.1	HiReTS	236
5.2.1.1	Critical review of experiments	237
5.2.2	AFTSTU	246
5.3	Proposed mechanism for deposition of insoluble fuel degradation products	248
6	Summary and Conclusions	251
6.1	Summary	251
6.2	Recommendations and future work	253
	Bibliography	266
	Appendices	267
A	Literature Review of Fuel Testing Devices	268
A.1	Laboratory scale test devices	269
A.1.1	CRC Coker (ASTM D1660)	269
A.1.2	JFTOT (ASTM D3241)	271
A.1.3	HiReTS (EI482 / ASTM D6811)	273
A.2	Large scale rigs / simulators	279
A.2.1	(Mini) Injector Feed Arm Rig ((M)IFAR)	280
A.2.2	Aviation Fuel Thermal Stability Test Unit (AFTSTU)	282
B	Hydrocarbon species	285

<i>CONTENTS</i>	x
C Fluid Properties	286
D Calibration data	288
E Heat transfer data	289
F Publications from this work	292

List of Figures

1.1	CFM 'LEAP' ALM injector	3
1.2	Components of a fuel system susceptible to fuel degradation products (taken from [1])	4
2.1	Shear flow between a moving and stationary plate	6
2.2	Shear in pipe flows	7
2.3	Shear forces on a volume element due to friction	8
2.4	Mass flux across a volume element $dx dy dz$	10
2.5	Momentum fluxes across a volume element $dx dy dz$	11
2.6	Surface forces (normal and shear)	12
2.7	Convective energy flux across a volume element $dx dy dz$	14
2.8	Reynolds decomposition of turbulent signal	18
2.9	Transfer of momentum due to fluctuating velocity	19
2.10	Typical correlation of $\overline{u'v'}$	20
2.11	TKE budget for the near wall region (DNS data of Kim et al [2])	24
2.12	Prandtl mixing length model	26
2.13	Universal smooth wall velocity distributions, DNS data of Kim et al [2]. Left: outer layer. Right: inner layer	30
3.1	Example composition of conventional and bio derived fuel	36
3.2	Basic liquid phase autoxidation mechanism	36
3.3	Effect of deoxygenation (taken from [3])	37
3.4	Effect of fuel processing on fuel thermal stability (taken from [1])	39
3.5	Deposition rates in arrhenius form for pure n-alkanes (taken from [4])	43
3.6	Effect of Re on deposition with no pre heating (taken from [5]) . .	46
3.7	Non dimensional turbulent boundary layer velocity profile - inner variables (log law: $u^+ = 1/\kappa \ln y^+ + 5.5$)	47
3.8	Effect of Re on the radial temperature distribution in the turbulent boundary layer (taken from [5])	48

3.9	Values of deposit thermal conductivity (taken from [6])	49
3.10	Deposition rates and micrographs of rough and smooth tubes observed in [7]	51
3.11	Original friction factor data of Nikuradse (taken from [8])	56
3.12	Hydraulically smooth, transitional and fully rough regimes (taken from [8])	57
3.13	Roughnesses of Schlichting (taken from [9])	58
3.14	Transitional roughness behaviour (taken from [10])	61
3.15	Hama roughness function with k^+ (taken from [11])	63
3.16	Smooth to fully rough behaviour expressed as the Nikuradse roughness function (taken from [12])	65
3.17	Collapse of the outer layer velocity defect profile (taken from [12])	66
3.18	Dimensions for 'd' type roughness	66
3.19	Hama roughness function intercept variation with roughness solidity (taken from [13])	68
3.20	Limited evidence for 'd' type behaviour. (taken from [14]). $\blacktriangle, \triangle$ [15]; \bullet, \circ [16], $\blacktriangledown, \triangledown$ [17]. Filled symbols corrected for k/δ according to [18]	69
3.21	Relationship between frequency of slot phase change and slot depth (taken from [19])	70
3.22	Top down view of streamwise vortices over a plate plate, $y^+ = 4.3$ (observed by Kline et al [20])	71
3.23	Comparison of ΔU^+ for various investigators (taken from [21]) . .	72
3.24	Increase in Reynolds shear stress over a d -type wall (taken from [15])	73
3.25	Variation in friction velocity over crests and cavities of a d -type wall (taken from [22])	74
3.26	Self sustaining turbulent boundary layer over a d -type wall (taken from [23]). Symbols represent different streamwise locations . . .	75
3.27	Variation of fluctuating velocities and Reynolds shear stress across a d -type wall cavity (taken from [23]). Symbols indicate height of measurement above the cavity	76
3.28	Effect of k^+ on streamwise turbulence intensity ($\frac{\overline{u'^2}}{U_*^2}$) for spherical roughness (taken from [24])	77
3.29	Effect of k^+ on turbulence kinetic energy production normalised by friction velocity (taken from [24]). $\odot, k^+ = 61$; $\triangle, k^+ = 34$; $\square, k^+ = 21$	78

3.30	Variation of turbulence intensity with k_s^+ (taken from [25]). Top left; streamwise, inner variables. Top right; streamwise, outer variables. Bottom left; wall-normal, outer variables. Bottom right; Reynolds shear stress, outer variables	79
3.31	Effect of k^+ on turbulence sweep-ejection cycle (taken from [25]) .	80
3.32	Normalised Reynolds stresses and turbulent kinetic energy profiles for different roughnesses with the same k^+ (taken from [26]). \circ , smooth wall; \square , mesh roughness; ∇ , rod roughness; $-$, DNS (Spalart 1988)	81
3.33	Third order moments of velocity fluctuations and skewness across the boundary layer for roughness with the same k^+ (taken from [26])	82
3.34	Profiles of turbulence intensity (top) and vorticity (bottom) (taken from [27]). Left: normalised by local U^* , Right: normalised by smooth wall U^*	83
3.35	Contours of instantaneous streamwise velocity at $y^+ = 5$. Top; smooth wall. Bottom; rough wall (taken from [27])	85
3.36	Comparison of heat transfer correlations over rough walls (taken from [28])	90
3.37	Nu vs Re for 2D wire roughness (taken from [29])	91
3.38	Variation in St^{-1} with k^+ (taken from [29])	92
3.39	Predictions of St with Re of various investigators (taken from [30])	94
3.40	Stanton number for Schlichting type roughness (taken from [31]). Left: hemisphere roughness. Right: truncated cone roughness. Top: $\frac{L}{D}=2$. Bottom: $\frac{L}{D}=4$	95
3.41	Turbulent flow particle deposition regimes. Taken from [32]	98
3.42	Stagnation point flow model for particle deposition across the viscous sublayer employed in [33]	100
3.43	Deposition over smooth and rough surfaces (taken from [34]) . . .	101
3.44	Results of Liu and Agarwal compared to free flight theories (taken from [35])	103
3.45	Concentration build up of particles close to the wall (taken from [36])	105
3.46	2D stagnation point flow field adopted by Fan and Ahmadi (taken from [37])	107
3.47	Dependence of deposition velocity on roughness (taken from [37])	108
3.48	Accumulation of particles in the viscous sublayer with time (taken from [38]). Sequence is (a) to (d)	110

3.49	Accumulation of particles in regions of lower than average fluid velocity (low speed streaks), top down view, $y^+ = 4$. Instantaneous contours of streamwise velocity (blue indicates negative u') and particle locations (taken from [38])	110
3.50	Correlation between sweeps and ejections and particles fluxes to and from the wall (taken from [39])	111
3.51	Conceptual model of low- Re quasi-streamwise vortices (taken from [40])	112
3.52	Proposed particle trapping mechanism. Iso-surfaces of vorticity and fluid streamlines. Green iso-surface: parent vortex (CCW). Red iso-surface: offspring vortex (CW). (taken from [38])	113
4.1	Observations in the spread of initial wall temperature with test on one fuel (ASTM D6811)	122
4.2	Repeatability of initial wall temperature for the same tubes (ASTM D6811)	123
4.3	SEM image of sectioned tubes. Top: standard capillary. Bottom: smoothed by EDM	125
4.4	Change in Re due to bulk fuel temperature increase from inlet to outlet	126
4.5	Change in viscous sublayer height with Re	127
4.6	Longitudinal sections. Top: drawn. Bottom: EDM	130
4.7	Set 1: EDM tubes 1 to 6	131
4.8	Set 2: EDM tubes 7 to 11	131
4.9	Set 3: EDM tubes 12 to 14	132
4.10	Drawn tubes 1 to 11	132
4.11	Demonstration of boundary tracing algorithm	134
4.12	Circumferential roughness profiles (note y axis scale). Top: R7. Bottom: EDM 4	135
4.13	Roughness height distribution. Top: R7. Bottom: EDM4	136
4.14	Pressure drop measurement apparatus	138
4.15	Friction factor data for EDM tubes 1 to 6 compared to the data of Nikuradse [8]	143
4.16	Friction factor data for EDM tubes 7 to 11 compared to the data of Nikuradse [8]	143
4.17	Friction factor data for drawn tubes 1 to 7 compared to the data of Nikuradse [8]	144

4.18	Friction factor data for EDM tubes 12 to 14 compared to the data of Nikuradse [8] and Ghajar [41]	144
4.19	Friction factor data for drawn tubes 8 to 11 compared to the data of Nikuradse [8] and Ghajar [41]	145
4.20	Comparison of drawn and EDM friction factors for set 3 tubes with similar diameters	145
4.21	Heat transfer measurement apparatus	149
4.22	Wall temperatures, drawn tubes 1-7	151
4.23	Wall temperatures, drawn tubes 8, 9, 11	152
4.24	Wall temperatures EDM tubes 1-8	153
4.25	Wall temperatures, EDM tubes 9-14	154
4.26	Nu vs Re , EDM tubes 1-6	155
4.27	Nu vs Re , EDM tubes 7-11	155
4.28	Nu vs Re , EDM tubes 12-14	156
4.29	Nu vs Re , drawn tubes 1-7	156
4.30	Nu vs Re , drawn tubes 8,9,11	157
4.31	St vs Re , EDM tubes 1-7	157
4.32	St vs Re , EDM tubes 7-11	158
4.33	St vs Re , EDM tubes 12-14	158
4.34	St vs Re , drawn tubes 1-7	159
4.35	St vs Re , drawn tubes 8,9,11	159
4.36	Energy balance across a differential control volume for tube flow .	161
4.37	HiReTS deposition test conditions	165
4.38	1D thermal resistance network for deposit formation	166
4.39	Hydrocarbon species breakdown for fuel 'A'	167
4.40	Fuel A, degradation in storage with time - standard HiReTS method. Top left; $HN_{125} = 188$. Top right; + 3 months, $HN_{125} = 546$. Bottom; + 6 months, $HN_{125} = 1193$	168
4.41	Standard HiReTS test for Fuel B. $HN_{125} = 800$	169
4.42	Summary of deposition test results	170
4.43	Set 1, Fuel A, $200^{\circ}C$. HiReTS number development with time . .	171
4.44	Set 1, Fuel A, $200^{\circ}C$. Initial and final wall temperatures	171
4.45	Set 1, Fuel A, $230^{\circ}C$. HiReTS number development with time . .	172
4.46	Set 1, Fuel A, $230^{\circ}C$. Initial and final wall temperatures	172
4.47	Set 2, Fuel A, $225^{\circ}C$. HiReTS number development with time . .	173
4.48	Set 2, Fuel A, $225^{\circ}C$. Initial and final wall temperatures	173
4.49	Set 1, Fuel A. Wall temperature rise with time and axial position	174

4.50	Set 2, Fuel A. Wall temperature rise with time and axial position	174
4.51	Set 3, Fuel B. 200°C. HiReTS number development with time . .	175
4.52	Set 3, Fuel B. 200°C. HiReTS number development with time . .	175
4.53	Set 3, Fuel B. 225, 230°C. HiReTS number development with time	176
4.54	Set 3, Fuel B. 225, 230°C. Initial and final external wall temperatures	176
4.55	Set 3, Fuel B. Wall temperature rise with time and axial position	177
4.56	Set 1, Fuel A, 200°C. Left: R1, 530 μ m. Right: EDM 1, 482 μ m. Top: wall temperature rise with time. Middle: bulk Re , viscous and buffer layer heights. Bottom: deposit thickness	178
4.57	Set 1, Fuel A, 230°C. Left: R3, 537 μ m. Right: EDM 6, 437 μ m. Top: wall temperature rise with time. Middle: bulk Re , viscous and buffer layer heights. Bottom: deposit thickness	179
4.58	Set 2, Fuel A, 225°C. Left: R7, 530 μ m. Right: EDM 11, 576 μ m Top: wall temperature rise with time. Middle: bulk Re , viscous and buffer layer heights. Bottom: deposit thickness	180
4.59	Set 3, Fuel B, 200°C. Left: R9, 528 μ m. Right; EDM 14, 611 μ m Top: wall temperature rise with time. Middle: bulk Re , viscous and buffer layer heights. Bottom: deposit thickness	181
4.60	Set 3, Fuel B. Left: R8, 527 μ m, 230°C. Right: EDM 12, 567 μ m, 225°C Top: wall temperature rise with time. Middle: bulk Re , viscous and buffer layer heights. Bottom: deposit thickness	182
4.61	Micrographs showing deposit. Top: EDM 1. Bottom: R2	183
4.62	Summary of capillary tube tests	184
4.63	Extrapolated vapour pressure data for Jet-A1	190
4.64	Universal mean velocity profile for the turbulent boundary layer .	196
4.65	Modified JFTOT heater tube - cross section	198
4.66	Illustration of build orientation in the ALM process	199
4.67	Profilometry data - ALM JFTOT heater tubes	201
4.68	Roughness metrics for ALM surfaces by optical profilometry . . .	202
4.69	ASTM D3241 visual deposit colour reference chart	203
4.70	Lightbox	204
4.71	Image processing example	205
4.72	JFTOT flow path	206
4.73	0 degree build	208
4.74	15 degree build	209
4.75	30 degree build	210
4.76	45 degree build	211

4.77	90 degree build	212
4.78	Machined tube	213
4.79	ALM tube - standard JFTOT geometry	214
4.80	Internal wall temperature with axial position	214
4.81	Left: maximum change in grayscale intensity. Right: absolute value of grayscale intensity (lower is darker)	215
4.82	Top: Combustor schematic. Bottom: AFTSTU simulated injector feed arm	220
4.83	SLM part edge parameters	222
4.84	3D optical profilometry contour plot of an ALM surface (0.94 x 1.26mm area)	223
4.85	Left; Full laser power on border and offset parameters, $S_a \approx 8\mu m$. Right; no border and offset, $S_a \approx 17\mu m$	224
4.86	ALM tubes as removed from the machine (dots are ID)	225
4.87	Pressure drop measurement apparatus	226
4.88	Friction factor data for ALM tubes	228
4.89	AFTSTU flow diagram	231
4.90	Injector feed arm deposition test conditions	231
4.91	Wall temperature rise (thermocouple B) over 10 hours for drawn and ALM tubes	233
4.92	Rate of wall temperature rise for drawn and ALM tubes	233
5.1	Change in k^+ with axial distance - HiReTS geometry	240
5.2	Estimated dependence of carbon deposition rate with k_s^+ - HiReTS geometry	242
5.3	Top: correlation of λ_{max} and Nu_{max} . Bottom: correlation of λ_{max} and $HN/\Delta T_{bulk}$	244
5.4	Deposition rate with k_s^+ - AFTSTU	247
A.1	CRC coker flow path (taken from [42])	270
A.2	JFTOT flow path (taken from [43])	272
A.3	HiReTS flow path	273
A.4	HiReTS correlation (taken from [44])	274
A.5	HiReTS repeatability (taken from [45])	277
A.6	HiReTS wall temperature reproducibility (taken from [45])	278
A.7	HiReTS repeatability assessed by the author	279
A.8	HiReTS wall temperature variation observed by the author	279
A.9	MIFAR flow path (taken from [46])	280

A.10 MIFAR correlation (taken from [46])	282
A.11 AFTSTU flow path (taken from [47])	283
B.1 Typical hydrocarbons in kerosene	285
C.1 Thermophysical properties of n-Heptane	286
C.2 Thermophysical properties of kerosene	287
D.1 Thermal camera black body source calibration data	288
D.2 Differential pressure transducer calibration data	288
E.1 Heat transfer data - Drawn tubes	291

List of Tables

1.1	Trends in aviation gas turbine engine development (adapted from [48])	2
2.1	Turbulent kinetic energy budget	24
2.2	Turbulent thermal energy equation terms	25
3.1	Review of experimental thermal stability literature, 1967-1997 . .	52
4.1	Typical test conditions for thermal stability rigs at LCCC	118
4.2	Rig suitability assessment	121
4.3	Image processing roughness metrology	137
4.4	Sources of uncertainty - pressure drop experiments	139
4.5	Pressure drop data - EDM tubes 1 to 11	140
4.6	Pressure drop data - EDM tubes 12 to 14	141
4.7	Pressure drop data - drawn tubes 1 to 7	141
4.8	Pressure drop data - drawn tubes 8 to 11	142
4.9	Sources of uncertainty - heat transfer experiments	150
4.10	Correlation for Nu vs Re . Valid for $6000 < Re < 10000$	163
4.11	Sources of uncertainty - deposition experiments	167
4.12	Average external wall temperature compared to the extrapolated saturation temperature for Jet-A1	191
4.13	ALM tube image processing results	215
4.14	SLM part edge parameters	224
4.15	ALM tubes - average and RMS roughness height data	226
4.16	Sources of uncertainty - pressure drop experiments	227
4.17	Friction factor data for tubes used in deposition tests	229
4.18	AFTSTU deposition test results	232
A.1	CRC Coker operating conditions	269
A.2	Coker tube colour rating scale [49]	270

A.3	JFTOT operating conditions	272
A.4	HiReTS operating conditions	273
A.5	AFTSTU operating conditions	284
E.1	Heat transfer data - EDM tubes	290

Nomenclature

Roman Variables

\dot{m}	Mass flow rate, $kg s^{-1}$
\dot{Q}	Volumetric flow rate, $m^3 s^{-1}$
\mathbf{u}	Particle velocity vector, $m s^{-1}$
\mathbf{v}	Fluid velocity vector, $m s^{-1}$
C_a	Species concentration, $kmol m^{-3}$
C_d	Stokes drag coefficient
c_p	Specific heat capacity at constant pressure, $J kg^{-1} K^{-1}$
c_v	Specific heat capacity at constant volume, $J kg^{-1} K^{-1}$
D_{AB}	Mass diffusion coefficient, $m^2 s^{-1}$
E_a	Activation energy, $J mol^{-1}$
j_h	Colburn j factor (heat transfer)
j_m	Colburn j factor (mass transfer)
q_s	Heat flux, $W m^{-2}$
S_L	2D roughness element spacing, m
w_a	Species mass fraction
A	Area, m^2
b	2D roughness element width, m
C	Log law intercept

c	2D roughness element gap width, m
D	Diameter, m
E	Total internal energy, J
e	Specific internal energy, m^2s^{-2}
F	Force, N or roughness plate area m^2
f	Functional dependence
g	Functional dependence
h	Specific enthalpy, m^2s^{-2} or convective heat transfer coefficient, $Wm^{-2}K^{-1}$
I	Intensity
K	Reaction rate constant
k	Thermal conductivity, $Wm^{-1}K^{-1}$ roughness height, m or turbulent kinetic energy, m^2s^{-2}
L	Characteristic length or roughness element spacing, m
l	Prandtl mixing length, m
m	Mass, kg
N	Particle mas flux, [no. of particles] $m^{-2}s^{-1}$
P	Pressure, Nm^{-2} or perimeter, m
Q	Heat rate, Js^{-1}
q	Magnitude of instantaneous turbulent fluctuation velocity, ms^{-1}
R	Radius, m or universal gas constant
r	Radial coordinate
S	Skewness
T	Temperature, K
t	Time, s

U	Velocity (mean), ms^{-1}
u	Streamwise velocity component, ms^{-1}
v	Wall-normal velocity component, ms^{-1}
w	Transverse velocity component, ms^{-1}
x	X coordinate
y	Y coordinate
z	Z coordinate
V_d	Deposition velocity, ms^{-1}

Greek Variables

α	Thermal diffusivity, m^2s^{-1}
β	Thermal expansion coefficient, K^{-1}
Δ	Change in
δ	Deposit or boundary layer thickness, m
ϵ	Offset origin for turbulent boundary layer mean velocity profile, m or turbulent dissipation, m^2s^{-3}
ϵ_h	Eddy diffusivity of heat, m^2s^{-1}
ϵ_M	Eddy diffusivity of momentum, m^2s^{-1}
ϵ_m	Eddy diffusivity of mass, m^2s^{-1}
ϵ_p	Particle diffusivity m^2s^{-1}
κ	Von Karman constant
λ	Friction factor
μ	Dynamic viscosity, $kgm^{-1}s^{-1}$
ν	Kinematic viscosity, m^2s^{-1}
ω	Vorticity, s^{-1}
ϕ	Viscous dissipation function, $Jm^{-3}s^{-1}$

ρ	Fluid density, kgm^{-3}
σ	Normal stress, Nm^{-2}
τ	Shear (tangential) stress, Nm^{-2}
τ_p	Particle relaxation time, s
ζ	Cunningham correction factor

Subscripts

∞	Free stream or maximum velocity
1	X component (index notation)
2	Y component (index notation)
3	Z component (index notation)
avg	Average
b	Bulk
cf	Constricted diameter
d	Deposit
ext	External
f	Fluid
fin	Final
init	Initial
int	Internal
p	Particle
r	Rough
rms	Root mean squared
s	Sand grain roughness
sat	Saturation

ss	Stainless steel
t	Turbulent or transitional
w	Wall

Superscripts

'	Fluctuating component
-	Time averaged quantity
+	Non dimensionalised by the viscous length scale

Dimensionless Groups

Nu	Nusselt number
Pr	Prandtl number
Re	Reynolds number
S	Strouhal number
Sc	Schmidt number
Sh	Sherwood number
St	Stanton number

Abbreviations

AFTSTU	Aviation Fuel Thermal Stability Test Unit
ALM	Additive Layer Manufacturing
CRC	Coordinating Research Council
DEM	Discrete Element Method
HiReTS	High Reynolds number Thermal Stability Tester
HN	HiReTS number
HPLC	High Performance Liquid Chromatography
ID	Inner diameter

JFTOT	Jet Fuel Thermal Oxidation Tester
LCCC	Low Carbon Combustion Centre
LDA	Laser Doppler Anemometry
MDA	Metal Deactivator Additive
MIFAR	Mini Injector Feed Arm Rig
OD	Outer diameter
ppb	Parts per billion
ppm	Parts per milion
SEM	Scanning Electron Microscopy
SLM	Selective Laser Melting
SS	Stainless steel
STHTR	Single Tube Heat Transfer Rig
VSI	Vertical Scanning Interferometry

Chapter 1

Introduction

1.1 Fuel thermal stability; past, present and future

The past

Thermal instability in aviation fuel is not a new phenomenon. The problem first became apparent in the 1950s, during development of a novel turbojet engine. It produced more thrust than any engine before it, but due to the higher pressure ratio (12.5:1), temperatures were boosted significantly across the engine, resulting in higher thermal loading to components and fuel. The design made it particularly susceptible to problems arising from thermally unstable fuel. Low fuel flow rates in the manifold upstream of the fuel injectors resulted in fuel being exposed to high compressor outlet temperatures for long periods of time. Thermal degradation of the fuel in these passages formed insoluble materials, which deposited on filters and injector nozzles - altering nozzle flow and ultimately causing irregular combustor heat release, turbine failures and reduced engine life.

As a result of these observations, the first investigations into aviation fuel thermal stability were performed. A several hundred thousand hour programme of flight testing was carried out on five fuels in the engine by the US air force. Simultaneously, the Coordinating Research Council (CRC) developed a dynamic fuel testing device, named the CRC Fuel Coker. The device (described in more detail in appendix A) assessed thermal stability by thermally stressing fuel through a heated annulus and analysing the deposit formed on the heated surface and the pressure drop over a heated filter. The coker test became the first standard test method for thermal stability of aviation turbine fuel (ASTM D1660) in 1959.

The Coker can be considered the first in the line of laboratory scale devices used for specification testing of aviation fuels and quantification of thermal stability. Since then, a quest for efficient and accurate methods to study thermal stability has led to the development of many devices, both small and large scale, which will be discussed in greater detail later. Specification testing of fuels based on dynamic thermal stressing has helped to whittle down potentially troublesome fuels and only isolated incidents relating to suspect fuels in the late 1980s have been reported more recently [50].

Table 1.1: Trends in aviation gas turbine engine development (adapted from [48])

Engine	Bypass ratio	Year	Compression ratio	Relative fuel consumption	Compressor discharge temperature
JT4-11	0	1958	12.5:1	1	291
JT8-D	1	1960	17:1	0.88	360
JT9-D	5	1966	25:1	0.69	420
JT10D	6	1981	31:1	0.64	450
RR Trent 1000	10	2006	50:1	-	-
CFM LEAP	11	2016	40:1	-	-

The present

While specification testing has historically worked well in maintaining a minimum level of fuel stability to ensure safety, engine design has created an increasingly more hostile environment for fuel. The need for greater thrust and engine efficiency, combined with advances in materials technology has led to higher compressor outlet temperatures and pressure ratios, while fuel consumption has been reduced in part through higher bypass ratio designs. As a result, fuel is now exposed to higher temperatures at lower flow rates (see table 1.1). In addition, the continued depletion of sources for conventionally derived kerosene has driven the development of novel synthetic and bio fuels and blends - which maintains the requirement for accurate methods of assessment of the thermal stability of next generation fuels.

The future

Reduction of fuel consumption and emissions will remain a primary concern in aviation for some time. Lean burn engine architecture - where combustion takes place with excess air, can reduce NO_x emissions. However, when the fuel demand

is reduced, spill ratios (the ratio of burnt fuel to fuel recirculated around the fuel system) can increase, leading to longer residence times in hot sections of the engine, cyclic stressing and the potential for increased deposition from fuel thermal breakdown.

Future aviation will without doubt rely heavily on additive layer manufacturing (ALM). State of the art metal ALM methods (such as electron beam melting, selective laser melting and direct metal deposition) provide numerous advantages over traditional machining methods. ALM allows manufacturers to produce near net shape components, with little waste and dramatically truncated lead times. The resulting components can be made lighter than those made with traditional methods. The CFM LEAP engine, due in service in 2016, will feature the first fuel nozzles made by ALM, which are 25% lighter than a conventional nozzle. One problem with ALM that must be considered is the number of variables in the build process. Powder quality, step height, laser power and spot size, scanning speed and build orientation can all alter the surface quality [51]. For external surfaces, the increased roughness is of little concern, as further processing may be used to achieve the desired surface roughness. For internal passages created via ALM however, post processing may not be possible at all and the resulting relative surface roughness of the channel may be large. With this in mind, it is more important than ever to understand the effect of surface roughness in the context of fuel thermal stability.



Figure 1.1: CFM 'LEAP' ALM injector

1.1.1 Implications for aircraft

Aviation fuel does not only become useful in an aircraft when injected into the combustion chamber for thrust generation, but is used as a heat sink to cool other components and thus is stressed thermally with varying severity around the aircraft. The following areas in an aircraft fuel system may be sensitive to deposit formation [50];

Heat exchangers

Fuel is used to cool lubricant and hydraulic fluid. The heat exchanger tubes, which are designed to have high heat transfer coefficients to reduce weight and volume, may be significantly adversely affected by fuel deposit.

Fuel control

Downstream of the heat exchanger, hot fuel passes through valves and actuators with small clearances. Flow rates are low, potentially resulting in lengthy exposure to high temperatures. The fuel metering system may be impaired by fuel deposit.

Fuel injector feed arms and nozzles

Heated fuel passes through small passages eg. flow-divider valves, spin chambers and metering orifices. There is additional heat flux to the fuel from the compressor case and compressor discharge air stream, which flows around the nozzle stem. Flow divider valve operation can be severely affected by small amounts of deposit. Thick deposit can form on interior surfaces of the nozzle where fuel residence time is long. Deposit may flake off and obstruct passages downstream.

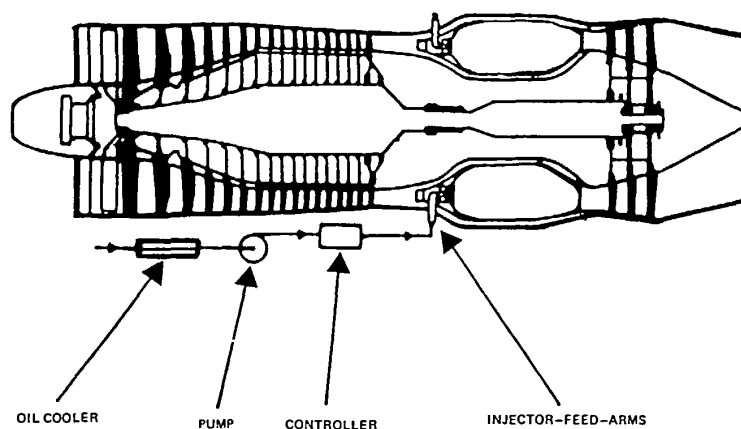


Figure 1.2: Components of a fuel system susceptible to fuel degradation products (taken from [1])

Chapter 2

Theoretical Introduction

The flow in an aircraft fuel system can be described by the conservation equations of mass, momentum and energy for viscous Newtonian fluids. Ultimately, this chapter presents the well known Navier-Stokes equations, whilst introducing aspects of fluid mechanics essential to the study of wall bounded flows. Of particular relevance are the relations of fluid viscosity, shear stress and the velocity and temperature distribution in the turbulent boundary layer. The approach towards the governing equations follows that of Prandtl [52] and Schlichting [53].

2.1 Fluid viscosity

Understanding the role of viscosity is vital to understanding the mechanics of real fluid flows. In some cases, considering a fluid as 'ideal' (or being inviscid) may yield an approximation of sufficient accuracy, perhaps in the case of particularly low viscosity fluids (eg. gases), far removed from the presence of boundaries. In these cases, only pressure forces normal to the fluid element are considered important. In reality however, viscosity is always at work, as a tangential force, or 'inner friction' of the fluid, working to oppose any forces acting to change the shape of a packet of fluid.

The effect of fluid viscosity can be demonstrated by considering a force balance for the simple case of two-dimensional flow between two long parallel plates. One plate is at rest, while the other plate moves with velocity U . Assuming that (due to friction), the fluid velocity at the surface of each plate is equal to the plate velocity (the no-slip boundary condition), and the fluid is Newtonian such that there is a linear distribution of fluid velocity between the two plates, the fluid

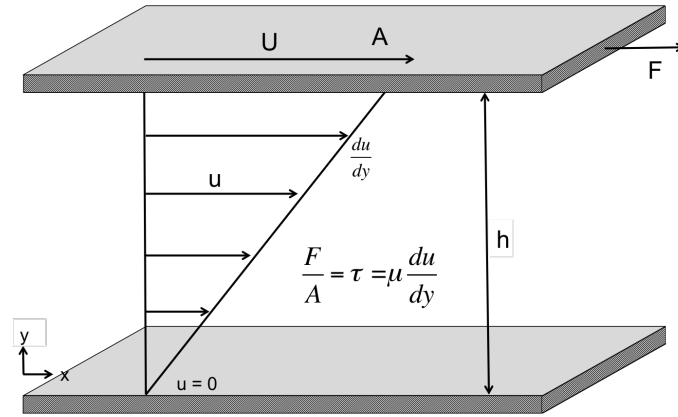


Figure 2.1: Shear flow between a moving and stationary plate

velocity is proportional to the distance from the lower plate;

$$u_{(y)} = \frac{y}{h} U \quad (2.1.1)$$

The viscosity of the fluid acts to oppose the motion of the upper plate (an equal and opposite force is exerted on the lower stationary plate) and the force per unit area may be described by;

$$\frac{F}{A} = \text{const} \frac{u}{y} \quad (2.1.2)$$

The force on the plate per unit area ($\frac{F}{A}$) is more commonly denoted as the shear stress (τ), and the term $\frac{u}{y}$ can be replaced by the gradient, $\frac{du}{dy}$. In practice, it is observed that to overcome the shear stress and keep the plate moving at velocity U , a force must be applied to the top plate.

In differential form the result is Newton's law of friction;

$$\tau = \mu \frac{du}{dy} \quad (2.1.3)$$

The constant of proportionality, μ is known as the dynamic viscosity of the fluid, and has units of kg/ms or Ns/m^2 . A further viscosity term, the kinematic viscosity may be derived by equating the fluid dynamic viscosity and density ($\nu = \frac{\mu}{\rho}$), the usefulness of which will be described later.

With this simple equation for fluid viscosity, it is possible to derive the Hagen-Poiseuille law for pressure drop for viscous flow in a circular pipe:

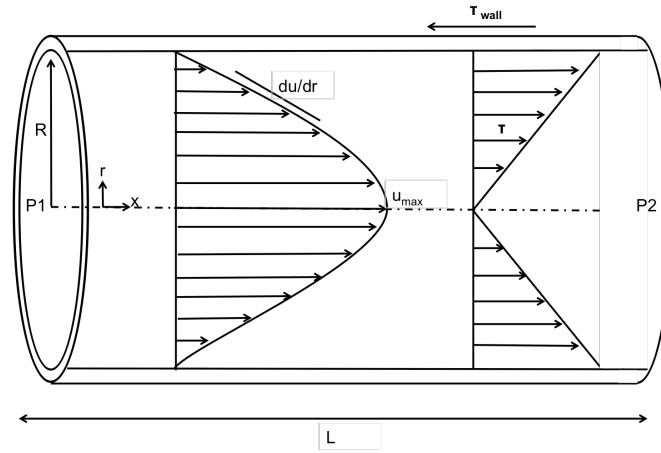


Figure 2.2: Shear in pipe flows

A pressure difference across the pipe ($P_1 - P_2$) results in a force $(P_1 - P_2)\pi r^2$ on a cylindrical element of fluid (radius, r). An equal and opposite force is produced by friction on the pipe wall ($2\pi r l \tau$). Equating the forces results in;

$$-\tau = \frac{P_1 - P_2}{l} \frac{r}{2} \quad (2.1.4)$$

substituting equation (x.x) into $\tau = \mu \frac{\partial u}{\partial r}$, rearranging and integrating gives the velocity profile;

$$u(r) = \frac{P_1 - P_2}{4\mu l} (R^2 - r^2) \quad (2.1.5)$$

The volume flow rate is thus;

$$Q = \int_0^R u 2\pi r dr = \frac{\pi R^4}{8\mu} \frac{P_1 - P_2}{l} \quad (2.1.6)$$

2.2 Reynolds number

Considering the volume element (dx, dy, dz) and evaluating the balance of frictional and inertial forces acting on the element (for steady flow in the x direction);

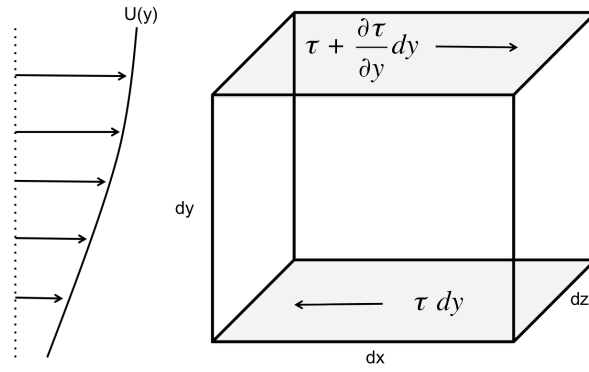


Figure 2.3: Shear forces on a volume element due to friction

The inertia force is expressed by;

$$\rho \frac{du}{dt} = \rho \frac{\partial u}{\partial x} \frac{dx}{dt} = \rho u \frac{\partial u}{\partial x} \quad (2.2.1)$$

The frictional force is expressed by;

$$\left(\tau + \frac{\partial \tau}{\partial y} dy\right) dx dz - \tau dx dz = \frac{\partial \tau}{\partial y} dx dy dz \quad (2.2.2)$$

The frictional force per unit volume can be described in terms of Newton's law of friction;

$$\frac{\partial \tau}{\partial y} = \mu \frac{\partial^2 u}{\partial y^2} \quad (2.2.3)$$

Therefore;

$$\frac{\text{inertia force}}{\text{friction force}} = \frac{\rho u \frac{\partial u}{\partial x}}{\mu \frac{\partial^2 u}{\partial y^2}} \quad (2.2.4)$$

Relating the velocity at any point to a characteristic velocity ' U ' and a characteristic length ' D ' (the duct diameter), then;

$$\frac{\partial u}{\partial x} \sim \frac{U}{D} \text{ and } \frac{\partial^2 u}{\partial y^2} \sim \frac{U}{D^2} \quad (2.2.5)$$

Thus the ratio of inertia force to friction force is;

$$Re = \frac{\rho U^2 / D}{\mu U / D^2} = \frac{\rho U D}{\mu} = \frac{U D}{\nu} \quad (2.2.6)$$

The Reynolds number can be shown to be dimensionless by evaluating the units;

$$\frac{\rho U D}{\mu} = \frac{kg}{m^3} \frac{m}{s} \frac{m}{kg} = 1 \quad (2.2.7)$$

Re is hugely significant - since two flows of different density and viscosity in

pipes of different diameters will show mechanical similarity if they have equal Re . Furthermore, considering a duct of constant area and for flow with constant density and viscosity, two conditions may be considered;

a) Frictional forces \gg inertia force

The flow is laminar, fluid flow is seen to move parallel to the pipe walls, in layers. There is no mixing (transfer of momentum) perpendicular to the flow direction.

b) Frictional force \ll inertia force

The flow is turbulent - displaying highly irregular, random, fluctuating motion. Wall-normal mixing is greatly enhanced.

2.3 Conservation equations for viscous, incompressible, laminar flow

By evaluating the normal and tangential components of fluxes and stresses on an infinitesimally small three dimensional fluid element, it is possible to derive general equations of motion for fluid flow. The equations can be simplified by making further assumptions about flow (ie. constant fluid properties and / or steady state flow). Turbulence further complicates the system of equations and will be introduced later. Although the fluid element is considered infinitesimally small, the size of the element is still much larger than the intermolecular distance such that the fluid obeys continuum mechanics.

2.3.1 Mass continuity

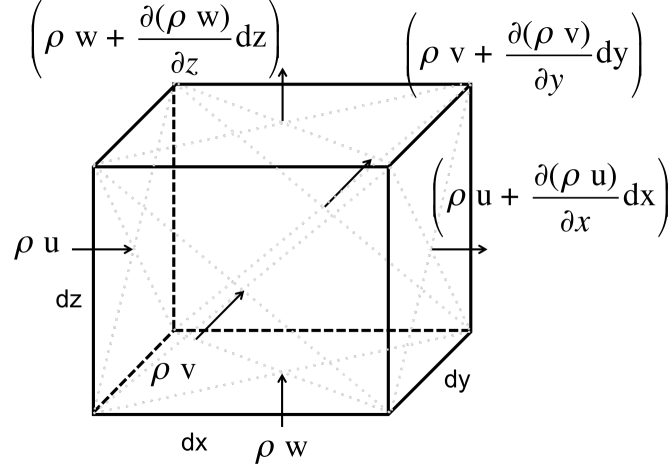


Figure 2.4: Mass flux across a volume element $dx dy dz$

Considering the mass flux in the x direction;

Rate of change of mass in the element = mass flux in - mass flux out

$$\frac{\partial \rho}{\partial t} dx dy dz = \rho u dy dz - \left(\rho u + \frac{\partial(\rho u)}{\partial x} dx \right) dy dz \quad (2.3.1)$$

(with similar expressions in y and z). Thus;

$$\begin{aligned} \frac{\partial \rho}{\partial t} dx dy dz &= \left(\rho u - \left(\rho u + \frac{\partial(\rho u)}{\partial x} dx \right) \right) dy dz \\ &\quad + \left(\rho v - \left(\rho v + \frac{\partial(\rho v)}{\partial y} dy \right) \right) dx dz \\ &\quad + \left(\rho w - \left(\rho w + \frac{\partial(\rho w)}{\partial z} dz \right) \right) dx dy \end{aligned} \quad (2.3.2)$$

Which, for an incompressible fluid ($\frac{d\rho}{dt} = 0$) reduces to;

$$\frac{\partial u}{\partial x} + \frac{\partial v}{\partial y} + \frac{\partial w}{\partial z} = 0 \quad (2.3.3)$$

Or, in compact, vector form;

$$\nabla \cdot \mathbf{v} = 0 \text{ where } \nabla = \left(\frac{d}{dx}, \frac{d}{dy}, \frac{d}{dz} \right) \quad (2.3.4)$$

2.3.2 Conservation of momentum

The same approach is applied to the momentum flux through the volume. The analysis is complicated by the fact that momentum is a vector quantity, and all

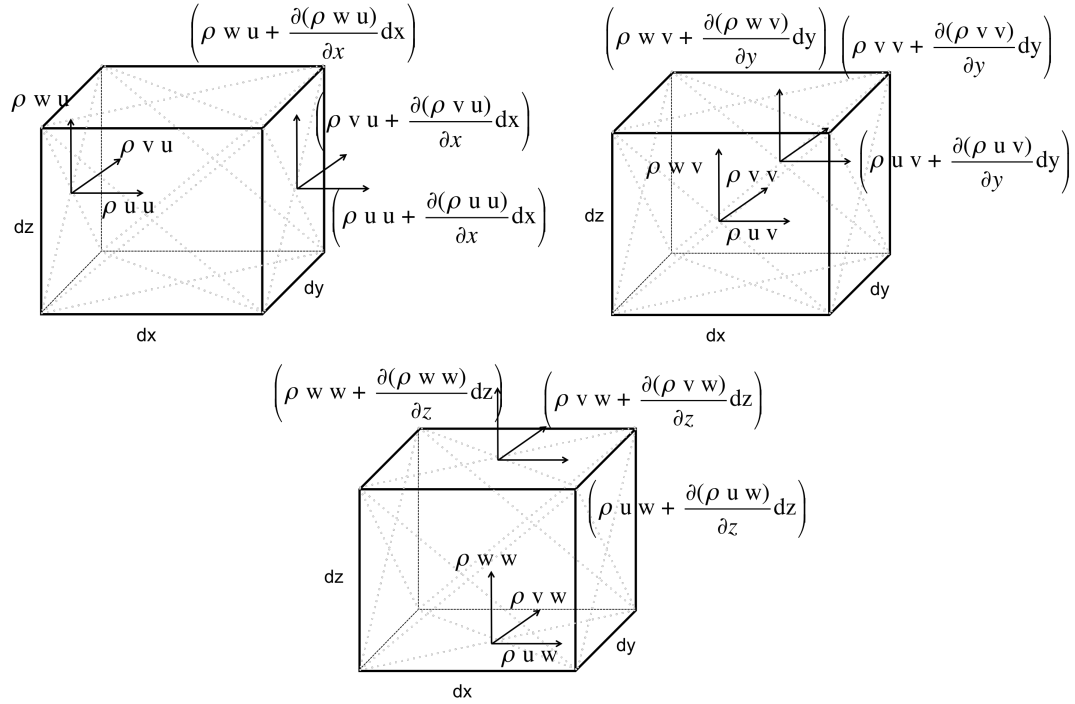


Figure 2.5: Momentum fluxes across a volume element $dx dy dz$

three velocity components must be evaluated.

$$\begin{aligned}
 &\text{Rate of change of momentum in the volume} = \\
 &\quad \text{sum of momentum flux in} \\
 &\quad - \text{sum of momentum flux out} \\
 &\quad + \text{sum of surface shear and normal stresses} \\
 &\quad + \text{body forces acting on the volume mass}
 \end{aligned}$$

Considering only the x component of momentum;

Rate of change of momentum;

$$\frac{d(\rho u)}{dt} dx dy dz \tag{2.3.5}$$

Momentum flux in;

$$(\rho u) u dy dz = \rho u u dy dz \tag{2.3.6}$$

Momentum flux out;

$$\left(\rho u u + \frac{\partial(\rho u u)}{\partial x} dx \right) dy dz \tag{2.3.7}$$

Equivalent expressions are formulated for surfaces $dx dz$ and $dx dy$ but with components of velocity v and w . Thus there are 3 expressions for momentum flux for

each surface (9 in total for momentum flux).

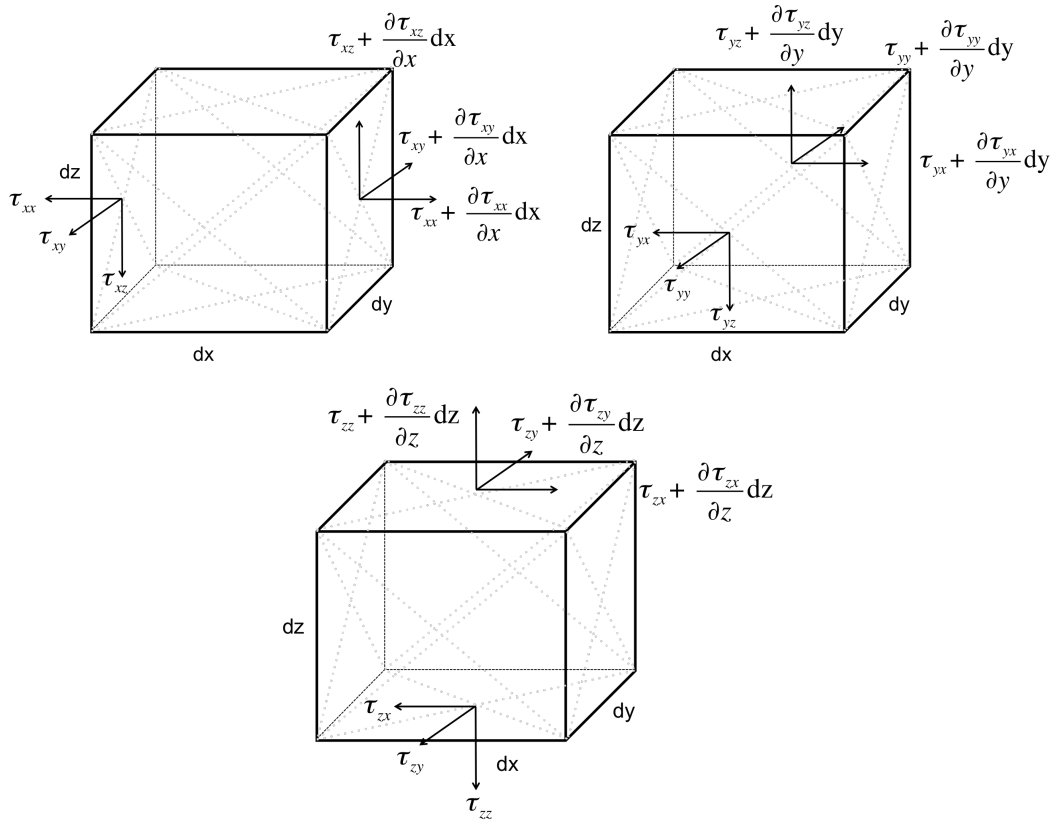


Figure 2.6: Surface forces (normal and shear)

Now the change in momentum arising from normal and tangential stresses (surface forces) and external forces (body or volume forces) must be considered.

The stress terms as defined as $\tau_{1,2}$, where index 1 indicates the surface on which the stress acts, and index 2 indicated the direction of the force from the resulting stress. A force is positive if the surface normal points in the positive coordinate direction and negative if it points in the negative coordinate direction.

The three normal and shear stress terms for the x component of momentum are;

$$\left(-\tau_{xx} + \left(\tau_{xx} + \frac{\partial \tau_{xx}}{\partial x} dx \right) \right) dy dz \quad (2.3.8)$$

$$\left(-\tau_{yx} + \left(\tau_{yx} + \frac{\partial \tau_{yx}}{\partial y} dy \right) \right) dx dz \quad (2.3.9)$$

$$\left(-\tau_{zx} + \left(\tau_{zx} + \frac{\partial \tau_{zx}}{\partial z} dz \right) \right) dx dy \quad (2.3.10)$$

The volume force term (eg. for gravitational effects) is defined as $\mathbf{F} = (F_x, F_y, F_z)$, therefore the total momentum balance in the x direction is;

$$\partial \frac{(\rho u)}{\partial t} + \frac{\partial(\rho u u)}{\partial x} + \frac{\partial(\rho u v)}{\partial y} + \frac{\partial(\rho u w)}{\partial z} = F_x + \frac{\partial\tau_{xx}}{\partial x} + \frac{\partial\tau_{yx}}{\partial y} + \frac{\partial\tau_{zx}}{\partial z} \quad (2.3.11)$$

(with equivalent expressions in the y and z directions).

The surface stresses are the sum of the hydrostatic pressure and viscous stresses from velocity gradients. Decomposing the normal stresses into components of pressure (p) and fluid friction ($\sigma_{xx,yy,zz}$), eg;

$$\tau_{xx} = \sigma_{xx} - p$$

and substituting;

$$\frac{(\partial\rho u)}{\partial t} + \frac{\partial(\rho u^2)}{\partial x} + \frac{\partial(\rho u v)}{\partial y} + \frac{\partial(\rho u w)}{\partial z} = F_x - \frac{\partial p}{\partial x} + \frac{\partial\sigma_{xx}}{\partial x} + \frac{\partial\tau_{yx}}{\partial y} + \frac{\partial\tau_{zx}}{\partial z}$$

with equivalent expressions in the y and z directions.

Expressing the normal and shear viscous stresses in terms of velocity gradients;

$$\sigma_{xx} = 2\mu \frac{\partial u}{\partial x} - \frac{2}{3}\mu \left(\frac{\partial u}{\partial x} + \frac{\partial v}{\partial y} + \frac{\partial w}{\partial z} \right) \quad (2.3.12)$$

(with similar expressions for $\sigma_{yy,zz}$. For incompressible flow, the continuity equation = 0 therefore the last term can be omitted).

$$\tau_{yx} = \tau_{xy} = \mu \left(\frac{\partial v}{\partial x} + \frac{\partial u}{\partial y} \right) \quad (2.3.13)$$

$$\tau_{zx} = \tau_{xz} = \mu \left(\frac{\partial u}{\partial z} + \frac{\partial w}{\partial x} \right) \quad (2.3.14)$$

$$\tau_{yz} = \tau_{zy} = \mu \left(\frac{\partial w}{\partial y} + \frac{\partial v}{\partial z} \right) \quad (2.3.15)$$

Resulting in the Navier-Stokes equations for laminar, incompressible flow;

Full form

$$\rho \left(\frac{\partial u}{\partial t} + \frac{\partial u^2}{\partial x} + \frac{\partial v u}{\partial y} + \frac{\partial w u}{\partial z} \right) = F_x - \frac{\partial p}{\partial x} + \frac{\partial}{\partial x} \left[2\mu \frac{\partial u}{\partial x} \right] + \frac{\partial}{\partial y} \left[\mu \left(\frac{\partial u}{\partial y} + \frac{\partial v}{\partial x} \right) \right] + \frac{\partial}{\partial z} \left[\mu \left(\frac{\partial w}{\partial x} + \frac{\partial u}{\partial z} \right) \right] \quad (2.3.16)$$

Non-conservative form

$$\rho \left(\frac{\partial u}{\partial t} + u \frac{\partial u}{\partial x} + v \frac{\partial u}{\partial y} + w \frac{\partial u}{\partial z} \right) = F_x - \frac{\partial p}{\partial x} + \mu \left(\frac{\partial^2 u}{\partial x^2} + \frac{\partial^2 u}{\partial y^2} + \frac{\partial^2 u}{\partial z^2} \right) \quad (2.3.17)$$

Vector form

$$\rho \left(\frac{\partial \mathbf{v}}{\partial t} + (\mathbf{v} \nabla) \mathbf{v} \right) = \mathbf{F} - \nabla p + \mu \Delta \mathbf{v} \quad (2.3.18)$$

2.3.3 Energy conservation

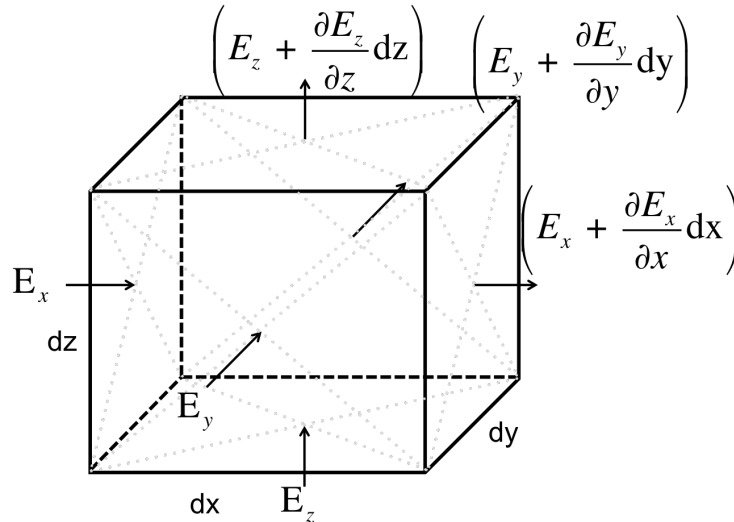


Figure 2.7: Convective energy flux across a volume element $dx \, dy \, dz$

Rate of change of total energy in a volume element =
 sum of energy fluxes entering and exiting the flow
 + sum of energy fluxes entering and exiting by means of heat conduction

- + sum of work done on volume element due to pressure, normal stress and shear stress forces
- + external energy input
- + work done per unit time due to effect of volume forces

The total energy within volume element is the sum of the internal energy and the kinetic energy;

$$\rho e dx dy dz + \rho \frac{\mathbf{v}^2}{2} dx dy dz \quad (2.3.19)$$

Therefore the rate of change within element is;

$$d\dot{E} = \frac{\partial[\rho(e + \frac{\mathbf{v}^2}{2})]}{\partial t} dx dy dz \quad (2.3.20)$$

Considering energy flux in and out for all faces;

$$\begin{aligned} \dot{E} = & \left[\rho(e + \frac{\mathbf{v}^2}{2})u - \left(\rho(e + \frac{\mathbf{v}^2}{2})u + \frac{\partial(\rho(e + \frac{\mathbf{v}^2}{2})u)}{\partial x} dx \right) \right] dy dz \\ & + \left[\rho(e + \frac{\mathbf{v}^2}{2})v - \left(\rho(e + \frac{\mathbf{v}^2}{2})v + \frac{\partial(\rho(e + \frac{\mathbf{v}^2}{2})v)}{\partial y} dy \right) \right] dx dz \\ & + \left[\rho(e + \frac{\mathbf{v}^2}{2})w - \left(\rho(e + \frac{\mathbf{v}^2}{2})w + \frac{\partial(\rho(e + \frac{\mathbf{v}^2}{2})w)}{\partial z} dz \right) \right] dx dy \end{aligned}$$

Which simplifies to;

$$\dot{E} = - \left(\frac{\partial(\rho(e + \frac{\mathbf{v}^2}{2})u)}{\partial x} + \frac{\partial(\rho(e + \frac{\mathbf{v}^2}{2})v)}{\partial y} + \frac{\partial(\rho(e + \frac{\mathbf{v}^2}{2})w)}{\partial z} \right) dx dy dz \quad (2.3.21)$$

Taking into account conduction via temperature gradients across the element ($d\dot{Q}$);

$$\dot{q} = -k \frac{dT}{dx} \quad (2.3.22)$$

As above, $d\dot{Q} = q_{in} - (q_{out} + \text{change in } \dot{q} \text{ over the elemental length})$, thus for all three faces;

$$d\dot{Q} = \left(\frac{\partial}{\partial x} \left(k \frac{\partial T}{\partial x} \right) + \frac{\partial}{\partial y} \left(k \frac{\partial T}{\partial y} \right) + \frac{\partial}{\partial z} \left(k \frac{\partial T}{\partial z} \right) \right) dx dy dz \quad (2.3.23)$$

Taking into account the work done $d\dot{A}$ on the volume element by pressure (p),

normal stress (σ_{xx}) and shear stress ($\tau_{xy,xz}$) (as in the previous expressions, the in and out terms cancel - the simplified form is shown for brevity);

$$d\dot{A}_x = \left(-\frac{\partial(pu)}{\partial x} + \frac{\partial(\sigma_{xx}u)}{\partial x} + \frac{\partial(\tau_{xy}v)}{\partial x} + \frac{\partial(\tau_{xz}w)}{\partial x} \right) dx dy dz$$

$$d\dot{A}_y = \left(-\frac{\partial(pv)}{\partial y} + \frac{\partial(\tau_{yx}v)}{\partial y} + \frac{\partial(\sigma_{yy}v)}{\partial y} + \frac{\partial(\tau_{yz}w)}{\partial y} \right) dx dy dz$$

$$d\dot{A}_z = \left(-\frac{\partial(pw)}{\partial z} + \frac{\partial(\tau_{zx}u)}{\partial z} + \frac{\partial(\tau_{zy}v)}{\partial z} + \frac{\partial(\sigma_{zz}w)}{\partial z} \right) dx dy dz$$

$$(\partial\dot{A} = \sum d\dot{A}_x, d\dot{A}_y, d\dot{A}_z)$$

The total energy balance is thus;

$$\begin{aligned} \frac{\partial(\rho[e + \frac{v^2}{2}])}{\partial t} = & - \left(\frac{\partial(\rho(e + \frac{v^2}{2})u)}{\partial x} + \frac{\partial(\rho(e + \frac{v^2}{2})v)}{\partial y} + \frac{\partial(\rho(e + \frac{v^2}{2})w)}{\partial z} \right) dx dy dz \\ & + \left(\frac{\partial}{\partial x}(k \frac{\partial T}{\partial x}) + \frac{\partial}{\partial y}(k \frac{\partial T}{\partial y}) + \frac{\partial}{\partial z}(k \frac{\partial T}{\partial z}) \right) dx dy dz \\ & + \left(-\frac{\partial(pu)}{\partial x} + \frac{\partial(\sigma_{xx}u)}{\partial x} + \frac{\partial(\tau_{xy}v)}{\partial x} + \frac{\partial(\tau_{xz}w)}{\partial x} \right) dx dy dz \\ & + \left(-\frac{\partial(pv)}{\partial y} + \frac{\partial(\tau_{yx}v)}{\partial y} + \frac{\partial(\sigma_{yy}v)}{\partial y} + \frac{\partial(\tau_{yz}w)}{\partial y} \right) dx dy dz \\ & + \left(-\frac{\partial(pw)}{\partial z} + \frac{\partial(\tau_{zx}u)}{\partial z} + \frac{\partial(\tau_{zy}v)}{\partial z} + \frac{\partial(\sigma_{zz}w)}{\partial z} \right) dx dy dz \\ & + \mathbf{F} \cdot \mathbf{v} + \rho \dot{q}_s \quad (2.3.24) \end{aligned}$$

where $\mathbf{F} \cdot \mathbf{v}$ is the work done due to the effect of volume forces and $\rho \dot{q}_s$ is a source term for external energy.

Recalling equations 2.3.12 - 15 for the formulation of normal and shear stresses in terms of velocity gradients and using the continuity equation results in the energy equation (in conservation form), in terms of internal energy;

$$\begin{aligned} \rho \left(\frac{\partial e}{\partial t} + u \frac{\partial e}{\partial x} + v \frac{\partial e}{\partial y} + w \frac{\partial e}{\partial z} \right) = \\ \left(\frac{\partial}{\partial x} \left[k \frac{\partial T}{\partial x} \right] + \frac{\partial}{\partial y} \left[k \frac{\partial T}{\partial y} \right] + \frac{\partial}{\partial z} \left[k \frac{\partial T}{\partial z} \right] \right) \\ - p (\nabla \cdot \mathbf{v}) + \mu \phi + \rho \dot{q}_s \end{aligned} \quad (2.3.25)$$

where ϕ is the dissipation function, accounting for the rate at which kinetic energy is converted to thermal energy due to viscous effects. Note that for incompressible flow, $\nabla \cdot \mathbf{v} = 0$.

The energy equation can be expressed in alternative forms using the thermodynamic relations;

$$\begin{aligned} e &= c_v T \\ h &= e + \frac{p}{\rho} = c_p T \\ e &= c_p T - \frac{p}{\rho} \end{aligned}$$

$$\begin{aligned} \rho c_p \left(\frac{\partial T}{\partial t} + u \frac{\partial T}{\partial x} + v \frac{\partial T}{\partial y} + w \frac{\partial T}{\partial z} \right) = \\ \beta T \left(\frac{\partial p}{\partial t} + u \frac{\partial p}{\partial x} + v \frac{\partial p}{\partial y} + w \frac{\partial p}{\partial z} \right) + \left(\frac{\partial}{\partial x} \left[k \frac{\partial T}{\partial x} \right] + \frac{\partial}{\partial y} \left[k \frac{\partial T}{\partial y} \right] + \frac{\partial}{\partial z} \left[k \frac{\partial T}{\partial z} \right] \right) \\ + \mu \phi + \rho \dot{q}_s \end{aligned} \quad (2.3.26)$$

where β is the coefficient of thermal expansion. The energy equation can be expressed in more compact form, assuming constant c_v , μ , k , ρ ;

$$\rho c_v \frac{dT}{dt} = k \nabla^2 T + \phi \quad (2.3.27)$$

2.4 Reynolds Averaged Navier-Stokes Equations

When the inertial forces in a flow are very much greater than the resistance to motion provided by the fluid viscosity, shear dominates and highly chaotic, rotational structures (eddies) of many sizes dominate the flow. The eddies are in

a continual state of creation and dissipation, with the largest structures, driven by the external conditions, disintegrating into smaller areas of rotation, and so on. As a result, mixing between fluid layers is greatly enhanced, and flow quantities deviate from the stable nature of ordered laminar flow. Reynolds first visualised the radically different structure of turbulent flow with respect to laminar flow by injecting dye into the fluid and noting the dispersion of the dye. Reynolds also provided a simple mathematical description of turbulence via analysis of the fluctuation of a flow quantity with time.

Following the approach of Reynolds, the flow quantities (eg. velocity, pressure and temperature) in turbulent flow may be described by decomposition into a time-averaged component ($\bar{\mathbf{a}}$) and an instantaneous fluctuation (\mathbf{a}'). For example;

$$\mathbf{a}(x, y, z, t) = \bar{\mathbf{a}}(x, y, z) + \mathbf{a}'(x, y, z, t) \quad (2.4.1)$$

where $\bar{\mathbf{a}} = \frac{1}{T} \int_0^T u(x, y, z, t) dt$

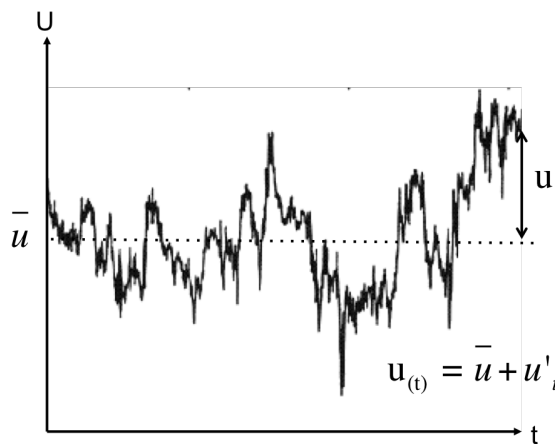


Figure 2.8: Reynolds decomposition of turbulent signal

The fluctuating components influence the mean components in such a way that the mean components experience an apparent resistance to motion, termed the 'apparent', 'turbulent' or 'eddy' viscosity'.

2.4.1 Reynolds stresses

Considering the momentum transfer across a small area of fluid, ' dA ' (surface normal perpendicular to the bulk fluid) in turbulent flow as a result of a turbulent fluctuation normal to the surface (v'). Fluid particles pass from a lower region,

through the surface to an adjacent upper region.

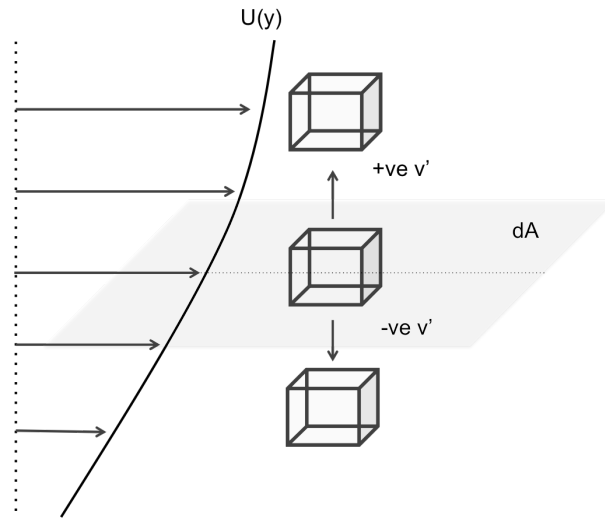


Figure 2.9: Transfer of momentum due to fluctuating velocity

The mass flow rate of fluid passing through dA is;

$$\rho v' dA \quad (2.4.2)$$

The x component of momentum flux of the fluid moving through dA is;

$$\rho v' dA u' \quad (2.4.3)$$

The increase in momentum is accompanied by a decrease in momentum of the fluid in the adjacent upper layer. The horizontal force (rate of change of momentum) acting on the fluid element dA due to the passing of fluid through the surface is therefore;

$$(\rho v' dA)(-u') = -\rho u'v' dA \quad (2.4.4)$$

Since rate of change of momentum = force, dividing by dA gives a term with the units of stress. Thus, the turbulent shear stress $\tau'_{xy} = -\rho \overline{u'v'}$ where $\overline{u'v'}$ (as the notation suggests) is the time average of the product of the fluctuating velocity components u' and v' . An important note is that while $\overline{a'} = 0$, $\overline{a'b'} \neq 0$.

This is more easily realised by considering a physical description. The fluid packet is projected upwards in the flow by the fluctuation $v' > 0$. The fluid packet comes from a region with lower average streamwise velocity \bar{u} , resulting in a negative u' effect for the fluid layer above the surface dA . Conversely, fluid passing downwards

through the surface as a result of a $v' < 0$ fluctuation comes from a higher average streamwise velocity, therefore the fluid layer below dA feels an increase in u' . In essence, positive u' is associated with negative v' , and vice versa. The time average $\overline{u'v'}$ is non zero and usually negative.

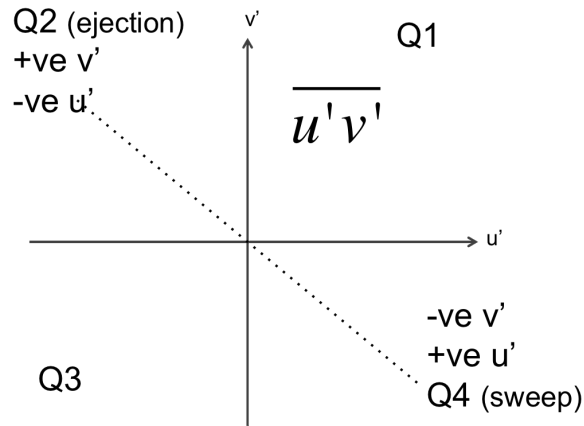


Figure 2.10: Typical correlation of $\overline{u'v'}$

The additional apparent stresses due to turbulence must be added to the steady laminar stresses and are included in the turbulent Reynolds equations.

2.4.2 Reynolds equations for turbulent flow

For turbulent flow, decomposition of the flow quantities into mean and fluctuating components and time averaging complicates the general equations of motion for laminar flow (as derived earlier) by introducing additional terms to the momentum and energy equations.

In the process of time averaging the general equations, some rules are implemented (a and b are flow quantities):

$$\begin{aligned}\frac{\overline{\partial a}}{\partial b} &= \frac{\partial \bar{a}}{\partial \bar{b}} \\ \overline{a + b} &= \bar{a} + \bar{b} \\ \overline{ab} &= \bar{a}\bar{b} \\ \overline{a'} &= 0\end{aligned}$$

2.4.2.1 Continuity equation

For brevity, index notation will be used ($i=1,2,3$ where $1=x$, $2=y$, $3=z$);

Time averaging and Reynolds decomposition of the continuity equation (incompressible flow) yields:

$$\overline{\frac{\partial u}{\partial x} + \frac{\partial v}{\partial y} + \frac{\partial w}{\partial z}} = 0 \quad (2.4.5)$$

$$\overline{\frac{\partial \bar{u}_i + u_i'}{\partial x_i}} = 0 \quad (2.4.6)$$

$$\overline{\frac{\partial \bar{u}_i + u_i'}{\partial x_i}} = \frac{\partial \bar{u}_i}{\partial x_i} + \frac{\partial u_i'}{\partial x_i} = \frac{\partial \bar{u}_i}{\partial x_i} \quad (2.4.7)$$

The continuity equation is unaffected by time averaging since the term $\overline{\frac{\partial u_i'}{\partial x_i}} = 0$, therefore

$$\frac{\partial \bar{u}}{\partial x} + \frac{\partial \bar{v}}{\partial y} + \frac{\partial \bar{w}}{\partial z} = 0 \quad (2.4.8)$$

2.4.2.2 Momentum equations

The momentum equation in the x direction will be used for example. Taking the time average;

$$\rho \overline{\left(\frac{\partial u}{\partial t} + \frac{\partial u^2}{\partial x} + \frac{\partial(uv)}{\partial y} + \frac{\partial(uw)}{\partial z} \right)} = F_x - \frac{\partial p}{\partial x} + \frac{\partial \sigma_{xx}}{\partial x} + \frac{\partial \tau_{yx}}{\partial y} + \frac{\partial \tau_{zx}}{\partial z}$$

Decomposition of the velocity components results in;

$$\begin{aligned} \frac{\partial(\overline{u+u'})^2}{\partial x} + \frac{\partial(\overline{u+u'})(\overline{v+v'})}{\partial y} + \frac{\partial(\overline{u+u'})(\overline{w+w'})}{\partial z} = \\ \frac{\partial(\overline{u^2})}{\partial x} + \frac{\partial(\overline{u'^2})}{\partial x} + \frac{\partial(2\overline{u u'})}{\partial x} + \frac{\partial(\overline{u v})}{\partial y} + \frac{\partial(\overline{u v'})}{\partial y} + \frac{\partial(\overline{u' v})}{\partial y} + \frac{\partial(\overline{u' v'})}{\partial y} \\ + \frac{\partial(\overline{u w})}{\partial z} + \frac{\partial(\overline{u w'})}{\partial z} + \frac{\partial(\overline{u' w})}{\partial z} + \frac{\partial(\overline{u' w'})}{\partial z} \end{aligned}$$

Since the barred square terms are already constant with time they remain unchanged. Terms which are linear in the fluctuating quantities drop away ($\frac{\partial u'}{\partial t}$ and $\frac{\partial^2 u'}{\partial x^2}$). Terms which are quadratic in the fluctuating quantities remain ($\overline{u'^2}$ and $\overline{u'v'}$);

$$= \frac{\partial(\overline{u^2})}{\partial x} + \frac{\partial(\overline{u'^2})}{\partial x} + \frac{\partial(\overline{u v})}{\partial y} + \frac{\partial(\overline{u' v'})}{\partial y} + \frac{\partial(\overline{u w})}{\partial z} + \frac{\partial(\overline{u' w'})}{\partial z}$$

Thus the Reynolds averaged momentum equations become;

$$\begin{aligned} \rho \left(\frac{\partial(\overline{u})}{\partial t} + \frac{\partial(\overline{u^2})}{\partial x} + \frac{\partial(\overline{u v})}{\partial y} + \frac{\partial(\overline{u w})}{\partial z} \right) = F_x - \frac{\partial \overline{p}}{\partial x} + \frac{\partial \overline{\sigma}_{xx}}{\partial x} + \frac{\partial \overline{\tau}_{yx}}{\partial y} + \frac{\partial \overline{\tau}_{zx}}{\partial z} \\ - \rho \left(\frac{\partial(\overline{u'^2})}{\partial x} + \frac{\partial(\overline{u' v'})}{\partial y} + \frac{\partial(\overline{u' w'})}{\partial z} \right) \quad (2.4.9) \end{aligned}$$

$$\begin{aligned} \rho \left(\frac{\partial(\overline{v})}{\partial t} + \frac{\partial(\overline{v u})}{\partial x} + \frac{\partial(\overline{v^2})}{\partial y} + \frac{\partial(\overline{v w})}{\partial z} \right) = F_y - \frac{\partial \overline{p}}{\partial y} + \frac{\partial \overline{\tau}_{xy}}{\partial x} + \frac{\partial \overline{\sigma}_{yy}}{\partial y} + \frac{\partial \overline{\tau}_{zy}}{\partial z} \\ - \rho \left(\frac{\partial(\overline{v' u'})}{\partial x} + \frac{\partial(\overline{v'^2})}{\partial y} + \frac{\partial(\overline{v' w'})}{\partial z} \right) \quad (2.4.10) \end{aligned}$$

$$\rho \left(\frac{\partial(\bar{w})}{\partial t} + \frac{\partial(\bar{w}\bar{u})}{\partial x} + \frac{\partial(\bar{w}\bar{v})}{\partial y} + \frac{\partial(\bar{w}^2)}{\partial z} \right) = F_z - \frac{\partial\bar{p}}{\partial z} + \frac{\partial\bar{\tau}_{xz}}{\partial x} + \frac{\partial\bar{\tau}_{yz}}{\partial y} + \frac{\partial\bar{\sigma}_{zz}}{\partial z} - \rho \left(\frac{\partial(\overline{w'u'})}{\partial x} + \frac{\partial(\overline{w'v'})}{\partial y} + \frac{\partial(\overline{w'^2})}{\partial z} \right) \quad (2.4.11)$$

Note that the complete stresses due to viscosity and turbulence then become (for example);

$$\sigma_{xx} = 2\mu \frac{\partial\bar{u}}{\partial x} - \rho\overline{u'^2}$$

$$\tau_{xy} = \mu \left(\frac{\partial\bar{u}}{\partial y} + \frac{\partial\bar{v}}{\partial x} \right) - \rho\overline{u'v'}$$

2.4.2.3 Energy equation

The turbulent kinetic energy (k) equation

The kinetic energy equation or 'budget', is useful for the study of turbulent flows and describes the balance of convection, production, diffusion (turbulent and viscous) and dissipation of turbulent kinetic energy.

The turbulent kinetic energy is usually defined as;

$$k = \frac{1}{2}\overline{q^2} = \frac{1}{2}(\overline{u'^2 v'^2 w'^2}) \quad (2.4.12)$$

For steady flow and constant fluid properties, the turbulent kinetic energy equation is;

$$\begin{aligned}
 (1) & \rho \left(\bar{u} \frac{\partial k}{\partial x} + \bar{v} \frac{\partial k}{\partial y} + \bar{w} \frac{\partial k}{\partial z} \right) = \\
 (2) & - \frac{\partial}{\partial x} \overline{[u'(p' + \frac{\rho q^2}{2})]} - \frac{\partial}{\partial y} \overline{[v'(p' + \frac{\rho q^2}{2})]} - \frac{\partial}{\partial z} \overline{[w'(p' + \frac{\rho q^2}{2})]} \\
 (3) & + \mu \left[\frac{\partial^2}{\partial x^2} (k + \overline{u'^2}) + \frac{\partial^2}{\partial y^2} (k + \overline{v'^2}) + \frac{\partial^2}{\partial z^2} (k + \overline{w'^2}) \right. \\
 & \quad \left. + 2 \left(\frac{\partial^2 \overline{u'v'}}{\partial x \partial y} + \frac{\partial^2 \overline{v'w'}}{\partial y \partial z} + \frac{\partial^2 \overline{w'u'}}{\partial z \partial x} \right) \right] \\
 (4) & - \rho \left(\overline{u'^2} \frac{\partial \bar{u}}{\partial x} + \overline{u'v'} \frac{\partial \bar{v}}{\partial x} + \overline{u'w'} \frac{\partial \bar{w}}{\partial x} \right. \\
 & \quad + \overline{u'v'} \frac{\partial \bar{u}}{\partial y} + \overline{v'^2} \frac{\partial \bar{v}}{\partial y} + \overline{v'w'} \frac{\partial \bar{w}}{\partial y} \\
 & \quad \left. + \overline{u'w'} \frac{\partial \bar{u}}{\partial z} + \overline{v'w'} \frac{\partial \bar{v}}{\partial z} + \overline{w'^2} \frac{\partial \bar{w}}{\partial z} \right) \\
 (5) & - \rho \epsilon
 \end{aligned} \tag{2.4.13}$$

Table 2.1: Turbulent kinetic energy budget

Term	Describes
(1)	Convection by mean flow
(2)	Turbulent diffusion
(3)	Viscous diffusion
(4)	Turbulence production
(5)	Dissipation

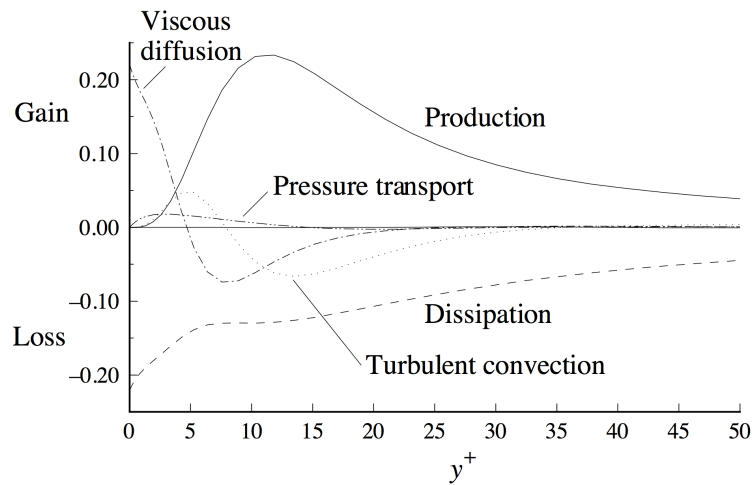


Figure 2.11: TKE budget for the near wall region (DNS data of Kim et al [2])

Turbulent thermal energy equation

For turbulent flow, two additional terms occur in the thermal energy equation due to turbulent heat transport and dissipation. The thermal energy equation becomes (assuming constant physical properties);

$$\begin{aligned}
(1) \quad & \rho c_p \left(\bar{u} \frac{\partial \bar{T}}{\partial x} + \bar{v} \frac{\partial \bar{T}}{\partial y} + \bar{w} \frac{\partial \bar{T}}{\partial z} \right) = \\
(2) \quad & k \left(\frac{\partial^2 \bar{T}}{\partial x^2} + \frac{\partial^2 \bar{T}}{\partial y^2} + \frac{\partial^2 \bar{T}}{\partial z^2} \right) \\
(3) \quad & - \rho c_p \left(\frac{\partial \overline{u' T'}}{\partial x} + \frac{\partial \overline{v' T'}}{\partial y} + \frac{\partial \overline{w' T'}}{\partial z} \right) \\
(4) \quad & + \phi \\
(5) \quad & + \rho \epsilon
\end{aligned} \tag{2.4.14}$$

Table 2.2: Turbulent thermal energy equation terms

Term	Describes
(1)	Convection by mean flow
(2)	Molecular heat transport
(3)	Turbulent heat transport
(4)	Direct dissipation
(5)	Turbulent dissipation

2.4.3 Closure of the Reynolds equations

The additional Reynolds stresses arising from turbulent fluctuations are unknown, and leave the Reynolds equations unclosed. Additional equations are required to express the Reynolds stresses based on the mean flow quantities.

2.4.3.1 Boussinesq eddy viscosity hypothesis

Considering a simplified form of the x-momentum equation for the boundary layer:

$$\rho \left(u \frac{\partial u}{\partial x} + v \frac{\partial u}{\partial y} \right) = -\frac{\partial p}{\partial x} + \frac{\partial}{\partial y} \left(\mu \frac{\partial u}{\partial y} - \rho \overline{u' v'} \right) \tag{2.4.15}$$

therefore, the total shear stress due to viscosity and the resistance to motion by turbulence fluctuations;

$$\tau_{total} = \mu \frac{\partial \bar{u}}{\partial y} - \rho \overline{u'v'} \quad (2.4.16)$$

Boussinesq proposed that the contribution of shear stress due to turbulent fluctuations be analogous to Newton's law of friction and be related to the mean velocity;

$$\tau_{turb} = \mu_t \frac{\partial \bar{u}}{\partial y} \quad (2.4.17)$$

where μ_t is called the eddy / turbulent viscosity or ν_t (the kinematic eddy viscosity or the eddy diffusivity of momentum). The total shear stress can then be formulated as;

$$\tau_{total} = (\mu + \mu_{turb}) \frac{\partial \bar{u}}{\partial y} = \rho(\nu + \nu_{turb}) \frac{\partial \bar{u}}{\partial y} \quad (2.4.18)$$

2.4.3.2 Prandtl mixing length

Prandtl developed a model for turbulent viscosity based on the idea of the 'mixing length'. Key to the idea is the correlation between u' and v' and that $\overline{u'v'} \neq 0$

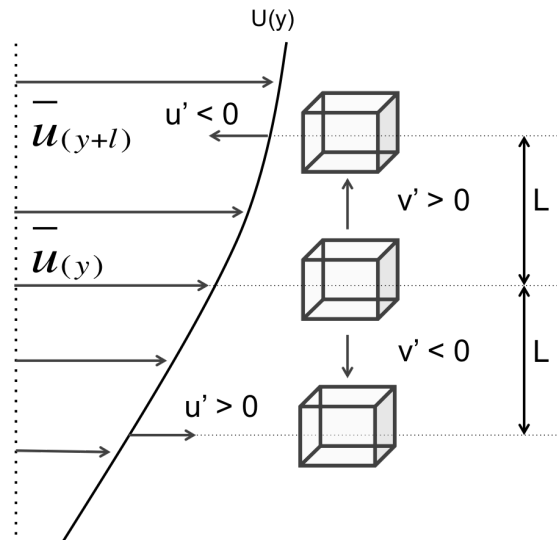


Figure 2.12: Prandtl mixing length model

Considering a liquid element in the boundary layer with mean velocity $\bar{u}(y)$ displaced from position y to $y + L$ by a velocity fluctuation.

$$\Delta u = \bar{u}(y + L) - \bar{u}(y) \text{ or } \Delta u = l \frac{\partial \bar{u}}{\partial y} \text{ which is the same order of magnitude as } u'.$$

Prandtl then assumed u' and v' were the same order of magnitude resulting in;

$$\tau_{turb} = -\overline{(u'v')} = (\Delta u)^2 = \rho l^2 \left| \frac{\partial \bar{u}}{\partial y} \right| \frac{\partial \bar{u}}{\partial y} \quad (2.4.19)$$

Note: negative u' is associated with positive v' and vice versa, therefore the product $(u'v')$ is always < 0 . The absolute value $\left| \frac{\partial \bar{u}}{\partial y} \right|$ is taken to ensure negative $\frac{\partial \bar{u}}{\partial y}$ produces negative τ_t .

The eddy viscosity, ν_t can be expressed in terms of the Prandtl mixing length;

$$\nu_t = l^2 \left| \frac{\partial \bar{u}}{\partial y} \right| \quad (2.4.20)$$

2.4.4 Wall bounded turbulent flow - velocity profiles

For wall bounded flows, there are two important considerations;

- a) At the wall, due to the no slip boundary condition ($u_{(y=0)} = 0$), there must be a very small viscous region due to the reduction in fluid inertia caused by the frictional resistance of wall.
- b) The mixing length must tend to 0 at the wall.

2.4.4.1 Inner layer : Prandtl law of the wall

In the analysis that follows it is assumed that $\tau = \tau_{wall} = constant$

Recalling that;

$$\tau_{total} = \mu \frac{\partial \bar{u}}{\partial y} + \rho l^2 \left(\frac{\partial \bar{u}}{\partial y} \right)^2 \quad (2.4.21)$$

Assuming sufficiently large Re such that the second term is very much larger than the first viscous term, and sufficient distance from the wall such that viscous effects are negligible, in important term is defined called the friction velocity (U^*), which has the same order of magnitude as the the fluctuating velocities due to turbulence (u', v');

$$U^* = \sqrt{\frac{\tau}{\rho}} = l \frac{\partial \bar{u}}{\partial y} = \sqrt{u'v'} \quad (2.4.22)$$

The mixing length is assumed to be related to the distance from the wall, y such that;

$$l = \kappa y$$

where κ is the von Karman constant. Therefore;

$$U^* = \kappa y \frac{d\bar{u}}{dy}$$

$$\frac{d\bar{u}}{dy} = \frac{1}{\kappa} \frac{U^*}{y}$$

$$d\bar{u} = \frac{1}{\kappa} \frac{U^*}{y} dy$$

Integrating yields the logarithmic wall law;

$$\bar{u} = U^* \frac{1}{\kappa} \ln y + C \quad (2.4.23)$$

Or, alternatively by dimensional reasoning;

$$U = f(y, U^*, \nu)$$

$$\frac{\bar{u}}{U^*} = f\left(\frac{yU^*}{\nu}\right)$$

The dimensionless logarithmic velocity profile for the turbulent boundary layer becomes;

$$\frac{\bar{u}}{U^*} = \frac{1}{\kappa} \ln \left(\frac{yU^*}{\nu} \right) + C_1 \quad (2.4.24)$$

or,

$$u^+ = \frac{1}{\kappa} \ln (y^+) + C_1 \quad (2.4.25)$$

where $\frac{\nu}{U^*}$ can be considered as a viscous length, $u^+ = \frac{\bar{u}}{U^*}$ and $y^+ = \frac{yU^*}{\nu}$.

Prandtl proposed that the wall law for rough walls be of the form;

$$u^+ = \frac{1}{\kappa} \ln (k^+) + C_{1r} \quad (2.4.26)$$

for small roughness where $k^+ = \frac{kU^*}{\nu}$ is the roughness Reynolds number and the

viscous length scale is still relevant.

Or, for large roughness;

$$u^+ = \frac{1}{\kappa} \ln\left(\frac{y}{k}\right) + C_{1r} \quad (2.4.27)$$

2.4.4.2 Outer layer: velocity defect law (von Karman)

Towards the turbulent core, in the outer regions of the boundary layer, the viscous length scale ($\frac{\nu}{U^*}$) is no longer appropriate since the turbulent shear stress is many times greater than the viscous stress. The functional dependence of the velocity with the flow variables can be written as;

$$\frac{U_{max} - \bar{u}(y)}{U^*} = g(\eta) = g\left(\frac{y}{R}\right) \quad (2.4.28)$$

where normalisation is by the pipe radius, R in this case.

The non dimensional velocity distribution for the outer layer (also known as the velocity defect law) is;

$$\frac{U_{max} - \bar{u}(y)}{U^*} = -\frac{1}{\kappa} \ln\frac{y}{R} + C2 \quad (2.4.29)$$

The universal wall laws have been confirmed by experiment, yielding:

Inner law:

$$u^+ = \frac{1}{0.4} \ln(y^+) + 5.5 \quad (2.4.30)$$

Velocity defect law:

$$\frac{U_{max} - \bar{u}(y)}{U^*} = -\frac{1}{0.4} \ln\left(\frac{y}{R}\right) + 0.8 \quad (2.4.31)$$

although other constants have been calculated by for other types of flows (see [54]).

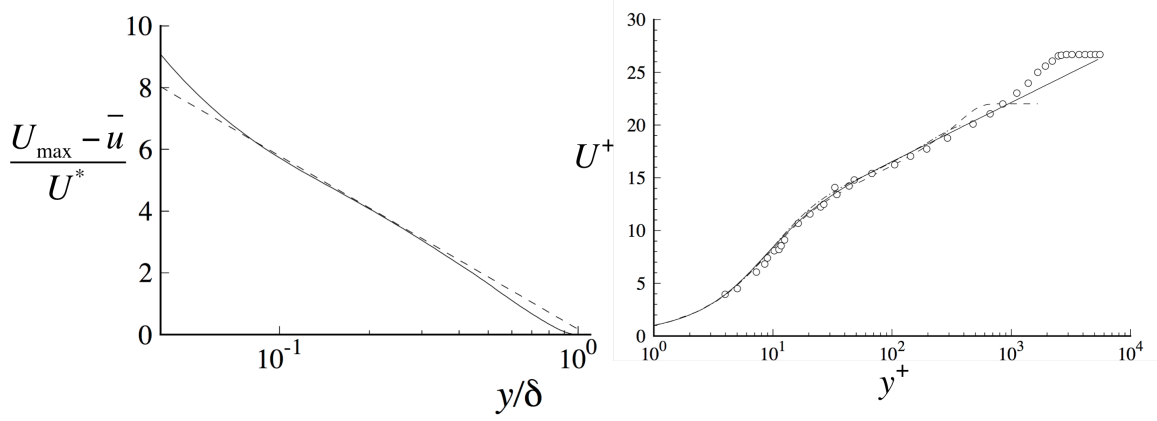


Figure 2.13: Universal smooth wall velocity distributions, DNS data of Kim et al [2]. Left: outer layer. Right: inner layer

2.4.5 Smooth pipe friction factor

The Darcy friction factor (λ) is defined as;

$$\lambda = \frac{8 \tau_w}{\rho U_{avg}^2} = 8 \left(\frac{U^*}{U_{avg}} \right)^2 \quad (2.4.32)$$

The friction factor can be calculated from the *average* bulk velocity, rather than the maximum velocity.

Laminar flow

The velocity profile in a circular pipe in laminar flow can be shown to be;

$$u(r) = -\frac{R^2}{4\mu} \left(\frac{dP}{dx} \right) \left(1 - \frac{r^2}{R^2} \right)$$

The average velocity is;

$$U_{avg} = \frac{2}{R^2} \int_0^R u(r) r dr = -\frac{R^2}{8\mu} \left(\frac{dP}{dx} \right)$$

$$U_{avg} = -\frac{R^2}{8\mu} \left(\frac{P_2 - P_1}{l} \right)$$

$$P_1 - P_2 = \frac{8\mu L U_{avg}}{R^2} = \frac{32\mu L U_{avg}}{D^2}$$

the pressure loss can be expressed as;

$$P_1 - P_2 = \lambda \frac{L}{D} \frac{\rho U_{avg}^2}{2}$$

therefore;

$$\lambda = \frac{64\mu}{\rho V D} = \frac{64}{Re} \quad (2.4.33)$$

Turbulent flow

With the velocity profile in the form;

$$\frac{U_{avg}}{U^*} = \frac{1}{\kappa} \ln \frac{U^* D}{\nu} + C'_2$$

where $\frac{U_0 - U_{avg}}{U^*} \approx 3.75$.

Forming $\frac{U^* D}{\nu}$ as the product $\frac{U_{avg} D}{\nu} \frac{U^*}{2U_{avg}}$ and recalling that $\lambda = 8 \left(\frac{U^*}{U_{avg}}\right)^2$ results in the Prandtl smooth pipe friction factor formula;

$$\frac{1}{\sqrt{\lambda}} = \frac{1}{\kappa\sqrt{8}} \ln (Re \sqrt{\lambda}) + C_3 \quad (2.4.34)$$

with experimentally determined constants $\frac{1}{\kappa\sqrt{8}} = 0.87$ and $C_3 = -0.8$

2.5 Analogies for momentum, heat and mass transfer for the boundary layer

The simplified forms of the 2D momentum, energy and species equations for the boundary layer may be non dimensionalised with the substitution of certain similarity parameters;

$$\text{Distance: } x^* = \frac{x}{L}, y^* = \frac{y}{L}$$

$$\text{Velocity: } u^* = \frac{u}{U_{avg}}, v^* = \frac{v}{U_{avg}}$$

$$\text{Temperature: } T^* = \frac{T - T_s}{T_\infty - T_s}$$

$$\text{Concentration: } C_a^* = \frac{C_a - C_{a_s}}{C_{a_\infty} - C_{a_s}}$$

Momentum (zero pressure gradient);

$$u \frac{\partial u}{\partial x} + v \frac{\partial u}{\partial y} = \nu \frac{\partial^2 u}{\partial y^2}$$

becomes;

$$u^* \frac{\partial u^*}{\partial x^*} + v^* \frac{\partial u^*}{\partial y^*} = \frac{\nu}{V L} \frac{\partial^2 u^*}{\partial y^{*2}}$$

or, since $Re = \frac{VL}{\nu}$;

$$u^* \frac{\partial u^*}{\partial x^*} + v^* \frac{\partial u^*}{\partial y^*} = \frac{1}{Re} \frac{\partial^2 u^*}{\partial y^{*2}} \quad (2.5.1)$$

Energy (neglecting the viscous dissipation term);

$$u \frac{\partial T}{\partial x} + v \frac{\partial T}{\partial y} = \alpha \frac{\partial^2 u}{\partial y^2}$$

becomes;

$$u^* \frac{\partial T^*}{\partial x^*} + v^* \frac{\partial T^*}{\partial y^*} = \frac{\alpha}{V L} \frac{\partial^2 u^*}{\partial y^{*2}}$$

or, with the Prandtl number, $Pr = \frac{\nu}{\alpha}$

$$u^* \frac{\partial T^*}{\partial x^*} + v^* \frac{\partial T^*}{\partial y^*} = \frac{1}{Re Pr} \frac{\partial^2 u^*}{\partial y^{*2}} \quad (2.5.2)$$

Species;

$$u \frac{\partial Ca}{\partial x} + v \frac{\partial Ca}{\partial y} = D_{AB} \frac{\partial^2 Ca}{\partial y^2}$$

becomes;

$$u^* \frac{\partial Ca^*}{\partial x^*} + v^* \frac{\partial Ca^*}{\partial y^*} = \frac{D_{AB}}{V L} \frac{\partial^2 Ca^*}{\partial y^{*2}}$$

or with the Schmidt number, $Sc = \frac{\nu}{D_{AB}}$

$$u^* \frac{\partial Ca^*}{\partial x^*} + v^* \frac{\partial Ca^*}{\partial y^*} = \frac{1}{Re Sc} \frac{\partial^2 Ca^*}{\partial y^{*2}} \quad (2.5.3)$$

2.5.1 Dimensionless gradients

Velocity gradient

$$\tau_w = \mu \frac{\partial u}{\partial y} = \left(\frac{\mu V}{L} \right) \frac{\partial u^*}{\partial y^*}$$

$$\lambda = \frac{8\tau_w}{\rho V_{avg}^2} = \frac{8\mu}{\rho V L} \frac{\partial u^*}{\partial y^*} = \frac{8}{Re} \frac{\partial u^*}{\partial y^*}$$

From equation 2.5.1;

$$u^* = f_1(x^*, y^*, Re)$$

$$\frac{\partial u^*}{\partial y^*} = f_2(x^*, Re)$$

Therefore;

$$\lambda = \frac{8}{Re} f_2(x^*, Re) \quad (2.5.4)$$

Temperature gradient

Combining Fourier's law for conduction at the solid-fluid interface;

$$q_s = -k_f \frac{\partial T}{\partial y} \Big|_{y=0}$$

with Newtons law of cooling:

$$q_s = h(T_s - T_\infty)$$

The heat transfer coefficient for the thermal boundary layer becomes;

$$h_x = \frac{-k \frac{\partial T}{\partial y}}{T_s - T_\infty} = -\frac{k}{L} \frac{T_\infty - T_s}{L(T_s - T_\infty)} \frac{\partial T^*}{\partial y^*} = \frac{k}{L} \frac{\partial T^*}{\partial y^*}$$

Rearranging, the Nusselt number is formed;

$$Nu_x = \frac{h_x L}{k} = \frac{\partial T^*}{\partial y^*} = g_2(x^*, Re, Pr) \quad (2.5.5)$$

$$Nu_{avg} = \frac{h_{avg} L}{k} = g_3(Re, Pr) \quad (2.5.6)$$

The Nusselt number is commonly expressed as a power law of the form;

$$Nu = C Re^m Pr^n \quad (2.5.7)$$

Concentration gradient

Combining expressions for mass diffusion and convection;

$$\bar{j}_A = \frac{\dot{m}_A}{A_s} - \rho D_{AB} \frac{\partial w_a}{\partial y} = h_{mass}(w_a - w_{a,\infty}) \quad (2.5.8)$$

The Nu equivalent for mass transfer, the Sherwood number is;

$$Sh = \frac{h_{mass} L_c}{D_{AB}} \quad (2.5.9)$$

2.5.2 Reynolds analogy

When $Pr = 1$, the forms of the non dimensional boundary layer momentum and energy equations become identical;

$$\frac{\partial u^*}{\partial y^*} = \frac{\partial T^*}{\partial y^*} \quad (2.5.10)$$

The friction factor and convection coefficient can be related according to;

$$\lambda \frac{Re}{8} = Nu \quad (2.5.11)$$

or alternatively;

$$\frac{\lambda}{8} = St = \frac{Nu}{Re Pr} = St_m = \frac{Sh}{Re Sc} \quad (2.5.12)$$

where St is the Stanton number, St_m the mass transfer Stanton number, Sh the Sherwood number ($\frac{h_m L}{D_{AB}}$) and Sc the Schmidt number ($\frac{\nu}{D_{AB}}$).

For $Pr \neq 1$, the analogy was modified by Chilton and Colburn;

$$\lambda \frac{Re}{8} = Nu Pr^{-1/3} \quad (2.5.13)$$

or;

$$\frac{\lambda}{8} = St Pr^{2/3} = St_{mass} Sc^{2/3} \quad (2.5.14)$$

valid for $0.6 < Pr < 60$ and $0.6 < Sc < 3000$

Chapter 3

Literature Review

3.1 Physical and Chemical Aspects of Thermal Stability

The following is a review of the literature describing mainly experimental work which established the foundation for understanding fuel thermal stability. The bulk of the studies were performed between 1960-2000. More recent experimental work has been focused towards the quantification of reaction products and the validation of reduced chemical kinetics mechanisms and numerical models by experiment. For this reason, this review is centered around the earlier experimental work, which is more relevant to this thesis.

3.1.1 Chemical aspects

Conventional aviation fuel is primarily composed of kerosene - hydrocarbons distilled from petroleum between 150 and 290°C with between 5-15 carbon atoms per molecule ($C_5 - C_{15}$). A variety of hydrocarbon species may be found: alkanes (straight or branched), cyclo-alkanes, aromatics and alkenes (see appendix B for molecular structures). Typical concentrations for alkenes are around 1-3% vol [55] and aromatics are limited to 25% vol [56]. Trace compounds commonly found in aviation fuel include those of sulphur (the most abundant and limited by specification to 0.3%), nitrogen and oxygen. Fuels may be further processed to convert trace compounds or reduce their concentration; for instance, sweetening - in which thiols are converted to disulphides and hydrotreatment - which removes or reduces many trace components as well as acids and alkenes [49]. Example compositions of a conventional fuel and an alternative bio-fuel (Hydroprocessed

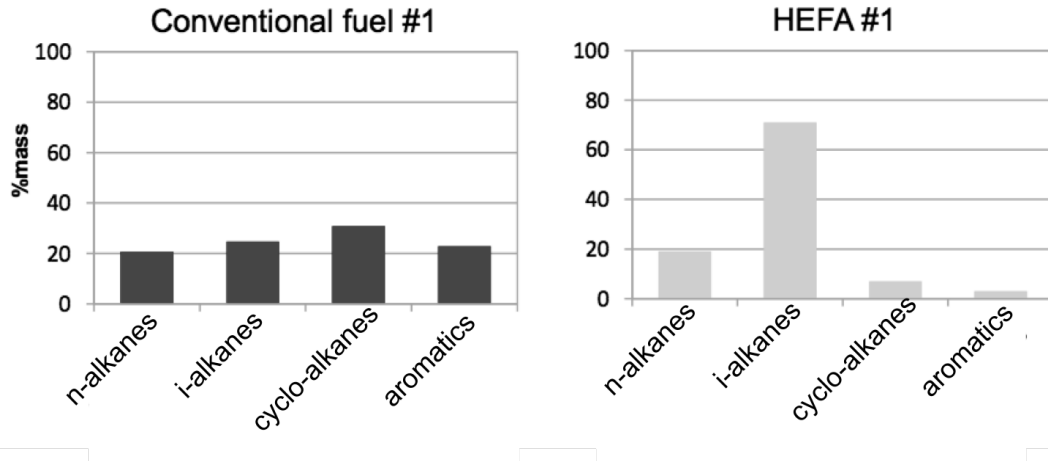


Figure 3.1: Example composition of conventional and bio derived fuel

Esters and Fatty Acids) can be seen below.

The complete degradation mechanism is very complex, since kerosene is a mixture of thousands of compounds, all of which react slightly differently. What can be said with confidence is that for the bulk fluid temperature regime relevant to most aircraft (100-300°C), insoluble species form primarily through the interaction of fuel constituents with dissolved oxygen (liquid phase autoxidation). In its simplest form, autoxidation can be described by a chain of several reactions, involving free radicals, as shown in figure 3.2.

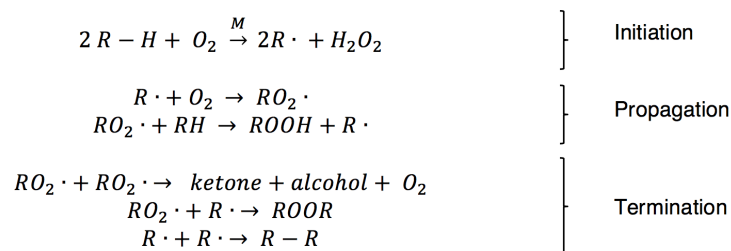


Figure 3.2: Basic liquid phase autoxidation mechanism

In the initiation step, thought to be metal catalyzed [50], an alkyl free radical ($R\cdot$) is formed. The alkyl free radical reacts with oxygen to form an unstable alkylperoxy radical ($RO_2\cdot$). The alkylperoxy radical reacts mainly with a fuel molecule (RH) to form stable hydroperoxide ($ROOH$) and another alkyl radical ($R\cdot$). It is further reactions of the unstable peroxide radical with trace compounds that are thought to form species that are insoluble in fuel and which ultimately form deposit [55] [57]. The rates of reaction are controlled by temperature, hy-

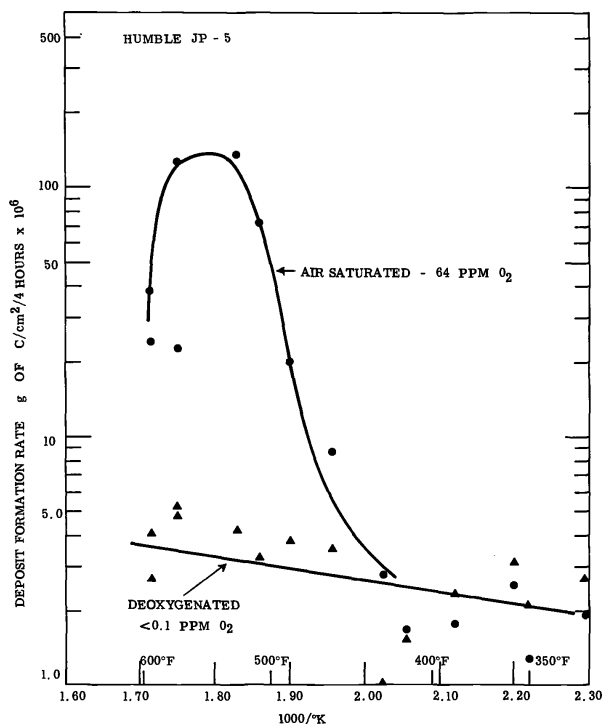


Figure 3.3: Effect of deoxygenation (taken from [3])

drocarbon structure and oxygen concentration [50]. Evidence of the importance of autoxidation reactions to deposition was found by Taylor [3], who observed a reduction in rate of deposit formation for most fully ($\approx 0\text{ppm}$) deoxygenated fuels (see figure 3.3). However, Ervin and Williams [58] found that for intermediate levels of dissolved oxygen and partial consumption of the available oxygen (due to temperature or residence time), deposition may actually be higher than the air saturated case. In their experiments, initial oxygen concentrations of around 12ppm produced the greatest amount of deposit. Deposition was lowest when the inlet dissolved oxygen concentration was of the same magnitude as the amount of oxygen consumed.

Hydrocarbon type

Taylor [4] observed that for alkanes, rate of deposit formation decreased with increasing carbon number. For the same carbon number, branched alkanes were found to deposit more than straight chain alkanes. Addition of aromatics and cycloalkanes to n-decane inhibited deposition (between $100\text{-}180^\circ\text{C}$) but the effect was reduced at higher temperatures. Addition of alkenes to n-decane generally increased deposit formation, with the effect strongly dependent on the type of alkene added. A linear dependency was found between alkene concentration and

rate of deposition. Wong and Bittker [59] studied the deposition from 4 aerated pure hydrocarbons (n-decane, cyclohexane, 1-hexene and benzene) between 150-450°C. At low temperatures, all 4 fuels produced only a small amount of deposit. At 350°C, 1-hexene formed the largest amount of deposit, followed by cyclohexane. Decane and benzene formed much less deposit. Alkenes are considered the most deleterious to thermal stability due to their unsaturated nature and faster rate of oxidation compared to other hydrocarbons. Alkanes and cycloalkanes contain certain stronger carbon-hydrogen bonds resulting in a slower rate of oxidation [49].

Hetero-atomic species

The concentration of sulphur, oxygen and nitrogen has been found to be much greater in deposit than in unstressed fuel. Elemental analysis from several investigators was presented in [57]. Oxygen was the second most abundant element after carbon. Nitrogen was found to be highly concentrated in deposits with a concentration factor (mass in deposit / mass in fuel) of between 10000 - 300000. The concentration factor for sulphur was 54 or greater. This presents a problem in fully understanding the degradation process, since the reacting species found abundantly in deposit represent only a tiny fraction of the composition of the unstressed fuel ($< 0.1ppm$) [49]. The hydrogen-carbon ratio of deposit was found to be significantly less than that of the fuel, indicating that the deposit is aromatic in nature [60], [50].

Taylor [61] investigated the effect of trace sulphur on deoxygenated jet fuel by addition of 3000ppm of certain sulphur compounds that could potentially be present in jet fuel to a thermally stable fuel. Polysulfides, disulfides, sulfides and thiols increased the rate of deposit formation. Mills and Kendall [62] also found that rate of fouling increased with sulphur content on tests of 11 fuels in the Single Tube Heat Transfer Rig (STHTR). Taylor also tested addition of nitrogen and oxygen compounds to stable deoxygenated fuel [63]. The nitrogen compounds were found to have little effect on deposit formation but peroxides significantly enhanced deposition and some acids, esters and ketones were mildly deleterious. Hazlett showed JFTOT breakpoint results that showed a reduction in thermal stability with increasing nitrogen content in shale-derived fuels [57].

Treatment process

The effect of trace hetero-atomic species may also be seen through comparison

of fuels that have been subject to different processing methods. Taylor [61], [3] noted one fuel from the aforementioned studies that did not show a reduction in deposition rate when deoxygenated. The behaviour was attributed to an increase in the concentration of disulphides from the 'doctor sweetening' process. Kendall et al [1] showed data displaying a clear distinction between the rate of deposition for sweetened and hydrotreated fuels (figure 3.4). Hydrotreatment significantly reduces concentrations of heteroatomic compounds and alkenes, which have been shown to be detrimental to fuel thermal stability [49].

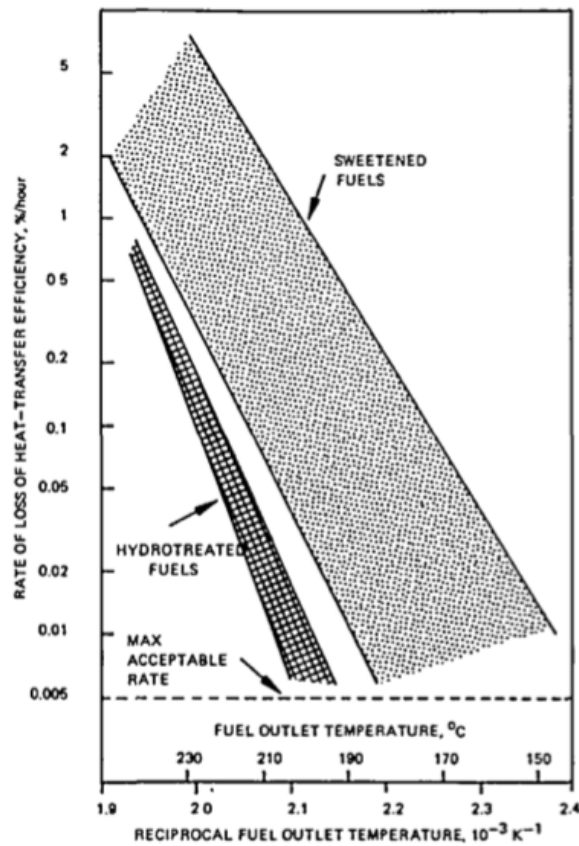


Figure 3.4: Effect of fuel processing on fuel thermal stability (taken from [1])

Effect of metal surfaces and dissolved metals

Fuel may be exposed to metals at many points from refinery to aircraft. As a result, trace amounts of metals may be dissolved in fuel, some of which have been shown to be detrimental to thermal stability. In these cases, oxidation reactions responsible for deposit formation are believed to be catalysed homogeneously. The oxidation reaction may also be catalysed heterogeneously at a heated metal wall.

Copper has been found by many investigators to significantly reduce thermal stability, even in small concentrations ($10ppb$). Iron, zinc and lead have also been identified as deleterious trace metals, although the concentrations to reduce thermal stability were higher ($200ppb$ lead, $100 - 200ppb$ zinc and $25 - 100ppb$ iron) [50]. Taylor [64] doped a fuel with $50ppm$ of Iron, Nickel, Copper and Cobalt metal acetylacetonates. Deposition rate was increased by a factor of 40 with respect to the baseline fuel. Copper was the most deleterious and there was no discernible difference between the other metals. Copper and high vanadium content titanium alloy surfaces were found to have a strong worsening effect on thermal stability, indicating the role of heterogeneous wall reactions in free radical production. Mills and Kendall [62] found that a fuel of average thermal stability exhibited an increase in deterioration of heat transfer coefficient from 0.26% to 5.9% when doped with $30\mu g/L$ of copper. Colbert and Nowack [65] tested fuels with dissolved copper concentrations between $50 - 800ppb$ with the HiReTS and found a good correlation between dissolved copper concentration and carbon deposition rate. It was also suggested that deposits from fuels with large copper concentrations were compositionally different than copper-free fuels, since post-test carbon burn off analysis showed poor correlation with the observed rise in outer wall temperature from the insulating effect of the deposit on the test section. Difference in deposit colour from copper containing fuels was also described in [50].

Smith [66] investigated the effect of many different metal surfaces using the CRC coker. Metal was either applied as a foil or flame sprayed on the standard aluminium heater tube. Tests were conducted with fuel-surface contact times equal to $10s$ and $360mins$ and the threshold temperature (highest temperature at which there was an appreciable change in tube deposit rating and filter pressure drop) was compared against the standard aluminium case. Most steels studied had no effect on severity of deposition. Nickel alloys were found to have a slight harmful effect above $165^{\circ}C$, as were some alloys containing up to 4% copper. Titanium was not observed to worsen deposition. The worst performing metals were copper, copper alloys and brazing alloys (containing 17% copper), which were noted to promote significant deposition. It was also observed that harmful amounts of copper were picked up by the test fuel at ambient temperatures from alloys such as brass and gunmetal - highlighting the importance of fuel transportation and storage to the overall thermal stability problem.

Hazlett [67] used heater tubes of three metallurgies during tests of n-dodecane

with the JFTOT. A small difference was observed in rate of oxidation, with 6061 aluminium having the least effect and 304 / 316 stainless steel being slightly worse. Heater tube metallurgy was not found to alter the yield of reactant products. Wong and Bittker [59] also compared aluminium and 316 SS heater tubes in their study of n-decane in the JFTOT. Breakpoint temperatures for the aluminium tube were around 30°C higher than for steel. In addition, Clark and Thomas [68] found stainless steel to produce a 50% enhancement in deposition after 1 hour in the JFTOT compared to an aluminium tube. Beyond a certain point, deposition rate became constant and independent of tube material - highlighting the fact that wall metallurgy is only relevant until the surface becomes fouled. It was also reported that for long duration tests, deposition on 6061 aluminium tubes was greatly reduced with respect to stainless steel. This was attributed to migration of magnesium to the tube surface having a retarding effect on deposition. For this reason, aluminium heater tubes for the JFTOT must not be reused. Similarly, Stavinoha et al. [69] studied 316SS, 304SS, aluminium, magnesium, gold and copper coatings on a JFTOT heater tube. Tests were conducted between $300\text{-}380^{\circ}\text{C}$ with a low sulphur Jet-A fuel with a breakpoint of 254°C . Deposit thicknesses were measured via two methods. There was some disagreement between the methods in ranking the metals. Auger ion milling ranked the materials (in order of decreasing deposit thickness): copper > magnesium = 316SS > gold > aluminium. The dielectric strength method (ASTM D149) ranked the materials: 316 SS > 304SS > gold > magnesium = aluminium = copper. The difference in rankings was suggested to be due to the dielectric method being strongly influenced by metal ions in the deposit. It was also noted that for magnesium, the deposit was hemispherical, while flat, platelet type deposits were found for the other metals.

Ervin et al [70] tested stainless steel heater tubes and tubes treated with a non reactive silica layer (silicosteel). They measured the rate of oxygen consumption for temperature ranges corresponding to thermal-oxidative and pyrolytic conditions for two fuels - a neat Jet-A and a Jet-A with additives. Complete oxygen consumption was achieved with a bulk fuel temperature approximately 20°C higher for both fuels with the treated tubes. The decreased rate of autoxidation in the treated tube case was suggested to be due to the lack of active sites taking part in the catalysed thermal disassociation of alkyl-hydroperoxides (free radicals associated with this chemical process propagate and accelerate the oxidation reaction). For the untreated tube, the rate of oxygen consumption was quickest for the neat Jet-A. Additives appeared to have a small effect. The additive package

included an antioxidant (intended to react with alkyl-peroxy free radicals and slow the rate of autoxidation) and also Metal Deactivator Additive (MDA) - a chelating agent for dissolved trace metals. The treated tube test with Jet-A plus additives showed the slowest rate of autoxidation. It was also observed that in tests where the length of treated surface was increased, the deposition profiles were shifted upstream by practically the same distance. SEM analysis of the deposit formed on the treated surface showed less numerous, smaller micro-spherical particles compared to the untreated stainless steel wall.

3.1.2 Physical aspects

Time

Clark and Stevenson [46] observed the change of deposition rate with time using the Mini Injector Feed Arm Rig (MIFAR) (see Appendix A), noting three main phases to the deposition process. Initially, there was an induction period in which limited deposition occurred (0-5hrs), followed by a period of higher, constant rate deposition (5-15hrs) and finally, a drop in deposition rate (15-20hrs). Similar observations were made in [65], [7], [71], [60], [72], [73]. Clark and Stevenson suggested that the induction period was due to the difference in heat transfer between the initially clean metal surface and the rougher, fouled surface. Smith [71] came to the same conclusion. The ultimate reduction in deposition rate was attributed to the insulating effect of large accumulations of deposit limiting the heat flux to the fuel. Clark and Stevenson also showed that the induction period and the post induction deposition rate for a particular fuel are directly related; fuels with lower thermal stability tend to have a shorter induction period and higher rate of deposition than a more thermally stable fuel.

Temperature

Smith conducted one of the first detailed investigations into fuel thermal instability in [71]. Using the Single Tube Heat Transfer Rig (STHTR), the rate of decrease in heat transfer coefficient was recorded for fuel outlet temperature between 150 - 208°C for eight fuels. The rate of decrease in heat transfer coefficient appeared to increase almost exponentially with temperature.

Taylor [4] investigated the rate of deposit formation for various pure hydrocarbons from 93 - 260°C. The rate of deposit formation was found to be well represented by the Arrhenius expression for reaction rate:

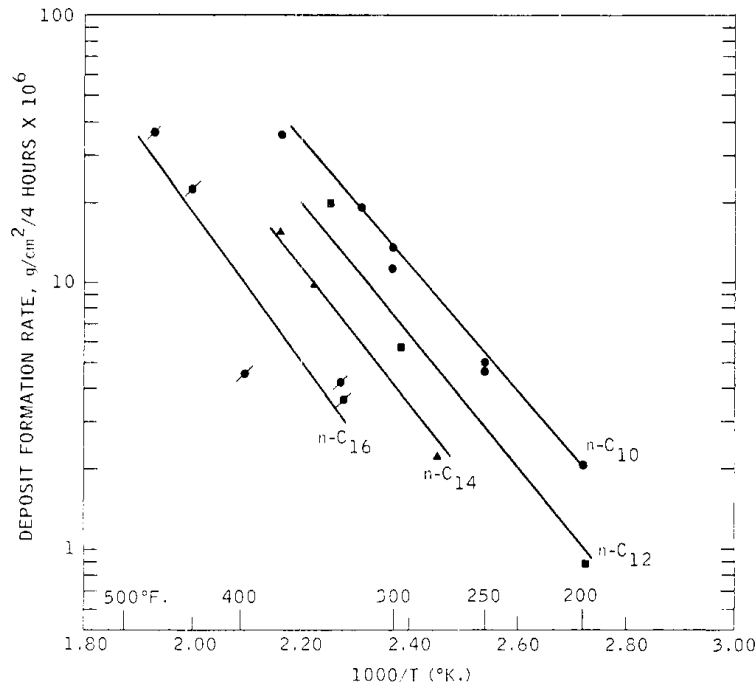


Figure 3.5: Deposition rates in arrhenius form for pure n-alkanes (taken from [4])

$$K = A e^{-E_a/RT} \quad (3.1.1)$$

where K is the rate constant, T is the absolute temperature, E_a is the activation energy, R is the universal gas constant and A is a pre-exponential factor which depends on the fuel chemistry. Taking the natural logarithm results in:

$$\ln k = \frac{E_a}{R} \frac{1}{T} + \ln(A) \quad (3.1.2)$$

thus, plotting the natural logarithm of the deposition rate against $1/T$ yields a straight line (see figure 3.5).

Marteney and Spadaccini studied the effects of temperature on JP-5 fuel in [72]. Dependence of deposition rate on initial wall temperature was again observed to be well suited to an Arrhenius relationship, which qualitatively matches the results obtained on JP-5 by Taylor [4]. The maximum rate of change of deposition rate with temperature occurred between $277 - 327^\circ\text{C}$. Deposition rate peaked between $327 - 377^\circ\text{C}$ and reduced in excess of 377°C . The inflection of deposition rate past 377°C was suggested to be due to either oxygen depletion or the onset of pyrolysis - a chemically different mechanism of thermal decomposition to autoxidation at higher temperatures. The global activation energy was determined

as 40kcal/mole . TeVelde and Glickstein [6] explored wall temperatures from $260\text{-}480^\circ\text{C}$ and reported similar findings to those in [72]. Deposit formation rate increased sharply, before plateauing at 370°C and decreasing linearly up to 480°C . Mills and Kendall [62] presented data for 11 fuels in a well defined 'envelope' of results in Arrhenius form and Kendall et al [1] showed that fuels may be clearly differentiated by processing method when presented in Arrhenius form (see fig. 3.4).

The significance of the Arrhenius relationship is that deposition rates may be extrapolated across temperatures with reasonable confidence - thus providing a justification for accelerated testing of fuels at higher temperatures for shorter durations.

Pressure

Taylor [3] stressed two fuels between $18 - 69\text{bar}$. No effect of pressure was observed with one fuel, while a reduction in deposition was observed at higher pressure with the other. It was proposed that higher pressures might cause a change in solubility of the fuel and thus a reduction in deposition. Marteney and Spadaccini [72] found deposition rate to be independent of pressure from 17 to 54bar . Hazlett [49] briefly summarised findings from many researchers and reasoned that fuel system pressure should be kept higher rather than lower - in light of the findings of Taylor and in order to keep the fuel in the liquid phase.

Flow Rate and Reynolds number

Smith investigated the effect of flow rates on deposition (through changes in heat transfer coefficient) in [71]. Flow rates ranged from $9 - 18\text{l/hr}$ ($4500 < Re < 10000$), with maximum fuel outlet temperatures between $150 - 248^\circ\text{C}$. Heat transfer data was recorded across a second heated test section, after significant pre-heating. Deposit thermal resistance increased with Re . However, it was observed that above a critical fuel throughput (equivalent mass of fuel for each flow rate), deposit thermal resistance was higher for the lowest flow rate than the highest. Smith proposed that in the early stages of deposition, when the viscous region adjacent to the wall is reasonably intact, effects of increasing Re (ie. enhanced wall-normal transport of deposit precursor, increased turbulence, reduced viscous sublayer thickness and deposit roughness) work against the reduction in residence time in a complicated and finely balanced state of deposit formation. When the viscous sublayer is all but destroyed by deposit and the effect of deposit roughness

tends to zero (after the point of equivalent throughput), Smith proposed that the increased residence time at lower flow rates results in a greater deposit thermal resistance for equivalent mass of fuel. It was acknowledged that the effect of deposit roughness on the heat transfer and fluid flow was a complicated variable early in the deposition process, but reduced to zero as the deposit roughness height became approximately equivalent to the extent of the viscous sublayer.

Chin and Lefebvre [74] conducted experiments to understand effect of Re on deposition by varying both the flow velocity and the test section diameter ($1000 < Re < 7000$). Tests were performed using a rig with a fuel preheater (so that some tests could be performed with an isothermal test section to minimise heat transfer from tube to fuel). Deposition rate was found to increase with Re following the relationship;

$$k = C_1 Re^{0.65} \quad (3.1.3)$$

The analysis was extended to include the effect of temperature for isothermal and non-isothermal cases. The following correlation was obtained:

$$k = C_1 e^{\left(\frac{-C_2}{T_f}\right)} e^{\left(\frac{T_w - T_f}{166}\right)} Re^{0.65} \quad (3.1.4)$$

Where the constant C_1 is dependent upon the fuel composition and condition of the wall. C_2 represents the activation energy of the auto-oxidation reaction and is solely fuel composition dependent. For the particular kerosene used in the study, they found $C_1 = 3.63$ and $C_2 = 546$. Their rationale for the relationship was that with increasing Reynolds number, heat and mass transfer between the wall and the fluid is enhanced.

The effect of flow rate was briefly studied in an examination of the HiReTS device in [65]. A decrease in Re from 13000 - 5000 was found to significantly increase deposition. Marteney and Spadaccini tested JP-5 at flow velocities of 0.3, 2.1 and 15m/s - equivalent to $Re_{in} = 400, 3000$ and 21000 in [72]. Tests were conducted from 150 - 600°C using a single, heated tubular test section. The laminar and transitional flow regimes exhibited similar deposition behaviour up to 330°C, although the peak of deposition rate in the laminar case occurred at a lower temperature. It was suggested that deposition was limited in the laminar case by either the reduced rate of transport of reactants to the wall, or oxygen depletion due to the

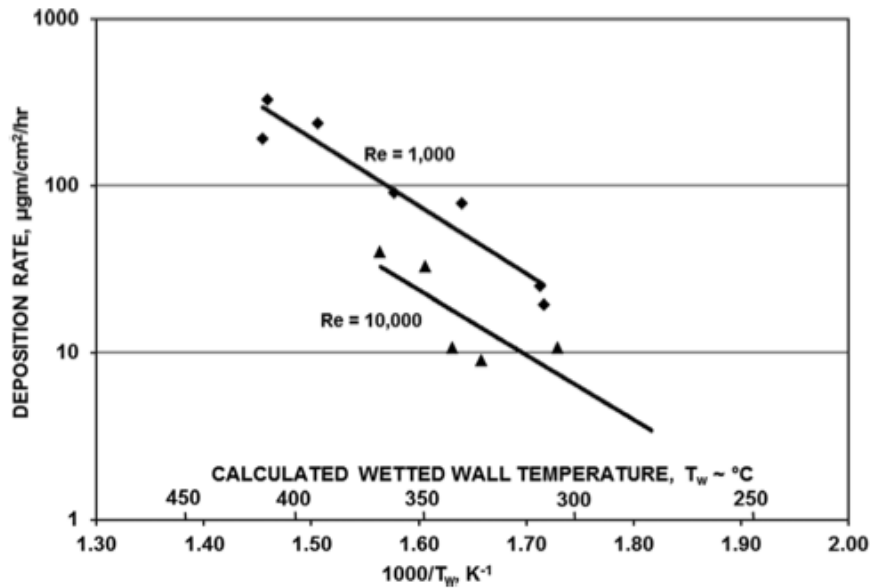


Figure 3.6: Effect of Re on deposition with no pre heating (taken from [5])

increased residence time. The deposition rate was consistently slightly higher up to $\approx 280^\circ\text{C}$ for the highest flow rate - attributed to increased convection, transport of reactants to the wall and a greater quantity of fuel being thermally stressed.

Moses [5] reported findings contrary to those of Smith [71] and Chin and Lefebvre [74]. In experiments with two tube geometries ($51\text{cm} \times 0.39\text{cm}$ ID, $50 < Re < 5000$ and $0.64\text{cm} \times 0.051\text{cm}$ ID, $1000 < Re < 10000$), where the only heat flux to the fuel was via the tube wall, increasing Re was observed to decrease deposition rate.

Considering the universal mean velocity profile for the turbulent boundary layer and a smooth tube (figure 3.7), Moses calculated the reduction in thickness of the viscous sublayer and buffer layer with increasing Re , before applying the momentum-heat transfer analogy to produce normalised radial temperature profiles for $5000 < Re < 20000$, a wall temperature of 315°C and bulk fluid temperature of 150°C (figure 3.8). The analysis showed that approximately two thirds of the temperature change from the wall to the fluid bulk occurs over the viscous sublayer - a tiny proportion of the overall flow field. Furthermore, Moses applied the rate expression for insoluble gum formation found by Negaeli [75] to the temperature profile, which showed that 99% of deposit precursors formed within the viscous sublayer for those boundary conditions. The reduction in deposition rate with Re observed experimentally was explained thus; increasing Re thins the viscous sublayer, shifting the temperature profile closer to the wall

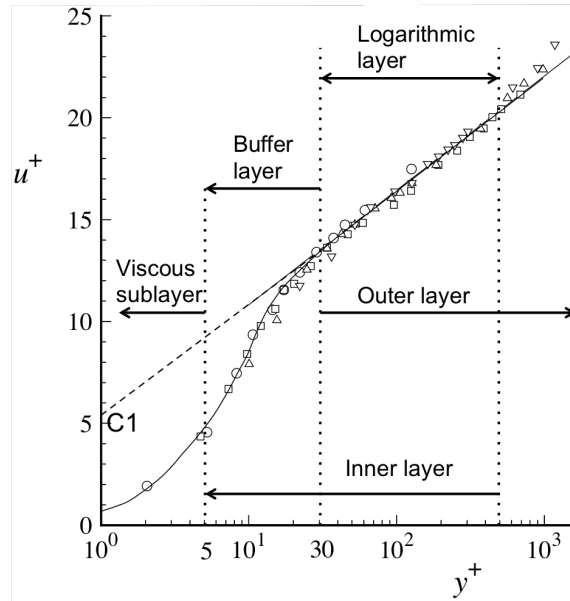


Figure 3.7: Non dimensional turbulent boundary layer velocity profile - inner variables (log law: $u^+ = 1/\kappa \ln y^+ + 5.5$)

and reducing the amount of fluid that can be sufficiently heated to form deposit precursors. In experiments where increasing Reynolds number was seen to increase deposition, Moses theorised that because the fuel in these cases underwent sufficient preheating, precursors formed in the bulk fluid. An increase in Re in these cases would then result in increased transport of deposit precursors to the wall and explain a higher rate of deposition.

Nature of Deposits

Smith [71] noted that the nature of deposit changed with temperature. At lower temperatures (below the fuel breakpoint temperature), deposit adhered loosely to the tube wall and was easily removed by tapping or fluctuating the fuel flow. Above the breakpoint temperature, deposit was firmly adherent. TeVelde and Glickstein [6] compared deposits obtained from 18 and 5 hour tests from the same tube location. Deposit from the long duration test was rougher than the short duration test. In addition, deposit from areas of light accumulation was found to be soft and powdery, while deposit from areas of heavy accumulation was hard, crystalline and covered by a soft powdery coating. It was suggested that not only would deposit roughness alter heat transfer characteristics, but also that the thermal conductivity of powdery deposit would be different to that of hard, adherent deposit - further complicating the heat transfer considerations. TeVelde and Glickstein calculated the deposit density to be $1g/cm^3$ and developed an

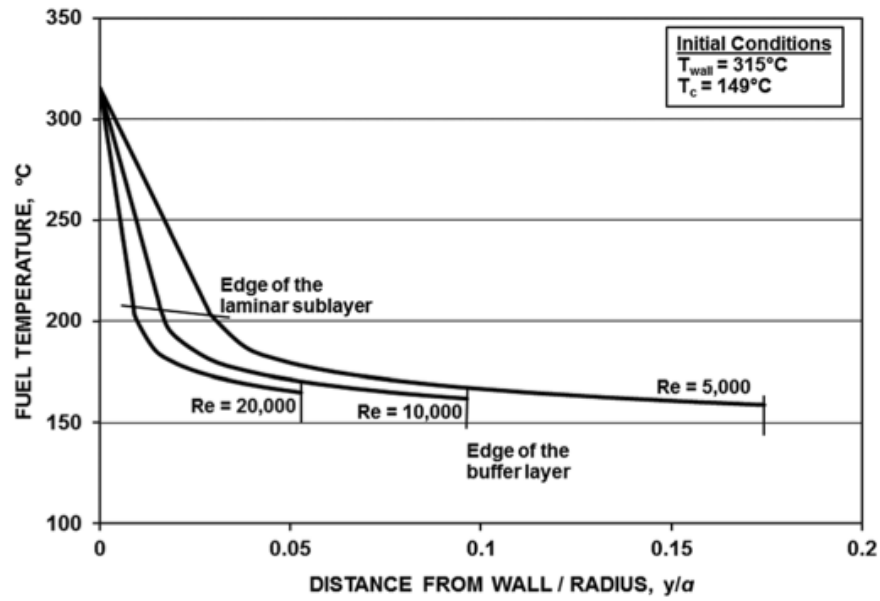


Figure 3.8: Effect of Re on the radial temperature distribution in the turbulent boundary layer (taken from [5])

expression for deposit thermal conductivity based on deposition rate data and heat transfer measurements;

$$k_d = C(t_d \cdot 10^{3.2(1 - \frac{T_w}{T_{ref}})})^n \quad (3.1.5)$$

Where t_d is the deposit thickness and C and n are correlation constants. Typical values of deposit thermal conductivity are shown in figure 3.9.

Szetela et al [76] studied deposits formed at low Reynolds numbers. Deposits obtained were characterised as thick, porous, and non-uniform in nature. Deposit density based on carbon content was $0.08g/cm^3$. Schirmer [77] studied the morphology of deposits using Scanning Electron Microscopy (SEM), with samples taken from various fuel stressing devices covering a wide range of temperature regimes. Deposits were noted as being remarkably consistent in form, built of soft, micro-spherical particles, approximately $0.1\mu m$ in diameter. The micrographs suggested that particles accumulate in randomly formed structures, agglomerate and undergo plastic flow and fusion on heated surfaces. Particles collected on surface imperfections (ie. machining grooves), and Schirmer proposed that surfaces should be highly finished to reduce deposition. Furthermore, the analysis indicated that the fluid flow might affect the deposit morphology - as areas where fluid was accelerated towards the surface appeared eroded. Ervin and Williams [78] reported

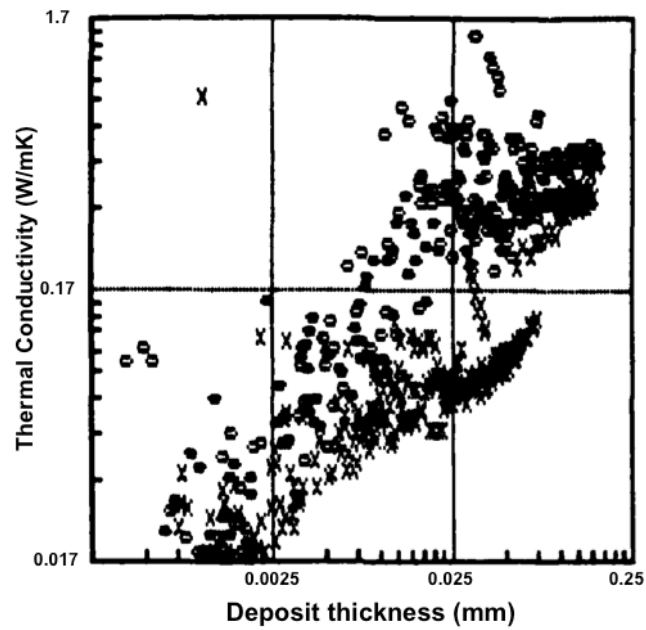


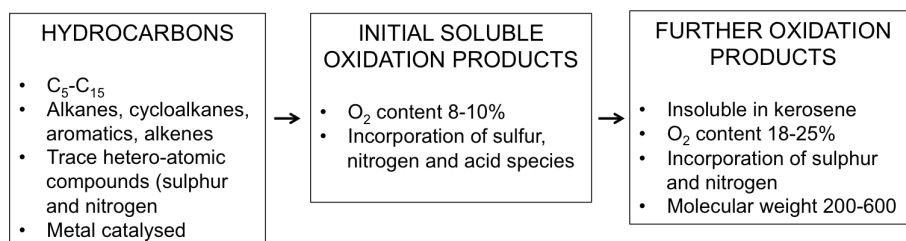
Figure 3.9: Values of deposit thermal conductivity (taken from [6])

microstructures similar to Schirmer for heated tubes, although deposits formed in a cooled section (post heated tube) were film like - conforming to the micro geometry of the tube wall. Chemical differences in the deposit were also noted between tests with air saturated fuel and fuel with reduced dissolved oxygen concentrations.

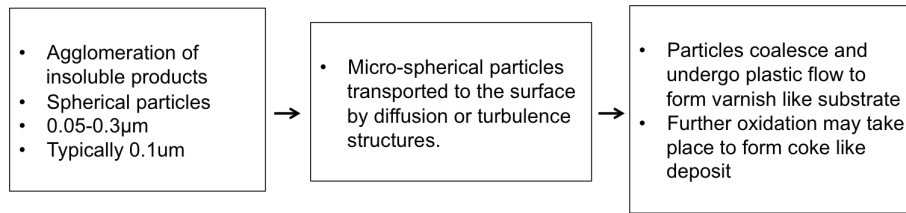
Summary: The Overall Deposition Mechanism

At this point, a broad description of the chemical and physical process associated with deposition of thermally stressed aviation fuel has been given. This can be summarised in the overall deposition mechanism as proposed by Taylor [48]:

Chemical processes



Physical processes



The effect of roughness on deposition

Literature discussing the effect of surface roughness on fuel deposition is very limited. A knowledge gap analysis can be found in table 3.1, which summarises the nature of experimental investigations of fuel thermal stability for the years of peak experimental activity. Smith investigated the effect of promoted turbulence on deposit formation [71]. Smooth bore tubes were compared to tubes with inwardly protruding hemispherical indentations at Reynolds numbers in excess of 4000. For tubes with turbulence promoters, the heat transfer coefficient (h) was observed to decrease almost linearly with formation of deposit, whereas for the smooth bore tube the rate of change was a function of time. At the highest bulk fuel outlet temperatures, decreases in h (averaged over 25 hours) were significantly lower for the rough tubes. At lower temperatures, roughened tubes always exhibited an immediate decrease in h , whereas for the smooth tube sometimes a rise in h was observed, followed by a sharp decline. The immediate improvement in heat transfer for the clean, smooth tube case was suggested to be attributed to the initial formation of deposit influencing the viscous sublayer and enhancing heat transfer. For the roughened tube, it was supposed that no initial improvement in heat transfer was observed since the extent of the viscous region was already reduced - thus the effect of deposition formation was an immediate decrease in heat transfer effectiveness from the thermal resistance of the low thermal conductivity deposit. For the smooth tubes, micrographs (after 50 hours at 150°C) showed the deposit roughness height was generally slightly less than the calculated height of the viscous sublayer. It was suggested that only after the deposit roughness height exceeds the height of the viscous sublayer (or disrupts it such that it is all but replaced by turbulence) that a decrease in heat transfer coefficient ensues for initially smooth tubes.

Perhaps the only published explicit observation of the effect of surface roughness on deposition rate was made by Bradley et al [7]. In testing of a simulated fuel system manifold (an electrically heated tube, 7mm ID x 3m) in the full scale Advanced Aircraft Fuel System Simulator, significant offset in the induction period was observed between tests. For tests with the shortest induction period, manifold

tubes were shown to have noticeably greater surface roughness, as shown in figure 3.10. However, no further effort was made to quantify the roughness geometry.

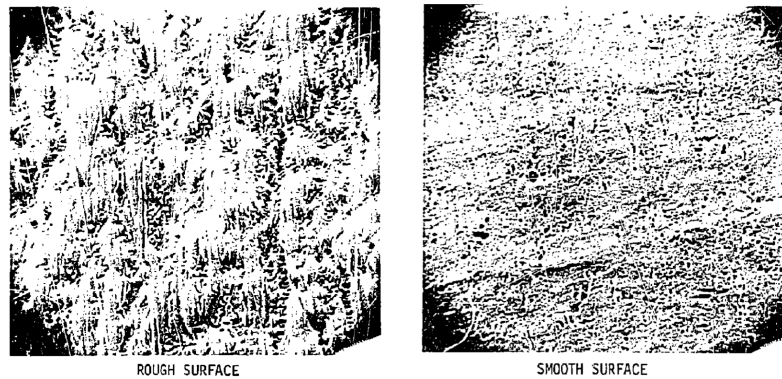
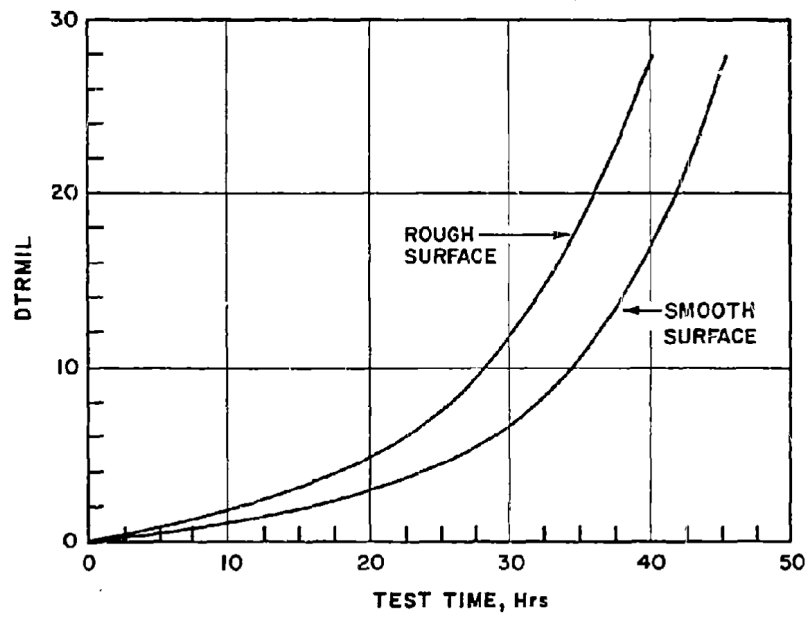


Figure 3.10: Deposition rates and micrographs of rough and smooth tubes observed in [7]

3.1.3 Gap analysis

Table 3.1: Review of experimental thermal stability literature, 1967-1997

Year	Author	Investigation of	Range of variables	Rig Used	Conclusions	Roughness considered?
1967	Smith	Metal effects	21 metals/alloys	Coker	Copper deleterious	
1969	Smith	Heat transfer (T, FR, Re)	150-243oC, Re 3000-5200	STHTR	Deposition increases with FR, LSL important	✓
1969	Taylor	Fuel composition	C number	ESSO AKU	Deposition occurs at lower T for lower CN	
1969	Taylor	Metal Effects	6 metals/alloys	ESSO AKU	Metal surfaces or dissolved metals catalyse free radical initiation	
1970	Schirmer	Deposit morphology	Deposit nature vs. T	Many	1000A Diameter, consistent shape	
1972	Bradley et al	fuel system component performance	simulated engine cycles (T, P, FR)	AAFS		
1972	Goodman et al	fuel system component performance	HTC, Deposit thickness	AAFS	Roughness noted to increase deposition	✓
1974	Taylor	O ₂ conc, T, P	<649oC, 69atm	ESSO AKU	Removal of O ₂ reduced deposition for most fuels	
1976	Taylor	S compound conc	540oC, 3000ppm S, O ₂ <1ppm	ESSO AKU	Effect of deoxygenation dependent on sulphur conc	
1977	Hazlett et al	Metal effects	190-538oC, SS304, SS316, Al	JFTOT	Reaction products at temperatures	
1980	Vranos, Marteney	T, P, FR (Re)	2.5-25gal/hr, 300-750F, 100-300psi, Re (outlet) 6k-34k	UTRC simulator	Arrhenius for T vs d.rate, FR affects deposition, deoxygenation reduces dep	
1982	Wong, Bittker	HC type, T, metal effects	alkane, alkene, cycloalkane, aromatic, 150-450oC, Al & SS316	mod JFTOT	JFTOT results for different HCs, SS deposits > Al	
1983	TeVelde, Glickstein	Heat transfer (T, FR, P, Metallurgy)	400, 800 psi, <900oF, 60-120lb/h Re (inlet) 3k-6k, 1-20hrs	UTRC resistance heated HT rig	HT characteristics of fuels, thermal conductivity	
1986	Szetela et al	Deposit characteristics	500K (50-700hr), 600K (4-20hr), Re 60, 34 atm	Isothermal tubes	deposit thickness approx ~ time ³	
1986	Mills & Kendall	Deposition rate for 11 fuels	T _{fuel out} 172-243oC, Re 5230-8100	STHTR, flask oxidation	Arrhenius for T vs d.rate, sulphur and metals deleterious	

1986	Marteny & Spadaccini	Time, T, P, Re	8-32hr, Re 400 - 21000, T fuel out 475-615K, 17-54atm	same as [13]	Local surface temperature, Re and T affect deposition rate	
1988	Clarke & Thomas	FR, metallurgy	3-7ml/min, Al/SS, 350oC	JFTOT	Mass transfer effects important for laminar flows, SS > Al	
1990	Naegeli et al	Metal effects	SS316,304, Al, Mg, Au, Cu, 300-380oC	HLPs (JFTOT)	deposit thickness measurement questionable	
1990	Clark & Stevenson	Deposition in simulated feed arms	Tfuel in 165oC, TIW 300oC, 250psi, Re 8000	MIFAR	3 phases of deposition, pre heating alters deposition	
1993	Chin & Lefebvre	T, P, FR, Re	50-375psi, Twall 413-673K, Re 1k-8k	Single pass rig w/ preheating	deposition increases with Re	
1993	Heneghan et al	Deposition, O2 depletion	Tblock 550-600K, 6-12hrs	Pheonix (known roughness)	Block T and time increased deposition non linearly	
1995	Heneghan et al	O2 depletion & additives	Tbulk 450-520K	Pheonix (known roughness)	flowrate greatly affected dep. downstream of hot section for lower block Ts	
1995	Daggett et al	AFTSTU rig	LP: 300K, 483kPa, HP: 433-455K, 4831kPa, Nozzle: 475-600K Tinit	AFTSTU		
1996	Ervin & Williams	T, FR, Re, deposit, O2 cons	62, 100 ml/min, Re 1500, 2500 - 2500,3500, 24, 15hrs, 1-70ppm O2	Pheonix	deposition may increase for intermediate ppms and partial O2 consumption	
1997	Naegeli	Deposit precursors		static reactor	rate expression for precursor formation	

3.2 Roughness Effects on Momentum, Heat and Mass Transfer

As seen in the proceeding section, the fuel deposition mechanism is strongly dependent on temperature and Reynolds number. Without bulk heating of the fuel, formation of insoluble material is limited to the viscous sublayer, where the temperature gradient follows the velocity gradient, which is dependent upon Re and roughness. The viscous layer is the 'breeding ground' for insoluble material since the residence time is long and the temperatures are highest in the flow field. The concentration of precursor is distributed across the viscous layer according to the temperature gradient - therefore insoluble material formed off the wall must be transferred to the wall either by diffusion or by some disturbance to the viscous layer from the outer flow. Turbulent fluctuations will supply precursor material to the inner region of the boundary layer. In the case of preheating, precursor and / or insolubles will be formed in the core flow and transferred to the viscous region by wall normal turbulent velocity fluctuations. Thus the deposition for flow with and without preheating is quite different.

Understanding the effect of roughness on the turbulent boundary layer velocity and temperature profiles will allow inferences to be made on how roughness may effect deposition of thermally stressed fuel. In the following review, studies are presented with the aim of providing a broad perspective on the effect of roughness on momentum, heat and mass transfer mechanisms in turbulent flows. Most attention is paid to momentum transfer, since it is the driving mechanism for heat and mass transfer and has been thoroughly investigated. The sections start by outlining some early seminal works before presenting the effect of roughness on mean flow quantities for primarily 3D and 2D artificial roughnesses. More advanced studies are then discussed which relate to the measurement of higher order turbulent statistics. In contrast to the literature on fuel thermal stability, the volume of research on turbulent boundary layers is extremely large, and a complete review would be somewhat excessive. The purpose of this review is to summarise the important concepts in rough walled turbulent flows, in order to formulate hypotheses on the effect of roughness and provide context for subsequent experimental work.

3.2.1 Momentum transfer

3.2.1.1 3D roughness

The logical starting points for this review are the seminal works on roughness which are still widely cited today and were conducted by Nikuradse and Schlichting (students of Prandtl at Göttingen university in the 1930s). Nikuradse [8] used a gravity fed tank to study the flow of water through drawn brass tubes of various diameters, roughened with well characterised grains of sand from $Re = 600$ to 10^6 . Care was taken in the application of the sand to the tube wall to ensure that no grains were scoured from the wall by the flow. The upstream 'calming length' to ensure fully developed flow was $50D$. The grains were sieved to grade the sand to within $0.1 - 0.8mm$ ($\pm 0.04mm$) and the grain size was verified using a micrometer and microscopy. The friction factor, λ was calculated from the pressure drop along the tube, which was measured with a pitot-static tube. Six relative roughnesses were tested, from $\frac{\tau}{k} = 15$ to 507. The calculated friction factors were plotted against Re for the six roughnesses considered.

Three distinct regions were observed for $\lambda = f(Re)$. In the first, termed 'hydraulically smooth', which spanned laminar and turbulent flow regimes, the friction factor was found to be independent of roughness. In the laminar regime, the friction factor obeyed the laminar relation $\lambda = \frac{64}{Re}$ and for turbulent flow, the friction factor was found to match the resistance law for smooth pipes obtained by Prandtl (equation 2.4.34). In the second 'transitionally rough' region, roughness effects started to be observed through an increase in friction factor with Re and relative roughness. The degree of the increase in λ with Re was more pronounced for the highest relative roughnesses. Furthermore, the departure from the smooth behaviour occurred at a lower Re for the roughest surfaces. In the final 'fully rough' regime, the friction factor became constant, independent of Re and only dependent on the relative roughness.

Nikuradse explained the behaviour by considering the interaction of the roughness elements with the near wall viscous region of the turbulent boundary layer. In the hydraulically smooth regime, the viscous sublayer is very much larger than the height of the roughness elements. As such, energy losses are equal to those of a smooth pipe. As the Reynolds number increases, the extent of the viscous near wall region is reduced. At the point where the roughness elements start to protrude through and disturb the viscous region, vortices are generated by

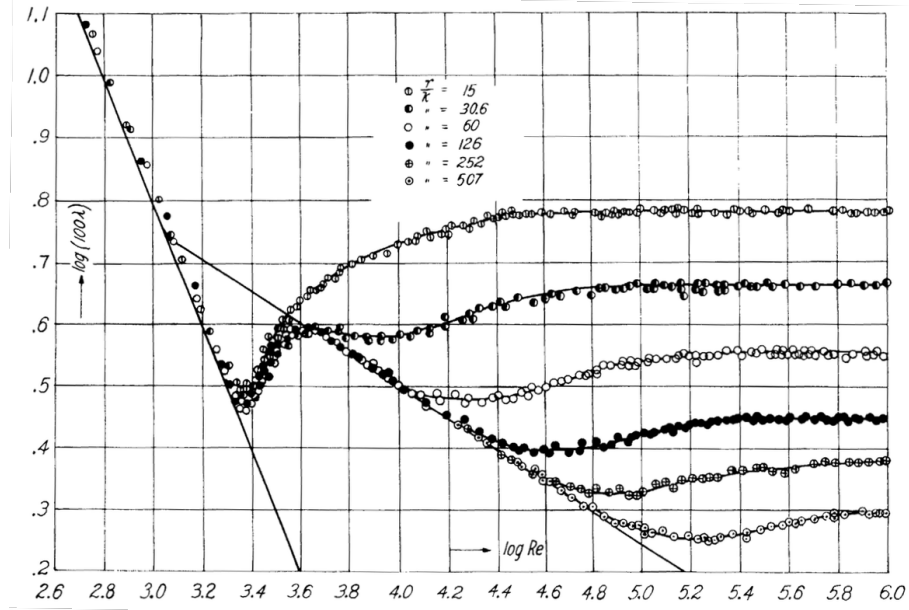


Figure 3.11: Original friction factor data of Nikuradse (taken from [8])

the roughness which contribute to additional loss of energy and an increase in friction factor. Eventually, the viscous layer becomes completely disturbed by the roughness, at which point the loss in energy created by the roughness becomes constant, and the friction factor becomes independent of Reynolds number.

For the fully rough regime, the dependence of friction factor with relative roughness was:

$$\lambda = \frac{1}{(1.74 + 2 \log \frac{r}{k})^2} \quad (3.2.1)$$

Nikuradse derived a general expression for the dependence of friction factor with roughness Reynolds number ($k_s^+ = \frac{k_s u_*}{\nu}$) where k_s was the sand grain diameter. Rearranging the above equation and plotting $\frac{1}{\sqrt{\lambda}} - 2 \log \frac{r}{k}$ against $\log k^+$ showed similarity in behaviour for all relative roughnesses considered, with a fully rough asymptote (1.74) and a linear relationship with k^+ for the hydraulically smooth regime; $\frac{1}{\sqrt{\lambda}} - 2 \log \frac{r}{k} = 0.8 + 2 \log k^+$. The transitional regime was described approximately by three lines with equations of the form $\frac{1}{\sqrt{\lambda}} - 2 \log \frac{r}{k} = a + b \log k^+$, where the constants a and b were dependent upon the roughness Reynolds number.

Nikuradse also recorded the mean radial velocity distributions for 3 pipes for $Re = 10^4$ to 10^6 . He showed the relationship of u^+ against y^+ for $\frac{r}{k} = 15$ to 507 with Re . For a particular relative roughness, the mean velocity profile was shifted

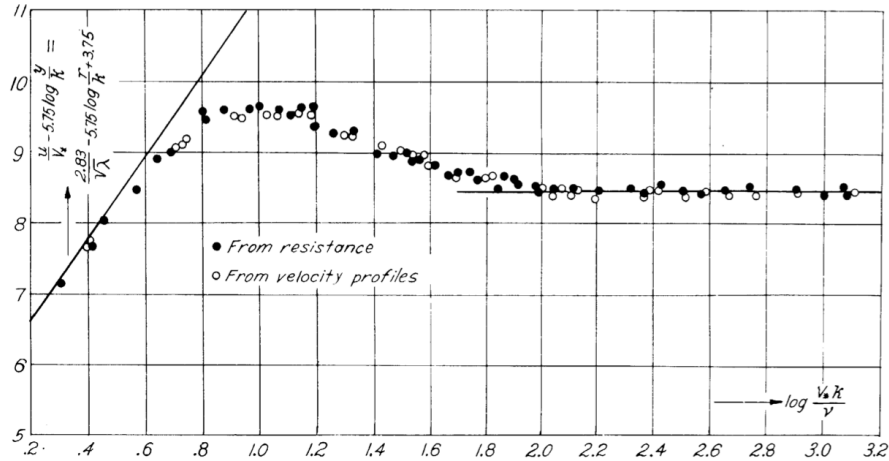


Figure 3.12: Hydraulically smooth, transitional and fully rough regimes (taken from [8])

downwards with increasing Re with respect to the smooth pipe velocity profile but remained parallel to the smooth wall profile. With the non dimensional velocity distribution of the form

$$u^+ = \frac{1}{\kappa} \log y^+ + C_r \quad (3.2.2)$$

(where C_r , sometimes referred to as the Nikuradse roughness function, represents the rough wall additive constant of integration, rather than the smooth wall value), Nikuradse produced the following expressions for the smooth and fully rough regimes:

$$\text{Smooth } (k_s^+ \leq 3.5) : C_r = \frac{1}{\kappa} \log k_s^+ + 5.5 \quad (3.2.3)$$

$$\text{Fully rough } (k_s^+ \geq 68) : C_r = 8.48 \quad (3.2.4)$$

and a 3 part linear profile for the transitional regime. The significance of this work should not be underestimated. A large complication of roughness research is the measurement of the surface features, which often are highly irregular. By using one, well defined roughness length scale (k_s) and non-dimensionalising, one needs only to measure the pressure drop in a conduit to the fully rough asymptotic condition to be able to calculate an 'equivalent sand grain roughness' which can be used effectively in further calculations.

Despite its usefulness, the above study considers only one length scale, and

only one arrangement of roughness - spheres packed at near maximum density. Schlichting [9] focused on the effect of roughness density (solidity) on frictional resistance, for arrays of simple element geometries including spheres, hemispheres, cones, short and long angles and sand. The elements were soldered onto test plates (21 were tested in total), which formed one side of a rectangular water channel - the other three sides were considered to be smooth. The shapes and arrangements of the roughness elements are shown in figure 3.13. Schlichting defined roughness solidity as $\frac{F_r}{F}$ and $\frac{F_1}{F}$ where F_r was the projection of roughness elements on a plane normal to the direction of the flow, F was the plate area and F_1 was the area of the smooth parts in between the roughness elements. The static pressure was recorded at 8 positions along the channel, and the velocity distribution measured with a pitot tube at the outlet of the rough wall test section.

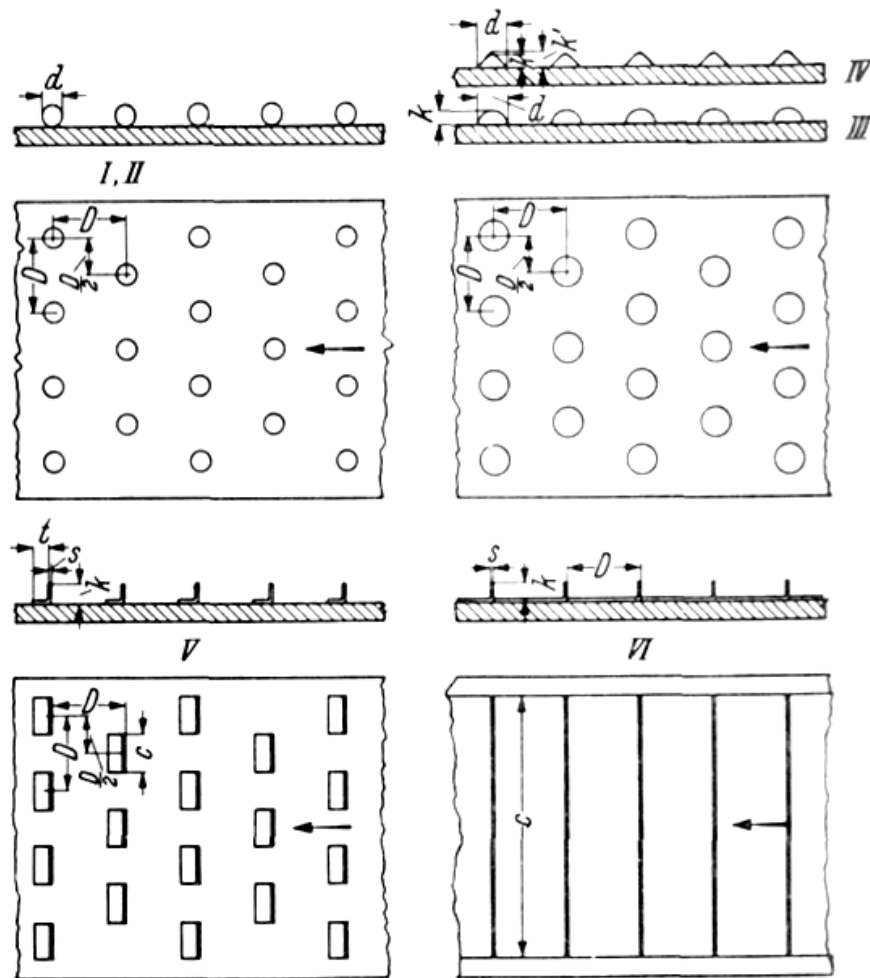


Figure 3.13: Roughnesses of Schlichting (taken from [9])

Schlichting first proposed the use of an equivalent sand grain roughness, defining a parameter $\alpha = \frac{k_s}{k}$ (where k was the absolute roughness height) and showed by example that the data of Hopf [79] and Fromm [80] (who tested wire netting, 'waffle' sheet metal and saw profile roughness) could be converted into an equivalent sand grain roughness through application of the fully rough formula of Nikuradse and the relative roughnesses used in the experiments.

To use the equivalent sand grain approach, it was assumed that the relative roughness of his plates was sufficient that the tests were conducted in the fully rough regime, and for each roughness, Schlichting calculated the constant B_r of the measured velocity profile and the equivalent sand grain roughness for each type of roughness and density. Plotting results for all roughnesses in terms of k_s , it was found that all velocity distributions matched well with the fully rough equation of Nikuradse. For tests with sand, the results differed from those of Nikuradse by around 1-2%.

For spherical roughness, the resistance initially increased with density, but the maximum resistance occurred with $\frac{F_r}{F} = 0.4$ - or when around 40% of the plate surface was covered with spheres. Hemispheres and cones appeared to show similar behaviour, although a clear maxima was not reached for those elements. Schlichting suggested that the elements of non-dense arrays were more effective in producing resistance to the flow than the most dense arrays, for which mutual sheltering results in an effective absolute roughness of only the radius or less. For the most dense arrangement of spheres and hemispheres, a lower resistance was found compared to sand grain roughness with equal diameter and height $\frac{k_s}{k} < 1$. For long angled segments, a very steep increase in resistance was observed up to a maximum resistance at $\frac{F_r}{F} = 0.1$

Many years later, Coleman et al [81] highlighted some discrepancies in Schlichting's approach, primarily the evaluation of the rough wall friction velocity. Schlichting calculated the friction velocity by two methods. The first involved applying a momentum balance to the channel;

$$U_r^{*2} = \frac{h}{\rho} \frac{dP}{dx} - U_s^{*2} \quad (3.2.5)$$

(where h is the channel height), calculating the smooth wall shear stress graphically from the smooth wall velocity distribution and measuring the pressure

drop. He neglected the shear force from the two other 'smooth' side walls. The second approach involved a graphical determination of the gradient of the velocity distribution above the sand grain roughened wall (using an offset wall distance) and comparing with the rough wall velocity distribution of Nikuradse (equation 3.2.2). The second method was found to generally exceed the first by around 5%, and so an average of the two was used.

Coleman et al recalculated the friction velocity with the contributions from the side walls included as well as a correction factor for the centre plane shear stress based on experimental data. Comparison of the original and corrected skin friction coefficients showed the original values to be larger by up to 73% - with the discrepancy dependent on Re and roughness configuration. Furthermore, they re-evaluated Schlichting's second calculation for rough wall friction velocity which relied upon an effective wall distance and found that the calculation was very sensitive to the value of wall offset. Unfortunately Schlichting's choice of effective wall location was slightly unphysical, and resulted in a much higher degree of uncertainty in the values of friction velocity compared to the pressure drop method. Also as a result of the choice of effective wall location, the equivalent sand grain roughness calculated by Schlichting was higher than corrected values by 26 - 500%. Coleman et al recalculated the roughness Reynolds numbers using the corrected friction velocity and the more accurate wall shift δz - defined as the origin location that produces the correct slope in the logarithmic region of the velocity profile (see [54]). In doing so they found that three of the plates were actually in the transitionally rough regime.

The issue of transitional roughness was explored by Colebrook and White [10]. They noted a distinct difference in the transition between smooth and fully rough flows for Nikuradse's uniform sand roughness and the transition for 'irregular' industrial roughnesses of galvanised and wrought iron pipes, which were much more gradual than the fairly abrupt transitional behaviour of sand grain roughness. They supposed that the contribution of a roughness element to the resistance only became significant when the local velocity was sufficiently high to initiate the shedding of eddies, before which the drag was only due to comparatively small form drag. By dropping sand grains of various sizes in water, they noted that the grains only slowed according to the square law of drag when the grains were above a certain size, ($k^+ > 14$) - which was shown to be around the point of inflection for sandgrain roughness (figure 3.14).

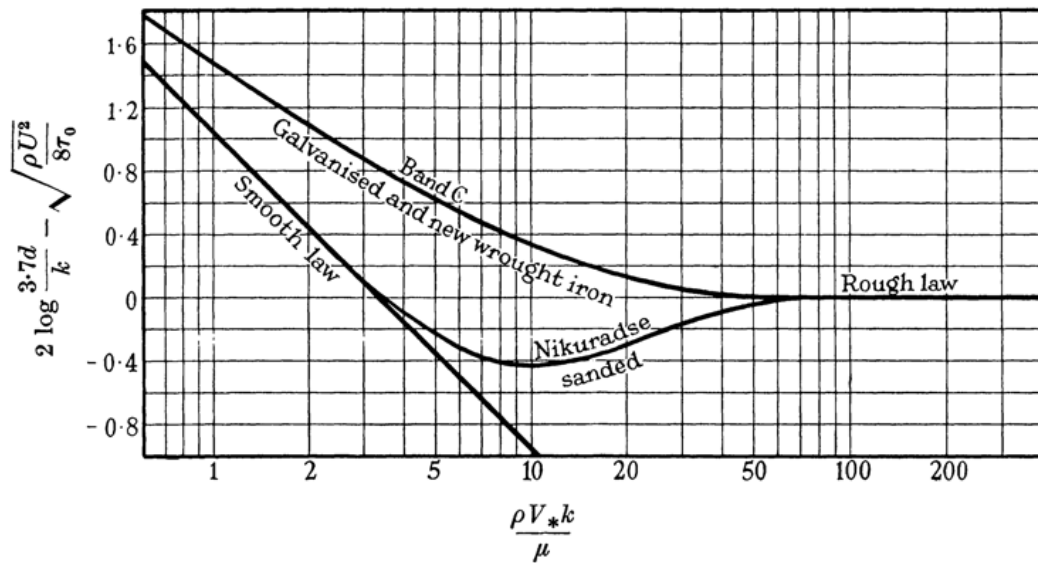


Figure 3.14: Transitional roughness behaviour (taken from [10])

To explore the role of different roughness element sizes, they conducted tests with air from $Re = 3000$ to 127000 using a $6m \times 5.3cm$ ID pipe, to which they applied 5 different roughnesses, created with combinations of two sizes of sand grain - $0.035cm$ and $0.35cm$. The surfaces were split into two 'series', with the first series having the area covered by large grains progressively increased and for the second series, the area of large grains was constant but the area of small grains was increased. 2% addition (by area) of large grains to a surface of uniform fine sand increased the resistance by around 12% at the highest Re and around 20% at $Re = 10000$. The form of the transition function was more gradual, perhaps extending up to $Re = 100000$ where the uniform fine sand surface had reached fully rough conditions. The surface with 5% area of large grains showed very similar but more exaggerated behaviour to surface two. Essentially the transitional behaviour became smoother with increasing area of large grains. In the case of surfaces with constant large grains and variable area of small grains, the transition curves were markedly different. For $Re < 20000$, the surfaces were indistinguishable from one another - suggesting a blocking effect from the larger grains. The Reynolds number at which the effect of fine grains was noticeable was three times greater with large grains present, and for the surface without closely spaced fine grains, no increase in friction factor was observed at higher Reynolds numbers. Overall, their experiments provided good evidence that non-uniform roughness results in more gradual transition from hydraulically smooth to rough behaviour.

Colebrook, with input from White [82], produced a theoretical formula for the transition region for non-uniform roughness by adding together the lower limits of integration of the wall distance term in the equations derived for the smooth ($\frac{1}{\sqrt{\lambda}} = 2 \log \frac{Re\sqrt{\lambda}}{2.51}$) and fully rough regimes ($\frac{1}{\sqrt{\lambda}} = 2 \log 3.7 \frac{d}{k}$), resulting in;

$$\frac{1}{\sqrt{\lambda}} = 2 \log \left(\frac{k}{3.7d} + \frac{2.51}{Re\sqrt{\lambda}} \right) \quad (3.2.6)$$

Colebrook validated the function against data from an assortment of industrial pipes, including galvanised, cast, wrought iron and tar coated cast iron pipes. The transition formula adequately represented the available data. Moody [83], made no new contributions to the study of roughness but packaged the Colebrook-White formula into a convenient chart for engineers - the now widely known 'Moody' chart.

The downwards displacement of the mean velocity profile caused by roughness, expressed by Nikuradse as modifications to C_r , the log-law intercept, was preferred in the form $\frac{\Delta U}{u_*}$ (or simply ΔU^+) by Hama [84] and Clauser [11]. It is more commonly used by investigators to describe the effect of roughness on the boundary layer velocity profile, which is expressed as

$$u^+ = \frac{1}{\kappa} \ln y^+ + C - \Delta U^+ \quad (3.2.7)$$

where

$$\Delta U^+ = \frac{1}{\kappa} \ln k^+ + C - C_r \quad (3.2.8)$$

or, in terms of the friction factor

$$\Delta U^+ = \left(\sqrt{\frac{\lambda}{f}} \right)_{smooth} - \left(\sqrt{\frac{8}{\lambda}} \right)_{rough} \quad (3.2.9)$$

C is the smooth wall log-law intercept (≈ 5). As shown by Hama, Clauser and Monin and Yaglom ([54]), for sufficiently large values of k^+ , the function ΔU^+ varies linearly with $\ln k^+$, which corresponds to the constant value of C_r , or fully rough conditions. The function plotted against k^+ also more clearly shows the variation in transitionally rough behaviour for different roughness types. When plotted against the roughness Reynolds number, ΔU^+ highlights the similarity in behaviour for geometrically similar roughness (data for transverse bars from two different investigators using different experimental apparatus showed excellent agreement).

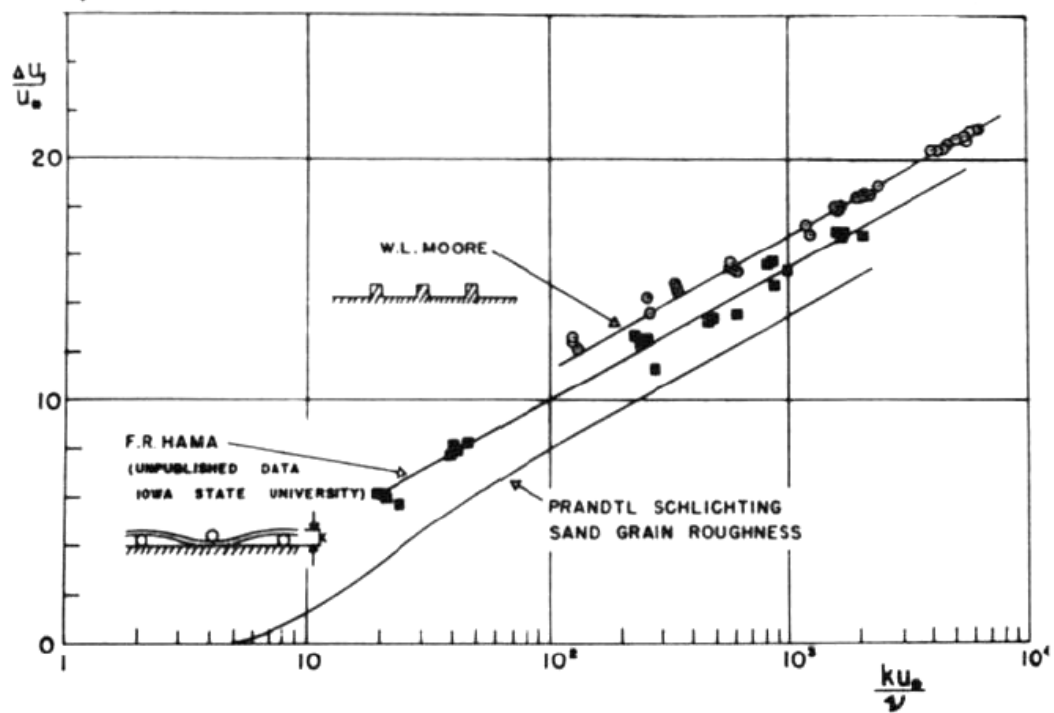


Figure 3.15: Hama roughness function with k^+ (taken from [11])

Experimentally, Hama tested 3D wire screen roughness in a wind tunnel where the roughness was altered through the mesh wire diameter and mesh density. The effect of roughness on the mean velocity was shown in terms of the roughness function against roughness Reynolds number. The outer layer velocity defect profile was found to be universal for smooth and rough surfaces.

Scaggs et al [85] used a water tunnel to measure friction factors of Schlichting type roughnesses from $Re = 10000$ to 600000 . Silicone sheets were moulded with 9 different roughness patterns - large hemispheres ($20 \leq k^+ \leq 1000$), small hemispheres, ($10 \leq k^+ \leq 300$) and cones ($20 \leq k^+ \leq 1000$) to test element size, shape and spacing. The uncertainty in friction factor was $\approx 5\%$. For each roughness type, the largest spacing ($\frac{L}{d} = 8$) gave the lowest resistance, with the smallest spacing ($\frac{L}{d} = 2$) producing the highest friction factors. For the intermediate spacing, despite the large hemispheres having 35% more projected area than cones, the friction factors produced from each surface were practically identical. For large and small hemispherical elements with the same density, doubling the element size was found to increase the friction factor by 2.5 times. The experimental data was used for comparison against a theoretical model for Schlichting-type roughness, named the 'Discrete Element Model'. The model considers roughness blockage and drag forces exerted on the fluid by the roughness

elements, which must be uniform and have circular cross sections - as such it is limited to spherical and conical elements. The model (a full description can be found in [86]) is formulated from the 2D turbulent boundary layer momentum equation for fully developed axisymmetric pipe flow:

$$0 = \frac{\mu}{R-y} \frac{d}{dy} \left((R-y) \beta_y \left(1 + \frac{\mu_t}{\mu} \right) \frac{du}{dy} \right) - \beta_x \frac{dP}{dx} - \frac{1}{2} \rho C_d \frac{u^2 d(y)}{(R-y)L^2/R} \quad (3.2.10)$$

The constants $\beta_{x,y} = \frac{1-\pi d^2(y)}{4(R-y)L^2/R}$, are formulated from the roughness geometry only with no empirical input, although a turbulence model is required to solve for turbulence viscosity (the Prandtl mixing length model was employed). The drag term was correlated from the corrected Schlichting data. Agreement between the model and the experimental data in all cases was good, within around 10%. Taylor et al [86] introduced a new definition for the three phases of rough flow, considering the Reynolds roughness number based on equivalent sandgrain roughness to be limited in usefulness by the single length scale. They preferred a definition based on R_τ , the ratio of apparent wall shear stress due to roughness to the total wall shear stress. From their data, Scaggs et al suggested the limits to be:

Smooth: $R_\tau < 0.05 - 0.1$

Transitionally rough: $0.1 < R_\tau < 0.6$

Fully rough: $R_\tau > 0.6$

A source of good quality modern data on high Reynolds number pipe flows has been the 'superpipe' at Princeton University. The salient feature of the experiments was the very low relative roughness of the pipe, which provided much needed data on roughness effects for low $\frac{k}{\delta}$ flows. Most previous experiments had been conducted on flows where the roughness height was a significant proportion of the boundary layer thickness. Jimenez [14] proposed that the contradiction between various results ([87], [88] (mesh and rod roughness, $\frac{k}{\delta} \approx \frac{1}{50}$), [89] (sand grain, woven mesh, $\frac{k_s}{\delta} \geq \frac{1}{40}$, [25] (bi-directional sanded plate, $\frac{k_s}{\delta} \leq 1 \times 10^{-3}$) with regard to outer layer similarity (if roughness effects extend into the outer layer) could reduce to a critical value of $\frac{k}{\delta}$, suggesting around $\frac{k}{\delta} = \frac{1}{50}$ to be the onset of the breakdown of the outer layer similarity hypothesis of Townsend [90].

Shockling et al [12] presented data for smooth to fully rough flow for a honed aluminium tube (129mm ID) with $\frac{k_{rms}}{D} \approx 2 \times 10^{-7}$ from $Re = 57000$ to 2×10^7 .

The range of k_s^+ was 0.17 to 44. The roughness of the pipe was measured using optical profilometry and was found to have a gaussian distribution, with $R_a = 0.116\mu\text{m}$ and $R_q = 0.15\mu\text{m}$. Careful measurements were made of the mean velocity and pressure drop with traversing pitot tubes and 21 static pressure taps. The transitionally rough friction factor was shown against the prediction of the Colebrook transitional formula and the smallest relative roughness tested by Nikuradse (shown for context rather than direct comparison). The transition curve from the smooth to fully rough laws was more similar to that of Nikuradse's sand grain roughness than the more gradual Colebrook transition function. This was clearly shown through the Hama roughness function (ΔU^+) and Nikuradse log law intercept (C_r) against k_s^+ . Departure from the smooth law for the honed pipe was deemed to occur at $k_s^+ \approx 3.5$, in agreement with Nikuradse's results, but the fully rough condition occurred marginally earlier with increasing k_s^+ . When corrected by ΔU^+ , all log-law profiles were found to collapse to the curve $U^+ = \frac{1}{0.421} \ln y^+ + 5.6$. When scaled in outer variables, the velocity profiles again showed excellent agreement and similarity - supporting the ideas of Townsend and Jimenez.

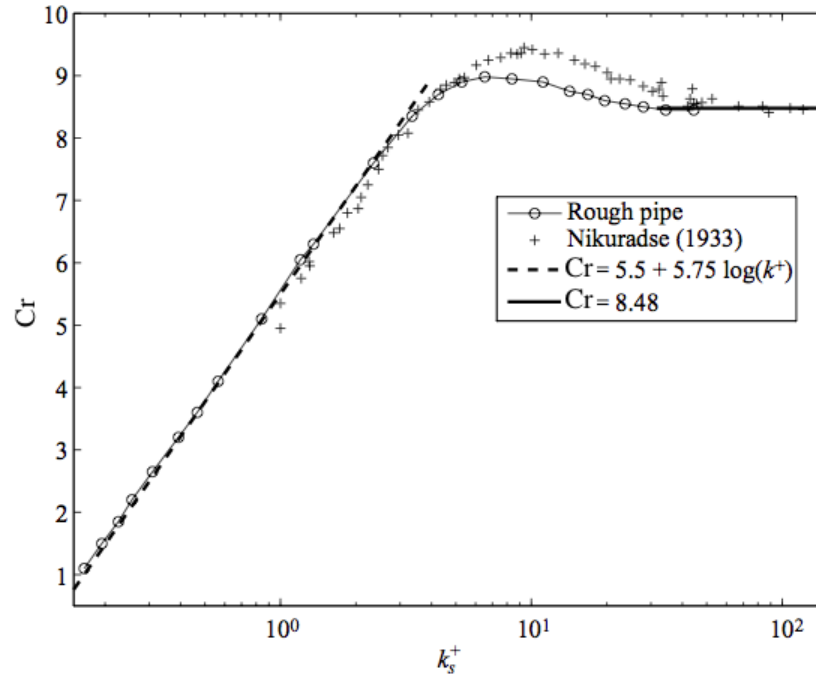


Figure 3.16: Smooth to fully rough behaviour expressed as the Nikuradse roughness function (taken from [12])

Bhaganagar et al [27] performed a Direct Numerical Simulation of 3D 'egg carton'

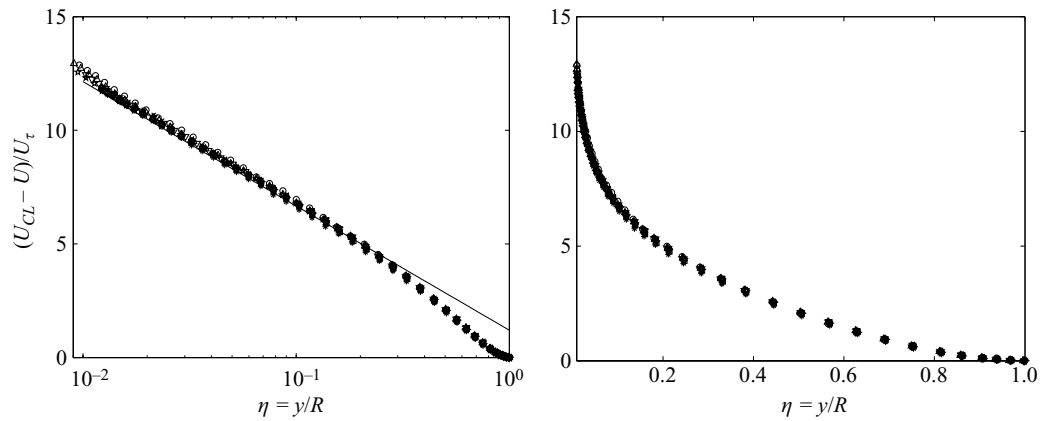


Figure 3.17: Collapse of the outer layer velocity defect profile (taken from [12])

roughness and studied the effect of height ($k_s^+ = 10, 20, 48$), streamwise spacing ($L_x = 0.04 - 1.2$) and spanwise spacing ($L_y = 0.01 - 0.5$) on the boundary layer turbulence. The mean velocity profiles showed the usual trends with roughness. Agreement was found with the relationship for U^+ with k^+ presented by Raupach et al [91], and the ratio $\frac{k_s}{k}$ was similar to Schlichting's values for closely packed spheres. The outer layer mean velocity profile was independent of roughness height. The spanwise spacing was shown to have a negligible effect on ΔU^+ , and variation of the streamwise spacing increased ΔU^+ only slightly. Their main focus was on the fundamental change to turbulence structure, which is discussed later.

3.2.1.2 2D roughness

Until now, only 3D roughnesses have been mentioned, but many studies have been performed on 2D, transverse roughness, for which the primary interest is the effect of spacing or density / solidity of the roughness elements.

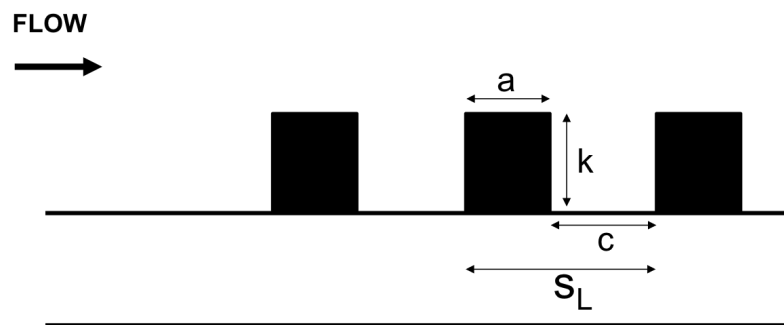


Figure 3.18: Dimensions for 'd' type roughness

Streeter [92] made early observations on the effect of roughness shape, depth and density by measuring fully rough friction factors of pipes roughened by cutting spiral grooves into the walls. For constant depth and spacing, a surface with peaks was found to have a slightly higher friction factor to an 'inverse' surface where the peaks became troughs. In addition, 'abruptly' shaped roughness elements gave a much higher friction factor than more rounded elements. When the depth and spacing was increased, the difference between abrupt and rounded elements was more pronounced. For the same depth of groove and similar shape, the groove spacing was found to have a strong effect on the equivalent sand grain roughness, with the less dense surface having an equivalent sand grain diameter 4 times that of the more densely spaced roughness.

Johnson [93] investigated 2D rectangular transverse roughness using a long flume with element gap to height ratios $\frac{c}{k}$ from 4 - 28. Also shown were other unpublished results from the same research group with different spacings. Johnson found that λ increased fairly rapidly upto $\frac{c}{k} \approx 8$, at which point the decrease slowed with a peak at $\frac{c}{k} = 12$. Beyond $\frac{c}{k} = 12$, the friction factor gradually decreased with spacing. Equivalent sand grain roughness results for $\frac{b}{k} = 4$ as well as $\frac{b}{k} = 1$ and $\frac{b}{k} = 1.25$ consistently showed a maximum at approximately $\frac{c}{k} = 12$. The equivalent sand grain roughness with $\frac{b}{k} = 4$ gave k_s^+ roughly twice that of the investigations around $\frac{b}{k} = 1$.

Bettermann [94] also tested 2D tranverse rods, with solidity ($\lambda_{sol} = \text{total frontal area} / \text{roughness area}$) from 1-8. The results were given in terms of ΔU^+ . Similar results to those of Johnson were obtained, whereby the roughness function was a maximum at some intermediate roughness solidity, around 8. Bettermann produced an expression for ΔU^+ in terms of the solidity, valid for $\lambda_{sol} = 1 - 5$;

$$\Delta U^+ = 5.6 \log k^+ + 17.35(1.625 \log_{10} \lambda_{sol} - 1) \quad (3.2.11)$$

Dvorak [13] showed data for C, (the ΔU^+ intercept) from Bettermann [94], Hama [84], Nikuradse [8], Schlichting [9] and Liu et al [21] for densities ($\lambda_{sol} = \frac{S_L}{a}$) ranging from 5 - 100. He extended the roughness function correlation for roughness densities greater than 5 based on the (limited) high density results of Bettermann and Schlichting;

$$\Delta U^+ = 5.6 \log k^+ - 5.95(1.103 \log_{10} \lambda_{sol} - 1) \quad (3.2.12)$$

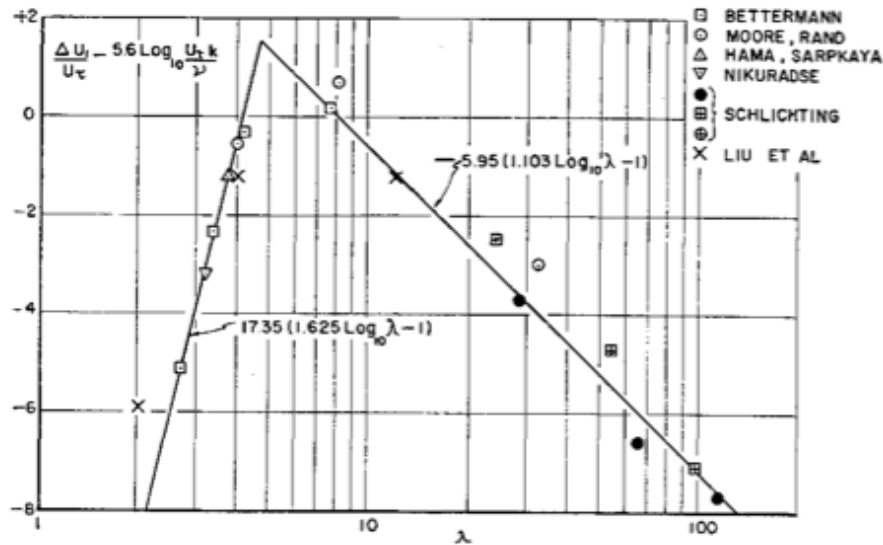


Figure 3.19: Hama roughness function intercept variation with roughness solidity (taken from [13])

One interesting result over 2D transverse roughness is that of Perry et al [16]. It was suggested that for flow over closely spaced grooves, (where stable vortices could persist within the cavity and vortex shedding from the roughness crests is negligible) it was less appropriate to scale the effect of roughness with the roughness height ' k '. They proposed that the behaviour of these type of rough walls may correlate better with outer flow length scales or ' d ' (the boundary layer thickness, δ) and introduced a classification for roughness as k or d type accordingly. They tested rough surfaces with $\frac{k}{c} = 1.1$ and $\frac{S_L}{k} = 3.6$ in a wind tunnel (d and k type respectively). ΔU^+ for the d -type wall was shown to correlate reasonably well with the roughness Reynolds number scaled by the boundary layer thickness, whilst no correlation was apparent with the roughness Reynolds number based on k . Conversely, the k -type wall ($\frac{S_L}{k} = 3.6$) correlated against k^+ and showed qualitative agreement with other previous k -type studies. However, as noted by Jiménez [14], the data of Perry et al is for a single case with high $\frac{k}{\delta}$. Jiménez compared Perry et al's data to d -type data from Wood and Antonia [15] and Bandyopadhyay [17], which showed that k_s was independent of a roughness dimension (the condition of d -type behaviour) only for some cases. Bandyopadhyay's data showed dependence of k_s on k and the ratio $\frac{k}{\delta}$ was lower (1/35). Jimenez considered the onset of k -type behaviour to be when the gap spacing ' c ' was around $3-4k$.

Townes and Sabersky [19] performed flow visualisations on 2D rectangular rough-

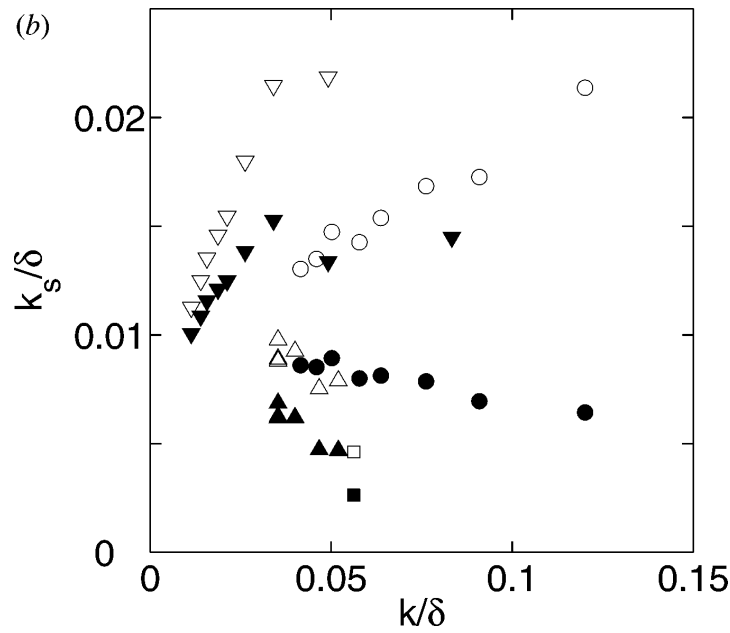


Figure 3.20: Limited evidence for 'd' type behaviour. (taken from [14]). ▲,△ [15]; ●, ○ [16], ▼,▽ [17]. Filled symbols corrected for k/δ according to [18]

ness using a water channel and dye injection. They noted differences in flow behaviour when the cavity depth, k^+ was varied from 12 to 259. For the deepest slots, or fully rough conditions, a quasi-steady vortex was observed, with some momentum exchange occurring around the top of the slot. For $k^+ < 150$, they observed periodic phases of vortex dispersion and reformation within the cavity, which they described as 'strong/weak exchanges'. In the strong exchange, a very noticeable outflow occurred from the cavity and any established vortex pattern was destroyed. In a weak phase, fluid was ejected from the downstream end of the cavity at a relatively small inclination to the flow and the recirculation within the cavity remained mainly intact. They found that the non-dimensional frequency (Strouhal number, $S = \frac{kf}{u^*}$) of the exchanges correlated reasonable well with k^+ . They proposed that the random exchanges they observed were due to the passage of streaky structures (quasi streamwise vortices - as observed by Liu et al [21] and Kline et al [20]) over the cavity. They supposed that for the deep slots, the structures were unable to penetrate into the cavity, leaving the vortex reasonably intact. However, for lower k^+ , the structures were able to transfer fluid from the cavity, which would then be replaced with a corresponding influx into the cavity. One key observation was that the exchanges occurred in adjacent slots simultaneously, suggesting the presence of a coherent structures of turbulence extending many slot lengths downstream.

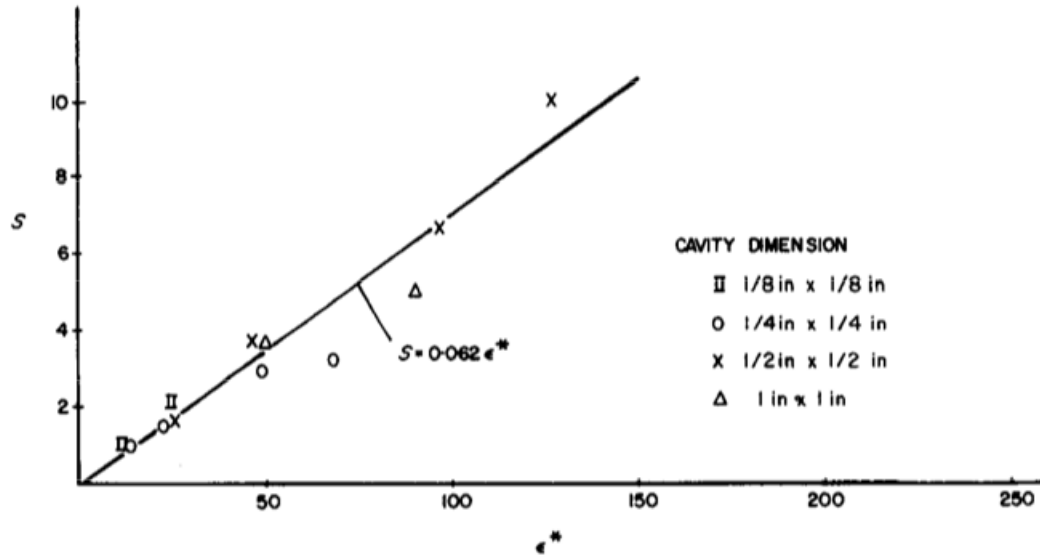


Figure 3.21: Relationship between frequency of slot phase change and slot depth (taken from [19])

A detailed early study of transverse rib roughness was conducted by Liu Kline and Johnston [21]. They observed the flow structure of the turbulent boundary layer over roughness with dye and hydrogen bubble visualisation and measured the mean and fluctuating components of velocity across the boundary layer using hot-wire anemometry. The element spacing ranged from $\frac{S_L}{k} = 2 - 96$. Determination of the origin for rough walls flows can be complicated, as previously mentioned in the case of Schlichting's experiments. In order to achieve the correct logarithmic velocity profile, an effective wall distance was used with the offset distance and the friction velocity calculated graphically following the approach by Perry and Joubert [95].

For the smallest spacing ($\frac{S_L}{k} = 2$), flow visualisation revealed a pattern of longitudinal streaks of alternating high and low speed fluid on the roughness crests - similar to that previously reported on smooth walls [20]. Further discussion of the significance of these streaky structures in the turbulent boundary layer will be provided later. Within the grooves, an almost stable vortex was formed although occasionally the vortex was interrupted and fluid was ejected from the groove into the boundary layer. At $\frac{S_L}{k} = 4$, flow separation occurred over the crests and the streaky structures were no longer present. The cavity vortex became stretched and less stable. At $\frac{S_L}{k} = 12$, the flow was a more complicated mix of separation and reattachment in between the crests and troughs. The three observed flow

patterns were described as 'skimming flow', 'wake-interference flow' and 'isolated roughness flow'.

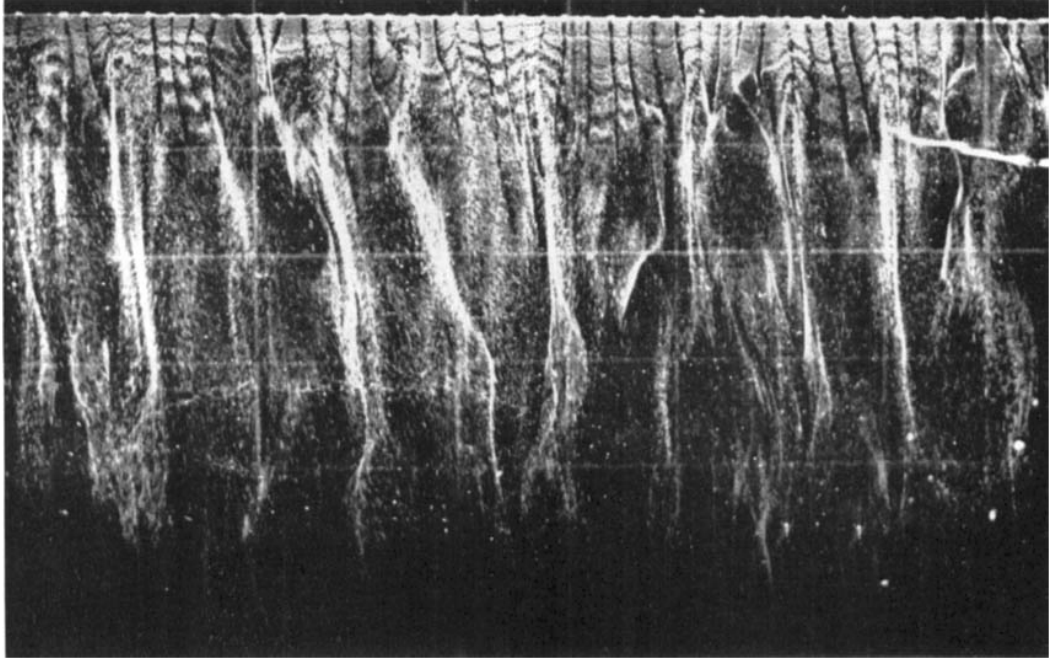


Figure 3.22: Top down view of streamwise vortices over a plate plate, $y^+ = 4.3$ (observed by Kline et al [20])

ΔU^+ was highest for the $\frac{S_L}{k} = 4$ and 12. ΔU^+ varied linearly with k^+ for a given spacing. Comparisons were made against the data of Perry and Joubert [95], Bettermann [94], Colebrook and White [10], Nikuradse [8] and Hama [84]. Generally good agreement was found between the datasets for transverse bar roughness at different spacings. With the roughness function expressed in terms of sand grain roughness, Liu et al's data for $\frac{S_L}{k} = 4$ and 12 matched the wire screen data of Hama, and the results for $\frac{S_L}{k} = 2$ (low k_s^+) were found to coincide with Nikuradse's results, providing support for the usefulness of both the spacing parameter, $\frac{S_L}{k}$ and the equivalent sand grain roughness, k_s for studies of 2D roughness. In the outer layer, they found the universality of the velocity defect law to hold.

Calculations of the ratio of eddy to kinematic viscosity showed that roughness increased the ratio of turbulence production to dissipation (with a maximum in between spacings of 4 - 12). The increase in eddy viscosity due to roughness effectively thickened the boundary layer in the same fashion as an increase in molecular viscosity. Measurements of streamwise fluctuating velocity (u'/u_{avg}) at

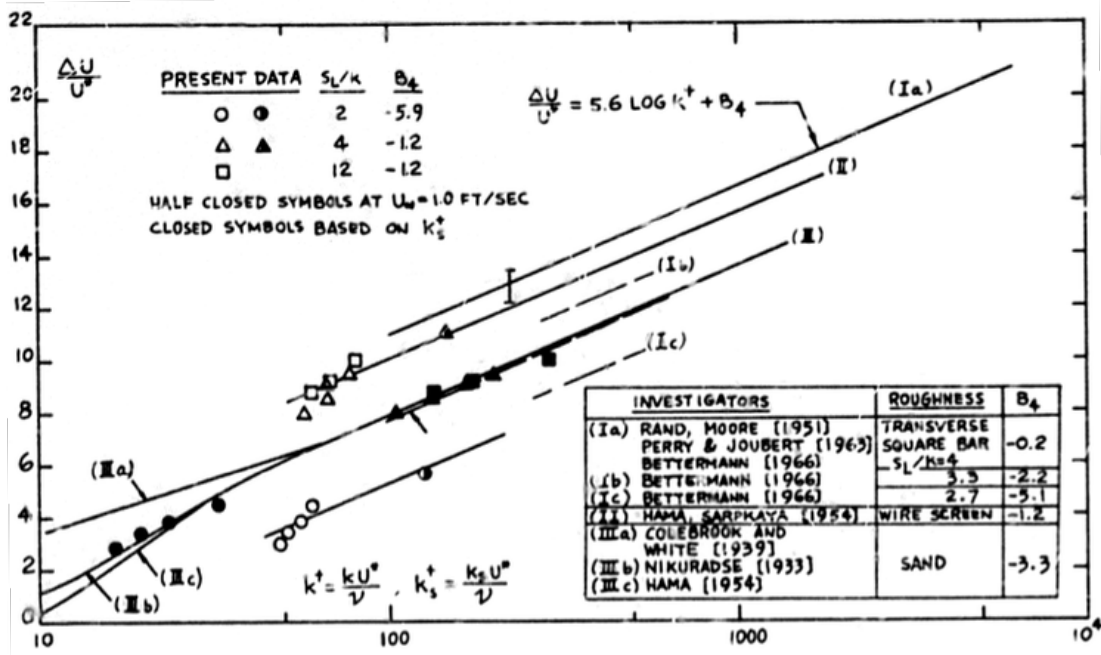


Figure 3.23: Comparison of ΔU^+ for various investigators (taken from [21])

one streamwise position across the boundary layer provided early evidence for the modification of near wall turbulence intensity by roughness.

3.2.1.3 More advanced studies of higher order turbulence statistics over 2D and 3D roughness

2D roughness

Wood and Antonia [15] measured mean and fluctuating velocities over a d -type wall ($\frac{S_L}{k} = 2$) in a manner similar to Liu et al (hot wire anemometry) and compared the results to a smooth wall and k -type roughness. The ratio of boundary layer thickness to roughness height was quite low ($\frac{\delta}{k} = 16$). The mean velocity distribution (in velocity defect form) showed excellent agreement with Perry et al [16] and Liu et al's [21] curve fell slightly below. The velocity profile displayed self similarity and was almost independent of streamwise location. The roughness function was well correlated with the roughness Reynolds number expressed in terms of the origin offset ($\frac{\epsilon U^*}{\nu}$ - as first discussed in [16]), but also showed some dependence k^+ , which invalidates the criteria for d -type walls.

Analysis of the three components of fluctuating velocity, $\overline{u'^2}$, $\overline{v'^2}$, $\overline{w'^2}$ (or turbulence intensity when normalised by friction velocity, $\sqrt{\overline{u'^2}}/U^*$) and the mean shear stress, $-\overline{u'v'}/U^{*2}$ suggested that differences between rough and smooth walls were

confined to the region very near to the wall, where a peak in mean shear stress was observed for the rough case. The skewness of the streamwise velocity component ($\overline{u^3}/(\overline{u^2})^{3/2}$), became positive close to the wall for d -type roughness, but remained negative in the case of smooth walls and k -type roughness. The positive value of S_u close to the wall was thought to be due to the influx of high velocity fluid to the wall following a burst event of low velocity fluid away from the wall - as observed in flow visualisations [21], [19].

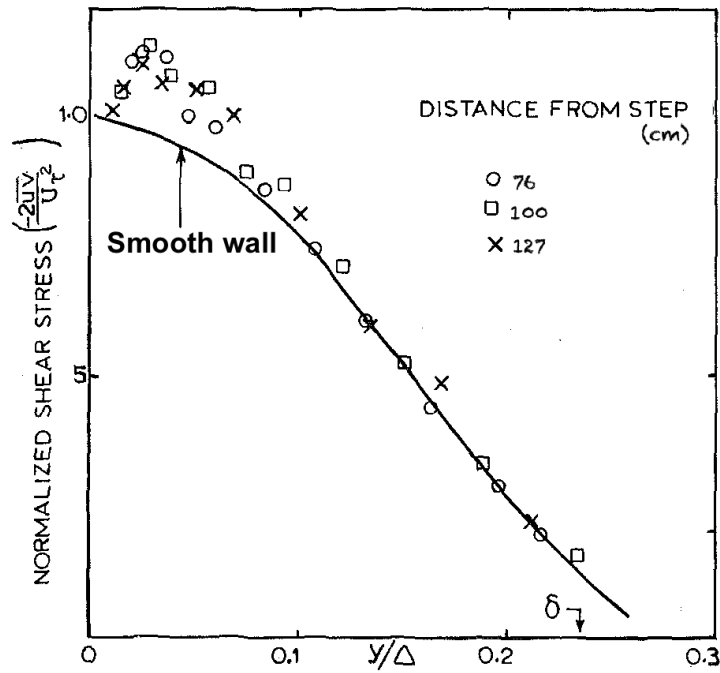


Figure 3.24: Increase in Reynolds shear stress over a d -type wall (taken from [15])

Djenidi et al [22] improved the fidelity of d -type rough wall studies by using laser doppler anemometry (LDA) to measure fluctuating components of velocity and dye injection / laser induced fluorescence (LIF) to visualise the flow field. They noted that hot wire probes (as used in [21] and [15]) lack reliability close to the wall, particularly for wall-normal velocity fluctuations. They compared their LDA measurements on a smooth wall against the DNS of Spalart [96] and found excellent agreement to the edge of the viscous sublayer. They made similar observations on the ejection of fluid from the cavities to those of Townes and Sabersky [19] and Liu et al [21] (ie. 'strong' and 'weak' exchanges from otherwise quasi-steady rotational cavity flow) and measured the mean ejection period and duration to be approximately $\frac{5.5\delta}{U_\infty}$ and $\frac{\delta}{U_\infty}$ respectively. They also captured the existence of quasi-streamwise vortices, which produced ejection events from 2 - 3 consecutive cavities. Further flow visualisations using two laser light sheets

revealed alternating outflow and inflow events along the span of cavities consistent with the passage of quasi-streamwise vortices across the surface. They estimated the outflow to have a spanwise distance of 100 viscous lengths ($100 \frac{U^*}{\nu}$) - comparable to the cavity dimensions. This observation was supportive to the observations of Townes and Sabersky [19], who noted the frequency of ejections to be related to the roughness height.

In contrast to [15], components of turbulence intensity were consistently higher for the rough wall than the smooth wall over most of the boundary layer (up to $y^+ \approx 400$), and values above cavities were slightly higher than above crests. The Reynolds shear stress ($-\overline{u'v'^+}$) was considerably higher than the smooth wall in the near wall region (suggesting an increase in average turbulent energy production from more intense sweeps and ejections), but collapsed to the smooth wall profile for $\frac{y}{\delta} > 0.4$.

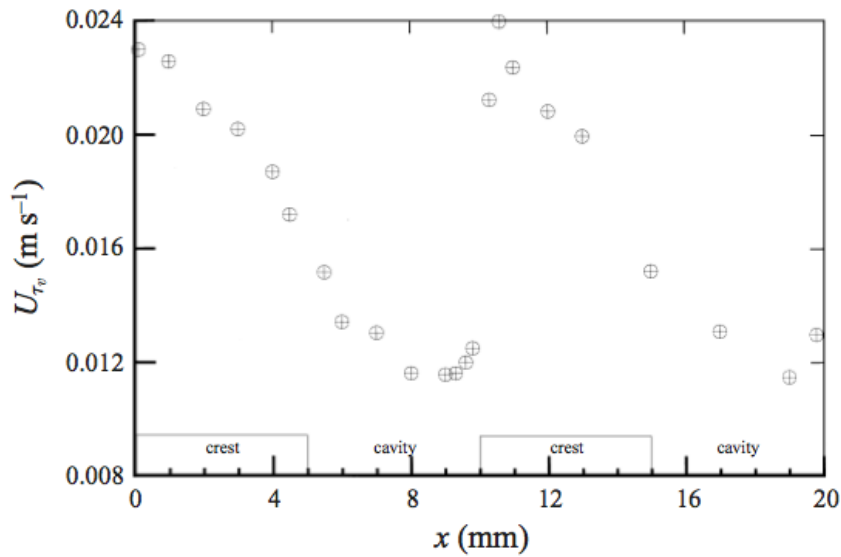


Figure 3.25: Variation in friction velocity over crests and cavities of a d -type wall (taken from [22])

In a later study, Djenidi et al [23] examined the self-sustaining nature of d -type roughness in greater detail. A periodicity was observed in the averaged velocity components above and between cavities, which decreased with distance from the wall. A periodic variation was also measured in the friction velocity over crests and cavities. The two measurements show that the wall boundary condition effectively modifies the fluid streamlines above the wall with a wavelength comparable to the roughness wavelength.

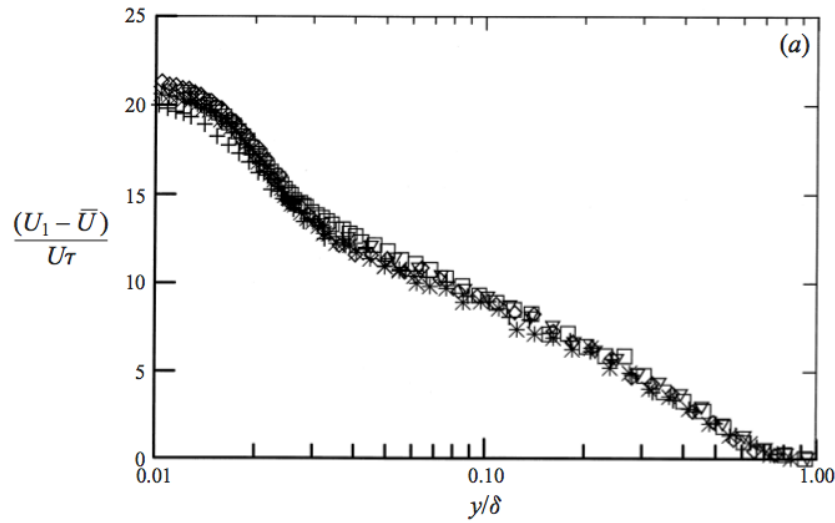


Figure 3.26: Self sustaining turbulent boundary layer over a d -type wall (taken from [23]). Symbols represent different streamwise locations

The distributions of turbulence intensity also displayed a streamwise periodicity. The Reynolds stresses were increased at the downstream end of the cavity, which correlated well with the visualisations of previous investigators who found influx and outflux to occur mainly at that location. As found in their previous investigation, all the Reynolds stresses were larger over the rough wall, with the greatest enhancement in v' and $-\overline{u'v'}/U_*^2$. Furthermore, each profile of Reynolds stress was shown to collapse reasonably well at different downstream locations - further evidence for self preservation. One quite interesting near wall observation was that the location of maximum Reynolds shear stress ($-\overline{u'v'}$) was roughly equal to the location of constant rate of change of $\frac{dU}{dy}$ (or $d^2U/dy^2 = 0$). The maxima in $-\overline{u'v'}$ was attributed to the change in wall boundary condition in conjunction with fluxes in and out of the cavity and represented the relative increase in turbulence production with respect to a smooth wall. The magnitude of the peak implied strong correlation between u and v components - associated with coherent structures of turbulence.

The observations in [22] and [23] show that the self sustaining quality of d -type walls is related to the upward displacement of low momentum fluid from the cavities and resulting vorticity ($\vec{\omega} = \nabla \vec{v}$) generation. Furthermore, although mean velocity profiles suggest that the effect of roughness is limited to the roughness sub-layer, measurements of Reynolds stress indicate that roughness effects extend into the outer regions of the boundary layer. They proposed that the surface boundary

condition (nature of roughness) modifies the near wall structures of turbulence (whether in size, shape or strength), which then exert some effect on the outer layer.

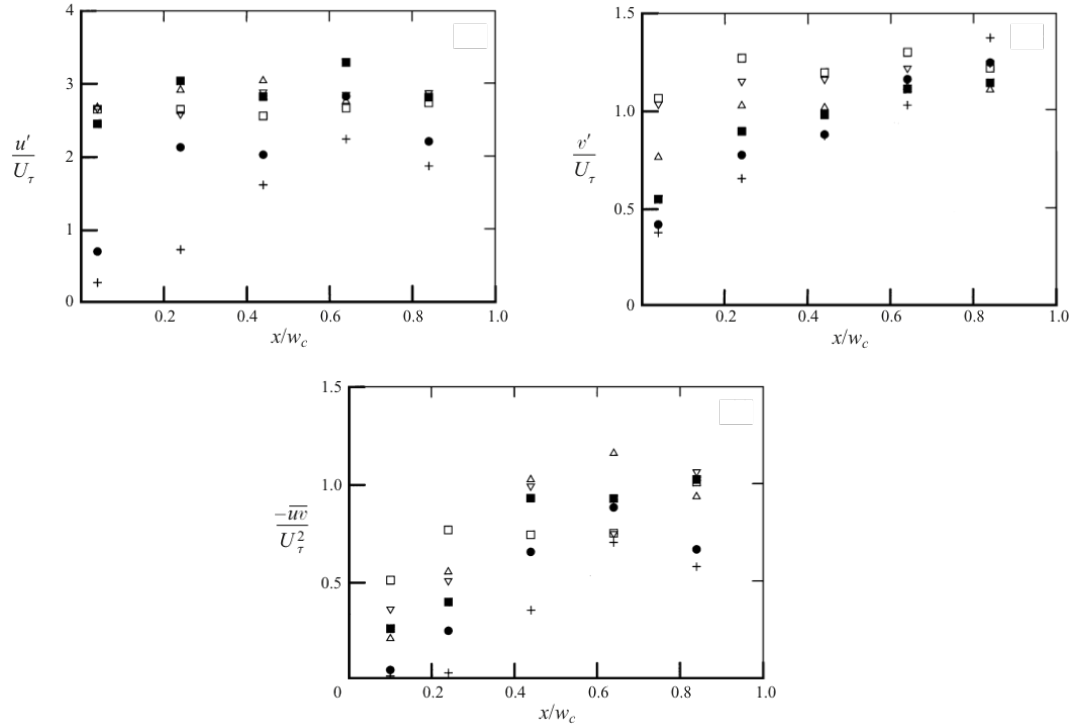


Figure 3.27: Variation of fluctuating velocities and Reynolds shear stress across a d -type wall cavity (taken from [23]). Symbols indicate height of measurement above the cavity

3D roughness

Ligrani and Moffatt [24] tested spherical roughness in the most dense arrangement in a wind tunnel from the transitional to fully rough regime. The roughness geometry was kept constant and k^+ was varied from 20 - 63 by increasing the free stream velocity. Hot wire anemometry was used to measure the mean and fluctuating components of velocity in three dimensions and subsequent calculation of the six Reynolds stresses. The maximum uncertainty in Reynolds stress was 10%. The transitional behaviour of the roughness was even more abrupt than Nikuradse's sand grain roughness, consistent with the earlier findings of Colebrook and White [10] on a similar surface of very uniform densely packed spheres.

The effect of increasing k^+ on turbulence was most easily observed by the profiles of streamwise turbulence intensity. For $k^+ > 55$ (fully rough flow), the profiles were invariant over the outer 98% of the boundary layer and for $k^+ < 22$, the

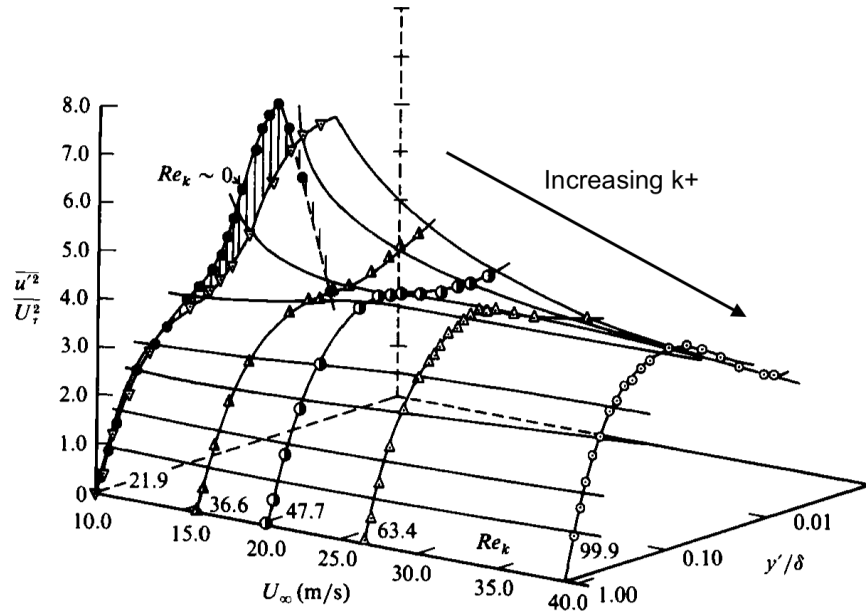


Figure 3.28: Effect of k^+ on streamwise turbulence intensity ($\frac{\overline{u'^2}}{U_*^2}$) for spherical roughness (taken from [24])

profile approached the smooth wall profile - characterised by a well defined near wall peak in turbulence intensity around $y^+ = 15$. With increasing k^+ , the near wall peak tended to be reduced and eventually destroyed altogether, while the profile generally flattened. At intermediate roughness Reynolds numbers, a plateau in turbulence intensity occurred for $100 \leq y^+ \leq 500$, which with increasing roughness Reynolds number formed a broad hump, with a maximum at around $y^+ = 250 - 400$ for fully rough conditions. In essence, the production of streamwise turbulent energy was transferred from a small region close to the wall to a wider region further from the wall. It was suggested that the hump in the profile was due to modification in the turbulence sweep ejection cycle, with increased quantities of low momentum fluid in the roughness cavities being ejected from the wall and colliding with high speed fluid.

Rough wall profiles of normal and transverse Reynolds stresses were generally higher than the smooth wall values. The profiles of turbulent kinetic energy ($\overline{q^2}/U_\infty^2$) for different k^+ showed similarity over the outer 60-70% of the boundary layer. Evaluating the turbulent kinetic energy balance and plotting the turbulence kinetic energy production term ($-\overline{u'v'}\partial U/\partial y$) across the boundary layer showed that maximum turbulence production in the inner layer occurred at $k^+ = 21$, with a peak at $y^+ = 20$. The inner layer production peak decreased with increasing k^+ and disappeared for $k^+ > 55$, when fully rough conditions had been

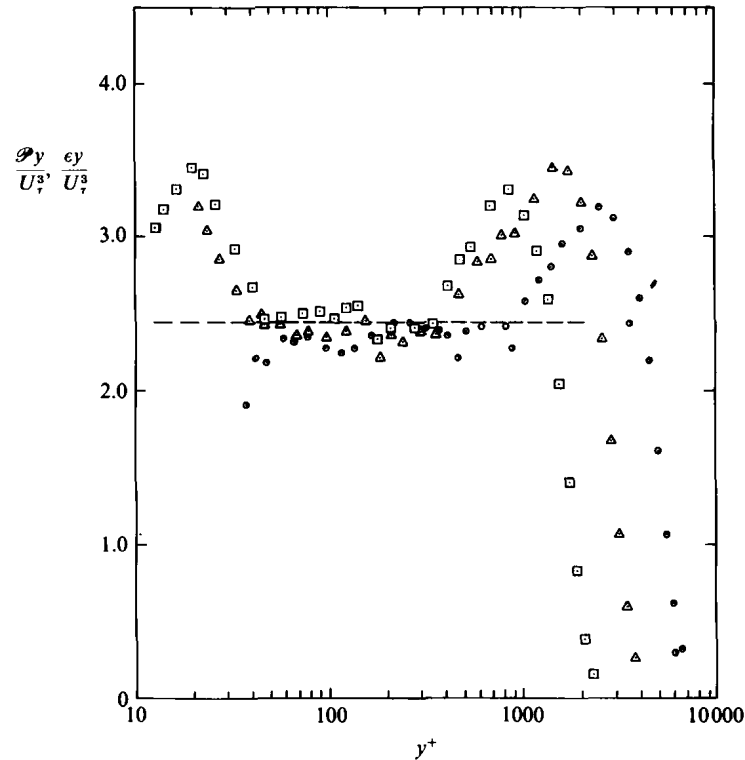


Figure 3.29: Effect of k^+ on turbulence kinetic energy production normalised by friction velocity (taken from [24]). \odot , $k^+ = 61$; \triangle , $k^+ = 34$; \square , $k^+ = 21$

achieved. In dimensional terms though the turbulence production at $k^+ = 60$ was an order of magnitude of more than for $k^+ = 20$. The authors mused that with transition from smooth to fully rough flow, the relative importance of the terms in the turbulent kinetic energy budget equation would be altered - for instance the production term increases by large amounts with increasing k^+ , however the effective turbulence dissipation of the viscous sublayer decreases with increasing k^+ .

Schultz and Flack [25] added to the dataset on low k/δ flows by measuring fluctuating velocity components and Reynolds stress distributions over a surface geometrically similar to the previously discussed surface of Shockling et al [12], created by bi-directional sanding of an acrylic plate. The rms roughness height was measured by optical profilometry to be $k_{rms} = 26\mu m$. They studied the surface using a water tunnel from smooth to fully rough conditions, ensuring that the roughness height was always at least three orders of magnitude smaller than the boundary layer thickness. Boundary layer velocity profiles were measured using Laser Doppler Anemometry with a maximum uncertainty in the Reynolds stress of 9%. Mean velocity profiles plotted in inner variables showed the typical downward shift with increasing k_s^+ , and in outer variables showed collapse to a

single curve across the boundary layer for all k_s^+ . The transitional roughness data overlaid that of Shockling et al, with upper and lower limits of roughness transition of $k_s^+ = 2.5$ and 25 respectively.

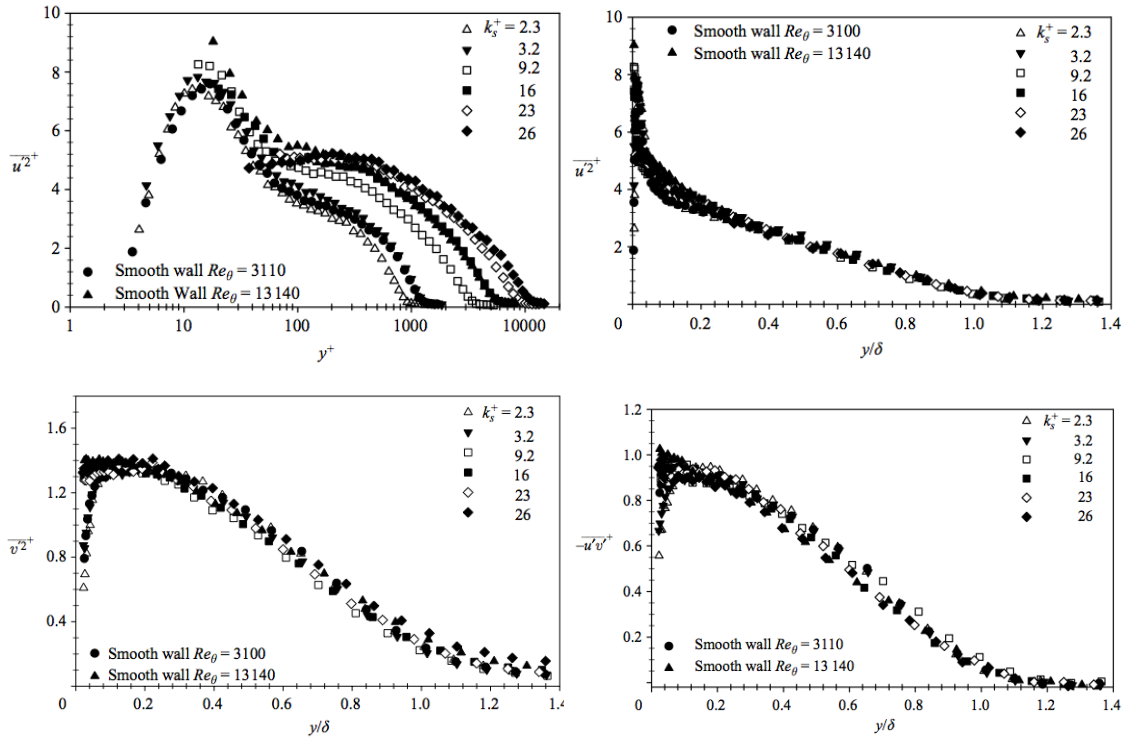


Figure 3.30: Variation of turbulence intensity with k_s^+ (taken from [25]). Top left; streamwise, inner variables. Top right; streamwise, outer variables. Bottom left; wall-normal, outer variables. Bottom right; Reynolds shear stress, outer variables

Profiles of streamwise Reynolds normal stress ($\overline{u'^2}$) in inner variables showed the same reduction in near wall peak with increasing k^+ as previously observed in [24]. With increasing k_s^+ , the profile plateaued between $y^+ = 100 - 1000$. In outer variables, $\overline{u'^2}$ collapsed and similarity was observed for smooth and rough walls. The wall normal Reynolds stress profile for smooth and rough walls matched to within the experimental uncertainty in the outer layer, although a plateau was observed close to the wall ($y/\delta < 0.2$). No significant difference was observed for the Reynolds shear stress profile in the outer layer, which is contrary to the results of Krogstad et al [87] and Antonia and Krogstad [26], but in agreement with the data reviewed by Raupach et al [91].

Quadrant decomposition analysis of the percentage contribution of low energy ejections and sweeps (Q2, Q4 - see figure 2.9) to the total Reynolds shear stress

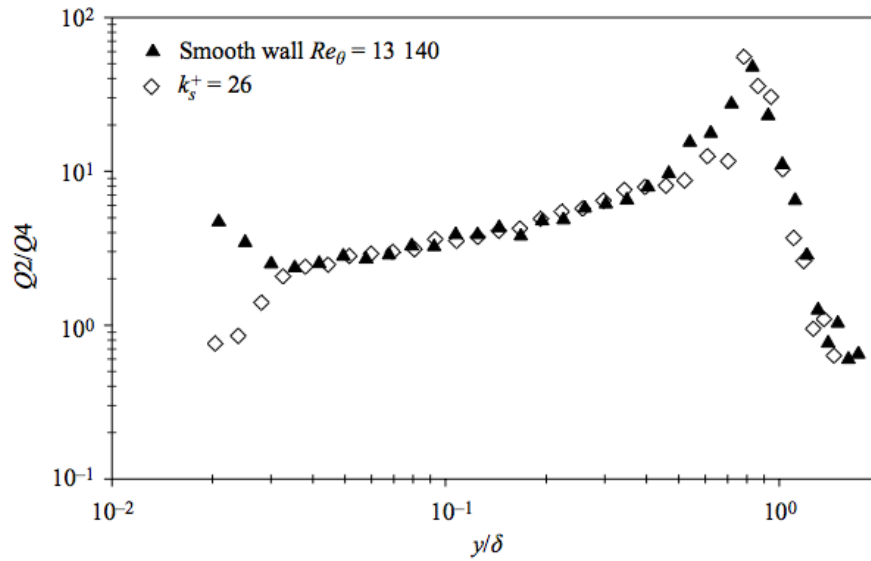


Figure 3.31: Effect of k^+ on turbulence sweep-ejection cycle (taken from [25])

showed no significant changes to the turbulence structure in the outer layer as a result of surface roughness. Similar results were obtained by Flack et al [89] over sandpaper and mesh roughness for much higher k/δ (1/62 and 1/45 respectively), although with $k/\delta = 1/15$, Krogstad et al [87] noted an increased contribution from Q2 and Q4 events over woven mesh roughness. With the sensitivity of the quadrant decomposition increased to isolate strong turbulent events, good agreement was again observed in the outer layer between smooth and rough walls. However, near the rough wall, ejections were found to be suppressed, while the contribution to the Reynolds shear stress from sweeps was increased. The opposite was noted for the smooth wall. The ratio, $Q2/Q4$ clearly showed that near the rough wall, sweeps contributed more to the total Reynolds shear stress than ejections.

The third order turbulence statistic ($\overline{u'^3}$) also showed similarity in the outer layer and significant differences in the inner layer. The rough wall profile became positive while the smooth wall remained negative. The destruction of the $\overline{u'^2}$ peak and change in sign of $\overline{u'^3}$ were suggested to be indicative of the modification of near wall quasi streamwise vortices and associated sweep-ejection cycle. Overall, the study of Schultz and Flack provided support for the outer layer similarity hypothesis of Townsend [90], and the theory of scale separation of Jimenez [14]. They note that the most noticeable effect of roughness on the outer layer turbulence seems to be from 2D transverse rod roughness.

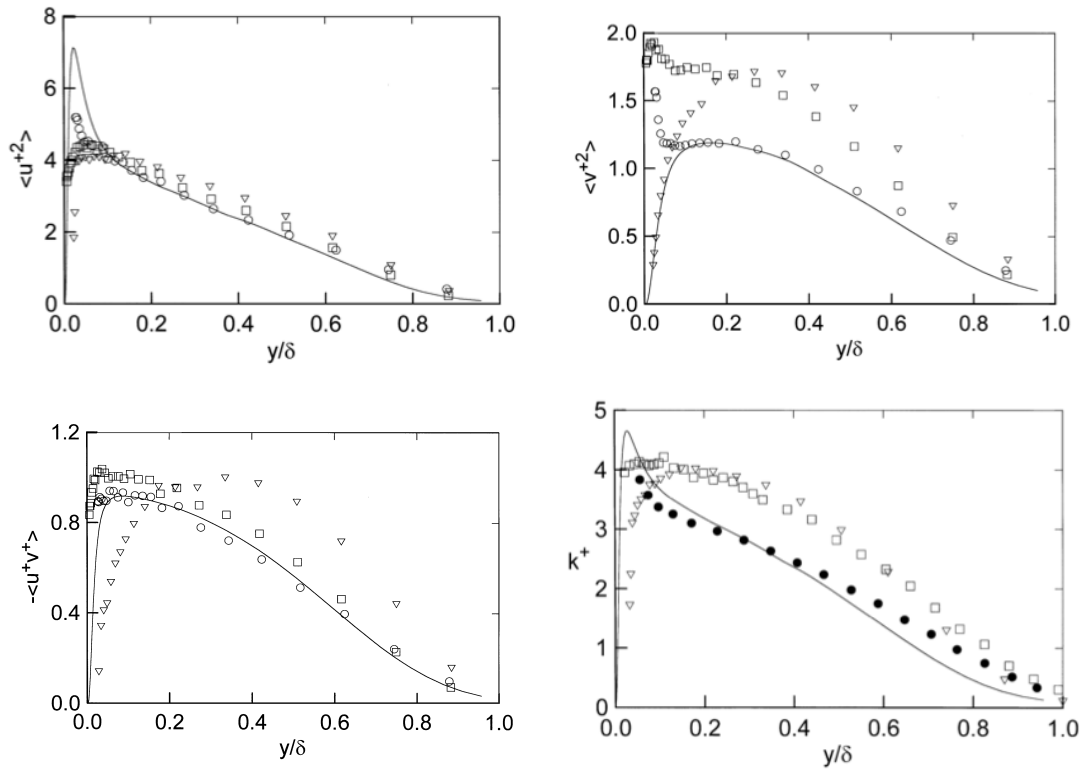


Figure 3.32: Normalised Reynolds stresses and turbulent kinetic energy profiles for different roughnesses with the same k^+ (taken from [26]). \circ , smooth wall; \square , mesh roughness; ∇ , rod roughness; $-$, DNS (Spalart 1988)

Antonia and Krogstad [87], [88], [26] tackled the issue of 2D and 3D roughness directly by studying the flow over spanwise circular rods and mesh screen roughness in a wind tunnel. Both surfaces had similar effects on the mean flow ($\Delta U^+ \approx 11$, $k_s^+ \approx 340$). k/δ in the experiments was $1/54$. The smooth wall DNS of Spalart [96] was used for reference. The streamwise Reynolds stress exhibited the smallest difference between the surfaces. When plotted in outer variables, the rod roughness was consistently higher than the mesh roughness, and differences between all three surfaces (greater than the experimental uncertainty) seemed apparent well into the outer layer. The wall normal and Reynolds shear stress displayed differences between the surfaces more clearly. While the mesh roughness retained a near wall peak with a plateau and gradual reduction in Reynolds stress towards the outer layer as shown previously, the rod roughness showed no near wall peak but a rapid increase away from the wall to a broad maxima around $\frac{y}{\delta} = 0.3$. The profile for rod roughness was then consistently higher than the mesh roughness for the outer portion of the boundary layer. This observation suggested that wall-normal turbulence is most greatly affected by the type of surface, and ultimately by rod

type roughness. In addition, surfaces with the *same* ΔU^+ can apparently modify turbulence in the boundary layer quite differently.

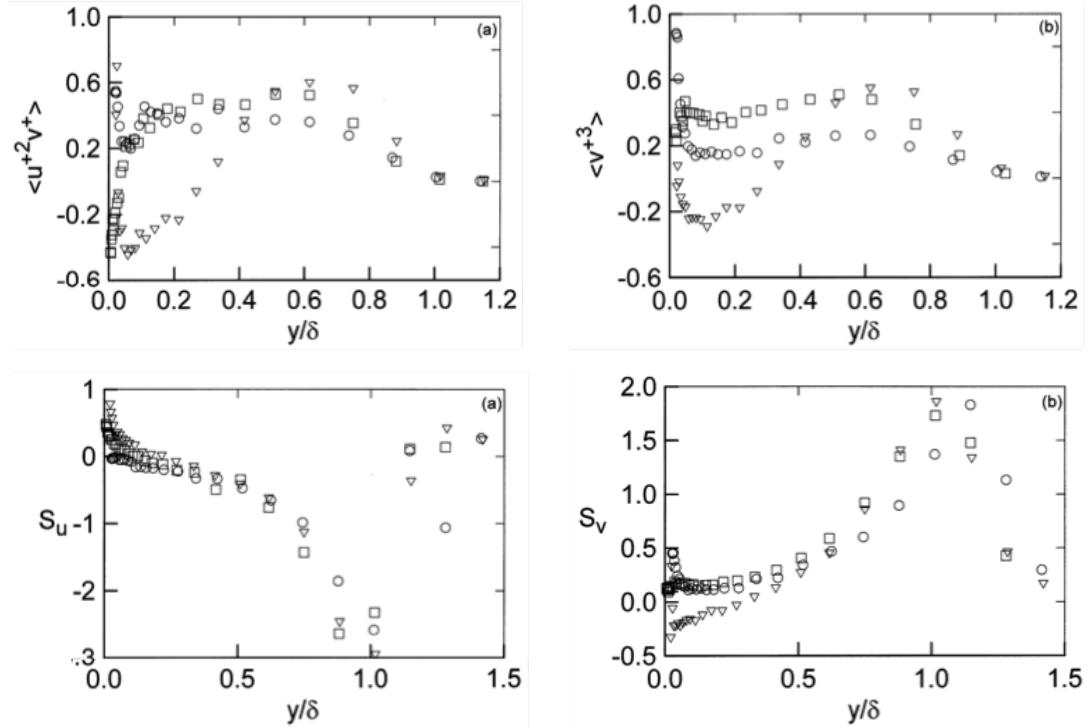


Figure 3.33: Third order moments of velocity fluctuations and skewness across the boundary layer for roughness with the same k^+ (taken from [26])

Major differences were seen for the third order moments of the streamwise and wall normal components of fluctuating velocity ($\overline{u'^+2 v'^+}$), ($\overline{v'^+3}$) between the surfaces for $y/\delta < 0.5$. The rod roughness had negative values at the wall for both moments, whereas the mesh roughness was only negative near the wall for $\overline{u'^2 v}$. The difference in triple products between the rod and mesh roughness highlighted the enhanced transport of momentum towards the walls for the rod roughness, in contrast to the transport of momentum away from the wall from 3D roughnesses. They also noted that since the y derivatives of the two triple products are associated with turbulent energy diffusion from the wall normal fluctuating velocity, there is a gain of turbulent energy over rod roughness. Skewness of the u velocity component, S_u changed sign near the wall for both types of roughness, but skewness of the v component, S_v only changed sign over rods. They suggested that the change in wall-normal skewness was indicative of the transport of momentum by wall-normal fluctuations into the cavities between the elements. Analysis of the anisotropy of the Reynolds stresses showed that roughness generally reduced

anisotropy. The 3D mesh roughness was found to have the greatest effect on isotropy. The findings are contrary to the outer layer similarity hypothesis of Townsend, but the value of k/δ is close to the limit proposed in [89] for the onset of breakdown of the hypothesis.

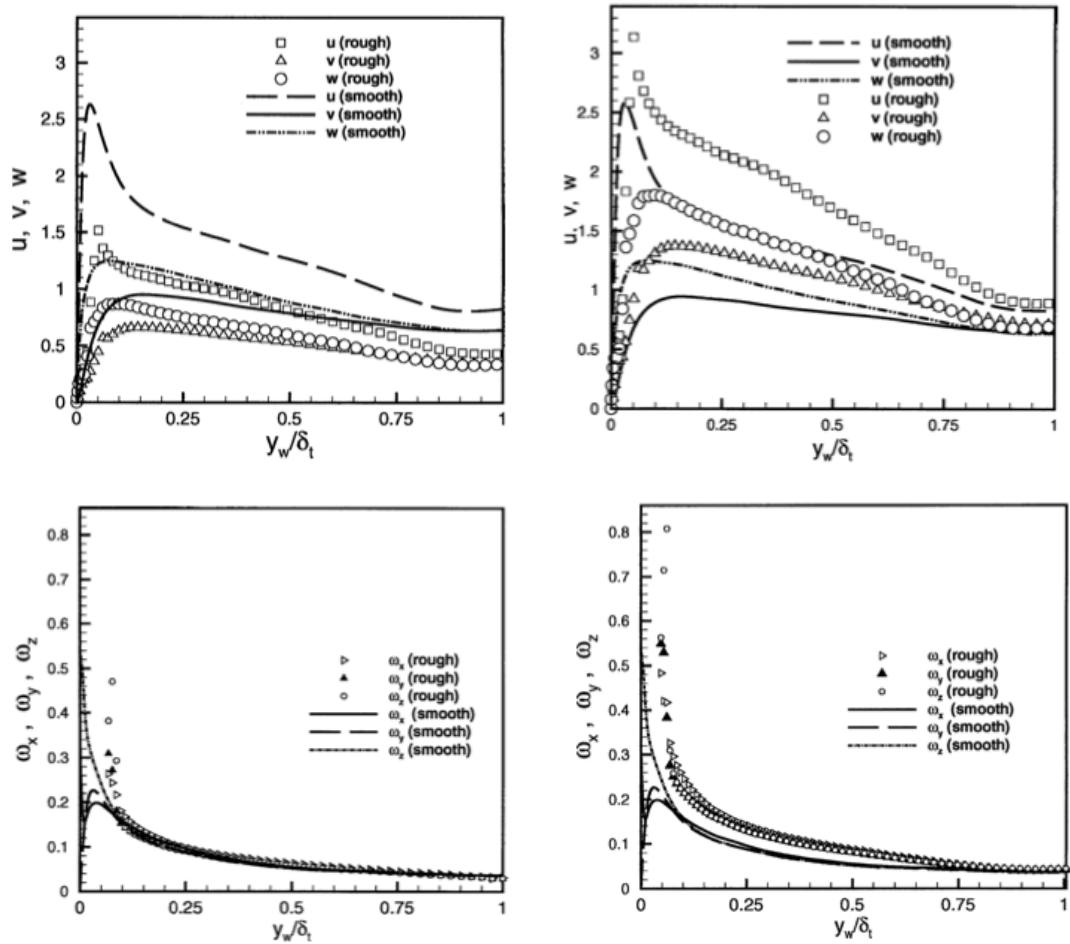


Figure 3.34: Profiles of turbulence intensity (top) and vorticity (bottom) (taken from [27]). Left: normalised by local U^* , Right: normalised by smooth wall U^*

Bhaganagar et al [27] performed a DNS of 3D 'egg carton' roughness in a plane channel and also produced findings contrary to the outer layer similarity hypothesis. They focussed mainly on the fundamental differences in inner and outer layer turbulence structure over a smooth and rough wall. Their findings on the mean flow have been discussed earlier. The rms velocity fluctuations (normalised by smooth wall U^*) across the channel width (normalised by channel half height) showed the typical increase in turbulence intensity over roughness, with the strength of the fluctuations becoming more extreme with increasing k^+ . With an alternative normalisation for y which considered the difference in boundary layer

thickness between the smooth and rough walls, differences in the rms fluctuations from roughness were shown to extend into the outer layer. Further differences in fluctuating velocity components across the boundary layer between smooth and rough walls were demonstrated when plotted in both inner and outer variables and normalised by the respective (smooth or rough) friction velocity. The results showed similarity to the findings of Antonia and Krogstad [26] for mesh roughness, who observed a near wall reduction in streamwise fluctuation and an increase in wall-normal fluctuation. Examination of the rms vorticity fluctuations showed an increase in absolute vorticity in the vicinity of roughness, but when scaled by the local U^* , no changes to the outer layer vorticity by roughness were noted. The authors suggested that the vorticity in the outer layer was unaffected by roughness since the structure of small scale turbulence in the outer layer was naturally more isotropic and of similar magnitude for smooth and rough walled flows. The effect of roughness on the isotropy of larger scales (as measured by rms velocity fluctuations) was in agreement with the work of Antonia and Krogstad.

Differences between smooth and rough walls were also noted in the skewness of the fluctuating velocity components. For a smooth wall, streamwise skewness changed from positive to negative around $y^+ = 10$, but for the rough case this occurred at $y^+ = 20$. The wall normal skewness displayed the most differences between smooth and rough - being predominantly negative beyond $y^+ = 30$ for the rough case, but positive for the smooth wall between $y^+ = 30 - 130$. These results suggested that turbulence transport in the wall-normal direction is most influenced by a change in wall roughness.

Bhaganagar et al also showed the effect of roughness on the terms of the turbulent kinetic energy transport equation (equation 2.4.13) across the boundary layer. When normalised by the smooth wall friction velocity, the maximum rate of production and dissipation of turbulent kinetic energy as well as the maximum rate of turbulent transport was higher over the rough wall. Differences to the viscous diffusion terms were also noted in the inner layer. Furthermore, analysis of the Reynolds stress transport terms ($\overline{u'^2v'}$, $\overline{u'v'^2}$ for $\overline{u'^2}$ and $\overline{u'v'}$ respectively) showed major differences for $\overline{u'^2v'}$ between smooth and rough surfaces across the inner layer. $\overline{u'v'^2}$ was not modified to the same degree. The energy budget and Reynolds stress transport terms confirmed modifications to the outer layer wall-normal transport behaviour by roughness. Contours of instantaneous streamwise velocity showed structures to be more elongated in the wall-normal direction

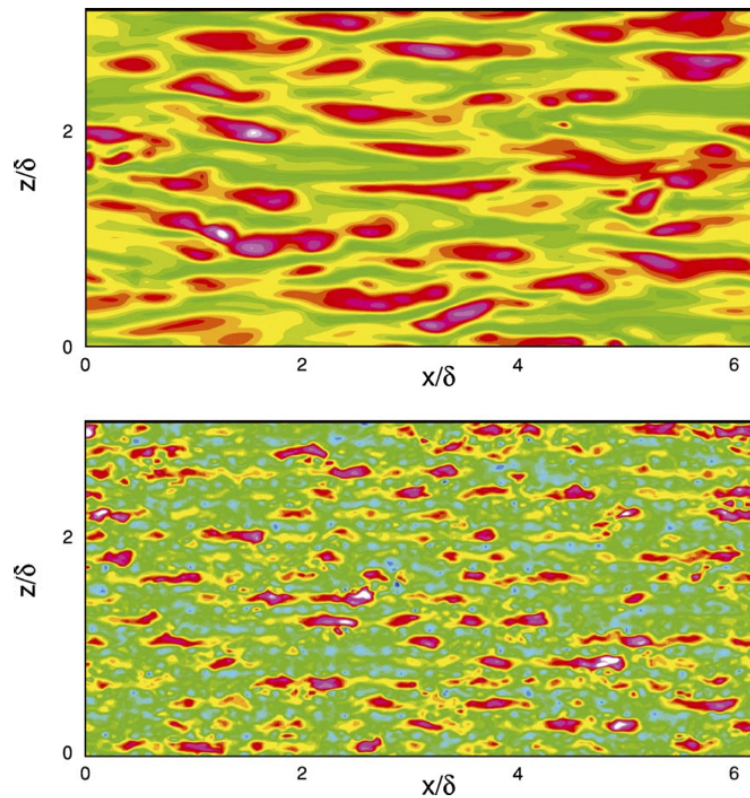


Figure 3.35: Contours of instantaneous streamwise velocity at $y^+ = 5$. Top; smooth wall. Bottom; rough wall (taken from [27])

above roughness and contours of vorticity showed increased activity and a change to the angle of inclination of the vortical structures. Contour plots of the three vorticity components showed irregular backflow occurring around the peaks and crests. Organised vorticity was evident over the roughness peaks and it seemed clear that roughness effects extended into the outer layer. The authors also noted that the near wall streamwise vortices were much stronger over the rough wall. The extent of the roughness sublayer was estimated as $1.5k$ for the large scale flow features and around $1.1k$ for the small scale turbulence structures. The spanwise element spacing was found to affect whether or not the outer region was affected by roughness. No significant differences were observed between roughnesses with variable streamwise spacing.

Summary

- Three roughness regimes: smooth, transitional, fully rough.
- Classified by sand grain roughness heights according to Nikuradse (other classifications available based on wall shear stress ratio).
- λ independent of Re in the fully rough regime.
- Transitional roughness profile may be inflectional (Nikuradse-type) or gradual (Colebrook-type).
- Roughness causes mean flow momentum loss and a downward shift in log law velocity profile, determined by ΔU^+ .
- $\Delta U^+ = f(k_s^+) = f(\text{roughness height, shape and density})$.
- Outer layer mean velocity distribution is universal.
- Reynolds normal and shear stresses are increased over roughness.
- Greatest effect normally for wall-normal turbulence fluctuations
- Magnitude and extent of the modification dependent on roughness type and ratio of k/δ .
- Near wall Reynolds stress profiles dependent on roughness type.
- Enhancement of momentum transport generally most extreme for 2D transverse roughness.
- Momentum flux from roughness cavities sustains the cycle of turbulence production and dissipation.
- Near wall turbulence anisotropy reduced over rough walls.

3.2.2 Heat transfer

Studies of the heat transfer over rough surfaces have generally lagged behind those of momentum transfer, due to the additional complexity of the measurements required. The mechanisms of momentum and heat transfer are similar and fields of velocity and temperature have been shown to be analogous (as discussed previously in the theoretical introduction). However, one important difference is that the heat transfer has an additional dependency on the thermal conductivity of the fluid, and therefore heat transfer processes are functions of roughness, Reynolds number and Prandtl number. It should be noted that while many forced convection correlations exist, most do not include a dependence on friction factor, and those that do [97] are still only intended for use with 'smooth' tubes [98]. A good review of early heat transfer studies on rough walled flows was conducted by [99] and for the enthused reader, the report of [100] is particularly thorough. Generally, the standard approach has been to produce empirical expressions for the dependence of heat transfer coefficients (Nu or St) with Re and Pr based on experimental datasets and theories about the near rough wall convection mechanism. One numerical model is discussed which seems most promising for predictions of heat transfer coefficients over rough walls.

Nunner [101] performed heat transfer experiments using pipes roughened with circumferential rings using air from $Re = 500$ to 8×10^4 . He found a fit to his data with the form;

$$Nu = \frac{\frac{f}{8} Re Pr}{1 + 1.5 Re^{-\frac{1}{8}} Pr^{-\frac{1}{6}} (Pr \frac{\lambda}{\lambda_0} - 1)} \quad (3.2.13)$$

where λ_0 is the smooth wall friction factor. The expression is noted to have two shortcomings [99] [28]) - notably that the reduction in St with λ in the fully rough regime is not reproduced, and that the expression is not accurate beyond $Pr > 1$.

One of the earliest correlations produced was that of Martinelli [102];

$$St Pr_f^{2/3} = \frac{\sqrt{\frac{\lambda}{8}} Pr^{2/3} \Delta t_{max} / \Delta t_{mean}}{5[Pr + \ln(1 + 5Pr) + 0.5 DR \ln \frac{Re}{60} \sqrt{\frac{\lambda}{8}}]} \quad (3.2.14)$$

where DR is the diffusivity ratio $\frac{\epsilon_H}{\epsilon_H + k / \rho C_p}$.

This correlation was noted to be somewhat better than that of Nunner, since the drop off in St with increasing Re in the fully rough regime is included. In

addition, Smith and Epstein [103] found Martinelli's expression to adequately represent heat transfer data from seven commercial pipes.

Owen and Thomson [104] tested 2D transverse ribs and Nikuradse type irregular 3D pyramids in the fully rough regime ($k^+ > 100$) in a wind tunnel. In order to derive an expression for Stanton number, they used a mass transfer analogy and measured the rate of sublimation of a solution of Camphor ($Pr \approx 3$) in methylated spirit from the surface. The boundary layer velocity profile was measured by pitot tubes. The derived Stanton numbers ($\log St^{-1}$) were plotted against $\log Re$ alongside the data of Nunner [101], and Dipprey [28] who made similar measurements for different roughness types and Prandtl numbers. From the available data, they found a relation for the dependence of Stanton number with k^+ ;

$$St = \frac{1}{\alpha} (k^+)^{-0.45} Pr^{-0.8} \quad (3.2.15)$$

where $0.45 < \alpha < 0.7$. The experimental data matched well with their proposed theoretical expression for St . Owen and Thomson proposed that (for fully rough flow) the main convective heat transfer mechanism at the wall was the sweep and ejection cycle created by quasi-streamwise vortices. They imagined a shallow sub-layer, with thickness comparable to that of the roughness height, where vortices in and around the roughness peaks and troughs would scour the surface and convect the heat (initially transferred by conduction from the wall to the wall adjacent fluid) towards the core flow.

At the same time, Dipprey and Sabersky [28] measured the friction factor and Stanton number of tubes with close packed sand grain type roughness as well as a smooth tube for comparison. They used distilled water as the working fluid and varied the bulk temperature to adjust the Prandtl number between $\approx 1 - 6$. The tubes were heated resistively and the roughness was created by electroplating nickel over mandrels coated with closely graded sand grains before chemically dissolving the mandrels to leave a nickel shell. The tube external wall temperature was measured with 3 sets of 3 thermocouples, spaced axially and circumferentially. The friction factors were generally in excellent agreement with Nikuradse's data for the equivalent sand grain roughness from $10^4 \geq Re \geq 10^6$. The suitability of the apparatus for heat transfer studies was validated through comparison of Stanton number data for the smooth tube with previous investigations. Profiles of St vs Re at four Prandtl numbers were plotted for three sand grain roughnesses.

For each roughness, the heat transfer coefficient generally reached a maximum towards the upper limit of the transitionally rough regime, before decreasing monotonically as fully rough conditions were met. The most pronounced maxima occurred for the highest Prandtl number case. Heat transfer coefficients were increased with decreasing Pr , and increased with relative roughness.

Dipprey and Sabersky then developed a 'heat transfer similarity law', based on the law of the wall of the turbulent boundary layer and the Reynolds analogy between momentum and heat transfer:

$$\frac{(\lambda/8)St - 1}{\sqrt{(\lambda/8)}} + B_r = g[k^+, Pr] \quad (3.2.16)$$

where C_r is the Nikuradse log law intercept in the fully rough region for the type of roughness in question. The validity of the expression was shown by plotting the function 'g' against k^+ and comparing with the experimental results - for which there was excellent agreement. Furthermore, by considering the rough wall as a series of small cavities with rotational flow as observed in [21] [19], they formed an expression for g in the fully rough condition based on a 'cavity heat transfer coefficient', St_c , calculated using the mean velocity, temperature and heat flux at the tips of the roughness elements;

$$g_{fr} = \frac{1}{A St_c[k^+, Pr]} \quad (3.2.17)$$

becoming ultimately

$$g_{fr} = k_f(k^+)^p Pr^m \quad (3.2.18)$$

when

$$St_c = \frac{1}{A k_f}(k^+)^{-p} Pr^{-m} \quad (3.2.19)$$

where k_f is a constant dependent on roughness (5.19 in their experiments), $p = 0.2$ and $m = 0.44$. The above formula was well represented by their experimental data, showing that $(Pr)^{-0.44}$ against k^+ collapsed to a single line with gradient $n = 0.2$ in the fully rough regime for all roughnesses and Prandtl numbers. In addition, the data of Nunner [101] for 2D ring roughness with various heights and spacings was shown to take the same form of g and also collapse to a single line in the fully rough regime (parallel and offset to the sand grain roughness results), providing support for the heat transfer similarity law. Plotting $2St/\lambda$ against

Pr for the roughest tube tested showed further good agreement between the similarity law and experimental data. The correlation of Martinelli [102] recreated the shape accurately but significantly under predicted the data, while the expression of Nunner deviated significantly from the data particularly with increasing Pr .

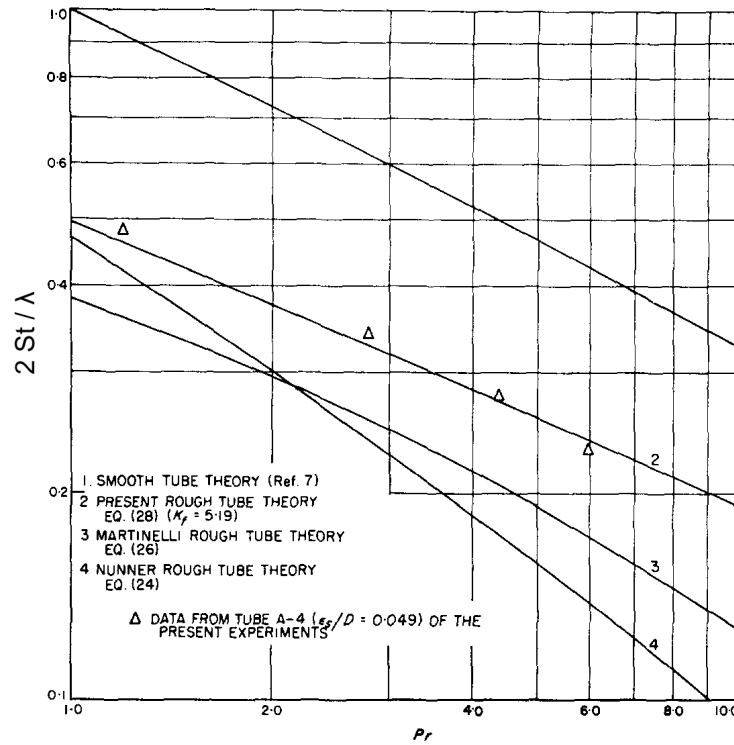


Figure 3.36: Comparison of heat transfer correlations over rough walls (taken from [28])

Sheriff and Gumley [29] used air and an annular test section with a central electrically heated tube to study the friction factor, heat transfer behaviour and mean velocity and temperature profiles of rough surfaces between $10^4 < Re < 2 \times 10^5$. The roughness was created by wrapping wire around the tube, with a constant pitch-height ratio of 10. 6 wire diameters were used and 21 thermocouples were positioned along the tube. Heat transfer enhancement with roughness was shown in terms of Nu vs Re . $\frac{dNu}{dRe}$ was highest for the transitionally rough regime and then decreased when fully rough conditions were achieved. The lower roughness cases showed a much more gradual transition, made evident by the less abrupt change in $\frac{dNu}{dRe}$ with Re . The same behaviour was equally evident when expressed as Stanton number - with the maxima occurring at greater Re for lower roughnesses. From measurement of the mean velocity profile, they found $C_r = 4.65$ and from comparison of the mean velocity and temperature profiles, found $\frac{\epsilon_H}{\epsilon_M}$ (the ratio of

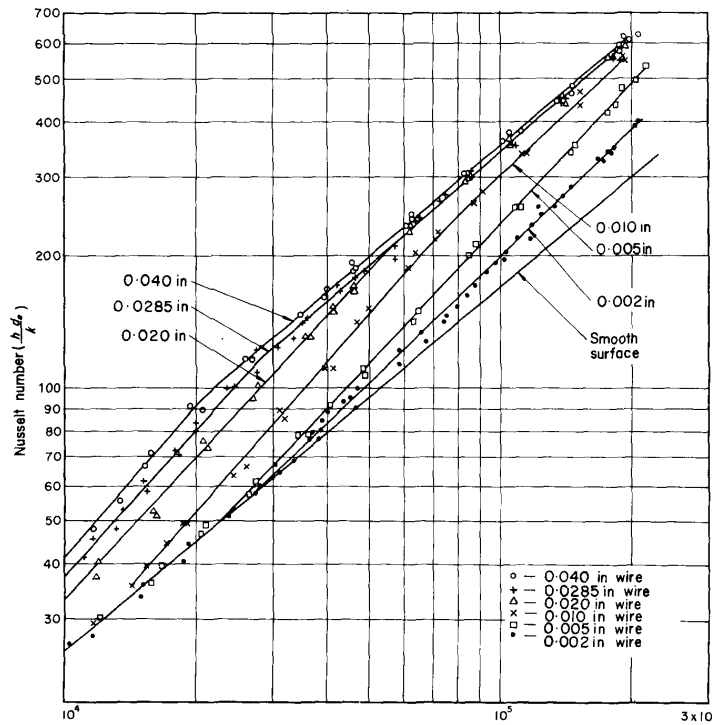


Figure 3.37: Nu vs Re for 2D wire roughness (taken from [29])

eddy diffusivity of heat to momentum) = 1.5.

For $k^+ > 50$, a correlation for the overall Stanton number was found of the form:

$$\frac{1}{St} = \sqrt{\left(\frac{8}{\lambda}\right)} \left(\sqrt{\left(\frac{8}{\lambda}\right)} + \frac{1}{St_w} + \delta m - 4.65 \right) \quad (3.2.20)$$

where the wall stanton number, $\frac{1}{St_w} = 5.37(k^+)^{0.199}$ was a minimum value when $k^+ \approx 35$ (representing optimum heat transfer). δm was dependent upon the value of $\frac{\epsilon_H}{\epsilon_M}$. The expression for $\frac{1}{St_w}$, extrapolated in k^+ beyond their experimental dataset showed qualitative agreement with the results of Nunner [101] for tubes roughened with semi circular rings with pitch to diameter ratios of 10 and 20.

Gowen and Smith [30] noted that the similarity law of Dipprey and Sabersky [28] neglected the difference between velocity and temperature profiles in rough pipes. They measured radial temperature profiles as well as heat transfer coefficients of rough tubes. In the study of radial temperature profiles, they used a mesh screen soldered to the inside of a brass pipe, with $k_s^+ = 0.051$. The range of Pr was $0.7 < Pr < 14.3$ (air, water and glycol) and Re_{max} was 50000. Temperatures were recorded axially with 12 thermocouples and radially with a traversing thermocou-

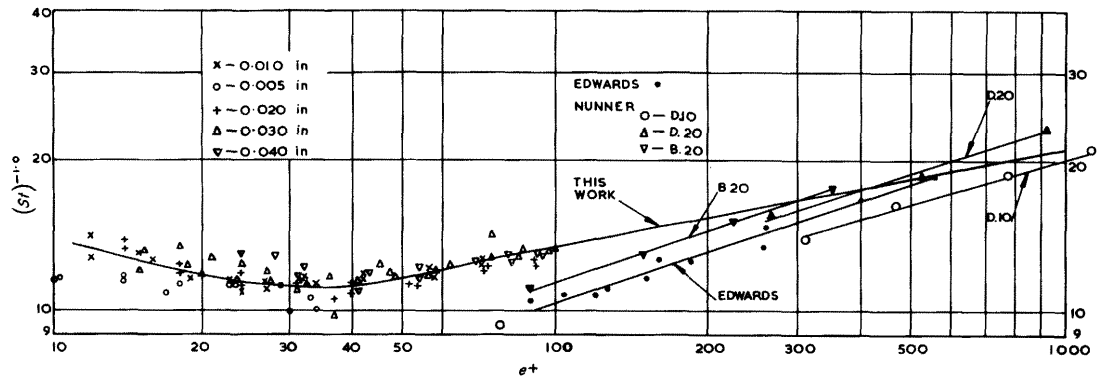


Figure 3.38: Variation in St^{-1} with k^+ (taken from [29])

ple. Heat was applied to the tube with a ribbon resistance heater. St vs Re for all three fluids showed a typical increase in St for rough tubes compared to smooth tubes. In addition there was further support that rough surfaces can achieve greater heat transfer efficiency than smooth surfaces in the transitionally rough regime for high Pr fluids. The efficiency ratio $\frac{St}{\lambda}$ against Re showed that the increase in frictional resistance is greater than the enhancement to heat transfer as Re increases.

Analysis of the non dimensional radial temperature profiles ($t^+ = A \ln y^+ + B$) revealed that the gradient A varied with roughness and Pr , unlike the slope of velocity profiles ($\frac{1}{\kappa} \approx 2.5$), which have been shown to remain constant regardless of wall surface condition. This indicates that the mechanism of heat transfer changes towards the turbulent core. The authors suggested that the slight increase in slope of the dimensionless temperature profile with Pr highlighted the significance of molecular diffusion of heat from eddies to turbulent heat transfer over both smooth and rough walls. The dimensionless temperature profiles showed a dependence on Re and Pr - being generally shifted upwards with increasing Re and Pr for rough tubes. The increase with Pr (also observed for smooth surfaces) was attributed to the shift in relative heat transfer resistance from the turbulent core to the wall region, and the increase with Re was suggestive of the reduced contribution of stagnant areas around roughness elements to the resistance to heat transfer. An empirical correlation for the non dimensional temperature profile was suggested of the form;

$$t^+ = A_r \ln \frac{y}{r} + \psi \quad (3.2.21)$$

with

$$\psi = \left(0.155 \frac{U^* D^{0.54}}{\nu} + \sqrt{\left(\frac{8}{\lambda} \right)} \right) Pr^{0.5} \quad (3.2.22)$$

The calculation of ψ was compared against the measured values for each case of Re and Pr and reasonable agreement was found.

Gowen and Smith then studied the heat transfer coefficients over seven rough surfaces up to $Re = 10^5$, using the same fluids as in the experiments detailed above. The roughnesses were imprinted onto thin brass sheets which were formed into tubes. The method resulted in well characterised roughnesses, which included square and triangular arrays of spherical elements ($\frac{k_s^+}{D} = 0.028$ and 0.04 respectively), a screen roughness ($\frac{k_s^+}{D} = 0.095$), inversions of the aforementioned patterns and a random roughness made from carborundum particles ($\frac{k_s^+}{D} = 0.026$). Whereas all the roughnesses became fully developed by $Re = 10000$, the St data showed the steady decrease with Re as noted by other investigators. The data was compared against predications from the expression;

$$St = \frac{\sqrt{2\lambda}}{\psi - 3.75 A_r / 2.5} \quad (3.2.23)$$

or, with A_r averaged over the range of Pr and taken as 3;

$$St = \frac{\sqrt{2\lambda}}{\psi + 4.5} \quad (3.2.24)$$

created through subtraction of the general expressions for non dimensional temperature and velocity gradients, as well as correlations of Nunner [101] and Dipprey and Sabersky [28]. Perhaps unsurprisingly, closest agreement to the data was achieved with their own correlation for all Pr considered, although the correlation was only able to match their data with a standard deviation of $\pm 25\%$. There was reasonable agreement with the correlations of Nunner and Dipprey and Sabersky for the low Pr cases, but the discrepancy increased with Pr . The correlation of Nunner - created with experiments in air, consistently under predicted the experimental data of Gowen and Smith, whereas the St values from the correlation of Dipprey and Sabersky were consistently too high. The authors noted that close agreement between the various correlations and datasets was unlikely, since each correlation contained empirical constants specific to the experiments they were generated with. Gowen and Smith noted that the lack of reliability of their equation in accurately predicting heat transfer coefficients was most likely due to the assumption that the friction factor completely describes the modification of

the boundary layer temperature profile by roughness.

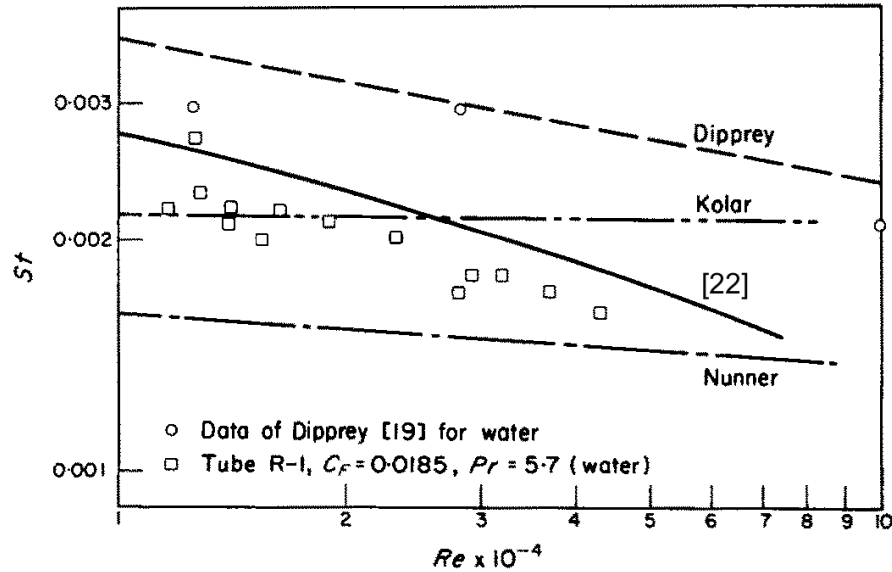


Figure 3.39: Predictions of St with Re of various investigators (taken from [30])

Hosni et al [105] studied heat transfer in the transitional and fully rough regimes using a wind tunnel on a surface roughened with 1.27mm diameter hemispherical elements, spaced $4D$ apart in a staggered array. The bottom wall of the wind tunnel consisted of 21 electrically heated plates. The range in Re was 10^5 to 10^7 , which was increased through the free stream velocity. The uncertainty in St was between 2-4%. St reduced with Re , and for all but the lowest two free stream velocities, St vs Re collapsed to a single curve - indicating fully rough conditions had been reached. Similar fully rough collapse was shown for a geometrically similar surface (although densely packed) tested by Pimenta [100]. The experimental data was compared to the St predictions of the Discrete Element Method [86] (briefly described in the momentum transfer section). Agreement with both datasets was excellent - which is noteworthy since the roughnesses were different and spanned the transitional to fully rough regimes.

The same investigators [31] later extended the study to truncated cones and hemispheres with two densities ($\frac{L}{D} = 2$ and 4). Increasing the roughness density was found to increase St . Compared to a smooth wall, the increase in St for $\frac{L}{D} = 4$ was 30%, while the $\frac{L}{D} = 2$ array increased St by 55% (for hemispheres, the respective values were 75% and 40%). Fully rough conditions were reached when the St vs Re curves collapsed asymptotically. Interestingly, for the highest density

truncated cone surface, the thermal fully rough condition seemed to be delayed with respect to the fully rough condition for momentum transfer. While skin friction coefficients for hemispheres and cones with equivalent diameters and densities showed negligible effect of shape (see also [85]), the heat transfer was shown to be a function of element shape and density, with more pronounced differences at higher densities. Typically the St data was 10% higher for hemispheres than cones at $\frac{L}{D} = 2$ and 2-4% higher at $\frac{L}{D} = 4$. Predictions from the Discrete Element Model again showed excellent agreement, particularly for the lowest density, although the data for truncated cones at the highest density was over predicted by the model.

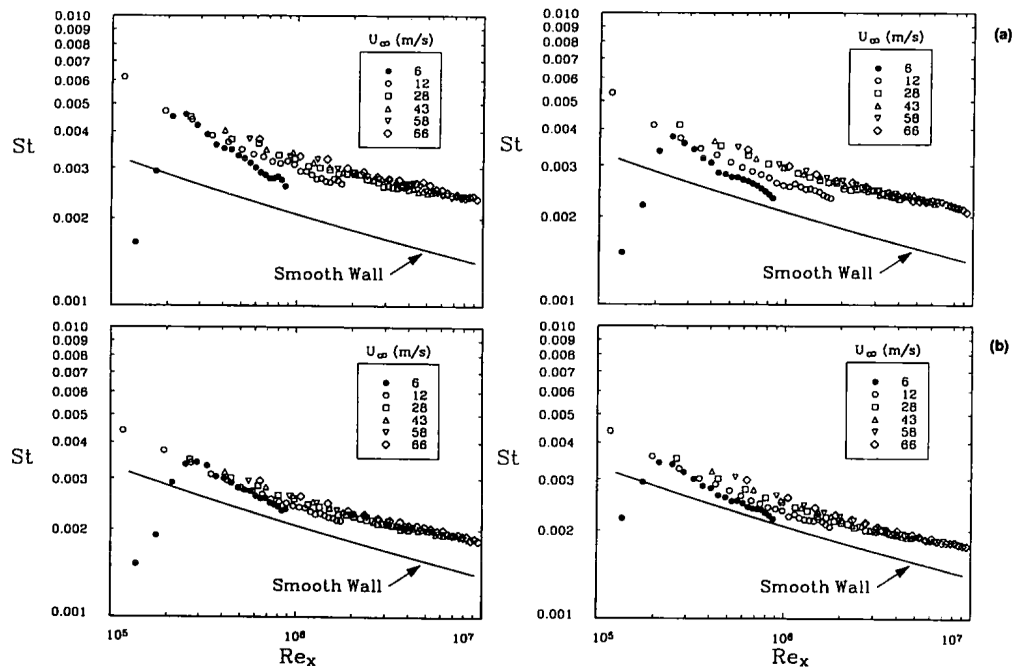


Figure 3.40: Stanton number for Schlichting type roughness (taken from [31]). Left: hemisphere roughness. Right: truncated cone roughness. Top: $\frac{L}{D}=2$. Bottom: $\frac{L}{D}=4$

Summary

1. Heat transfer coefficients expressed in dimensionless form as Nu or St .
2. Experimentally derived correlations for rough walled heat transfer generally limited in applicability.
3. Change in gradient of Nu vs Re for fully rough conditions (occurs at lower Re for rough walls).
4. St is a maximum prior to fully rough conditions, beyond which St decreases with Re and eventually converges asymptotically.
5. Enhancement of heat transfer with roughness associated with disruption of stagnant areas around roughness elements by turbulence structures.
6. $Nu, St = f(Re, Pr, \text{element shape, element density})$

3.2.3 Mass transfer

Numerous difficulties are associated with performing accurate deposition experiments. These include the generation, charge neutralisation, sampling and measurement of particles, particle bounce and re-entrainment, enhanced deposition at pipe joints and surface roughness [35]. For this reason, much of the early work on particle deposition in turbulent flow focused on the generation of theories to predict the deposition process over smooth walls with reference to limited experimental data. Some investigators attempted to extend the theories to rough walls. The most informative results on particle deposition in turbulent flows have come more recently, as a result of the advances in modern computing. Highly detailed simulations of turbulent flow fields can now be performed, through which the passage of discrete particles can be studied in great detail.

Mass transfer results are usually expressed in terms of the deposition velocity, V_d ;

$$V_d = \frac{N}{C_0} \quad (3.2.25)$$

where N is the particle mass flux to the surface (no. of particles/ $m^2 s$) and C_0 is the concentration of particles in the bulk flow (no. of particles/ m^3). As the name suggests, the deposition velocity has units (m/s), but is not related to the actual velocity of the particles as they reach the wall.

The deposition velocity may be made non dimensional by dividing by the friction velocity (U^*);

$$V_d^+ = \frac{V_d}{U^*} \quad (3.2.26)$$

Assuming spherical particles which are subject to drag by Stokes law, the particle relaxation time, τ_p describes the time required for particles to adjust to external changes in the flow field;

$$\tau_p = \frac{\rho_p D_p^2}{18\mu} \quad (3.2.27)$$

where ρ_p is the particle density, D_p is the particle diameter. A particle with large relaxation time (high ρ or D_p) is less sensitive to turbulent fluctuating velocities and will continue on a path as a result of its inertia, while a particle with a small relaxation time will follow the fluid streamlines more closely. It can also be made dimensionless;

$$\tau_p^+ = \frac{\tau_p U^*}{\nu} \tag{3.2.28}$$

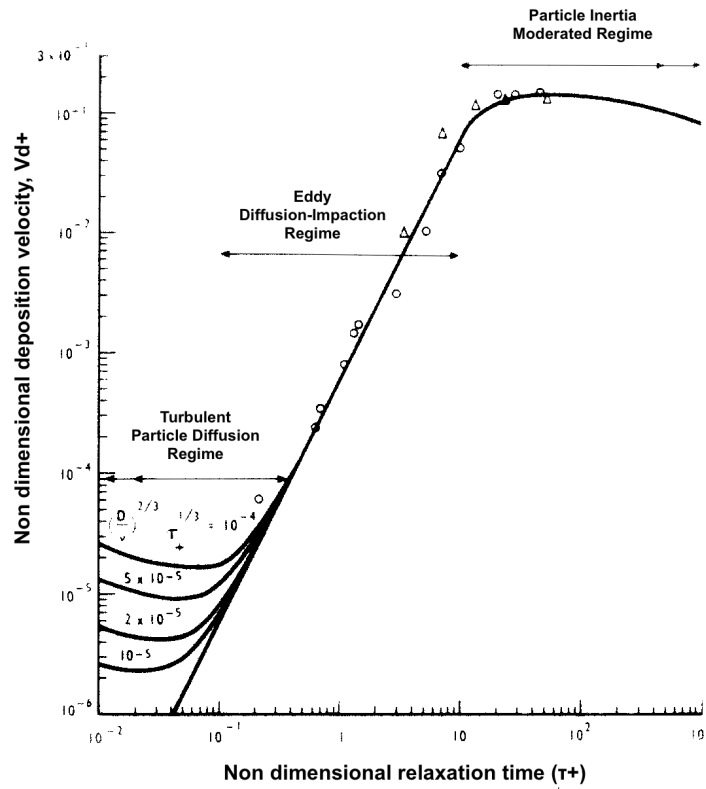


Figure 3.41: Turbulent flow particle deposition regimes. Taken from [32]

The dependence of deposition velocity with relaxation time has been shown to occur in three regimes. For $0.1 < \tau_p^+ < 10$, V_d^+ varies linearly with τ_p^+ . The regime is termed the eddy diffusion-impaction regime. Particles acquire wall-normal velocity through interaction with turbulence structures in the core and buffer layer, before traversing the quiescent viscous layer as a result of their inertia. For larger particles ($\tau_p^+ > 10$), the deposition velocity suddenly reduces, as the particles are less responsive to wall normal turbulent velocity fluctuations. For small particles ($\tau_p^+ < 1$), deposition is by a combination of Brownian and eddy diffusion [32].

Theories

Paparvergos and Hedley [106] provide a thorough review of the main theories of turbulent particle deposition. In 'free flight - stopping distance' models, particles are considered like a second fluid phase and classical concepts of turbulence are employed. The particles are transported by turbulent diffusion to within one 'stopping distance' from the wall - defined as the distance that a particle with a certain

momentum would travel by 'free flight' into the viscous sublayer. Kallio and Reeks [36] note that the initial free flight velocity had to be arbitrarily specified - opening the door for empiricism. In the original free flight model of Friedlander and Johnstone [107], the free flight particle velocity was taken as the radial rms velocity of the core flow, and as such was unrealistically high. If the local fluid rms velocity as the stopping distance was employed [108], deposition was generally under predicted by 1-2 orders of magnitude. Numerous modifications were made to the original theory in an effort to improve the agreement with experimental data. These involved adjusting the free flight distance and velocity, allowing the particle diffusivity and eddy diffusivity to not be equal or changing the concentration boundary condition at the free flight distance.

Other investigators took a probabilistic approach to the transport of particles, considering the interaction of particles with turbulent structures. Hutchinson et al [109] modelled the turbulent flow field as a series of eddies with constant length, lifetime and speed but with random direction. Particles executed a 2D random walk through the domain. The particle momentum gained from the interactions with the eddies was the determining factor for deposition. Particles with insufficient momentum to penetrate the viscous sub layer were considered to pass through the duct. As a result, the model under predicted deposition for small particles, but for larger particles the model gave good predictions. Cleaver and Yates [33] produced a sublayer model based on the turbulent sweep/ejection cycle associated with quasi-streamwise vortices in the turbulent boundary layer noted in [20], [110]. They took the flow field as a series of spatially intermittent sweeps - modelled by 2D stagnation point flows (as described by Schlichting (bookREF)) to replicate the viscous sublayer. Whether a particle was deposited on the wall depended on the position at which it entered the downsweep and whether the inertia of the particle allowed it to follow the fluid motion. The agreement with the experimental data for the probabilistic theories was generally better than the stopping distances models, which is attributed to the reduced number of assumptions employed.

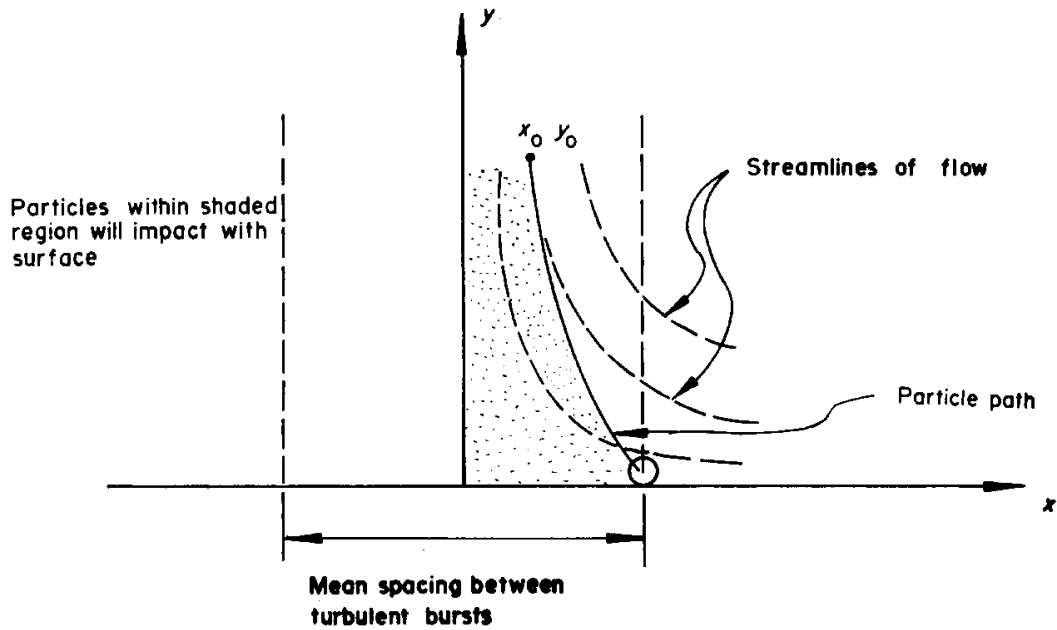


Figure 3.42: Stagnation point flow model for particle deposition across the viscous sublayer employed in [33]

Experimental observations and numerical simulations

Wells and Chamberlain [34] used radioactively tagged particles of various sizes to study the deposition by diffusion and impaction on a vertical surface. The particles varied in size from $0.17\mu\text{m}$ (Aitken nuclei) to $5\mu\text{m}$ (polystyrene spheres) with intermediate sized droplets of tri-cresyl phosphate. The deposition surface was a 5m long brass rod within a copper tube, which was roughened with filter paper. When covered in filter paper, the surface was considered to be at most transitionally rough, with k^+ around 20. The increase in friction velocity with the filter paper compared to the smooth brass rod was 10%. The deposition to the surfaces was assessed by placing sections of rod / rod and paper in a beta scintillation counter and measuring the radioactivity. V_d was shown against Re for the three sizes of tri-cresyl-phosphate particles. For both smooth and rough surfaces, the largest particles deposited the most and deposition increased with Re . On the filter paper surface, deposition velocity initially increased rapidly with Re , but the gradient reduced gradually with increasing Re . Profiles for the smooth surface were markedly different - taking an inflectional form with the point of inflection apparently occurring at the same Re for all three sizes of particles. For the same Re , deposition on the rough surface was several orders of magnitude larger than the smooth surface. It was suggested that the fibres of the filter paper, extending into the viscous sub layer, were very effective in trapping particles. The authors noted that other experiments using bluff rather than fibrous roughness

gave results in between the fibrous and smooth surfaces.

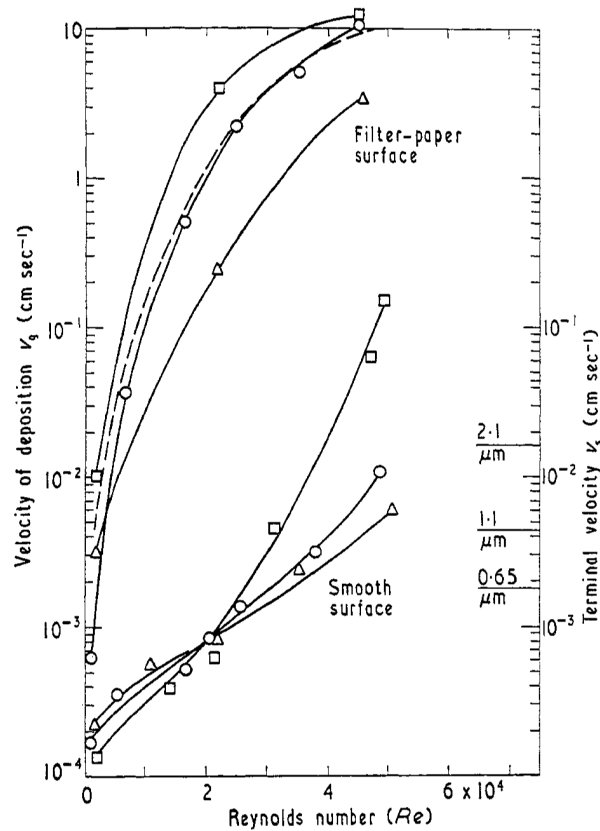


Figure 3.43: Deposition over smooth and rough surfaces (taken from [34])

Profiles of deposition coefficient, $K_{dep} \left(\frac{V_d}{U_m} \right)$, (the mass transfer Stanton number) were shown against particle diameter for three Reynolds numbers. The experimental data was compared against the theories of Davies [108] and Friedlander and Johnstone [107]. Results for the larger particles lay in between the two theoretical curves - but the results for the smallest particles (diffusion deposition mechanism) were well represented by both theories. A minimum in K_{dep} occurred for particles sizes around $0.5\text{-}2\mu\text{m}$.

Liu and Agarwal [35] presented data which improved upon the accuracy and range of previous investigations. They measured deposition of uniform spherical droplets of olive oil through a glass pipe for $10000 < Re < 50000$ with particle sizes between $1.4 - 21\mu\text{m}$. The droplets were tagged with a small quantity of fluorescent tracer (uranine-water solution), and the deposition was assessed by quantifying the amount of uranine deposited in each section of the test tube, as well as a quantity deposited on a filter at the outlet of the glass tube. Use of

a vibrating aerosol generator resulted in very uniform particles and allowed the particle size to be determined to a high degree of accuracy.

Between $1 < \tau^+ < 10$, V_d^+ varied with the second power of τ^+ , according to the relationship

$$V_d^+ = (6 \times 10^{-4}) \tau^{+2} \quad (3.2.29)$$

V_d^+ peaked around $\tau^+=30$, beyond which V_d^+ decreased gradually with increasing τ^+ . The experimental data was compared to the theories of Friedlander and Johnstone [107], [108] and Beal [111], which were all based on the 'free flight model' but with different formulations for the free flight velocity ($0.9U^*$, rms v' , and $0.5U_\infty$ respectively). The theory of Liu and Ilori [112] was also compared, which differed from the others in that the particle diffusivity, (ϵ_p) was not assumed equal to eddy momentum diffusivity (ϵ_m). For $\tau^+ < 20$, the theories of Friedlander and Johnstone and Beal predicted the data well. The theory of Liu and Ilori slightly overestimated V_d^+ for $\tau^+ < 2$. The theory of Davies [108], although qualitatively similar, significantly under predicted the experimental data.

Relatively few high fidelity experiments appear to have been performed to study particle deposition in turbulent flow. Fortunately, computational efficiency has increased sufficiently to permit numerical simulations of deposition, which can provide vast amounts of useful data that could not be measured practically. For example, particle-wall impact speed, angle, and adhesion and rebound characteristics.

Kallio and Reeks [36] cast doubt on the suitability of the 'diffusion - free flight' concept. They preferred to use a lagrangian approach, solving the particle equations of motion numerically and tracking them through a simulated 2D eulerian fluid phase. Their simulation was intended to provide data on the dependence of V_d^+ on τ^+ and $\frac{\rho_p}{\rho_f}$ (the particle-fluid mass density ratio), particle concentrations and particle rms velocity profiles for $0.3 < \tau^+ < 1000$.

The particle equation of motion was shown to be;

$$m_p \frac{dV}{dt} = 6\pi\mu r_p (U - V) + F_{body} \quad (3.2.30)$$

where the first term on the right hand side of the equation is the stokes drag force. In the equation of motion in the y direction, the Saffman lift force due to mean

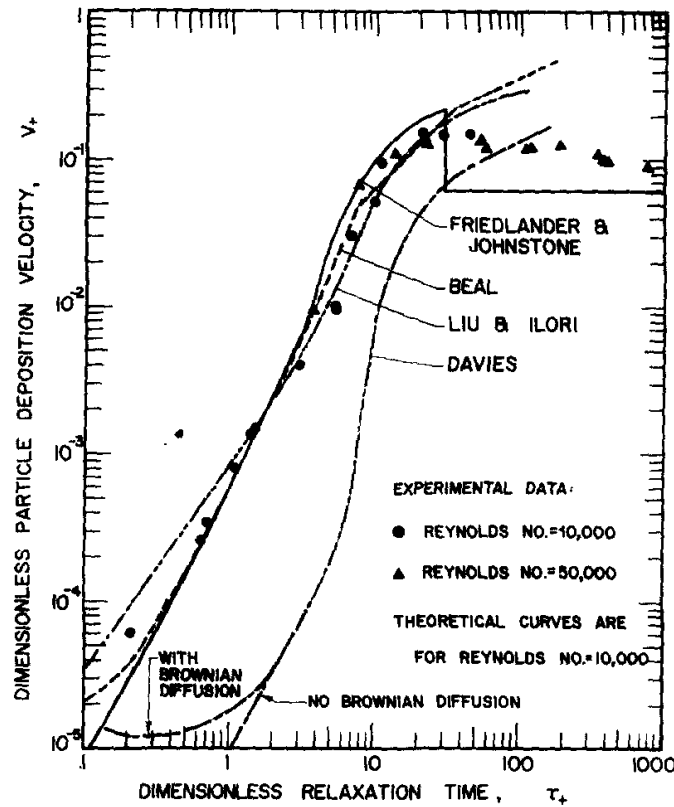


Figure 3.44: Results of Liu and Agarwal compared to free flight theories (taken from [35])

shear was included;

$$F_L = 6.46\mu r_p^2 \sqrt{\frac{\bar{K}}{\nu}} V_{rel} \quad (3.2.31)$$

where V_{rel} is the particle velocity relative to the fluid along the centre streamline. The turbulent flow field was constructed from the law of the wall relations for mean velocity and wall-normal rms fluctuating velocity data from a variety of experimental sources. A particle was modelled to pass through the boundary layer through a series of interactions with turbulent eddies, with each eddy having a random wall-normal rms velocity and time scale. Particles were released in the simulation from 20 evenly spaced locations between $0 < y^+ < 200$. A 'sticky' wall condition was imposed which did not allow for particle re-entrainment.

The results of the simulation were compared to the experimental data of Liu and Agarwal [35]. Profiles of deposition velocity against particle relaxation time showed excellent agreement, particularly between $5 < \tau^+ < 500$. The model accurately reproduced the reduction in deposition velocity observed in [35] for

$\tau^+ > 10$, attributed to the reduced rms velocity (and hence reduced deposition rate) of the largest particles. Inclusion of the Saffman lift force (which effectively increases the particle wall-normal rms velocity in the region of strong shear close to the wall, with the direction of the force depending on the relative particle-fluid velocity) was shown to increase deposition velocity between $1 < \tau^+ < 10$. The ratio $\frac{\rho_p}{\rho_f}$ had a strong effect on the deposition velocity, particularly for $\tau^+ < 5$. A higher particle-fluid density ratio incurred less deposition, which the authors attributed to a reduction in the effect of lift (and therefore rms wall-normal fluctuating velocity). Particle concentration profiles across the boundary layer showed that for lower τ^+ , particles clustered in a region around $y^+ = 1$, whereas more massive particles were more evenly distributed across the boundary layer. The peak in concentration near the wall was greater than the core concentration by an order of magnitude. It seemed that particles with insufficient inertia to be projected through the near wall viscous layer became effectively trapped under the very active buffer layer ($5 < y^+ < 30$). The simulation showed that particle and fluid rms velocities were significantly different, even for the lowest relaxation time. The results showed excellent agreement with LDA measurements of particle wall normal velocity [113]. For $y^+ > 15$, particle velocities were lower than the fluid velocity, with the difference becoming greater with increasing τ^+ . Close to the wall ($y^+ \leq 10$), more massive particles were shown to be able to achieve wall-normal rms velocities greater than that of the fluid - as a result of inertia provided by strong turbulent fluctuations in the core and damping of turbulence near the wall.

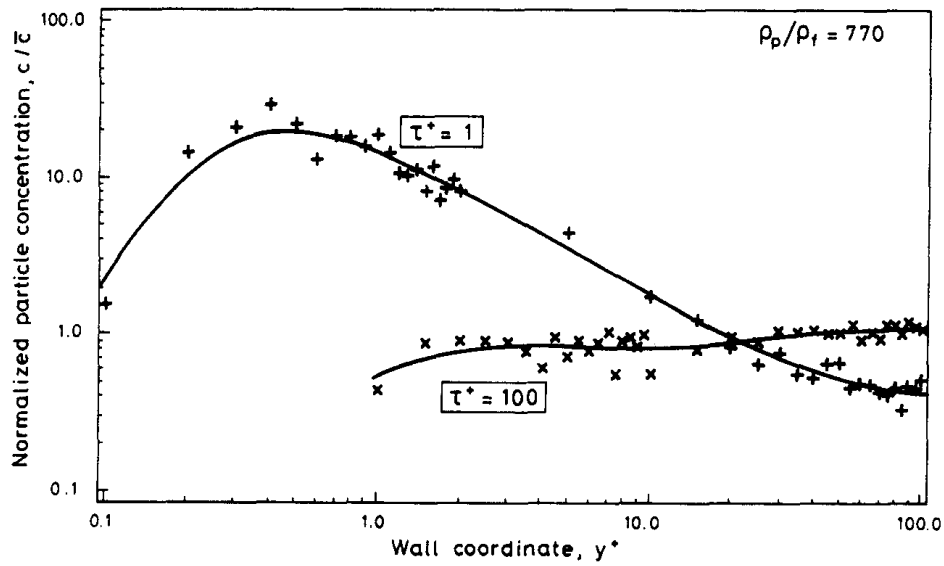


Figure 3.45: Concentration build up of particles close to the wall (taken from [36])

McLaughlin [114] performed a 3D Direct Numerical Simulation of vertical channel flow with rigid spherical particles ($2 < \tau^+ < 6$). The particles were assigned random initial locations with initial velocity equal to the local fluid velocity. The Saffman lift force was included in the particle equations of motion. The flow field was validated against the early low Re DNS of Kim et al [2]. Profiles of deposition velocity with relaxation time were compared against the data of Liu and Agarwal [35]. There was reasonably good agreement, although the simulation suggested a larger power law index than in Liu and Agarwal's relation. As in [36], McLaughlin also found a tendency for particles to accumulate in the viscous sublayer, at the edge of which, depositing particles tended to have normal components of velocity comparable to the fluctuating wall-normal component in the channel core. For $\tau^+ < 5$, particles were found to be carried to within a few wall units of the wall by strong, well organised turbulent structures (the magnitude of wall-normal component of fluid velocity was several times larger than the wall-normal turbulence intensity). Without the lift force (or for large particle-fluid density ratios), the particles could only reach the wall as a result of the wall-normal momentum provided by the fluid motion. The lift force was found to play a key role in the deposition mechanism only within the viscous sub layer. Despite the magnitude of the force being relatively small, the force provided additional momentum to the particles, helping them to pass through the quiescent viscous region and become deposited at the wall. It was noted that the lift force also provided momentum to particles moving away from the wall, but since they generally had much lower velocities, the effect was to increase the

accumulation of particles within the viscous sublayer.

Following from the work of Cleaver and Yates [33], Fan and Ahmadi [37] adopted a slightly different numerical approach. They simulated particle transport in a vertical duct with smooth and rough walls, modelling the effect of near wall sweeps using a viscous plane stagnation point flow and including the Saffman lift force and gravity in the particle equations of motion. The effect of roughness was considered by applying an offset to the origin of the mean velocity profile, and assuming the capture distance for the particles to be equal to;

$$y = k + \sigma_k - \epsilon + \frac{D}{2} \quad (3.2.32)$$

where k is the average roughness height, σ_k is the standard deviation of the roughness height, ϵ is the displacement of the velocity profile origin due to roughness and D is the particle diameter. The maximum value of k^+ was 2.13.

The particles were injected at $y^+ = 12$ with initial velocity being equal to the local fluid velocity. Their limiting trajectory approach assumed that particles brought towards the wall in a sweep would be captured if they came within the capture distance and if not, would be transported back to the outer region. Particle rebound was omitted and it was assumed that the particle concentration was uniform at $y^+ = 12$. Diffusion was included in the simulation (important for small particles $< 0.1 \mu m$), with the diffusion deposition velocity (V_d^+) calculated according to;

$$V_d^+ = 0.084Sc^{-2/3} \quad (3.2.33)$$

where Sc is the Schmidt number.

The overall deposition velocity was therefore the sum of the inertia-interception velocity and the diffusion deposition velocity $V_d^+ = V_d^+_i + V_d^+_d$

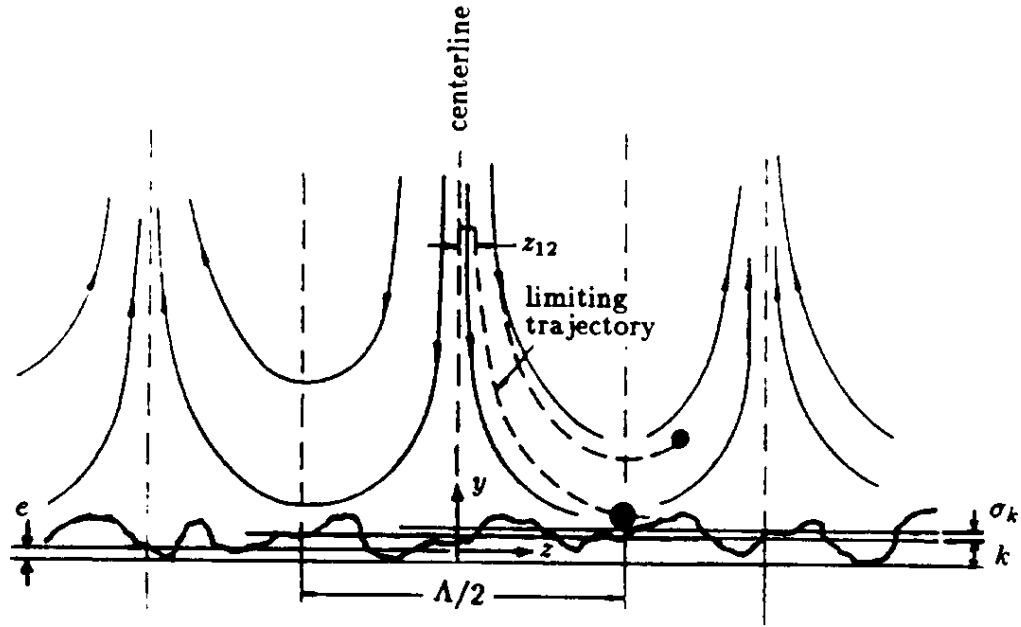


Figure 3.46: 2D stagnation point flow field adopted by Fan and Ahmadi (taken from [37])

Results for the smooth wall case were compared against the collection of experimental data shown by Papavergos and Hedley [106] and the simulation of McLaughlin [114]. Profiles of deposition velocity with relaxation time in the inertial deposition regime ($1 < \tau^+ < 10$) showed good agreement with the previous investigations (although the dataset is quite spread). For $0.1 < \tau^+ < 5$, increasing the particle-fluid density ratio decreased the deposition velocity, while for sub micron particles $\tau^+ < 0.1$, deposition velocity was enhanced with increasing density ratio. This was explained by the fact that for fixed particle relaxation time, the particle size decreases as the density ratio increases - therefore the interception process (capture by the wall) is less effective. Conversely, in the diffusion deposition range, Brownian motion is more significant for smaller particles - hence the deposition rate for small particles is slightly increased with increasing particle-fluid density ratio. As in [114], inclusion of the Saffman lift force increased the deposition rate for $1 < \tau^+ < 10$. Density ratio and lift force were found to be insignificant for $\tau^+ > 10$, since for large particles, the inertia force is dominant. Inertia - interception deposition was shown to be independent of Re but diffusion deposition for small particles was enhanced with Re . Gravity reduced deposition when in the opposite direction to the flow and enhanced deposition when aligned with the flow. The authors suggested that the spread in experimental data may be due to the various tube orientations and particle-fluid densities ratios employed.

The model showed a moderate increase in roughness to have a very strong effect on deposition rate, particularly for $\tau^+ < 5$. The deposition velocity for $\tau^+ \approx 0.1$ was around three orders of magnitude greater for the roughest wall ($k^+ = 2$) than the smooth case. The minimum in deposition velocity observed for smooth walls around $\tau^+ = 0.5$ (related to the crossover between diffusion and inertial-interception deposition mechanisms) was not present for $k^+ \geq 0.2$. In addition, with increasing roughness, the deposition velocity became almost independent of relaxation time for $0.01 < \tau^+ < 0.5$. For the largest particles with the highest inertia, the roughness was less significant. The model showed qualitative agreement when compared against the (rather limited) rough wall deposition data of Montgomery and Corn [115]. The effect of particle-fluid density ratio was reduced with roughness, and for small particles in the diffusion deposition regime, the effect of increased deposition rate with increasing density ratio observed for smooth walls was eliminated altogether. This observation was suggested to imply that the deposition by diffusion becomes much less significant over rough walls. The effect of flow orientation with respect to gravity was shown to be less significant over rough walls, in fact with increasing roughness the deposition became almost independent of the gravity direction.

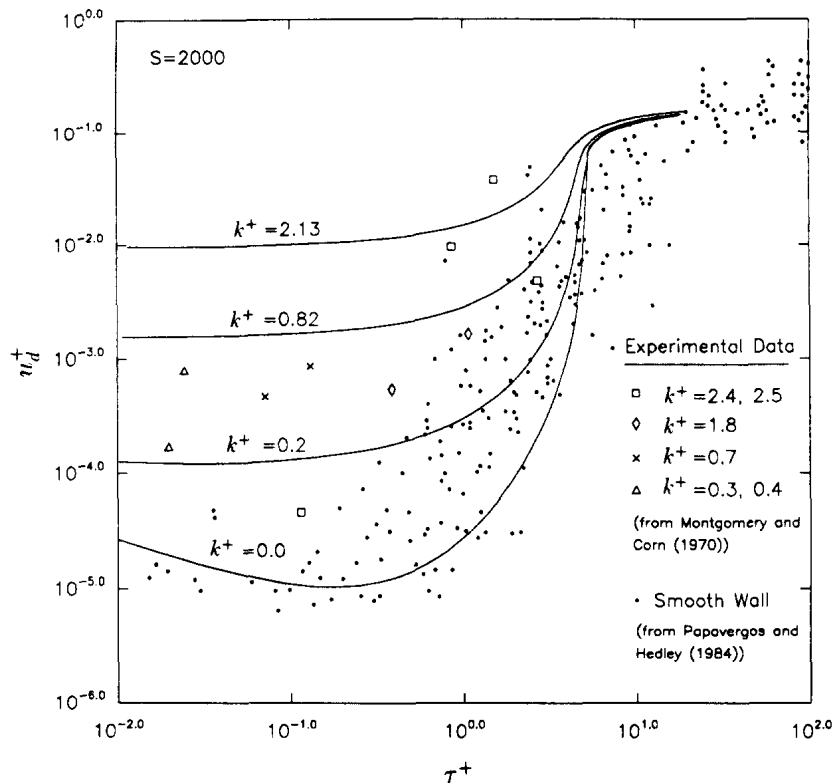


Figure 3.47: Dependence of deposition velocity on roughness (taken from [37])

Further insight has been provided on the mechanism of particle transport across the turbulent boundary layer courtesy of isothermal direct numerical simulations by Marchioli and Soldati [38] (channel flow) and Marchioli et al [39] (pipe flow). They simulated flows laden with randomly distributed fly-ashes of three sizes in air ($\frac{\rho_p}{\rho_f} = 769$, $\tau^+ = 3.8, 29.1, 116$). They aimed to resolve unanswered questions surrounding the phenomenon of particle accumulation in the viscous sublayer - specifically why the mechanisms of particle transfer to the wall seemed more effective than the mechanism for re-entrainment of particles into the outer flow. The particles were assumed rigid, spherical and to obey the equation of motion;

$$\frac{d\mathbf{V}}{dt} = \frac{C_d}{\tau_p}(\mathbf{u} - \mathbf{v}) + \left(1 - \frac{\rho}{\rho_p}\right)\mathbf{g} - \xi(\epsilon)\frac{6.46}{12\pi}\frac{d_p}{\tau_p}\left|\frac{\delta u_x}{\delta z}\right|^{\frac{1}{2}}(v_x - u_x)\mathbf{e}_z \quad (3.2.34)$$

where \mathbf{v} is the particle velocity vector, \mathbf{u} is the fluid velocity vector at the particle location, C_d is the stokes drag coefficient, \mathbf{g} is the gravitational acceleration and \mathbf{e}_z the unit vector in the wall normal direction. $\xi(\epsilon)$ is a correction factor for larger differences in velocity between the continuous and discrete phase.

For each particle size, there was the anticipated near wall accumulation. Qualitatively, particle clusters were observed to approach the wall through 'preferential avenues', striking the wall at approximately 45 degrees. Particles that remained in the centre of the channel formed elongated clusters, which were surrounded by circular voids of low particle concentration. The near wall accumulation was shown clearly for the channel and pipe flows by plots of the particle concentration against wall distance. The peak in particle concentration for both geometries occurred around $0.5 < y^+ < 1$ - which was in good agreement with the simulation of Kallio and Reeks [36]. In the pipe flow simulation, the intermediate size particles were organised more quickly by the turbulence. In both geometries, particles were found to accumulate in low speed streaks - characteristic regions of the turbulent boundary layer with lower than mean velocity. This observation was confirmed quantitatively by plotting the particle number density distribution as a function of the fluctuating streamwise velocity for $y^+ \leq 10$.

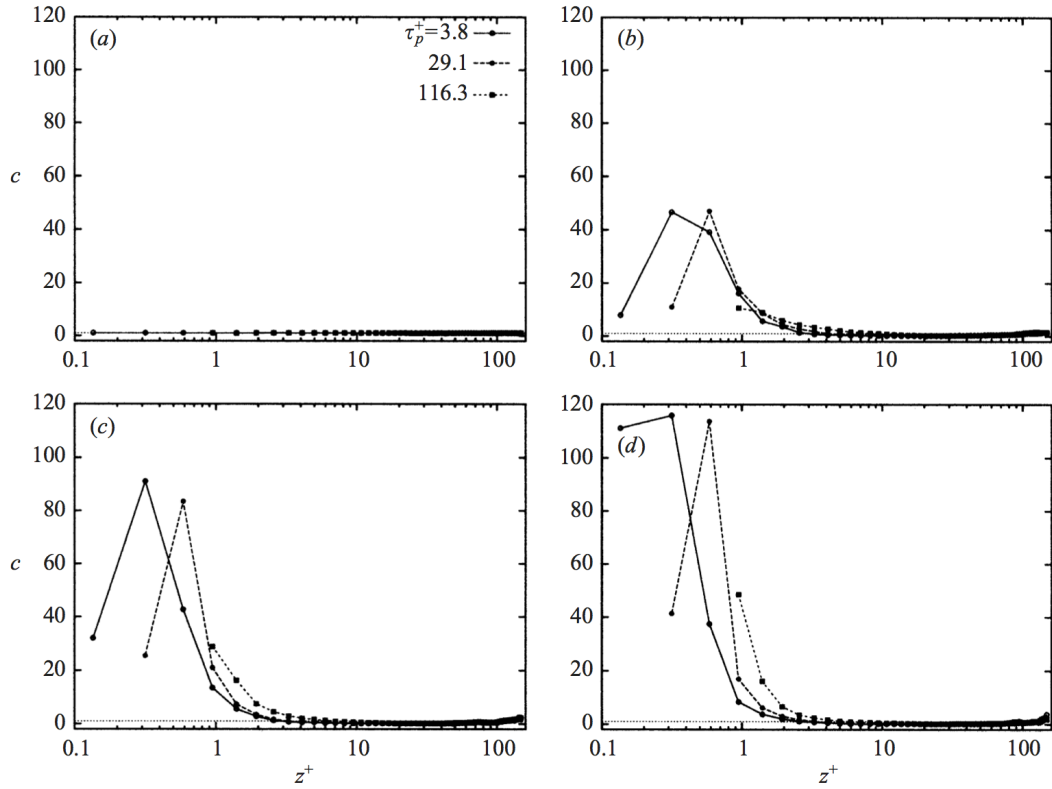


Figure 3.48: Accumulation of particles in the viscous sublayer with time (taken from [38]). Sequence is (a) to (d)

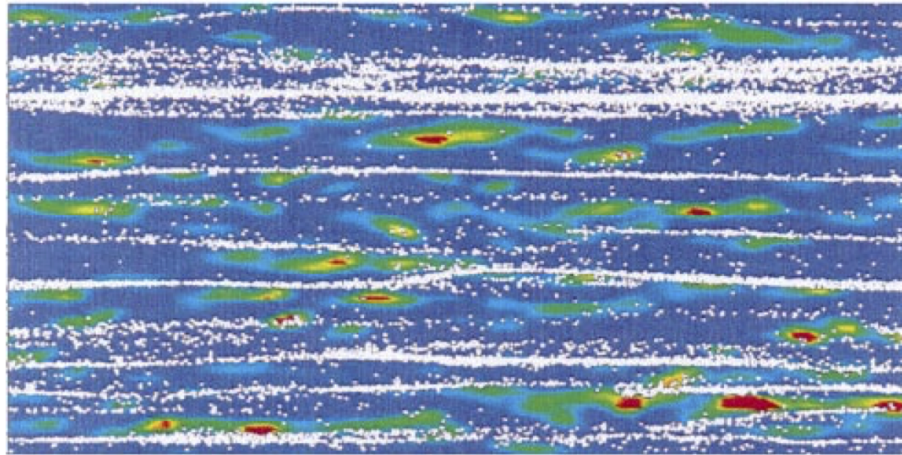


Figure 3.49: Accumulation of particles in regions of lower than average fluid velocity (low speed streaks), top down view, $y^+ = 4$. Instantaneous contours of streamwise velocity (blue indicates negative u') and particle locations (taken from [38])

Quadrant decomposition was employed to identify the relationship between sweeps and ejections and particle fluxes to and from the wall. In the uv plane, ejections (Q2 events, $u' < 0, v' > 0$) are outward motions of low speed fluid which produce

a local reduction in wall shear stress. Conversely, inward sweeps (Q4 events, $u' > 0, v' < 0$) locally increase the wall shear stress. Both Q2 and Q4 motions contribute to negative Reynolds stress, or an increase in turbulence production. For all particle sizes, there was a strong correlation between fluxes to the wall and high shear stress regions, and particle fluxes away from the wall and low shear stress regions. The particle fluxes were evaluated between $5 < y^+ < 15$. Furthermore, fluxes towards the wall were found to always have a greater intensity than fluxes away from the wall - with the trend being more evident for the smallest particle size. Similar observations were made for the pipe flow.

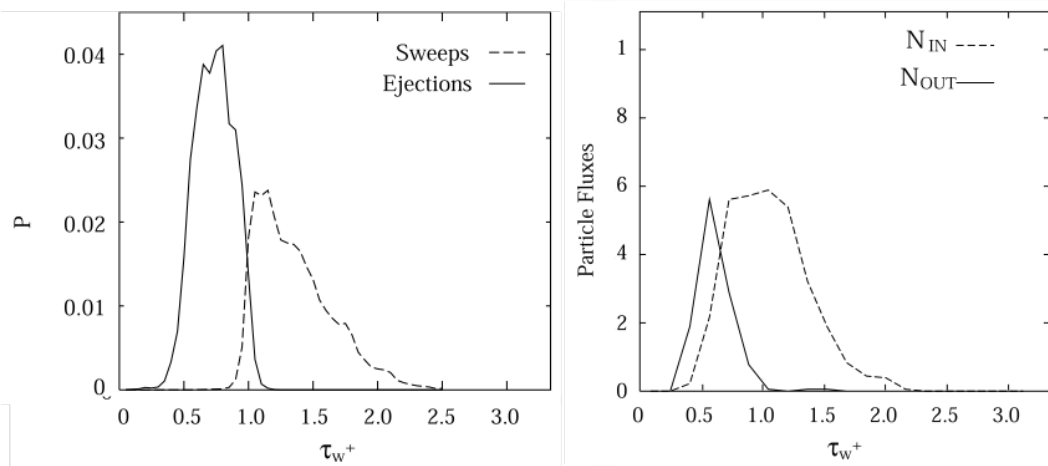


Figure 3.50: Correlation between sweeps and ejections and particles fluxes to and from the wall (taken from [39])

A firm correlation was shown between the instantaneous locations of strongly coherent turbulent structures and the locations of particles with outward or inward velocity. In fact, 98% of the smallest particles crossing a monitor plane either towards or away from the wall were in the vicinity of a strong sweep or ejection. For the largest particles, the figure was 91%. This shows clear evidence that the dominant mechanism for particle transfer is by quasi streamwise vortices. It was shown that smaller particles were more likely to 'follow' or be directed by the sweeps and ejections. The correlation of positive/negative wall-normal velocity with sweep/ejection location for the largest particles was weaker.

From instantaneous snapshots of particle distributions, iso-surfaces of vorticity and particle trajectories, Marchioli and Soldati suggested a mechanism for the particle trapping phenomenon. They noted that in many cases, a secondary counter-rotating vortex would be 'born' from a single mature vortex. Horseshoe type

vortices (with a pair of equal strength 'legs') were detected much less frequently. The secondary vortices appeared to obstruct particles and prevent them from being transferred to the region where they could be successfully entrained in the ejection zone of the parent vortex. As a result, only particles with specific trajectories may find a way into the 'ejection channel' to be re-entrained into the outer flow.

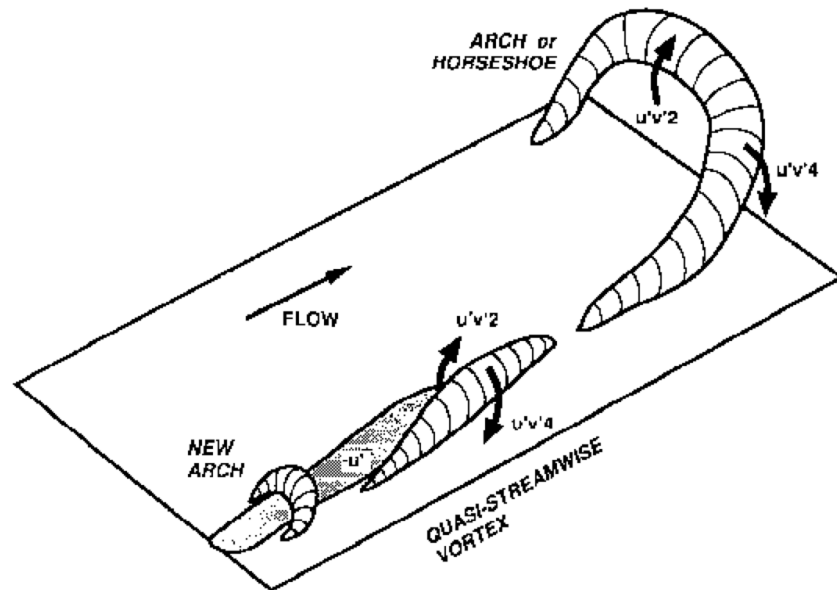


Figure 3.51: Conceptual model of low- Re quasi-streamwise vortices (taken from [40])

For non-isothermal flow (ie. particle transport over heated walls) the temperature gradient imparts an additional force to the particles (thermophoresis). Particles with small relaxation times that deposit by Brownian and turbulent diffusion may be pushed away from the wall due to the increased molecular bombardment from the hot side and as a result the deposition rate may be reduced for heated walls, or enhanced for walls cooler than the bulk flow [116]. Owen et al [117] studied deposition of sub-micron particles (Uranine-water solution) to a smooth heated surface and a heated surface with widely spaced roughness elements. The surface was heated to $95^{\circ}C$ and the bulk temperature was $25^{\circ}C$. At the highest temperature, the deposition was around 15-20% lower with respect to the isothermal case (the effect for the smooth surface was fractionally less than the ribbed surface), but for lower temperatures, the deposition reduction by thermophoresis over the ribbed surface was lower than the smooth case. The effect was also reduced for higher Reynolds numbers. The effect of thermophoresis was therefore reduced by enhancement of turbulent diffusion. Thermophoresis was found to be less

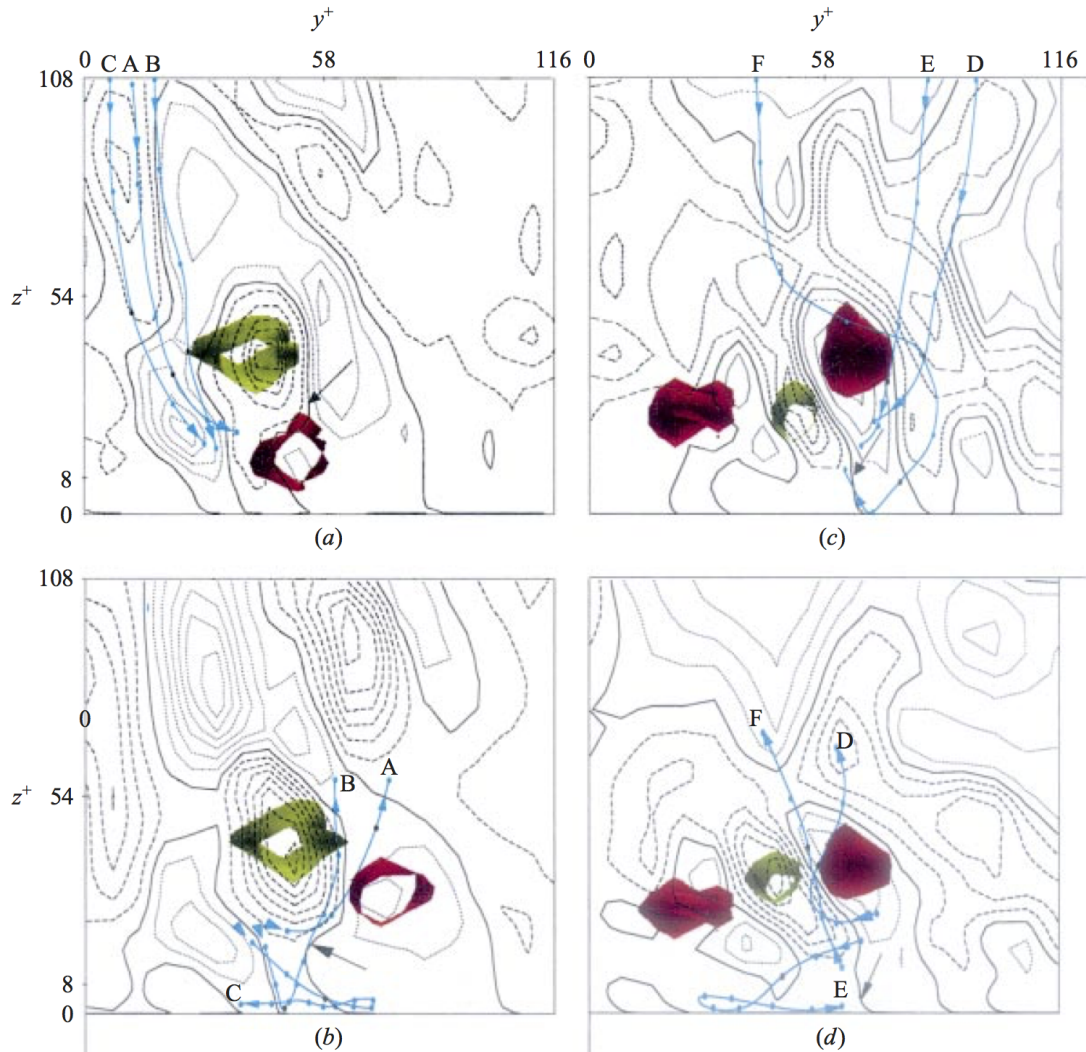


Figure 3.52: Proposed particle trapping mechanism. Iso-surfaces of vorticity and fluid streamlines. Green iso-surface: parent vortex (CCW). Red iso-surface: offspring vortex (CW). (taken from [38])

effective in reducing deposition rate for the smaller particles ($0.05\mu\text{m}$) than the larger particles ($0.25\mu\text{m}$) - attributed to the higher temperature gradient across larger particles. For the ribbed surface, the effect of particle size was less apparent. Overall, thermophoresis was observed to reduce deposition rate (although the effect was less than predicted by theoretical models eg. [108]) and the rate of deposition over the ribbed surface was around an order of magnitude greater than the smooth surface.

For aviation fuel deposition, Ervin et al [118] developed a 1D numerical model that included fluid dynamics and chemistry. Reactant species were calculated using a seven step global chemical kinetics scheme for Jet-A - employing 5 steps

for bulk fuel reactions and 2 surface reaction steps. Activation energies and pre exponential multipliers were based on experimental data. The authors highlighted the uncertainty surrounding the actual mechanism for insoluble formation (whether deposit forms directly on or off the wall and how the particles nucleate and grow in the bulk fuel). The wall surface condition was included in the equation for deposit formation rate through use of a 'sticking probability' based on the wall shear stress (also used by Beal [111]);

$$\frac{dD_{wall}}{dt} = \frac{c}{\tau_w^n} \left[\frac{\rho f_{pwall}}{M_p} \right] A e^{-E_a/RT} \quad (3.2.35)$$

where c is a constant, n is a constant (taken as 0.1 but 0.7 was used in [78]), f_{pwall} is the precursor mass fraction at the fuel - deposit interface and M_p is the molecular weight of the precursor.

The inverse relationship with wall shear stress is counter intuitive from a fluid mechanics perspective, given that turbulent diffusion is enhanced with increasing τ_w and deposition by interception is more effective for rough walls with higher wall shear stress. In addition, thermophoretic effects which tend to reduce deposition have been shown to be suppressed for high τ_w surfaces. The inverse relationship with shear stress can be traced back to the formulation of sticking probability given by Epstein [116];

$$S \propto \frac{\text{adhesive bond between the particle and surface}}{\text{shear stress on particle at surface}} = \frac{e^{-E/RT_{wall}}}{\tau_{wall}} \quad (3.2.36)$$

which considers the role of wall shear stress only in the *chemical attachment* of a particle to the wall, rather than the transport of the particle to the wall by shear induced turbulence.

Summary

- Mass transfer results expressed by V_d^+ against τ_p^+ .
- Three deposition mechanisms dependent upon τ_p^+ (particle size and density) - related to the interaction of particles with turbulence.
- Two classes of theories for particle deposition - free flight / stopping distance concept or probabilistic approach related to particle interaction with turbulence sweep and ejection cycle.
- Deposition rate shown to be enhanced for modest increases in roughness.
- Deposition by diffusion is more significant for smooth walls where the extent of the viscous layer is greater.
- Saffman lift and thermophoretic forces can enhance or reduce deposition based on tube orientation and thermal conditions at the wall.
- Small particles with insufficient inertia to deposit accumulate in low speed streaks close the wall.
- Particles provided with inertia to deposit by strong turbulent motions.
- Particle flux to the wall (by sweeps) is greater than flux away from the wall (by ejections).
- Inequality in particle fluxes thought to be due to obstruction to the ejection pathway by offspring vortices.

Chapter 4

Experimental Methods

4.1 Design Considerations

As noted in chapter 3 and table 3.1, at the time of writing the amount of published data on the effects of surface roughness on deposition is extremely limited. Previous work [7] suggested that a rough wall accelerates the initial stage of deposition formation, prior to a period with constant deposition rate. However, no roughness metrology was performed on the surface in question. The experimental work detailed in this chapter aims to fill the void in the present published material and provide new quantitative data to inform the study of roughness effects on fuel deposition.

To focus the design of experiments, the intended scope of the work is first considered and aims and objectives are presented. Then, considerations are given to the suitability of established thermal stability test apparatus to the study of roughness on fuel deposition based on a set of clear criteria. As a result, the experimental apparatus is ranked in terms of suitability. The experimental methodology adopted for each case is then outlined in detail.

4.1.1 Aims and Objectives

The experimental data generated should ideally have maximum relevance - for studies of fluid mechanics and heat transfer on a fundamental level and also for design of future engine components. On the other hand, from a pragmatic point of view, it must be anticipated that an all-encompassing study simply may not be possible, perhaps as a result of limitations in experimental apparatus or time. It

is important that any sources of error are minimised and the data must have an acceptable degree of experimental uncertainty. With these considerations in mind, some general aims and objectives are presented:

Aims:

- Establish whether a correlation exists between surface roughness and the deposition rate of thermally stressed aviation fuel.
- Provide more detailed information than is available in the current literature about the roughness geometry associated with any observed trend.
- Build a dataset for roughness geometry and deposition.

Objectives:

- Identify most viable test method/s.
- Establish data points for roughness.
- Characterise roughnesses as thoroughly as possible.
- Experimentally determine the effect of roughness on isothermal flow and heat transfer.
- Experimentally determine whether a trend exists between surface roughness and deposit formation rate.

4.1.2 Experimental Equipment

Three well established thermal stability test devices exist at the Low Carbon Combustion Centre, University of Sheffield which have the potential to be used in the investigation; the Aviation Fuel Thermal Stability Test Unit (AFTSTU), the High Reynolds number Thermal Stability Tester (HiReTS) and the Jet Fuel Thermal Oxidation Tester (JFTOT). Standard operating conditions of each device are compared in table 4.1 and detailed reviews of each rig can be found in appendix A. The devices were assessed for suitability in the proposed investigation by way of a suitability matrix, with criteria detailed below based upon the aforementioned experimental considerations. Each device was rated between 1-5 and investigative priority was assigned to the device with the highest score.

Table 4.1: Typical test conditions for thermal stability rigs at LCCC

	JFTOT	HiReTS	AFTSTU
Fuel outlet temp ($^{\circ}C$)	260	290	200
Fuel flow rate (l/hr)	0.18	2.1	23
Test duration (hrs)	2.5	2	150
Fuel vol (l)	0.45	5	3500
Res. time (s)	2.3	0.015	0.14
Test section	annular	270 μm ID capillary	2mm ID tube
Re_{approx}	30	2000 to 10000	10000
System pressure (bar)	34	20	34
Preheating	no	no	yes ($T_{bulk} \approx 170oc$)

Instrumentation

Quality of instrumentation is largely determined by the test section in each device. The HiReTS and the AFTSTU device have tubular test sections, which allows external or internal and external wall temperatures (HiReTS / AFTSTU respectively) to be recorded. Monitoring the rise in tube wall temperature as a result of the insulating effect of the deposit layer is arguably the only method for non destructive on-line deposition measurement (excluding gravimetric methods). In the JFTOT, no on-line temperature measurement is possible. The device does provide live filter pressure drop information - although this is not a direct indication of the level of deposition on the tube wall. The JFTOT relies upon post test visual analysis of the tube deposit which results in a low score in this category. Deposit thickness calculation by interferometry is now possible, but not for rough walls.

Flow relevance

A key factor with respect to the usefulness of the data is whether the flow in the device is laminar or turbulent. Both the HiReTS and the AFTSTU are turbulent flow devices, while the JFTOT is laminar. Flow in aircraft fuel systems is primarily turbulent, and theory would suggest that momentum and heat transfer is independent of roughness in the laminar regime. As a result, the JFTOT scores poorly in this category. The HiReTS scores slightly lower than the AFTSTU, since the thermal gradient and thus change in Reynolds number through the test section is very large in the HiReTS, while the flow in the AFTSTU is already pre heated and thus the change in Re is lower through the test section.

Roughness potential

Roughness potential indicates the likely range of roughness that could be investigated using the device. Since the JFTOT has an annular test section with the heater tube forming the centre of the annulus, there is more possibility to affect and study the surface of the material. Machining and/or additive manufacturing with post processing could be used to create roughnesses (2D or 3D) that would not be possible in the case of the internal walls of tubes with similar dimensions. For the AFTSTU, despite being internal tube flow, the dimensions of the test section offers potential. With the largest diameter of all of the considered devices, the standard drawn tubing used for the simulated burner feed arm section typically has a low relative roughness, providing a readily available smooth datapoint. Potential data points for 3D roughness could be created by using additive manufacturing or acid etching. 2D roughness could be created by fabricating tubes with a wire insert. Standard test sections for the HiReTS are $270\mu\text{m}$ drawn tubes which have been shown to have high relative roughness. The number of potential roughness data points is expected to be limited, since the tubes are in the micro scale. Tubes with higher or different roughness may exist, or it would be necessary to have a batch of tubes manufactured using different die shapes to influence the tube internal wall. It may be possible to smooth the surface of the standard, high roughness test section by electro discharge machining (EDM) or acid etching. Additive manufacturing would not be possible at this scale.

Flow pre conditioning

Thermal stressing of the fuel prior to the roughness test section is deemed disadvantageous to the study from a fundamental sense - due to the additional complexity of the fuel path. Initial tests to establish a trend should ideally not be influenced by upstream fuel passages, although subsequent testing with thermal stressing upstream of the test section would be more indicative of in-service conditions. For these reasons, the AFTSTU scores low as the fuel undergoes significant recirculation through spill loops, metering components and temperature regimes prior to the test section location at the exit of the rig. Both the JFTOT and the HiReTS have a single path in which thermal loading is applied at the test section only.

Sample size

A small sample size is preferred to keep the cost of testing to a minimum. The JFTOT scores highly in this category with the smallest sample size (600ml), due

to the laminar nature of the device. The HiReTS requires 5l, while the AFTSTU requires typically hundreds of litres per run.

Industrial acceptance factor

The JFTOT has been the industry standard thermal stability specification test method for over 50 years and has been proven to be an effective tool in the quantification of fuel thermal stability. Results from the device are numerous in publications and have been thoroughly examined. Since JFTOT devices are so numerous, it would be relatively straightforward for another lab to reproduce the test conditions. The AFTSTU rig, originally conceived by Rolls-Royce is a fairly uncompromising fuel system simulator that is featured in several publications. The direct association to an engine manufacturer awards the device credibility in the thermal stability community. However, access to the device is very limited. Although the HiReTS features in several publications, lack of commercial backing and the widespread acceptance of the JFTOT as the go to specification test device has restricted the amount of published data generated from the device. Since the HiReTS is no longer in production, access to the device is limited.

Roughness measurement

Accurate quantification of roughness is vitally important to the study. Any external roughness can be measured in detail by interferometry. In this regard the JFTOT has an advantage over the other two devices. For internal flows, the quantification of roughness is less straightforward. The classical approach is to assess the roughness indirectly by measuring the pressure drop through the tube and calculating the associated friction factor. Tubes may be sectioned and optical microscopy / scanning electron microscopy used to investigate the 2D roughness geometry. the AFTSTU has a small advantage over the HiReTS, since the tube geometry is slightly larger, and is therefore easier to section.

Deposition measurement

In the literature, deposits are commonly quantified in several ways: change in wall temperature or heat transfer rate, post test carbon burn off, scanning electron microscopy or visual rating. While the HiReTS and AFTSTU devices record deposition via change in tube wall temperatures throughout the test, only post test quantification is available for the JFTOT. For all test methods, tubes can be sectioned and the deposit layer measured through microscopy. This provides the only potential method of deposit quantification for the JFTOT, since ellipsometry

of tubes with rough surfaces is not yet possible. In the case of the HiReTS and AFTSTU devices, temperature measurements provide a time history of the development of deposit, and the final value can be validated against measured deposit thicknesses. As a result, these devices score highly in this category. No carbon burn off analysers are available to the investigation.

Table 4.2: Rig suitability assessment

	JFTOT	HiReTS	AFTSTU
Instrumentation	1	5	4
Flow relevance	1	4	5
Roughness potential	5	3	4
Flow pre conditioning	5	5	2
Sample size	5	4	1
Industrial acceptance	5	3	4
Roughness measurement	4	4	4
Deposition measurement	1	4	4
	27	32	28

4.2 Tests with the HiReTS device

4.2.1 Repeatability validation

Repeatability and reproducibility of the HiReTS is discussed in the review of thermal stability test devices in Appendix A. While the device repeatability seems adequate according to the ASTM requirements, significant and consistent variations in initial tube outer wall temperature have been reported in [38] and observed in testing conducted by the author. Figure 4.1 shows 9 tube external wall temperatures recorded by thermography at the conclusion of a 5 minute warm up period prior to the start of tests conducted on the same fuel using the standard HiReTS method (ASTM D6811). At this point in the time, the rig has reached quasi-steady state conditions; the fuel outlet temperature is well controlled by the PID and it can be safely assumed that no measurable amount of deposit will have formed during the warm up period. If the variability in initial wall temperature cannot be assigned to differing pre-test methods or even different fuels, logic dictates that the variability in initial wall temperature must be a result of some aspect of the test device.

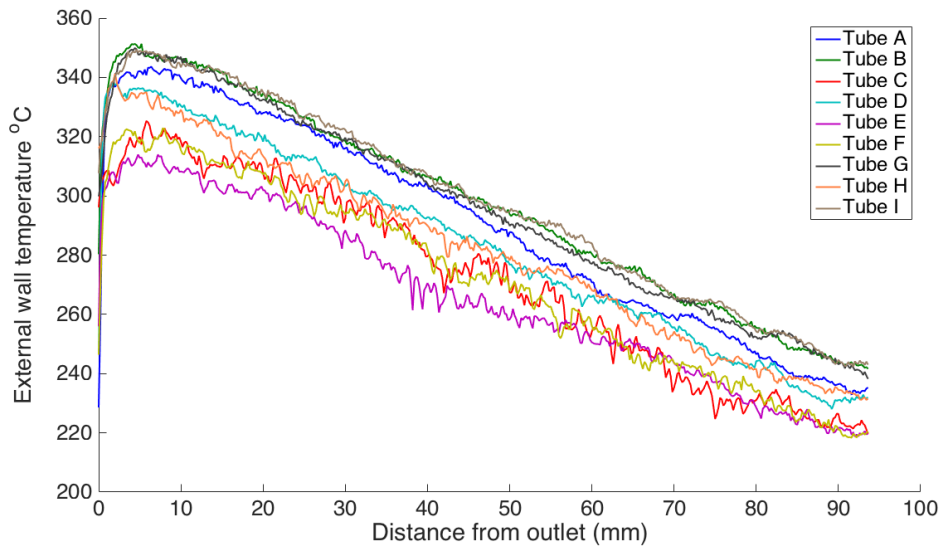


Figure 4.1: Observations in the spread of initial wall temperature with test on one fuel (ASTM D6811)

The test capillaries used in the HiReTS (supplied originally by Stanhope-Seta) are available in various batches. In the figure above, data from tubes from 3 batches are shown. It was necessary to assess whether the variability in wall

temperatures could be attributed to only the change in capillary and not a combination of tube and device variability. Figure 4.2 shows the initial external wall temperature profiles for three capillary tubes (batches 4604, 4204 and 0803C) after a five-minute warm up period. For each tube, two tests were performed to assess the ability of the device to reproduce wall temperatures for the same tube. The second test was performed on the following day to ensure the device had cooled completely. In order to ensure that no deposit was formed which could alter the temperature profiles, the fuel was deoxygenated via nitrogen purging for 10 minutes. Complete removal of oxygen was verified using an oxygen sensor. It is clear that the temperature profiles are identical between the two tests for all three tubes considered and the repeatability of the device in terms of initial wall temperature is confirmed. Also evident is the change in wall temperature profile between tube batches. What can be said with confidence is that either the tube diameter and / or roughness are variables which influence the standard test method.

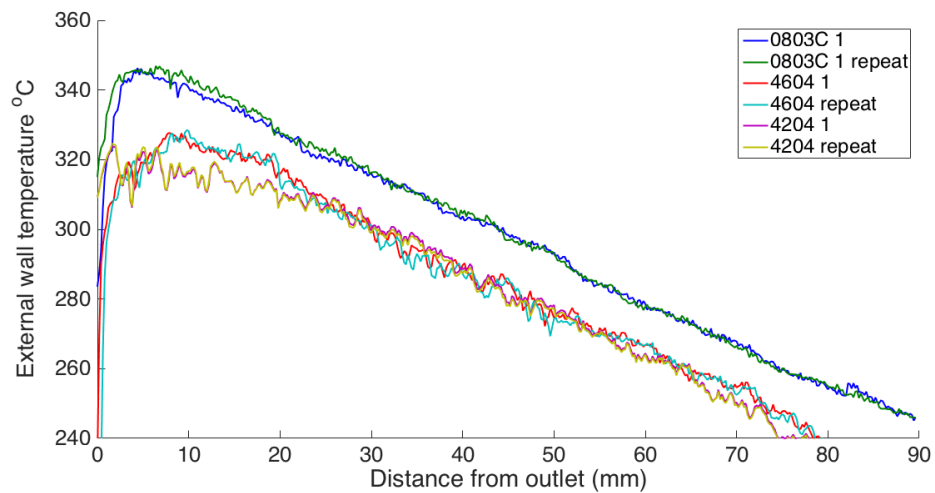


Figure 4.2: Repeatability of initial wall temperature for the same tubes (ASTM D6811)

4.2.2 Establishing roughness data points

Sectioning and microscopy of test capillaries used in previous fuel specification testing with the HiReTS device at the Low Carbon Combustion Centre has shown the tubes to exhibit very high surface roughness. Roughness peaks exceeding $20\mu\text{m}$ have been measured - resulting in relative roughnesses, $\frac{k}{D} = 0.07$. For testing using the standard method on the HiReTS (ASTM D6811), the tube diameter is required to be between $260\text{-}300\mu\text{m}$. The original tubes are typically approximately

270 μm in diameter. The tube stock used in the HiReTS is in fact technical grade 316SS capillary tubing for high performance liquid chromatography (HPLC). This particular tube geometry was originally selected for use in the HiReTS because of the requirement for a turbulent flow test with a small sample size.

4.2.2.1 Capillary tube smoothing

Wire electrical discharge machining (EDM) was identified as a potential method to smooth the internal wall of standard HiReTS tube stock. A tensioned 150 μm copper wire electrode is fed continuously through the tube, which is immersed in dielectric fluid. A high frequency current is discharged through the fluid across a small spark gap between the wire and the workpiece and the heat of the spark (8000 - 12000 $^{\circ}C$) erodes a small amount of material from the workpiece, which is flushed away by the fluid. Surface roughnesses as low as 0.04 μm (R_a) may be achieved.

Figure 4.3 shows sections from an initial test batch of tubes, smoothed by EDM, compared to a stock capillary tube. The method was successful in smoothing the large peaks and troughs exhibited in the stock tubes. A quantitative comparison is difficult, since the point of measurement of roughness peaks is rather arbitrary. Qualitatively, it can be seen that the roughness has been greatly reduced with respect to the stock tube, although the smoothed tubes do still exhibit deviations from an ideal circle.

4.2.2.2 Effect of tube diameter on test conditions

It is evident from the micrographs that in the EDM process, material is removed from the wall such that the diameter of the tube is significantly increased. The effect of tube diameter on the Reynolds number for an ideal smooth case is outlined below. In the calculations, the fuel flow rate and exit temperature for the standard HiReTS method was used (35ml/min, $T_{out} = 290^{\circ}C$).

$$U_{avg} = \frac{Q}{A} = \frac{Q}{\frac{\pi D^2}{4}} \quad (4.2.1)$$

$$Re = \frac{U_{avg} D}{\nu} = \frac{4Q}{\pi D \nu} \quad (4.2.2)$$

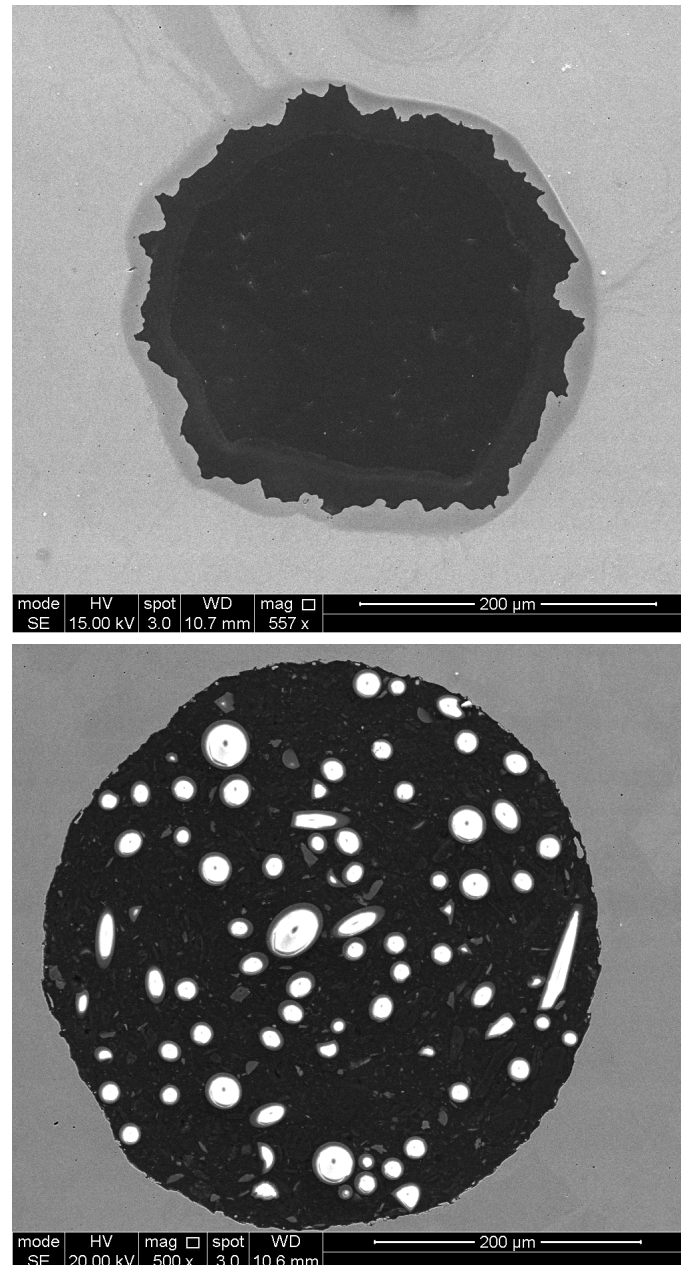


Figure 4.3: SEM image of sectioned tubes. Top: standard capillary. Bottom: smoothed by EDM

Taking into account temperature dependent material properties and assuming linear axial temperature increase (iso-flux thermal boundary condition), the profile of Reynolds number from inlet to outlet for tube diameters from 260 - 400 μm is shown in figure 4.4. The implications with regard to the study of roughness are quite significant. Fig 4.5 shows the change in viscous sub layer thickness across the tube length with Re for a theoretically smooth tube. The friction velocity was estimated from the Colebrook-White formula. It is clear that for constant flow

rate, a decrease in the tube diameter results in increase in Re and a decrease in viscous layer thickness across the tube. Since Re increases from inlet to outlet as a result of the reduction in bulk viscosity and density, significant changes in tube diameter will result in different transitional roughness behaviour along the tube - since the roughness elements will begin to disturb the viscous layer at different axial locations, depending on the diameter.

Furthermore, since the inlet flow under standard conditions is below the critical Reynolds number for pipe flow, transition to turbulence occurs. Changes to the point of transition through diameter will also have implications for the wall shear stress and heat transfer.

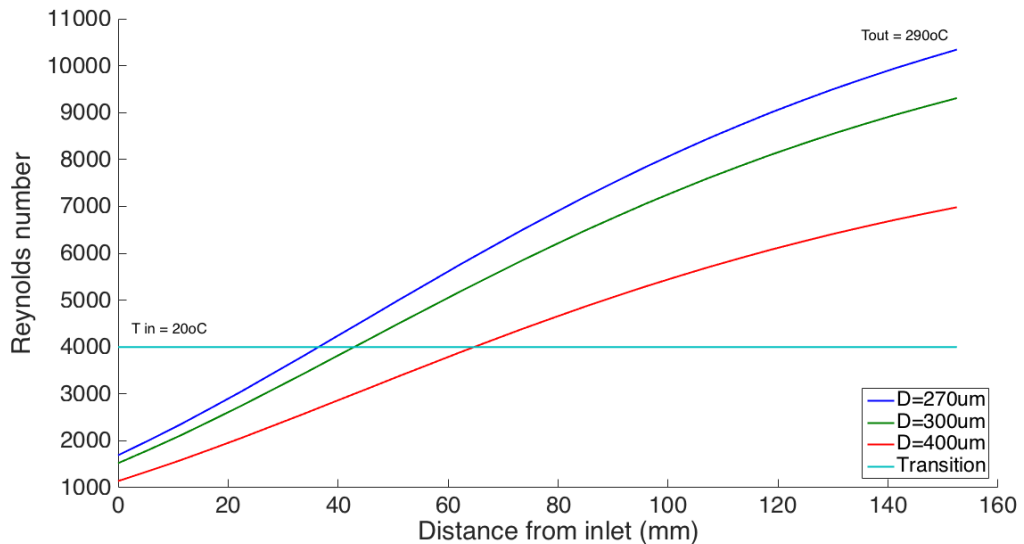


Figure 4.4: Change in Re due to bulk fuel temperature increase from inlet to outlet

With a-priori knowledge of the tube diameter, one approach could be to adjust the fuel flow rate to match the desired Re . However, this would result in a change to the energy required to heat the fuel to the outlet temperature, thereby invalidating the comparison. It is clear that for a fair study of deposition (regardless of roughness), changes in the Reynolds number and energy input to the fuel must be kept to a minimum. Therefore the diameters of smooth and rough tubes should ideally be as close as possible to minimise Reynolds number effects.

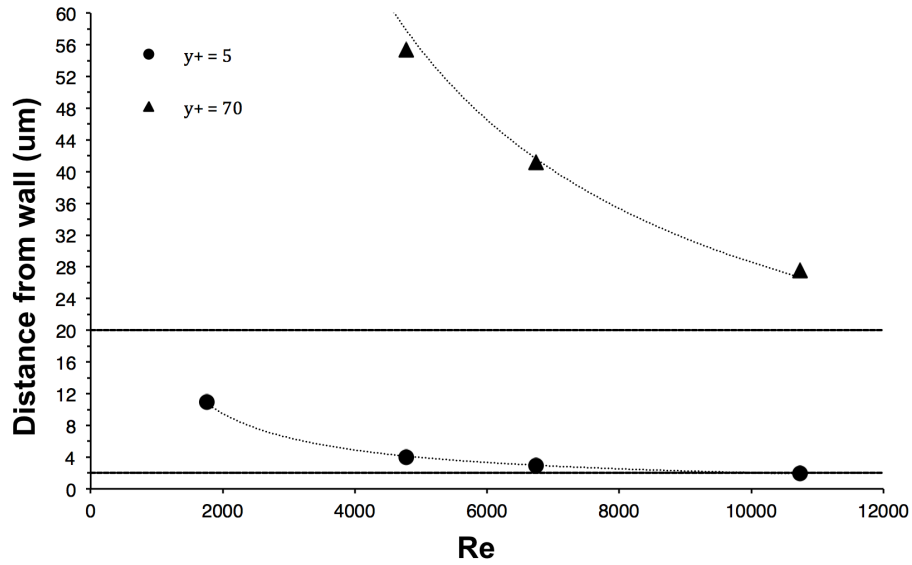


Figure 4.5: Change in viscous sublayer height with Re

4.2.2.3 Tube selection

Since the EDM process increases the 'donor' tube diameter significantly, an alternative supply of larger diameter drawn tubes was required for the rough wall comparison. Fortunately, 1.6mm OD HPLC capillary tubing is available in a variety of internal diameters, with the next available ($\approx 500\mu m$). To create the smoothed tubes, the smallest diameter donor tubes ($\approx 270\mu m$) were spark eroded by EDM to a target diameter of $500\mu m$. In all, 3 sets of smooth tubes were machined. The length of the tubes did not change with respect to the standard HiReTS method (152mm). 200mm long tubes were machined which were cut to size during the sectioning process, outlined below.

4.2.3 Roughness characterisation

Characterisation of the roughness in as much detail as possible is one of the key objectives of the study. The nature of the flow - internal as opposed to annular, makes the metrology of roughness somewhat difficult, as high fidelity optical profilometry is not possible. Some limited information may be gained through sectioning of the tubes and measuring surface features using microscopy as previously shown. Whilst this approach has the advantage of being able to directly measure some surface features, it is limited by the fact that each section is representative only of a very small region of the tube, and in addition, only the roughness features in the radial and circumferential directions are considered. In

the absence of micrographs of axial lengths (which are very hard to realise in practice due to the small diameters considered and precision of sectioning required), it is assumed that cold drawing of the tubes around a die results in 'extrusion' of the circumferential roughness profile (imparted to the tube wall by the die) along the tube length. As a result, the circumferential profile is expected to be reasonably consistent along the length of the tube. The extrusion of the peaks and valleys might result in a riblet-type roughness - aligned in the streamwise direction.

The classical approach, which does not rely on specific metrology of the surface features, has been to observe the effect of roughness on the fluid flow via measurement of the wall shear stress τ_w , which has been discussed at length in previous chapters. Pressure drop measurements along the tube (resulting in friction factor), essentially provides a quantification of the frictional resistance provided by the roughness elements averaged along the entire length of the tube. Clearly this is more representative of the roughness than a radial slice, and the friction factor carries more merit as a way of describing roughness than discrete measurements taken from a micrograph. The caveat in this approach is that in order to relate the friction factor to the classical work of Nikuradse to calculate an equivalent sand grain roughness, the pressure drop must be measured in the fully rough condition. If this is not possible then the analysis is hampered somewhat, and transitional formulas (such as the Colebrook-White equation) must be used for comparison.

4.2.3.1 Microscopy

To study the tubes optically, samples were prepared using established techniques for Scanning Electron Microscopy. The process is outlined below;

- Tubes were first sectioned to the required length (152mm). A 5mm slice was taken from the excess length using a precision abrasive ferrous cutting blade.
- The small length was hot mounted in bakelite.
- The sample was wet ground with successively finer abrasive paper (400-1200grit) to remove the scratches from the abrasive blade.
- The sample was polished with 2 μ m diamond suspension to remove the scratches from the abrasive paper.

- The sample was polished to a mirror finish with $0.06\mu m$ colloidal silica.

Micrographs of the EDM and drawn tubes are shown in figures 4.6 - 4.10. In addition, the diameters extracted from the micrographs are listed in table 4.3. It should be noted that the measurement of diameter (for the rough tubes in particular) directly from the microscope relies upon a somewhat arbitrary selection of a reference position for the radial measurement. In practice, the position was chosen by eye to achieve the best apparent fit to the inner bore, or to lie on a 'mean' locus ie. equidistant from the highest peaks and lowest troughs. In an attempt to quantify the 'worst case' error associated with the measurement of diameter for the rough tubes, minimum and maximum diameters were compared, where the minimum diameter used the tips of the roughness peaks as the reference position and the maximum diameter used the bottom of the troughs. The difference δD was around $50\mu m$, corresponding to a maximum uncertainty in the diameter of 11%. Since the bores of the EDM tubes were more regular, the level of ambiguity was reduced. The measurement of diameter was subsequently improved with image processing techniques.

The commercially available drawn tubes show a high degree of similarity. The roughness could be described as being composed of a complex mix of superimposed length scales; relatively broad protrusions or indents along which the surface is 'wrinkled' by the smaller scale roughness. The largest peaks and troughs seem to generally extend to approximately $20\mu m$ in the radial direction. One feature common to the tubes seems to be relatively deep and sharp 'crevasses'. The reduction in surface roughness from the EDM process is plain to see. On the whole, the bores are much more regular, although some tubes do possess 'soft indents' - deviations from an otherwise near perfect circular bore. The roughness protrusions are more difficult to measure since they are so small, but are probably around $1-2\mu m$.

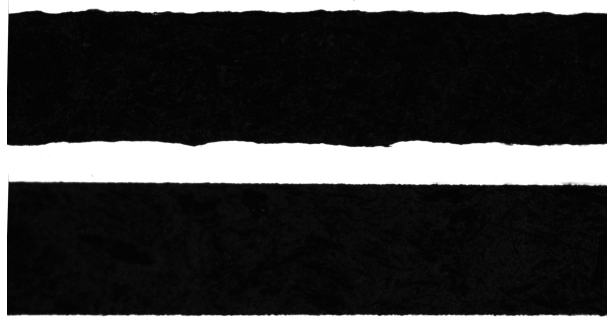


Figure 4.6: Longitudinal sections. Top: drawn. Bottom: EDM

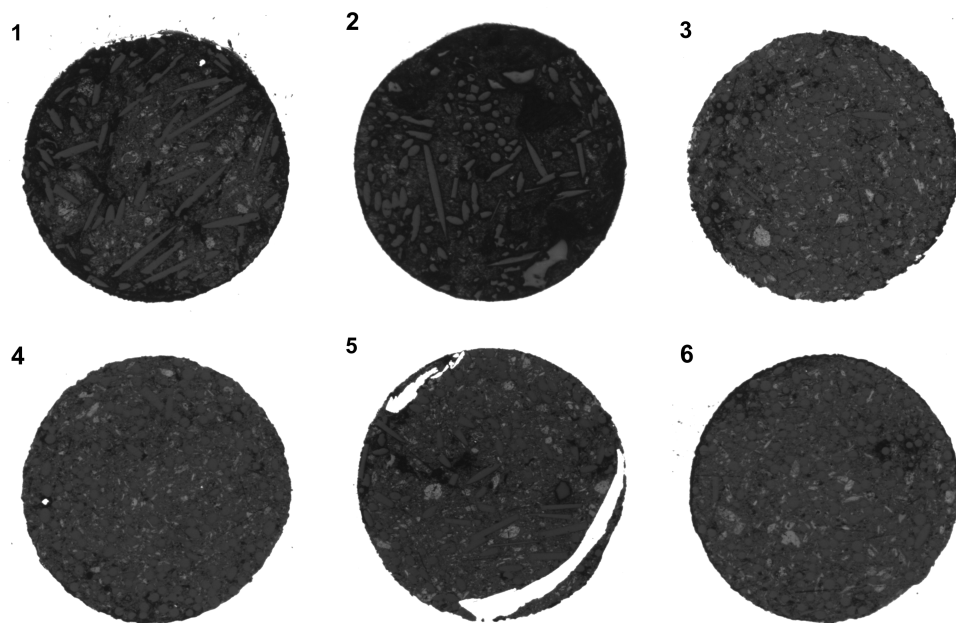


Figure 4.7: Set 1: EDM tubes 1 to 6

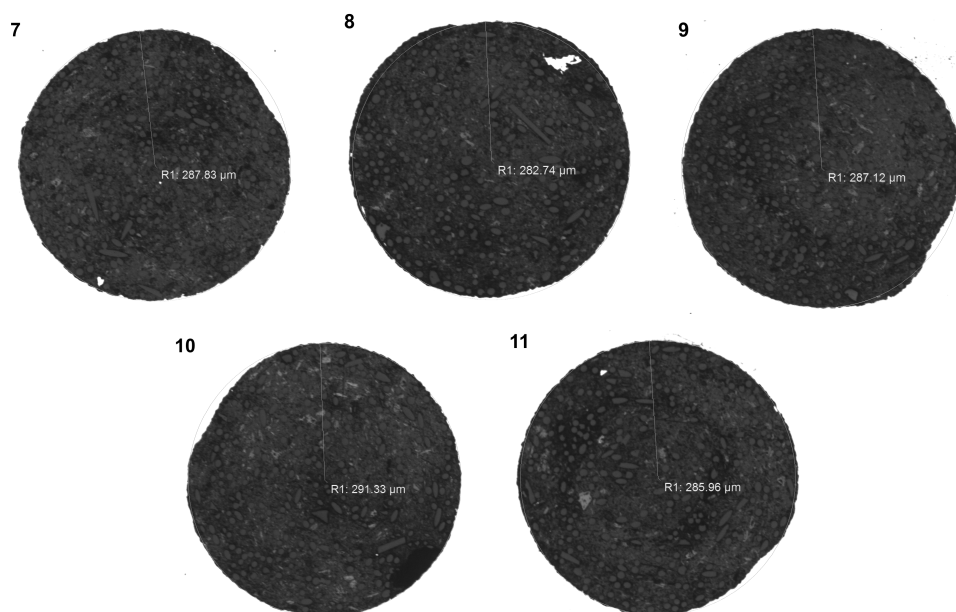


Figure 4.8: Set 2: EDM tubes 7 to 11

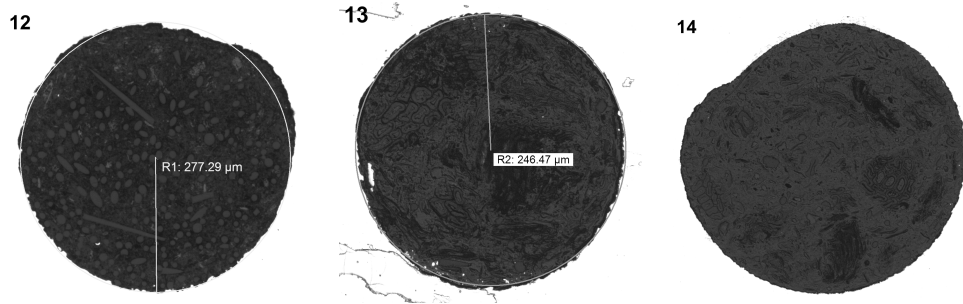


Figure 4.9: Set 3: EDM tubes 12 to 14

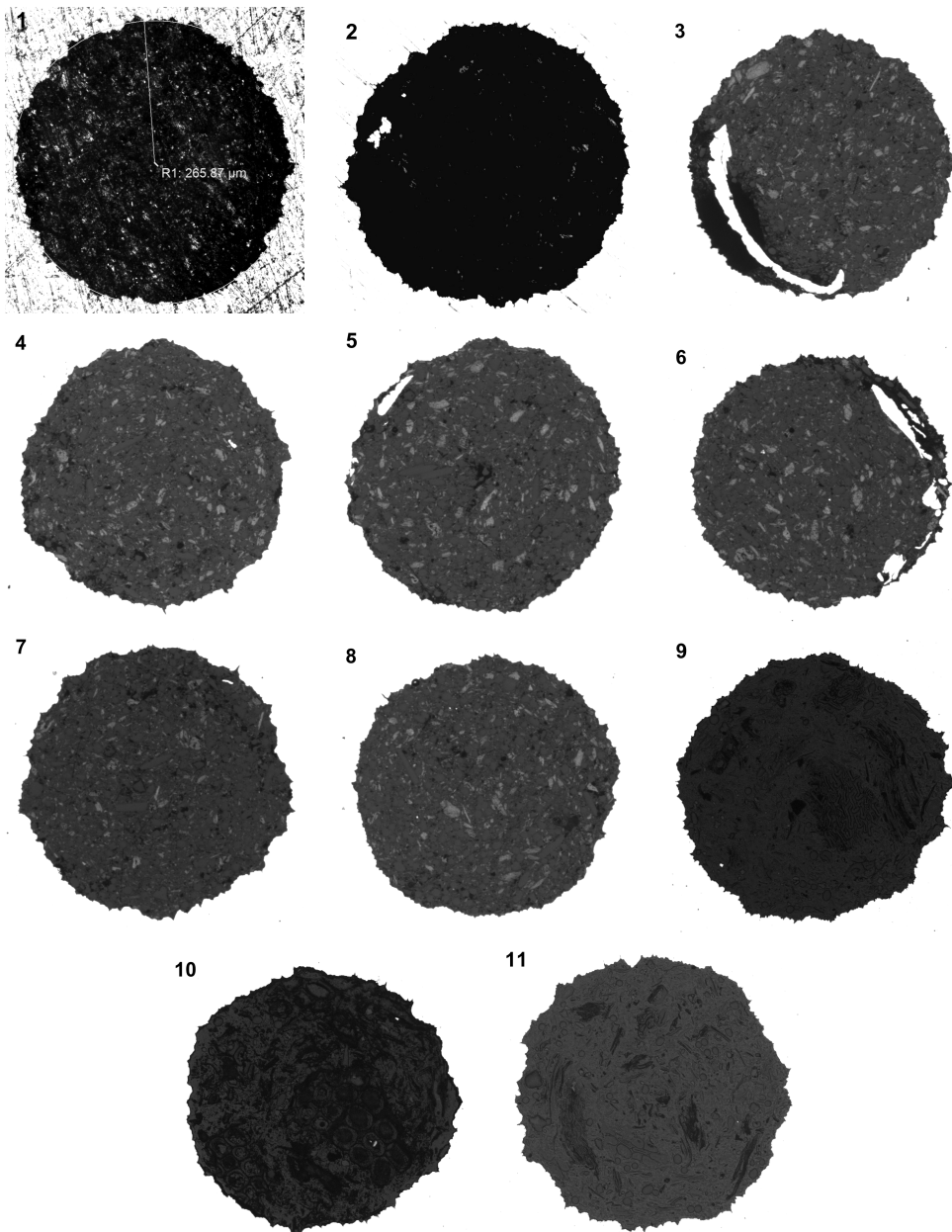


Figure 4.10: Drawn tubes 1 to 11

4.2.3.2 MATLAB image processing

In order to try and describe the roughness in more detail, image processing was used to trace the roughness profile. Crucially, good quality, highly polished samples were required, such that a clear distinction could be made between the tube wall and the bore. The micrographs were converted to binary images of only white or black pixels and a boundary tracing algorithm was used to trace the path formed by the intersection of white and black pixels, which were stored as a list of coordinates.

The centroid of the bore was calculated from the coordinates as;

$$(x, y)_{centroid} = \left(\frac{1}{n} \sum_1^n x \right), \left(\frac{1}{n} \sum_1^n y \right) \quad (4.2.3)$$

where n is the number of coordinate points. The distance from the centroid to each point (or the radius) was calculated by pythagorus' theorem;

$$r_{(n)} = \sqrt{(x_{cent} - x)^2 + (y_{cent} - y)^2} \quad (4.2.4)$$

and the average radius, measured from all points of the perimeter to the centroid was given by;

$$r_{avg} = \frac{1}{n} \sum_1^n r \quad (4.2.5)$$

The roughness height was defined as the difference between the local radius and the average radius;

$$y_k = r_{(n)} - r_{avg} \quad (4.2.6)$$

The result is equivalent to a 2D contact profilometer trace. Examples of the circumferential roughness profiles are shown in figure 2.7. From the roughness profile, the following 2D roughness metrics were calculated;

R_a , the arithmetic average roughness height;

$$R_a = \frac{1}{n} \sum_1^n |y_k| \quad (4.2.7)$$

R_q , the root-mean-squared (RMS) roughness height;

$$R_q = \sqrt{\frac{1}{n} \sum_1^n y_k^2} \quad (4.2.8)$$

R_v , the maximum valley depth;

$$R_v = \min(y_k) \quad (4.2.9)$$

R_p , the maximum peak height;

$$R_p = \max(y_k) \quad (4.2.10)$$

Histograms with overlaid normal distributions are also shown to visualise the distribution of roughness height.

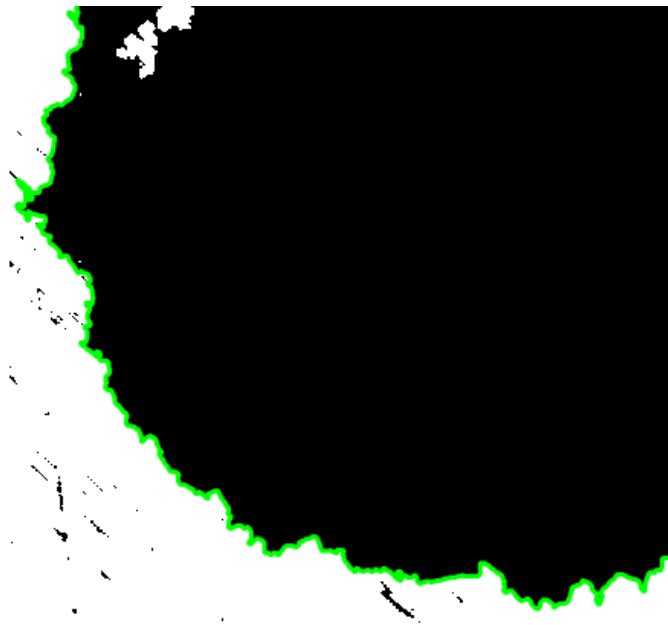


Figure 4.11: Demonstration of boundary tracing algorithm

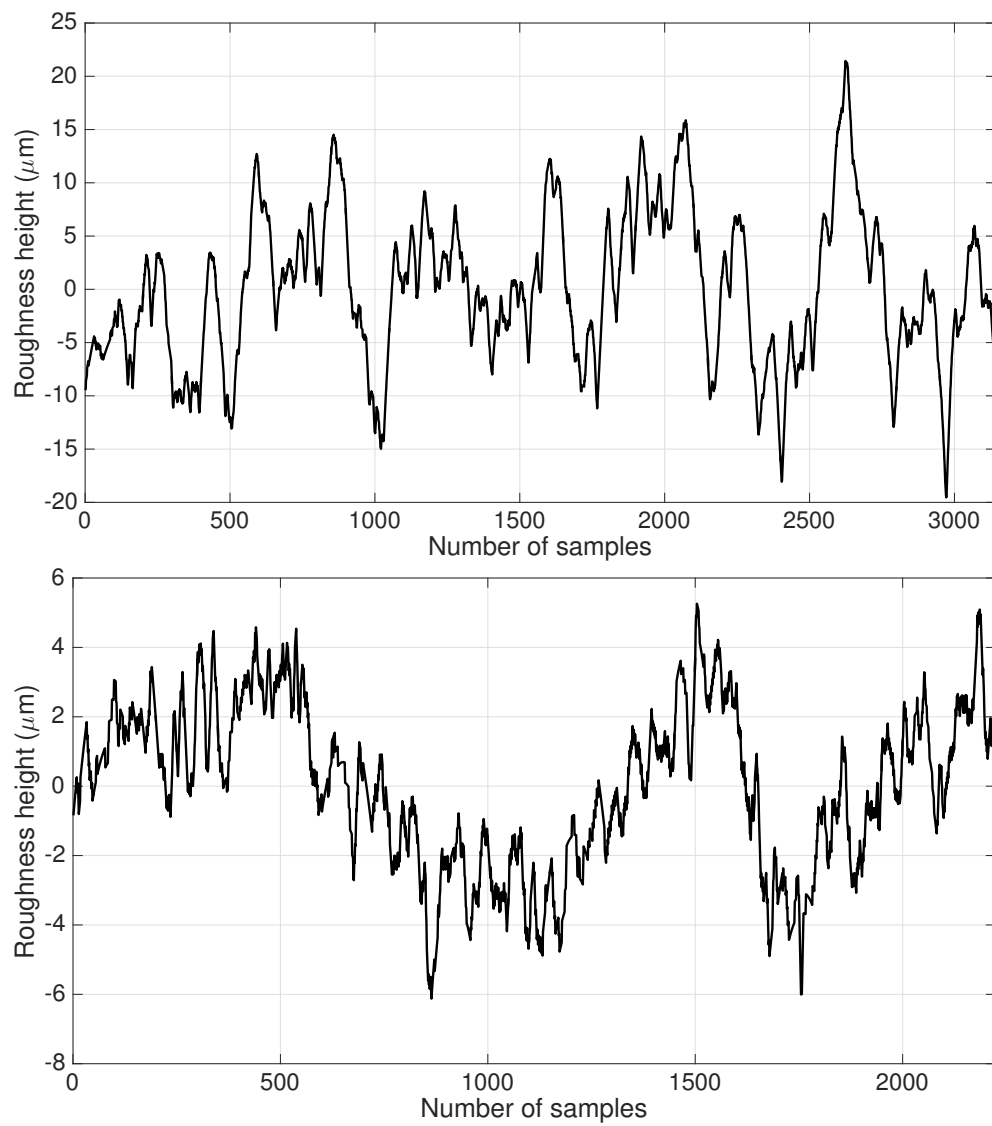


Figure 4.12: Circumferential roughness profiles (note y axis scale). Top: R7. Bottom: EDM 4

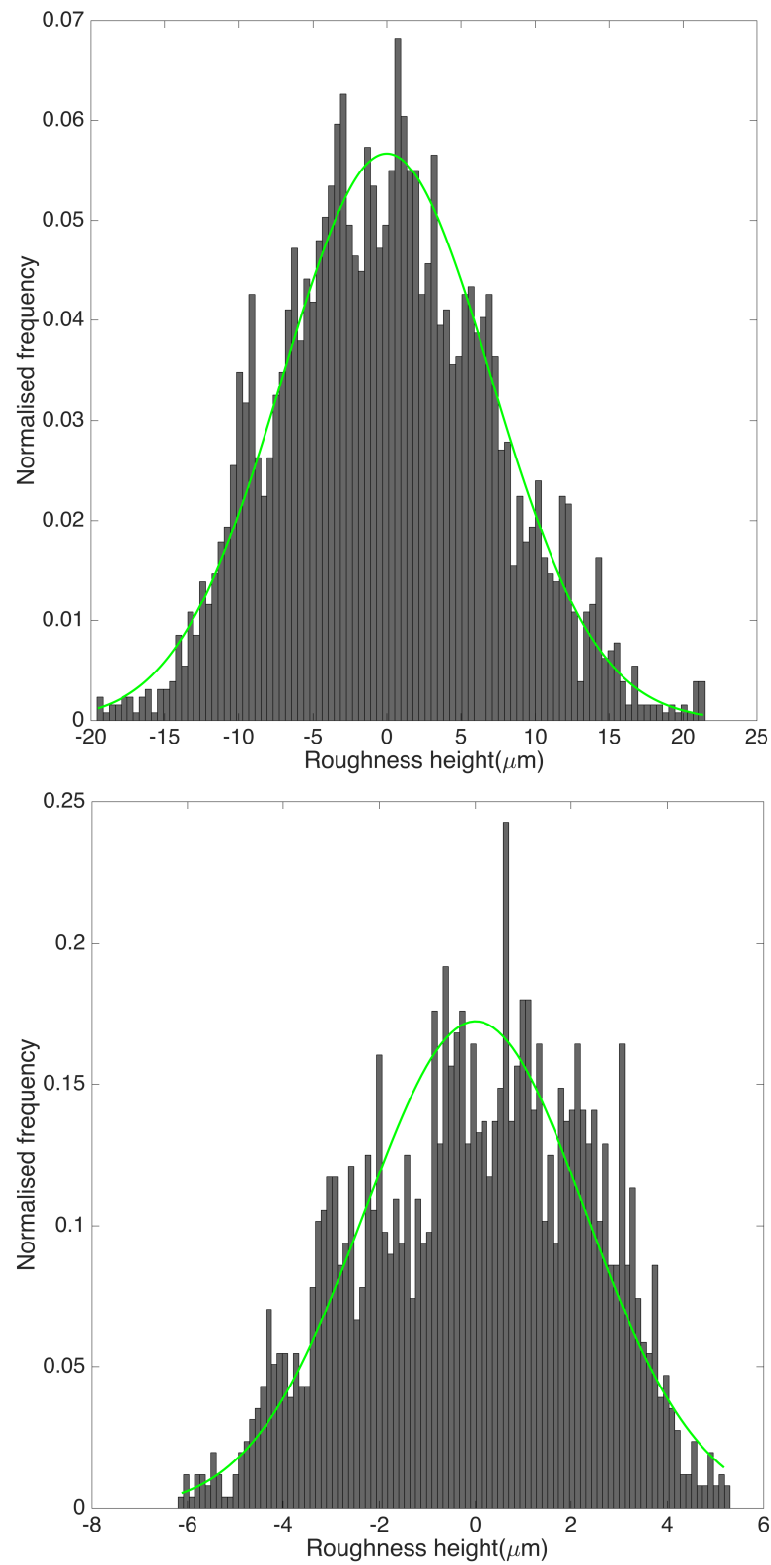


Figure 4.13: Roughness height distribution. Top: R7. Bottom: EDM4

Table 4.3: Image processing roughness metrology

Tube	D (μm)	A (μm^2)	P (μm)	P/ π D	R _a (μm)	R _q (μm)	R _p (μm)	R _v (μm)	k _{rms} /D (%)
R3	537	2.33E+05	2134	1.265	4.18	5.36	12.56	-17.68	1.00
R4	527	2.23E+05	2088	1.262	6.28	7.48	16.55	-21.04	1.42
R5	519	2.17E+05	1983	1.217	5.12	6.49	17.92	-16.97	1.25
R6	517	2.15E+05	2121	1.306	4.38	5.49	14.48	-13.40	1.06
R7	530	2.27E+05	2140	1.285	5.68	7.04	21.44	-19.54	1.33
R8	527	2.24E+05	2095	1.266	7.31	8.88	23.40	-16.66	1.69
R9	528	2.24E+05	2304	1.390	6.95	8.76	24.68	-18.31	1.66
R10	531	2.28E+05	2156	1.291	8.44	9.72	19.38	-24.14	1.83
R11	539	2.34E+05	2338	1.381	7.45	9.07	22.21	-20.98	1.68
avg	528	2.25E+05	2151	1.296	6.20	7.59	19.18	-18.75	1.44
EDM 1	482	1.89E+05	1769	1.168	9.15	10.53	24.16	-17.42	2.19
EDM 2	453	1.65E+05	1521	1.070	2.32	2.89	8.92	-5.89	0.64
EDM 3	472	1.80E+05	1744	1.176	2.41	3.10	10.95	-6.35	0.66
EDM 4	439	1.56E+05	1514	1.098	1.92	2.32	5.26	-6.12	0.53
EDM 5	500	2.02E+05	1780	1.134	3.36	4.36	14.12	-7.64	0.87
EDM 6	437	1.54E+05	1487	1.083	1.26	1.69	6.27	-3.84	0.39
avg	437	1.74E+05	1636	1.12	3.40	4.15	11.61	-7.88	0.88
EDM 7	575	2.67E+05	2199	1.217	5.27	6.27	15.96	-12.20	1.09
EDM 8	575	2.68E+05	2025	1.120	3.88	4.78	10.65	-11.06	0.83
EDM 9	574	2.66E+05	2111	1.172	5.18	6.37	18.62	-11.23	1.11
EDM 10	581	2.73E+05	2186	1.197	7.66	9.33	16.49	-20.89	1.60
EDM 11	576	2.68E+05	2142	1.184	4.64	5.24	14.11	-9.66	0.91
avg	576	2.68E+05	2133	1.178	5.33	6.40	15.17	-13.01	1.11
EDM 12	567	2.60E+05	1991	1.118	7.75	9.33	19.00	-12.53	1.65
EDM 13	495	1.98E+05	1923	1.237	4.34	5.23	14.99	-9.53	1.06
EDM 14	611	3.01E+05	2246	1.171	9.56	12.69	33.26	-25.08	2.08
avg	557	2.53E+05	2053	1.175	7.21	9.09	22.42	-15.71	1.59

4.2.4 Isothermal pressure drop experiments

As shown previously, the friction factor can be related to the pressure drop across a length L of pipe with diameter D according to;

$$P_1 - P_2 = \lambda \frac{L}{D} \frac{\rho U_{avg}^2}{2}$$

The bulk velocity, U_{avg} can be measured from the flow rate and area;

$$U_{avg} = \frac{Q}{A}$$

The theoretical friction factor for laminar flow is;

$$\lambda = \frac{64 \mu}{\rho V D} = \frac{64}{Re}$$

and the fully rough friction factor for turbulent flow according to Prandtl is;

$$\frac{1}{\sqrt{\lambda}} = 0.87 \ln (Re \sqrt{\lambda}) - 0.8$$

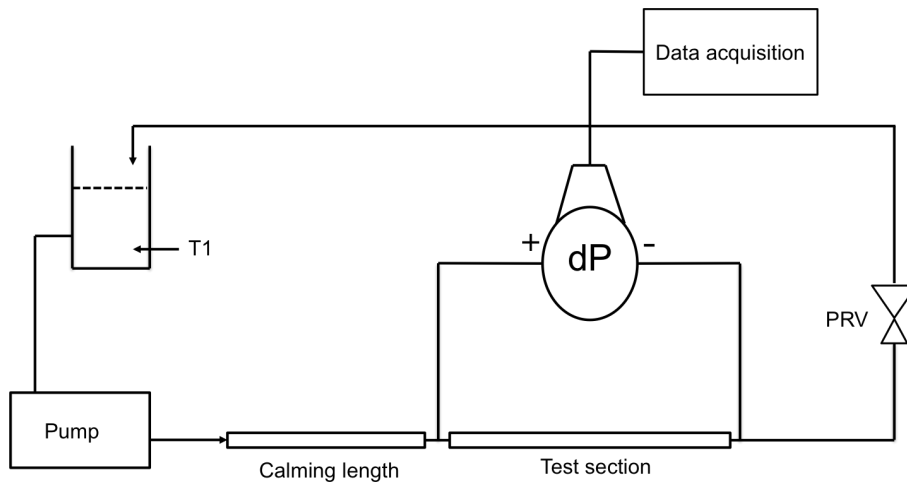


Figure 4.14: Pressure drop measurement apparatus

4.2.4.1 Apparatus

A schematic of the fluid path can be seen in figure 4.14. A Gilson 307 HPLC piston pump passed fluid through an entrance length of 1.6mm OD, 530μm ID SS316 capillary tubing. After the test section, the fluid was returned to the reservoir via an overpressure valve. Although a syringe pump may have provided greater flow rate accuracy, it was necessary to recirculate the fluid - which is not possible with 'single shot' type pumps. Positive and negative pressure ports

were created with 1.6mm OD cross unions at either end of the test section. The pressure drop across the tube was measured by a differential pressure transducer, with a maximum dP limit of 24bar. Fluid temperature was recorded by a k type thermocouple in the fluid reservoir. Data was recorded in LabView with a National Instruments CompactRio interface at 4Hz. Heptane was used as the working fluid.

4.2.4.2 Sources of uncertainty

The positive pressure tapping must be placed sufficiently far downstream from the inlet such that the flow is fully developed. Upstream of the point of complete development, the wall shear stress is not constant.

The turbulent hydrodynamic entry length can be approximated as;

$$\frac{L_e}{D} = 4.4 Re^{\frac{1}{6}} \quad (4.2.11)$$

Thus at $Re = 10,000$, the required entrance length is $20D = 10.6mm$. An upstream length of $100D$ was used.

A Budenberg dead weight tester was used to calibrate the pressure transducer from 0-23bar. The output from the pressure transducer was linear and the calibration data can be found in appendix D.

The flow rate was verified against a graduated measuring cylinder, and was consistently accurate to $\pm 2ml/min$

The maximum minor pressure loss from entrance and exit effects was calculated to be 0.2bar, assuming sudden expansion and contraction at the inlet and outlet.

Table 4.4: Sources of uncertainty - pressure drop experiments

Measurement	Instrument	Uncertainty
Differential pressure	ABB pressure transducer	$\pm 0.1\%$
Diameter	Microscope	$\pm 5\mu m(\text{edm})$ or $\pm 14\mu m(\text{d})$
Flow rate	Graduated cylinder	$\pm 2ml/min$

4.2.4.3 Method

The pressure drop across the tube was recorded from 60 - 100ml/min for sets 1 and 2, and 10 - 100ml/min for set 3. The maximum flow rate was limited by the pump head capacity. Heptane was selected as the working fluid since the dynamic viscosity is lower than kerosene - permitting testing at higher Reynolds numbers (see appendix C for material properties). Fluid was pumped for 2 minutes at each flow rate and the final dP value was taken as the average of the data from the second minute.

4.2.4.4 Results

Table 4.5: Pressure drop data - EDM tubes 1 to 11

Tube ID	D (μm)	A (m^2)	Q (ml/min)	U_{avg} (m/s)	dP (bar)	τ_w (kg/ms ²)	u^* (m/s)	Re	λ	δ Re	$\delta \lambda$
EDM 1	482	1.82E-07	60	5.41	1.32	107.02	0.396	4375	0.0427	177	0.0034
			80	7.22	2.27	183.63	0.518	5834	0.0412	198	0.0027
			100	9.02	3.15	254.25	0.610	7292	0.0365	223	0.0021
EDM 2	453	1.61E-07	60	6.43	1.85	136.95	0.447	4769	0.0387	199	0.0031
			80	8.57	3.13	231.87	0.582	6358	0.0369	225	0.0025
			100	10.72	4.37	324.37	0.689	7948	0.0330	255	0.0020
EDM 3	472	1.75E-07	60	5.86	3.02	234.36	0.585	4554	0.0797	187	0.0064
			80	7.82	5.49	426.37	0.790	6072	0.0816	210	0.0054
			100	9.77	7.82	606.98	0.942	7590	0.0743	237	0.0044
EDM 4	439	1.51E-07	60	6.64	1.98	144.30	0.459	4845	0.0383	203	0.0031
			80	8.85	3.49	254.67	0.610	6460	0.0380	231	0.0026
			100	11.06	4.88	355.97	0.721	8075	0.0340	262	0.0021
EDM 5	500	1.96E-07	60	5.24	1.17	96.52	0.376	4304	0.0411	174	0.0032
			80	6.98	2.12	174.19	0.505	5739	0.0418	194	0.0027
			100	8.73	2.94	241.76	0.595	7174	0.0371	217	0.0021
EDM 6	437	1.50E-07	60	6.73	1.73	125.35	0.428	4878	0.0324	205	0.0026
			80	8.97	3.04	220.41	0.568	6504	0.0320	233	0.0022
			100	11.21	4.24	307.44	0.670	8131	0.0286	265	0.0018
EDM 7	575	2.60E-07	60	3.86	0.63	59.44	0.295	3697	0.0466	143	0.0035
			80	5.15	1.13	106.82	0.395	4929	0.0471	156	0.0029
			100	6.44	1.85	174.42	0.505	6162	0.0492	172	0.0026
EDM 8	575	2.60E-07	60	4.00	0.61	56.41	0.287	3763	0.0412	146	0.0031
			80	5.34	1.1	102.26	0.387	5017	0.0420	160	0.0026
			100	6.67	1.79	166.19	0.493	6271	0.0437	177	0.0024
EDM 9	574	2.59E-07	60	3.86	0.62	58.26	0.292	3697	0.0456	143	0.0035
			80	5.15	1.12	105.68	0.393	4929	0.0466	156	0.0029
			100	6.44	1.82	171.37	0.501	6162	0.0483	172	0.0026
EDM 10	581	2.65E-07	60	3.76	0.59	56.46	0.287	3646	0.0467	140	0.0035
			80	5.01	1.07	102.68	0.387	4862	0.0478	153	0.0029
			100	6.26	1.74	166.82	0.494	6077	0.0497	169	0.0027
EDM 11	576	2.61E-07	60	3.89	0.63	59.12	0.294	3710	0.0457	143	0.0035
			80	5.19	1.16	109.43	0.400	4947	0.0475	157	0.0029
			100	6.49	1.91	179.85	0.513	6183	0.0500	173	0.0027

Table 4.6: Pressure drop data - EDM tubes 12 to 14

Tube ID	D (μm)	A (m^2)	Q (ml/min)	Qdot (m^3/s)	U_{avg} (m/s)	dP (bar)	τ_w (kg/ms^2)	u^* (m/s)	Re	λ	δ Re	$\delta \lambda$
EDM 12	567	2.52E-07	10	1.67E-07	0.69	0.05	4.31	0.080	655	0.1064	132	0.0427
			20	3.33E-07	1.38	0.11	10.23	0.123	1310	0.0631	134	0.0128
			30	5.00E-07	2.07	0.21	18.81	0.166	1964	0.0515	137	0.0071
			40	6.67E-07	2.76	0.37	33.47	0.222	2619	0.0516	141	0.0055
			50	8.33E-07	3.45	0.65	59.59	0.296	3274	0.0588	147	0.0052
			60	1.00E-06	4.14	0.96	87.35	0.358	3929	0.0598	153	0.0046
			70	1.17E-06	4.83	1.35	123.17	0.425	4583	0.0620	160	0.0042
			80	1.33E-06	5.52	1.68	153.37	0.474	5238	0.0591	168	0.0037
			90	1.50E-06	6.21	2.01	183.31	0.519	5893	0.0558	177	0.0032
			100	1.67E-06	6.90	2.34	213.08	0.559	6548	0.0526	186	0.0029
EDM 13	509	2.03E-07	10	1.67E-07	0.82	0.08	6.29	0.096	714	0.1097	144	0.0441
			20	3.33E-07	1.64	0.18	14.74	0.147	1428	0.0643	146	0.0131
			30	5.00E-07	2.46	0.33	27.20	0.200	2142	0.0527	150	0.0073
			40	6.67E-07	3.28	0.55	45.94	0.260	2856	0.0501	156	0.0054
			50	8.33E-07	4.10	0.89	74.87	0.331	3570	0.0522	163	0.0047
			60	1.00E-06	4.92	1.48	123.75	0.426	4284	0.0600	171	0.0047
			70	1.17E-06	5.74	2.14	178.79	0.512	4998	0.0637	180	0.0045
			80	1.33E-06	6.56	2.70	225.46	0.575	5712	0.0615	190	0.0040
			90	1.50E-06	7.38	3.22	269.04	0.628	6426	0.0579	201	0.0035
			100	1.67E-06	8.20	3.72	310.95	0.676	7140	0.0543	212	0.0031
EDM 14	624	3.06E-07	10	1.67E-07	0.54	0.03	3.26	0.069	582	0.1290	117	0.0518
			20	3.33E-07	1.06	0.08	7.86	0.107	1135	0.0817	115	0.0166
			30	5.00E-07	1.58	0.14	14.41	0.145	1688	0.0677	116	0.0093
			40	6.67E-07	2.13	0.26	26.16	0.196	2269	0.0680	121	0.0072
			50	8.33E-07	2.67	0.41	41.96	0.248	2851	0.0691	125	0.0060
			60	1.00E-06	3.19	0.59	60.36	0.298	3404	0.0697	129	0.0052
			70	1.17E-06	3.71	0.82	83.36	0.350	3957	0.0713	133	0.0047
			80	1.33E-06	4.25	1.01	102.88	0.389	4539	0.0669	140	0.0040
			90	1.50E-06	4.80	1.20	121.76	0.423	5121	0.0622	146	0.0034
			100	1.67E-06	5.34	1.39	140.70	0.454	5703	0.0579	153	0.0030

Table 4.7: Pressure drop data - drawn tubes 1 to 7

Tube ID	D (μm)	A (m^2)	Q (ml/min)	Qdot (m^3/s)	U_{avg} (m/s)	dP (bar)	τ_w (kg/ms^2)	u^* (m/s)	Re	λ	δ Re	$\delta \lambda$
R 1	530	2.21E-07	60	1.00E-06	4.53	1.26	113.99	0.408	3900	0.0649	265	0.0083
			80	1.33E-06	6.04	2.32	206.56	0.550	5200	0.0661	334	0.0079
			100	1.67E-06	7.55	3.74	329.83	0.694	6500	0.0676	405	0.0078
R 2	530	2.21E-07	60	1.00E-06	4.53	1.32	115.13	0.410	3900	0.0655	265	0.0084
			80	1.33E-06	6.04	2.41	209.85	0.554	5200	0.0672	334	0.0081
			100	1.67E-06	7.55	3.9	338.73	0.704	6500	0.0694	405	0.0081
R 3	537	2.26E-07	60	1.00E-06	4.47	1.18	103.58	0.389	3871	0.0608	261	0.0077
			80	1.33E-06	5.95	2.15	188.61	0.525	5161	0.0622	329	0.0074
			100	1.67E-06	7.44	3.52	308.07	0.671	6451	0.0651	400	0.0075
R 4	527	2.18E-07	60	1.00E-06	4.64	1.24	106.94	0.395	3945	0.0582	271	0.0075
			80	1.33E-06	6.18	2.3	197.78	0.538	5259	0.0605	342	0.0073
			100	1.67E-06	7.73	3.8	326.61	0.691	6574	0.0640	416	0.0075
R 5	519	2.12E-07	60	1.00E-06	4.64	1.26	108.55	0.398	3945	0.0590	270	0.0076
			80	1.33E-06	6.18	2.35	201.97	0.543	5259	0.0618	341	0.0075
			100	1.67E-06	7.73	3.86	331.59	0.696	6574	0.0649	414	0.0076
R 6	517	2.10E-07	60	1.00E-06	4.75	1.33	113.11	0.407	3990	0.0588	275	0.0076
			80	1.33E-06	6.33	2.38	202.60	0.544	5320	0.0592	348	0.0072
			100	1.67E-06	7.91	3.74	317.84	0.682	6650	0.0594	423	0.0070
R 7	530	2.21E-07	60	1.00E-06	4.40	1.25	110.72	0.402	3842	0.0669	258	0.0085
			80	1.33E-06	5.87	2.24	197.98	0.538	5123	0.0673	324	0.0080
			100	1.67E-06	7.33	3.51	309.53	0.673	6403	0.0674	394	0.0077

Table 4.8: Pressure drop data - drawn tubes 8 to 11

Tube ID	D (μm)	A (m^2)	Q (ml/min)	Qdot (m^3/s)	U_{avg} (m/s)	dP (bar)	τ_w (kg/ms^2)	u^* (m/s)	Re	λ	δ Re	$\delta \lambda$
R 8	527	2.18E-07	10	1.67E-07	0.76	0.06	5.34	0.088	681	0.1081	142	0.0448
			19.5	3.25E-07	1.48	0.15	13.22	0.139	1328	0.0704	157	0.0164
			29	4.83E-07	2.21	0.29	25.12	0.192	1974	0.0604	180	0.0106
			40	6.67E-07	3.04	0.56	48.68	0.267	2723	0.0616	211	0.0091
			50	8.33E-07	3.81	0.95	82.57	0.348	3404	0.0668	243	0.0091
			59	9.83E-07	4.49	1.38	119.90	0.419	4017	0.0697	274	0.0090
			70	1.17E-06	5.33	1.93	167.46	0.495	4766	0.0692	314	0.0085
			80	1.33E-06	6.09	2.38	207.36	0.551	5502	0.0656	354	0.0079
			90	1.50E-06	6.85	2.83	246.35	0.601	6190	0.0616	392	0.0073
			100	1.67E-06	7.61	3.26	283.45	0.645	6877	0.0574	430	0.0067
R 9	528	2.19E-07	10	1.67E-07	0.77	0.06	5.20	0.087	683	0.1037	143	0.0430
			20	3.33E-07	1.53	0.14	12.38	0.135	1367	0.0617	159	0.0141
			30	5.00E-07	2.30	0.27	23.58	0.186	2050	0.0522	183	0.0090
			40	6.67E-07	3.07	0.48	41.54	0.247	2734	0.0518	212	0.0077
			50	8.33E-07	3.83	0.89	76.91	0.336	3417	0.0613	245	0.0083
			60	1.00E-06	4.60	1.37	119.04	0.418	4142	0.0659	283	0.0085
			70	1.17E-06	5.37	1.93	166.81	0.494	4832	0.0679	319	0.0084
			80	1.33E-06	6.14	2.39	207.17	0.551	5523	0.0645	357	0.0078
			90	1.50E-06	6.90	2.85	247.11	0.602	6213	0.0608	395	0.0072
			100	1.67E-06	7.67	3.26	282.73	0.644	6903	0.0564	433	0.0066
R 10	531	2.21E-07	10	1.67E-07	0.77	0.05	4.71	0.083	697	0.0938	145	0.0389
			20	3.33E-07	1.53	0.13	11.34	0.129	1395	0.0565	162	0.0129
			30	5.00E-07	2.30	0.25	21.79	0.179	2092	0.0483	187	0.0083
			40	6.67E-07	3.07	0.45	38.96	0.239	2789	0.0485	217	0.0072
			50	8.33E-07	3.83	0.85	73.20	0.328	3486	0.0584	250	0.0079
			60	1.00E-06	4.60	1.28	109.98	0.402	4184	0.0609	285	0.0078
			70	1.17E-06	5.37	1.79	154.01	0.475	4881	0.0627	322	0.0078
			80	1.33E-06	6.14	2.22	190.56	0.529	5578	0.0594	360	0.0072
			90	1.50E-06	6.90	2.63	225.75	0.575	6275	0.0556	399	0.0066
			100	1.67E-06	7.67	3.02	259.41	0.617	7042	0.0517	442	0.0060
R 11	539	2.28E-07	10	1.67E-07	0.72	0.06	4.95	0.085	654	0.1130	136	0.0468
			20	3.33333E-07	1.43	0.14	12.27	0.134	1308	0.0700	151	0.0158
			30	0.0000005	2.15	0.27	24.27	0.189	1982	0.0615	175	0.0105
			40	6.66667E-07	2.87	0.58	51.52	0.275	2643	0.0734	202	0.0107
			50	8.33333E-07	3.59	0.91	81.50	0.346	3304	0.0744	232	0.0099
			60	0.000001	4.30	1.33	118.62	0.417	3965	0.0751	264	0.0094
			70	1.16667E-06	5.02	1.85	165.34	0.492	4626	0.0770	297	0.0093
			80	1.33333E-06	5.74	2.29	204.73	0.548	5287	0.0730	332	0.0086
			90	0.0000015	6.45	2.71	242.95	0.597	6007	0.0684	371	0.0079
			100	1.66667E-06	7.17	3.12	279.20	0.640	6675	0.0637	407	0.0072

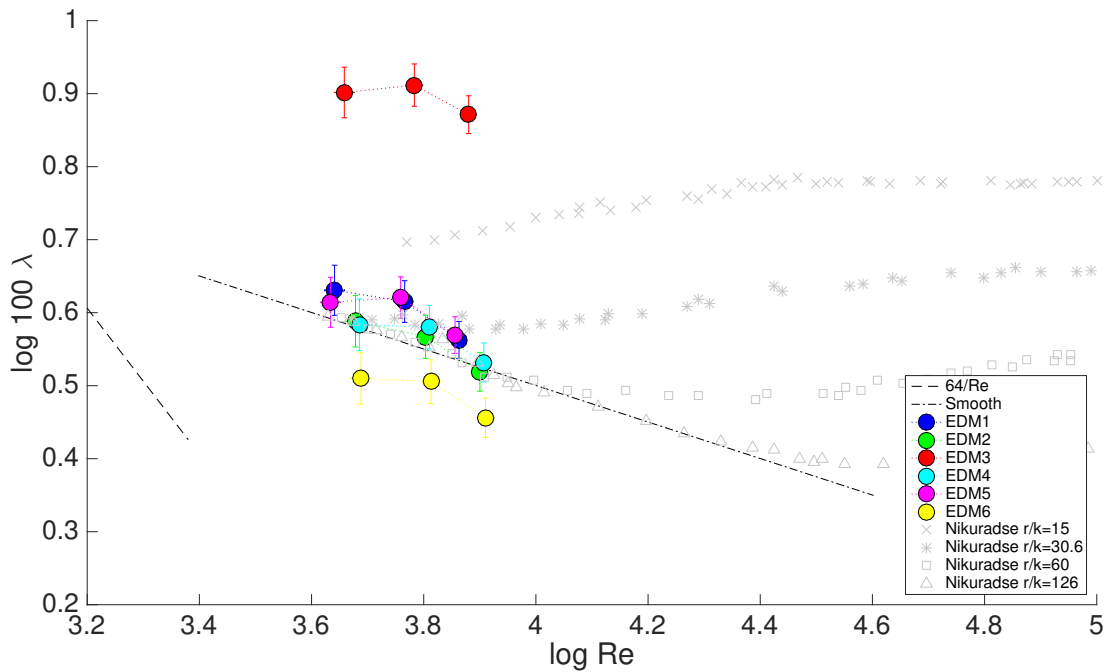


Figure 4.15: Friction factor data for EDM tubes 1 to 6 compared to the data of Nikuradse [8]

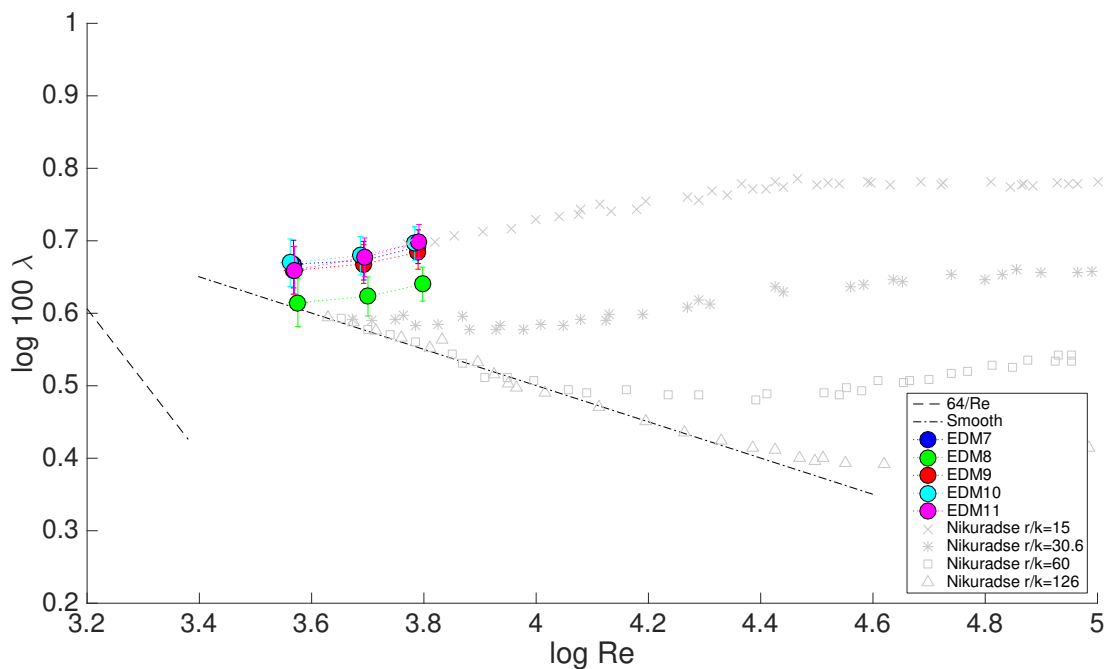


Figure 4.16: Friction factor data for EDM tubes 7 to 11 compared to the data of Nikuradse [8]

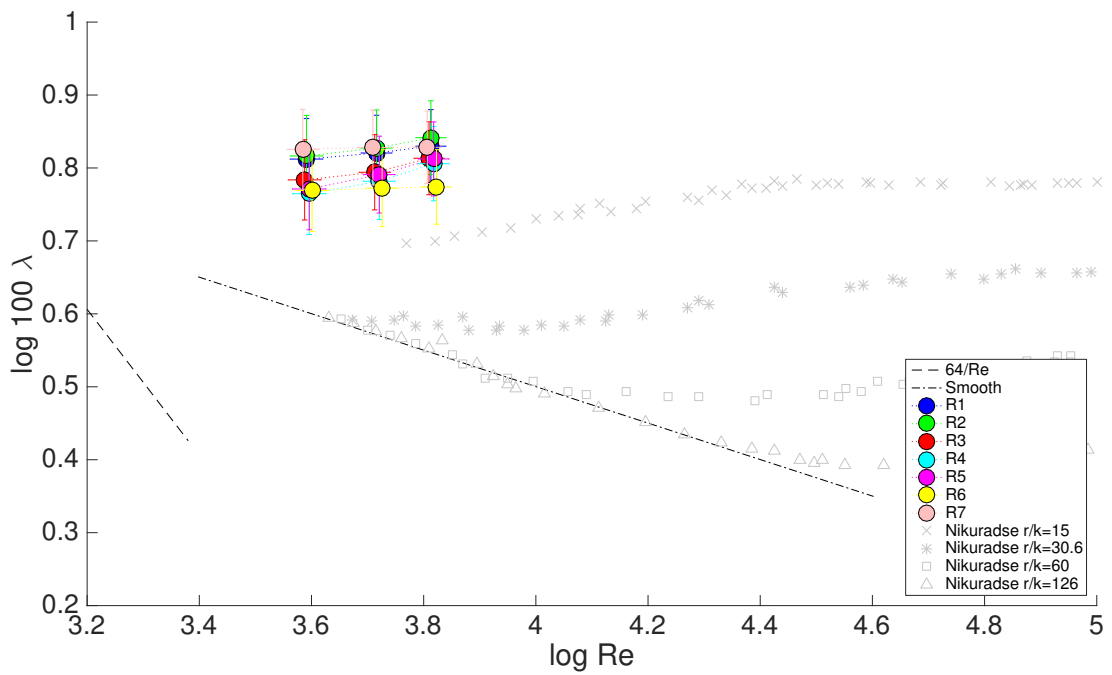


Figure 4.17: Friction factor data for drawn tubes 1 to 7 compared to the data of Nikuradse [8]

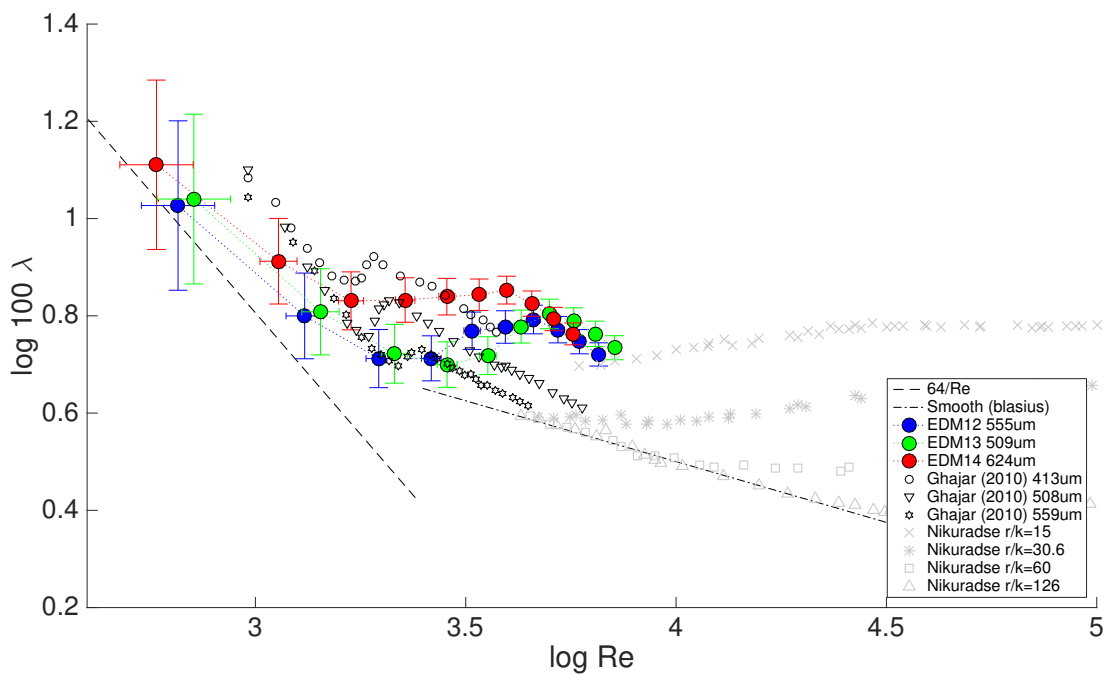


Figure 4.18: Friction factor data for EDM tubes 12 to 14 compared to the data of Nikuradse [8] and Ghajar [41]

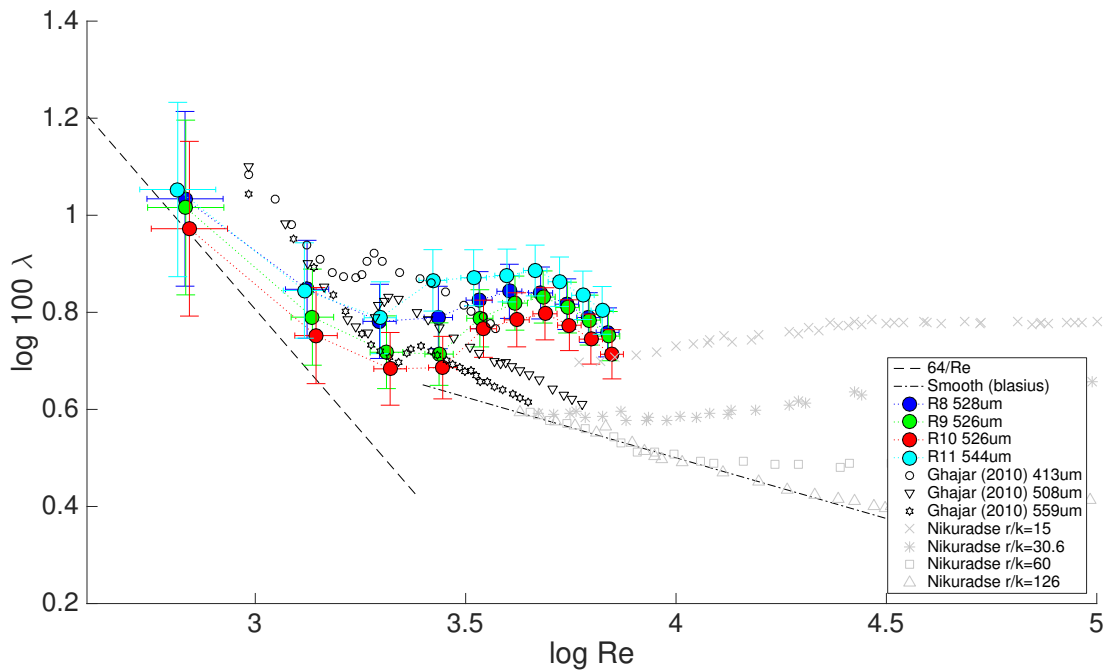


Figure 4.19: Friction factor data for drawn tubes 8 to 11 compared to the data of Nikuradse [8] and Ghajar [41]

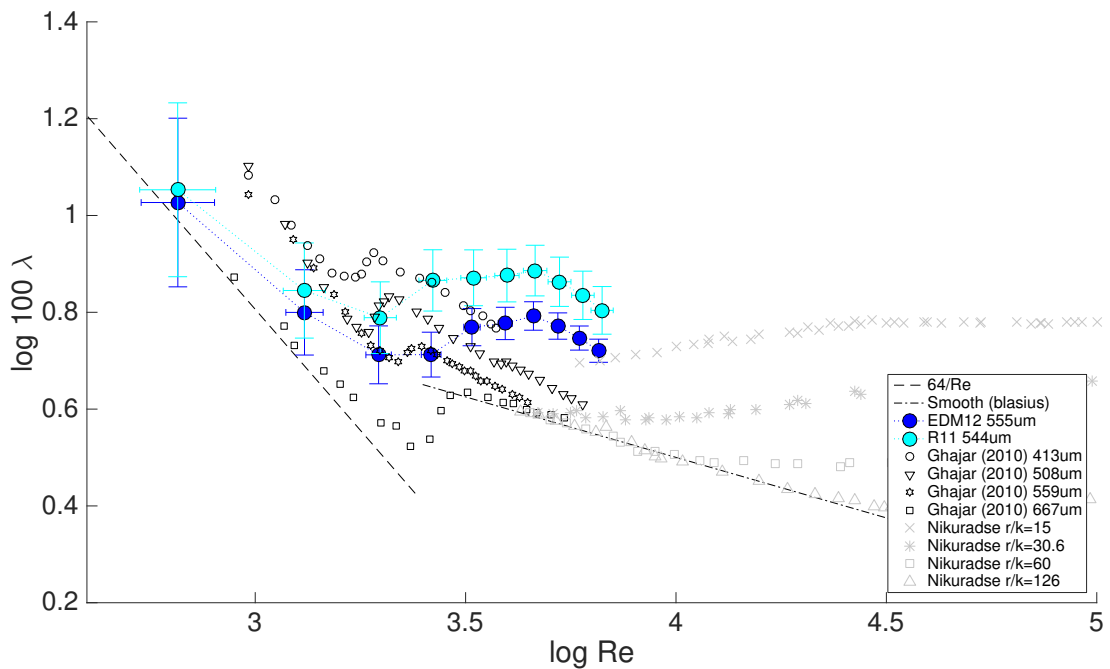


Figure 4.20: Comparison of drawn and EDM friction factors for set 3 tubes with similar diameters

4.2.4.5 Discussion

For the first sets of tubes, only three flow rates were considered, corresponding to the onset of fully turbulent flow ($Re > 4000$) to the maximum flow rate achievable with the available hardware. In later tests, the testing was extended to lower flow rates and the resolution of Re increased, in order to characterise the transitional behaviour of the tubes. It is an unfortunate consequence of the scale of the tubes that the fully rough condition could not be met. $100ml/min$ was the maximum flow rate that the particular model of HPLC pump used could provide. Some testing was attempted using kerosene and a pump with the capability of delivering several hundred litres per hour. However the actual range of Re was not extended - since due to the increased density and viscosity of kerosene, the pressure transducer reached the maximum upper limit at around the same maximum Reynolds number.

Drawn capillaries (R1-7)

This set of drawn capillary tubes all exhibit friction factors between 0.06 - 0.07. The data is tightly grouped, which is perhaps no surprise considering the large scale method of manufacture - resulting in consistent internal diameters and surface roughness. In contrast to hydraulically smooth conditions - where the dependence on Re is clear, these tubes appear to be not too far from the fully rough condition, since the variation in friction factor with Re is small. The shape of the profiles is consistent with the data for Nikuradse's largest sand grains, although the values are higher. The data suggests that the equivalent sand grain roughness (k_s) for these tubes would be in excess of $19\mu m$, somewhat higher than the average values measured by microscopy ($7.6\mu m (R_q)$), although similar to the maximum peak height. This is unsurprising since the surface features bear no resemblance to the tightly packed uniform sand grains used in Nikuradse's experiment. The relatively large error bars are associated with the increased uncertainty from the measurement of rough tube diameter from microscopy.

EDM Set 1 (Tubes 1-6)

Figure 4.15 shows that the EDM process was generally effective in producing a surface with less frictional resistance than the commercially available drawn tubing. EDM tubes 1,2,4 and 5 show a high degree of similarity in their shape and magnitude and lie close to the smooth curve of Blasius ($\lambda = \frac{0.3164}{Re^{0.25}}$). $\lambda \approx 0.035 - 0.004$ at the highest Re . Although it is not possible to quote an exact equivalent sand grain roughness since the fully rough condition was not met, these tubes would seem to have friction factors somewhat lower than Nikuradse's data for $\frac{r}{k} = 30$

(corresponding to $k_s < 8\mu m$). The results for EDM 3 and 6 present something of a mystery since the micrographs appear to show the tube wall to be consistent with the other tubes. In the case of EDM 3 the high friction factor could be a result of residue from the EDM process or swarf from the post EDM machining being lodged in the inside of the tube, producing an artificially high pressure drop. The result for EDM 6 lies below the Blasius smooth curve, suggesting some inaccuracy in the measurement.

EDM Set 2 (Tubes 7-11)

Tubes in set 2 exhibit slightly higher friction factors than those in set 1 ($\lambda \approx 0.0045 - 0.005$ at the highest Re), although they still lie below the values for the drawn capillaries. The increase in friction factor is reflected in the change in slope of the profiles, which instead of progressing downwards parallel to the smooth limit, trend slightly upwards. The consistency between the tubes is excellent, and shows a clear improvement over set 1. The set lies at the very lower end of the $\frac{r}{k} = 15$ data of Nikuradse, and could almost be a continuation of it, suggesting these tubes have $k_s \approx 19\mu m$. The difference between EDM set 1 and 2 is surprising, since a comparison of the micrographs yields no obvious differences. However, the micrographs only represent a single sample taken from one end and cannot be considered completely representative of the entire tube.

Set 3 (EDM 12-14, R8-11)

Figures 4.18 - 4.20 show the friction factors across the transitional Reynolds number range for EDM tubes 12 to 14 and drawn tubes 8 to 11. Firstly, the difference in the friction factors between the two sets of tubes is quite small. It is unclear why the EDM process was apparently less effective than in the first instances. Conversely for the drawn tubes, the friction factors in the third set are lower than in previous cases. It is interesting to note that the two sets of tubes, although machined through different methods, ended up with similar roughnesses. At first this would seem wholly unfortunate, but the deposition results for tubes with similar friction factors obtained through different means should be a robust test of the theory of a dependence on λ .

EDM and drawn capillaries of similar diameters are compared in figure 4.20, along with the data of Ghajar et al [41], who conducted a detailed study of the transitional friction factor behaviour for stainless steel tubes ranging from 337 to 2083 μm . The roughness of similar, but larger tubes used in their study was

$0.4\mu m$. They found that the transition from laminar to turbulent flow shifted towards lower Reynolds numbers with decreasing tube diameter, and the range of transition reduced. The friction factor profiles of the tubes in this study compare quite favourably to those of Ghajar. The departure from the smooth line ($\frac{64}{Re}$) occurs somewhere in between Ghajar's $559\mu m$ and $667\mu m$ tubes, but the range of transition appears much wider in this case. The completion of transition to turbulence for the tubes tested in this study is approximately 4000, considerably higher than 2500 in the case of Ghajar. The shape of the profiles is quite different from the data of Nikuradse, which prohibits an estimation of the equivalent sand-grain roughness. It would appear that both sets of tubes would have $\frac{r}{k} > 15$.

Summary

EDM tubes generally have a lower friction factor than the drawn capillary tubes. The difference was most evident for the first set of EDM tubes (1 to 6).

The first set of EDM tubes had approximate equivalent sandgrain roughness heights of less than $8\mu m$, the second set around $19\mu m$. Rough tubes 1 to 6 had friction factors that exceeded the maximum relative roughness tested by Nikuradse.

Transitional friction factors profiles for later tests compared well with the pressure drop data from similarly sized mini tubes of Ghajar et al [41]. The transition to turbulence occurred later than in their experiments, and the transitional range was wider overall. The departure from the laminar friction law $\lambda = \frac{64}{Re}$ occurred somewhere in between the $667\mu m$ and $559\mu m$ tubes of Ghajar.

4.2.5 Heat transfer experiments

To characterise each tube with respect to heat transfer, simple measurements were taken of the tube external wall temperature prior to the deposition tests.

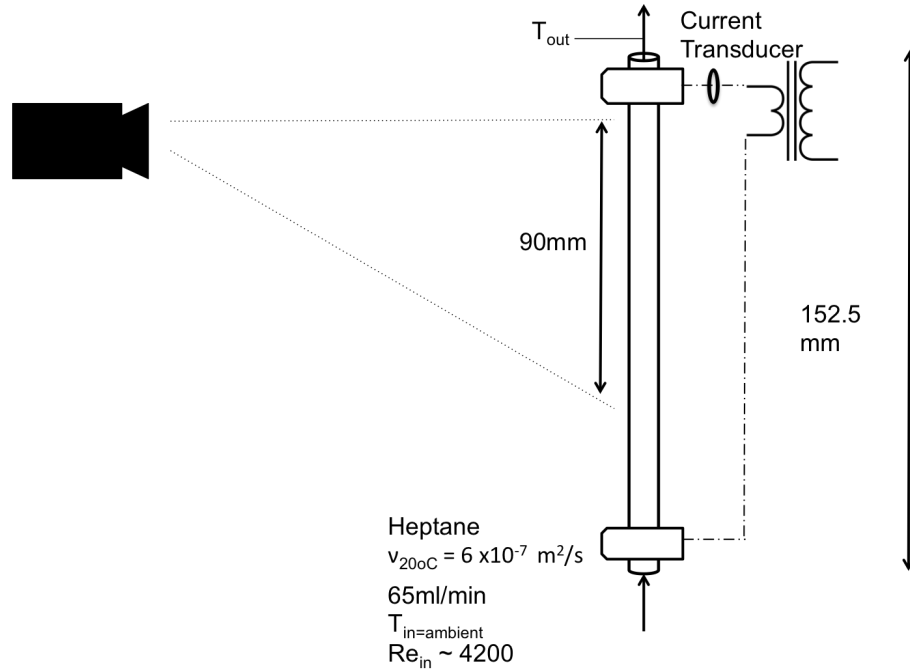


Figure 4.21: Heat transfer measurement apparatus

4.2.5.1 Apparatus

The HiReTS device was modified slightly from the original configuration. The test capillaries were clamped between two bus bars and heat was applied to the tube via direct resistance heating. The tube external wall temperature was measured with a FLIR A615 infra-red camera, rather than the original scanning pyrometer. The output from the thermal camera was verified against a black body source (emissivity = 0.95) between 300 - 600°C. The camera was accurate to within 2% at the highest temperatures (calibration data can be found in appendix D). Data from the camera was recorded in LabView. The thermal camera had the significant advantage of being able to record temperatures simultaneously along the tube length, rather than having to scan a pyrometer to discrete locations. To facilitate the thermography, the tubes were painted by aerosol with two coats of high temperature matte black paint (Rust-oleum 7778). The fuel exit temperature was recorded with a k-type thermocouple located within the exit reducer. The current supplied to the bus bars was recorded with a current transducer, and

controlled via a PID controller in LabView. The fuel flow rate was verified using a graduated measuring cylinder (accurate to $\pm 0.1ml$).

4.2.5.2 Sources of uncertainty

Table 4.9: Sources of uncertainty - heat transfer experiments

Measurement	Instrument	Uncertainty
External wall temperature	FLIR A615 thermal cam	$\pm 2^\circ C$ or 2%
Fuel exit temperature	K type thermocouple	$\pm 2.2^\circ C$ or $\pm 0.75\%$
Bus bar current	current transducer	$\pm 1.5\%$

4.2.5.3 Method

In an effort to minimise the risk of deposit formation which could affect subsequent deposition testing, the tests were kept brief, and high grade heptane was used (purity $>90\%$). Temperature profiles were recorded and averaged over 10 seconds at the end of a 5 minute warm up period to ensure the rig had reached close to steady state conditions. Current was applied from 40 to 60A and the fuel flow rate was fixed at $65ml/min$. The test conditions are shown in figure 4.21. Results are shown in tabulated form in Appendix E.

4.2.5.4 Results

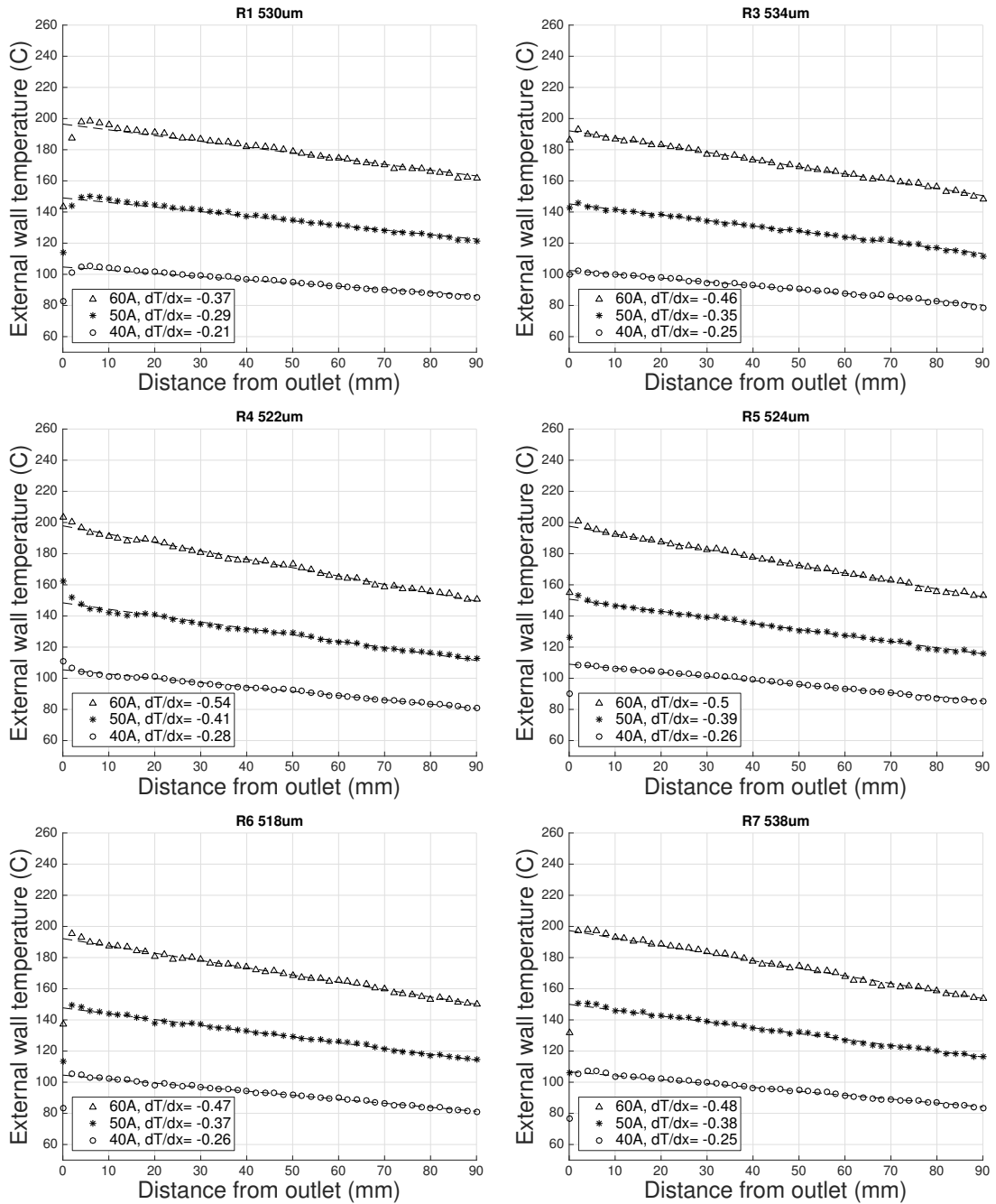


Figure 4.22: Wall temperatures, drawn tubes 1-7

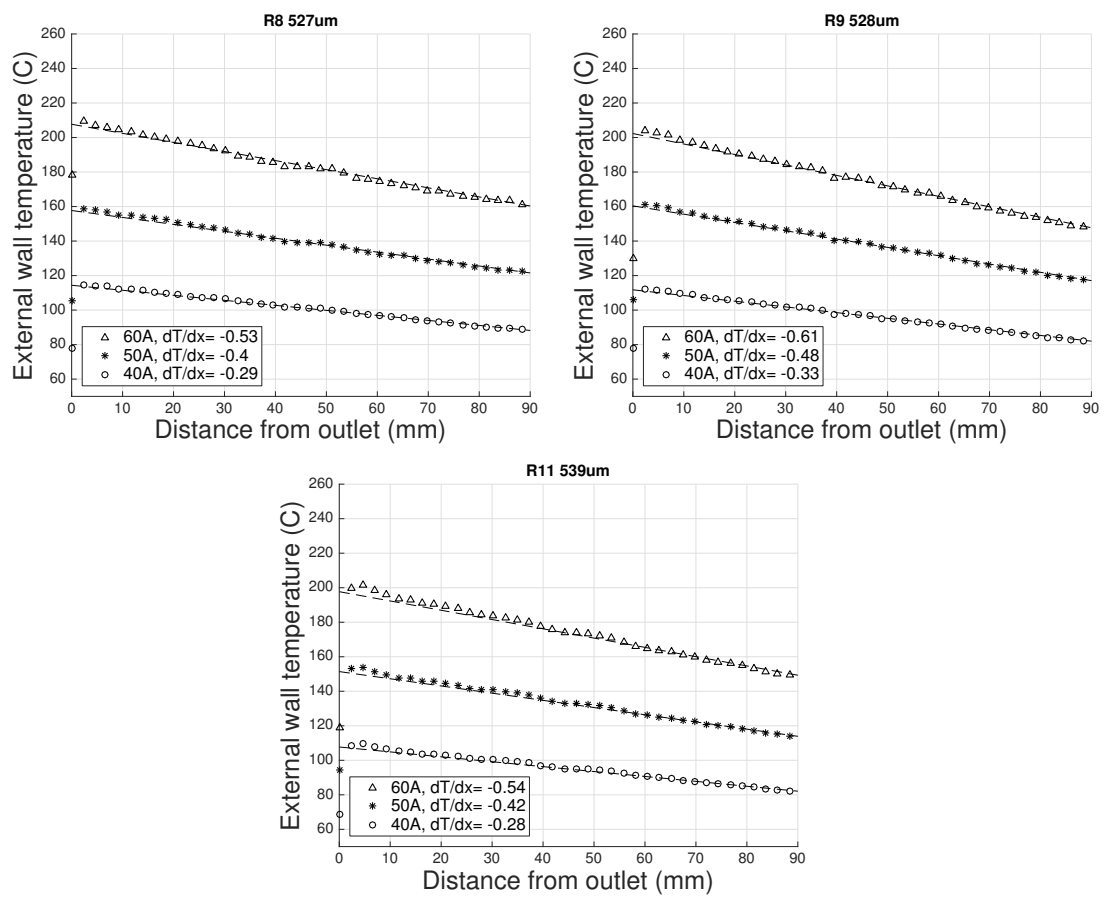


Figure 4.23: Wall temperatures, drawn tubes 8, 9, 11

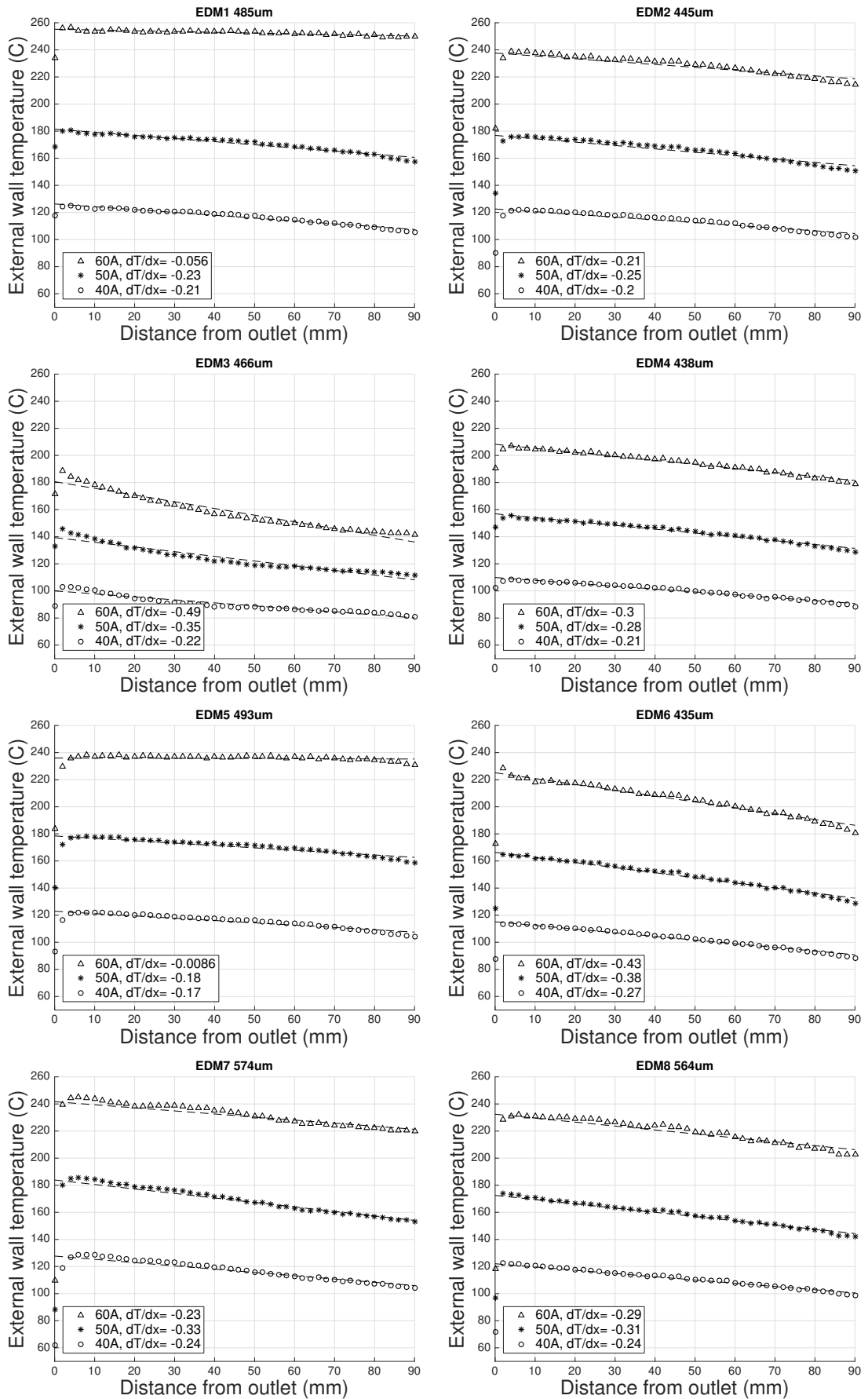


Figure 4.24: Wall temperatures EDM tubes 1-8

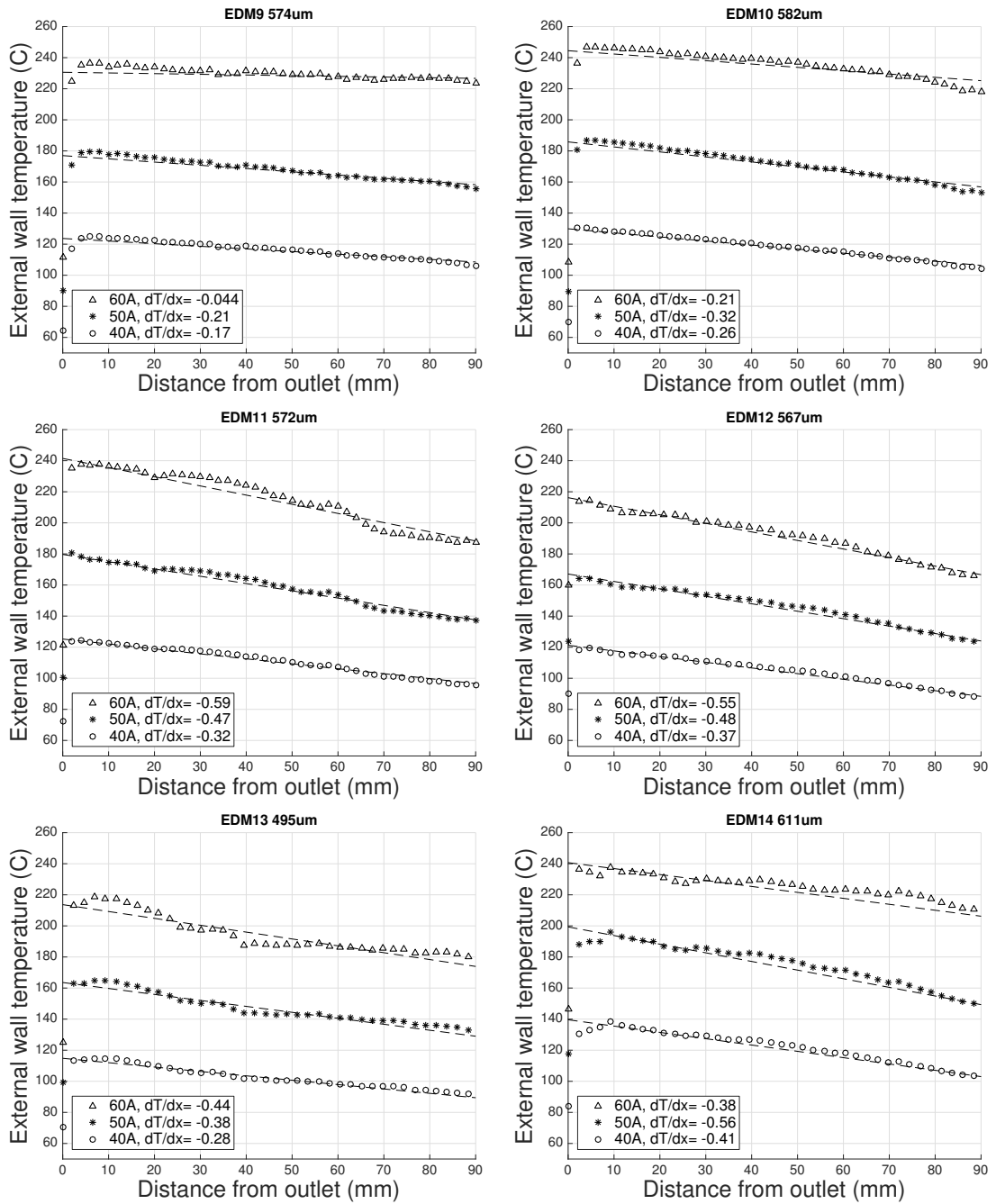


Figure 4.25: Wall temperatures, EDM tubes 9-14

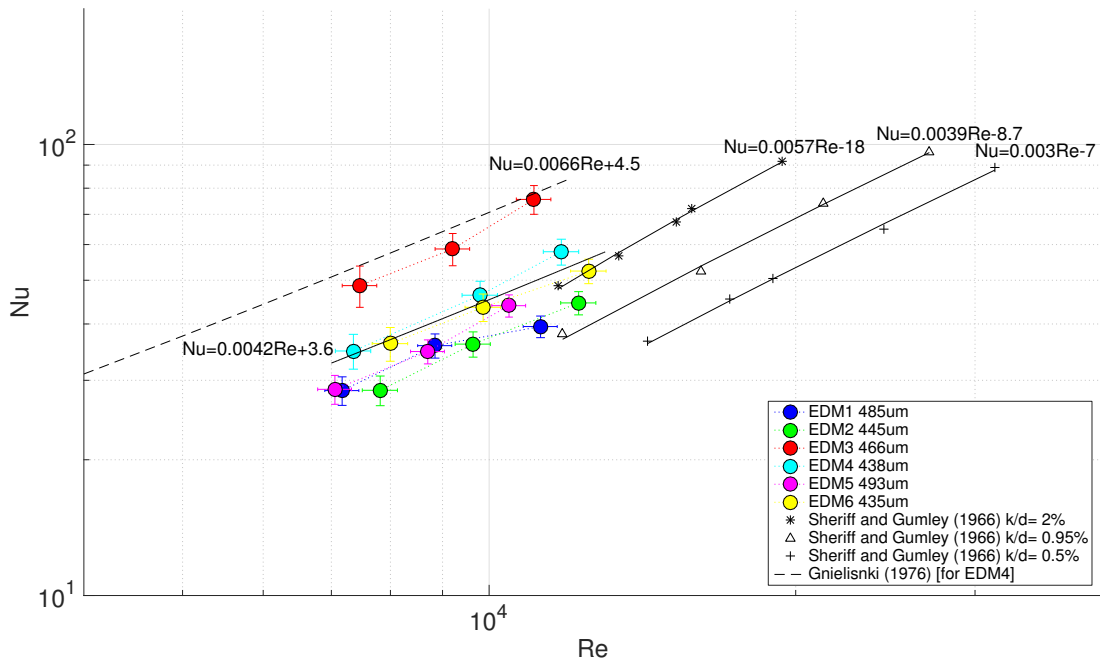


Figure 4.26: Nu vs Re , EDM tubes 1-6

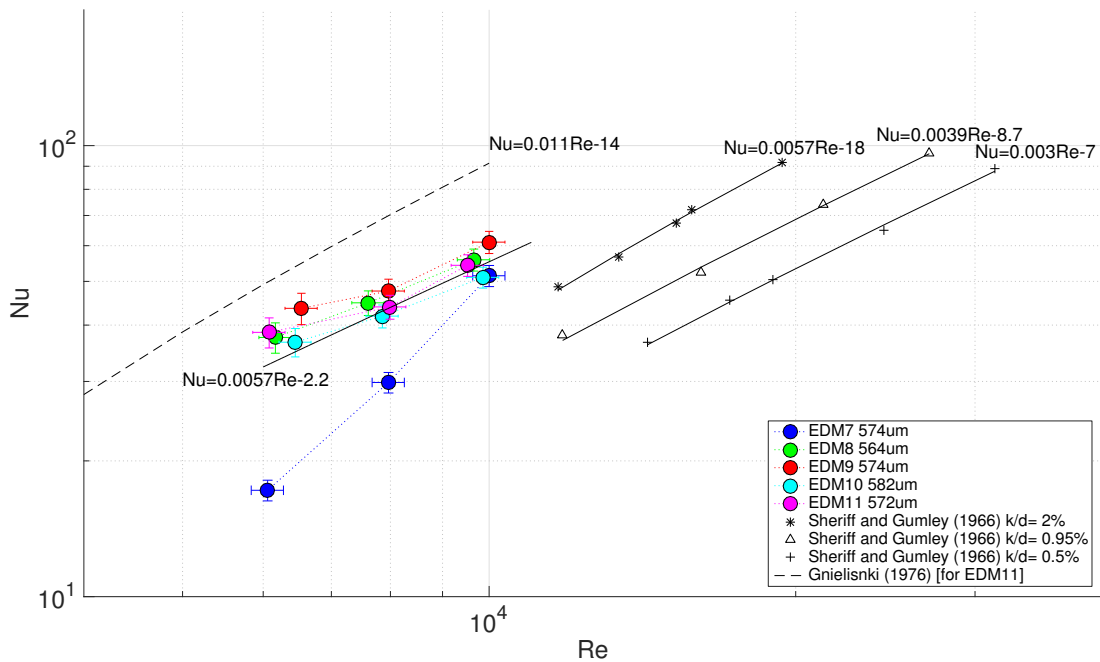


Figure 4.27: Nu vs Re , EDM tubes 7-11

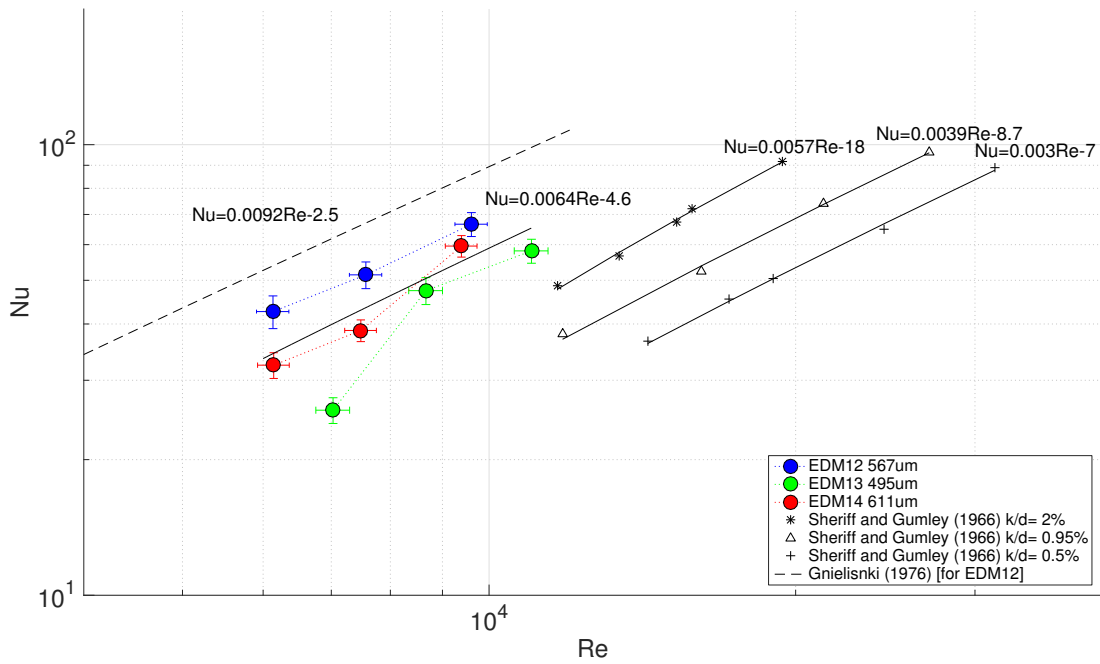


Figure 4.28: Nu vs Re , EDM tubes 12-14

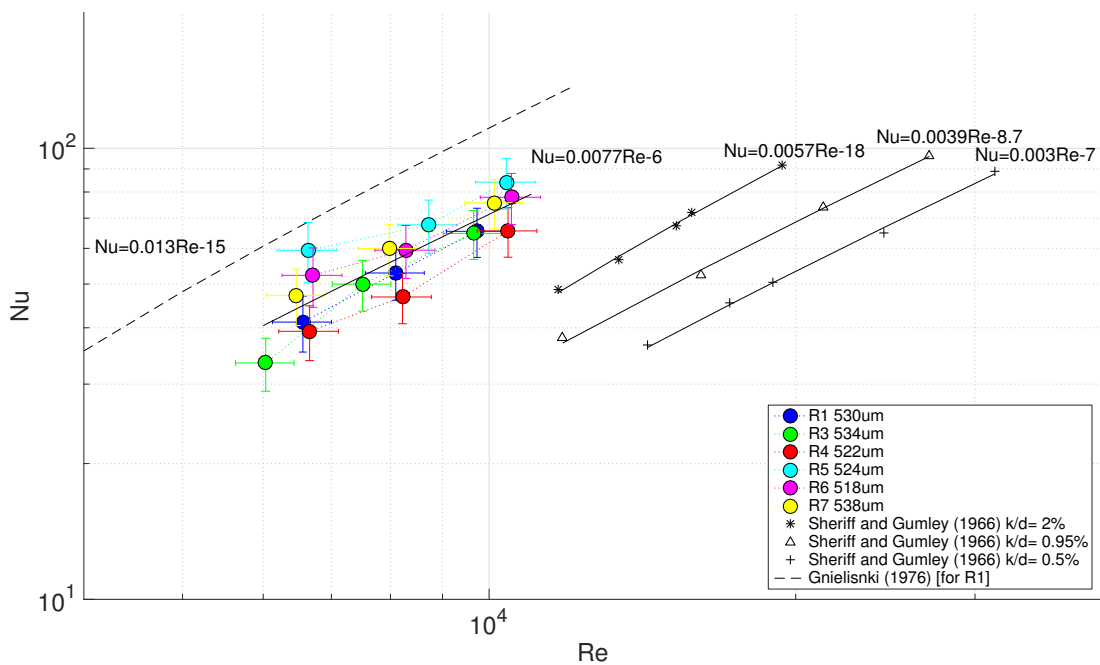


Figure 4.29: Nu vs Re , drawn tubes 1-7

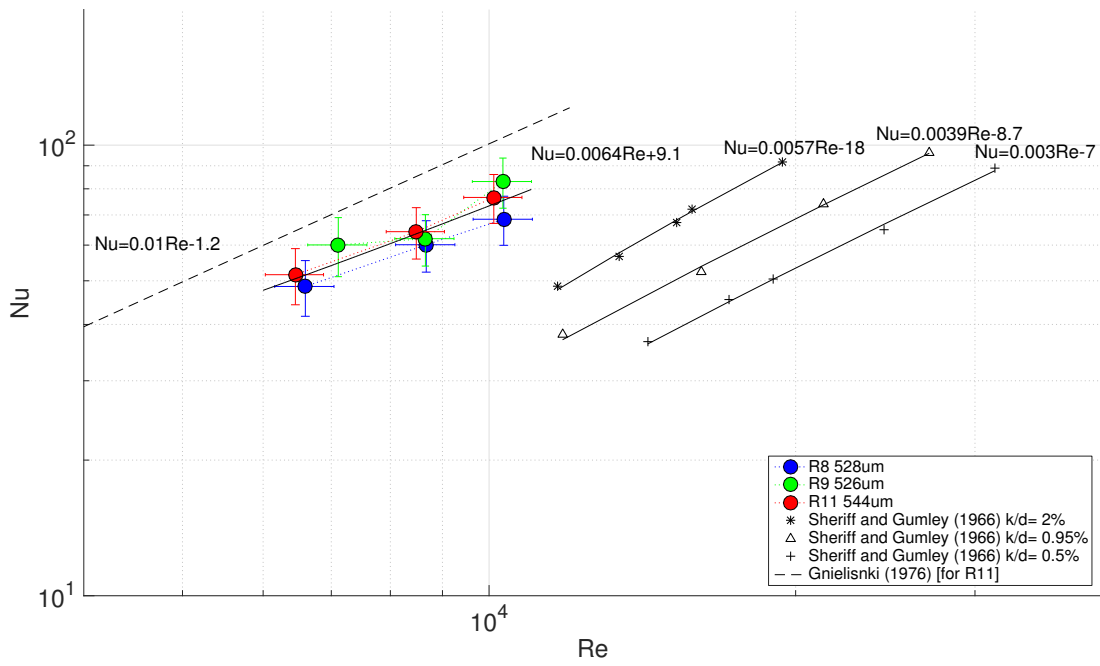


Figure 4.30: Nu vs Re , drawn tubes 8,9,11

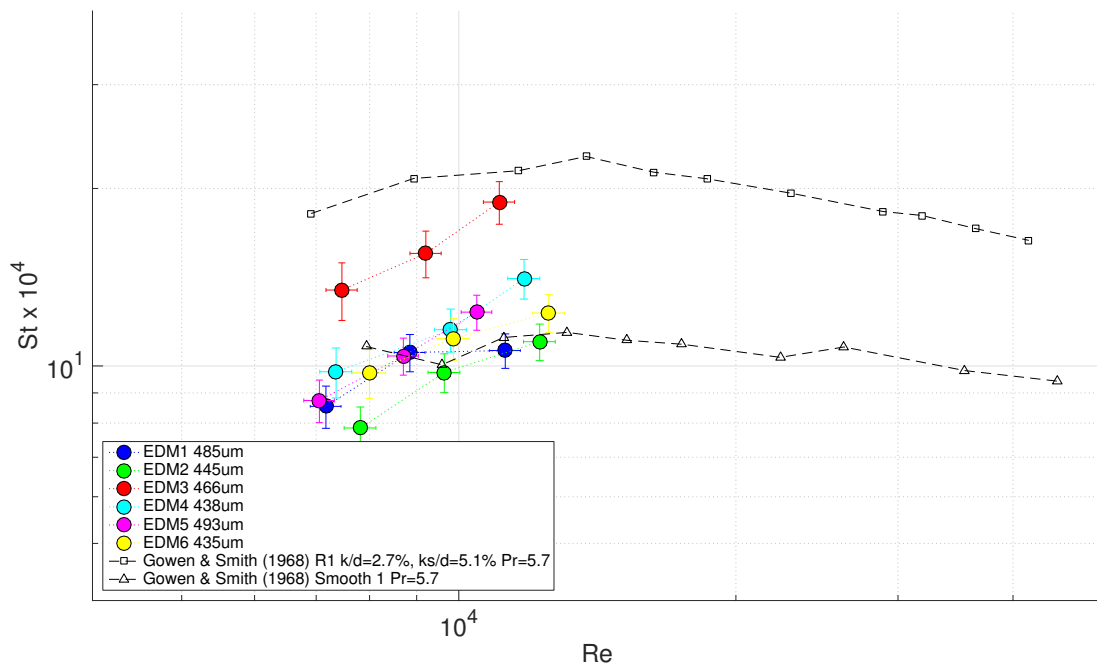


Figure 4.31: St vs Re , EDM tubes 1-7

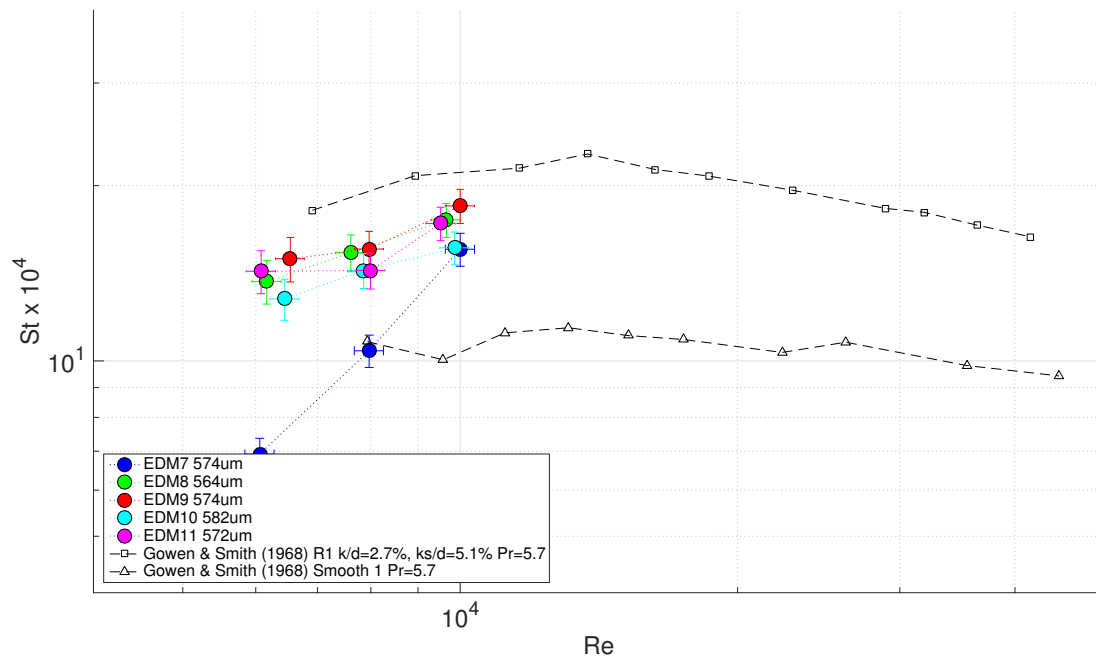


Figure 4.32: St vs Re , EDM tubes 7-11

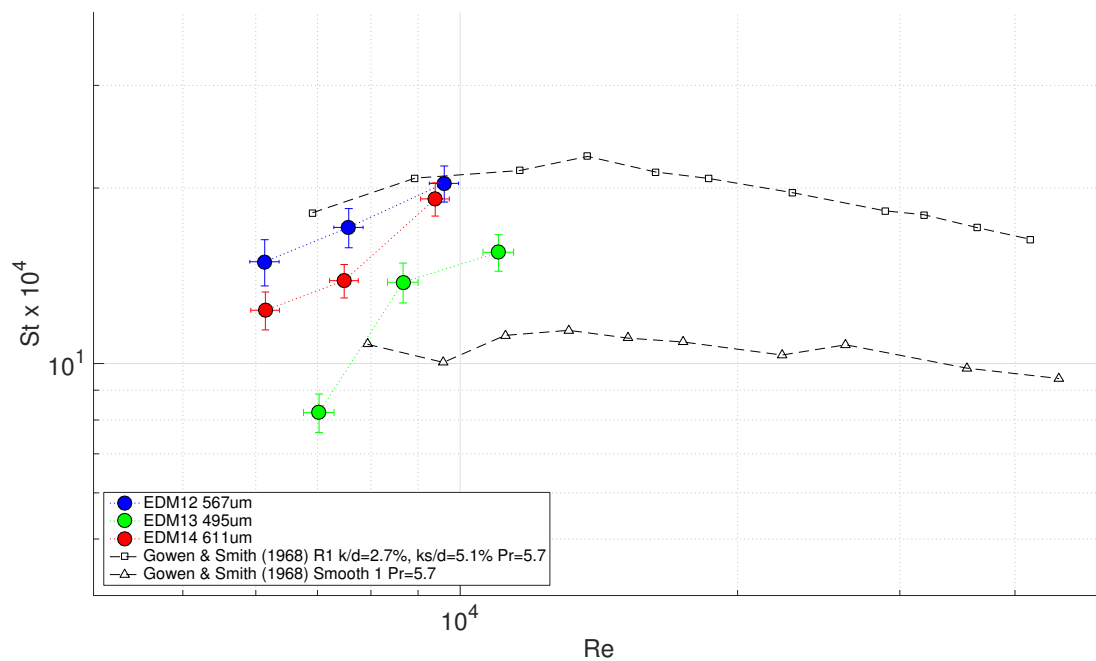


Figure 4.33: St vs Re , EDM tubes 12-14

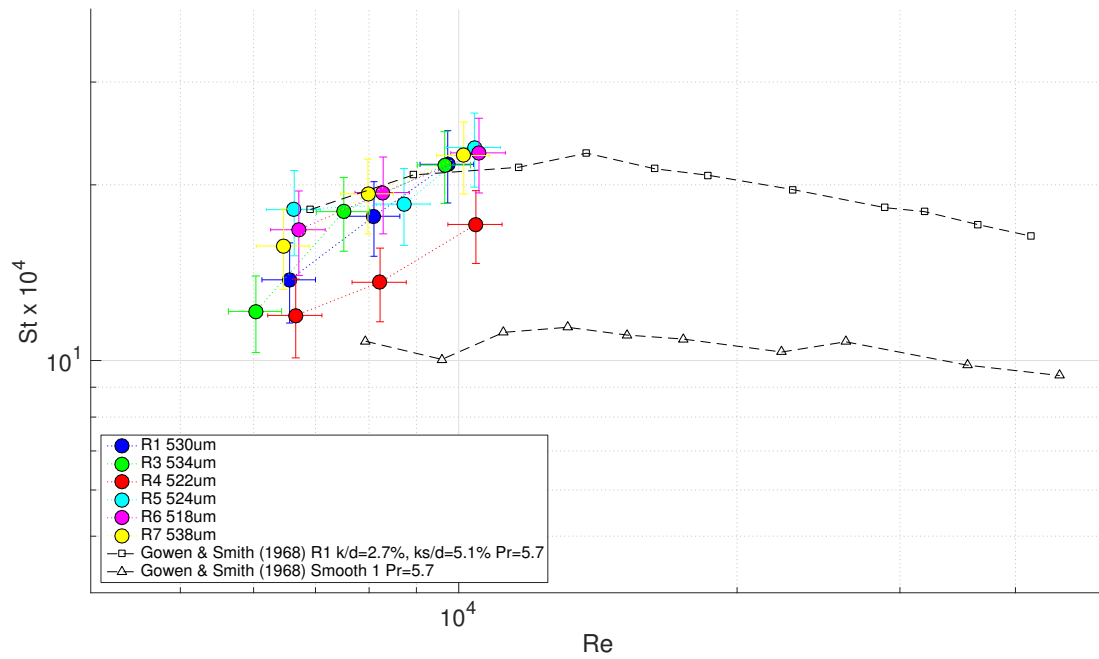


Figure 4.34: St vs Re , drawn tubes 1-7

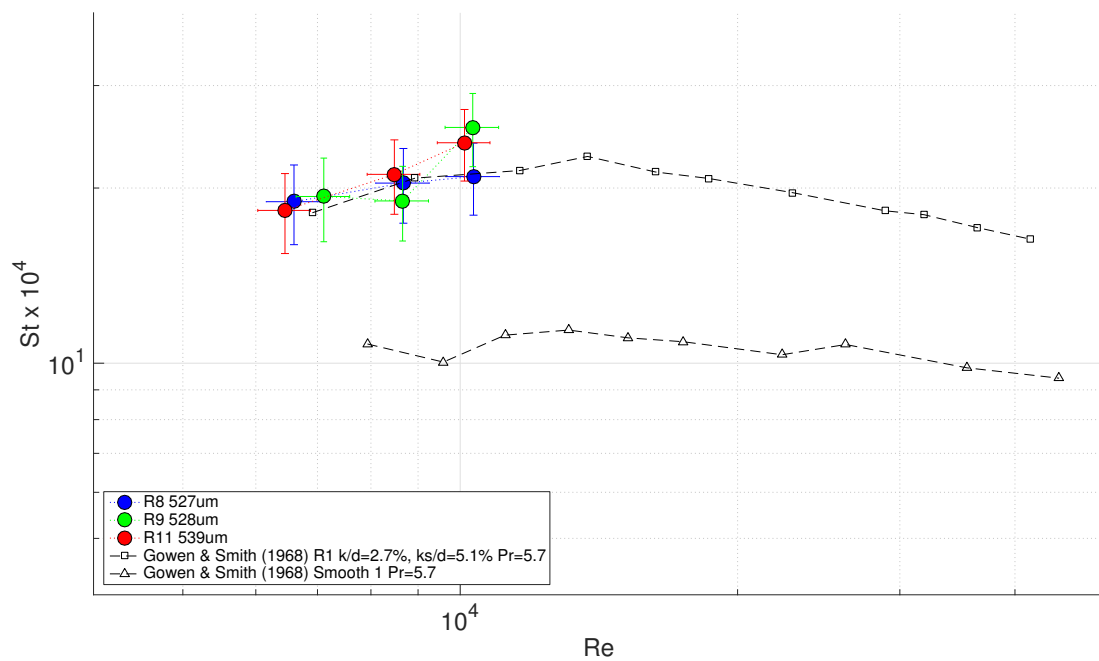


Figure 4.35: St vs Re , drawn tubes 8,9,11

4.2.5.5 Discussion

The heat transfer characteristics of each tube was assessed by measuring the external wall temperature and fuel exit temperature for constant heat rates ranging from around 80 to 220W (corresponding to bus bar currents of 40 to 60A). The heat rate derived from the current and electrical resistance of the tube is somewhat higher than the amount required to heat the fuel to the average inlet and outlet temperature according to $Q = \dot{m} C_p \Delta T$. This reflects the combined contributions to heat loss from natural convection and radiation on the outer tube surface and the heat lost by conduction in the bus bars. The contributions to the heat loss from natural convection and radiation were negligible ($< 1\%$ for the highest wall temperatures considered), suggesting that most of the additional heat was lost to the bus bars. The heat loss due to natural convection and radiation was calculated using a value of external wall temperature at the top of the range typically encountered.

The heat flux is expressed by;

$$q_s = \frac{\dot{m} C_p \Delta T}{\pi D_i L} \quad (4.2.12)$$

and the local convection coefficient (h_o) at the tube exit was calculated according to;

$$h_{exit} = \frac{q_s}{T_{sexit} - T_{bulkexit}} \quad (4.2.13)$$

The temperature at the inner surface of the tube was calculated by applying Fourier's law in the radial direction;

$$q_{local} = -2 \pi L k_{ss} \frac{(T_{ext} - T_{int})}{\ln\left(\frac{r_{ext}}{r_{int}}\right)} \quad (4.2.14)$$

giving;

$$t_{int} = t_{ext} - \frac{q \ln\left(\frac{r_{ext}}{r_{int}}\right)}{2 \pi k_{ss} L} \quad (4.2.15)$$

The difference in internal and external wall temperatures was around $2^\circ C$.

In the HiReTS device, heat is generated by direct resistance heating and is therefore iso-flux ($q_s = \text{constant}$). Considering the energy balance across a control volume in the tube;

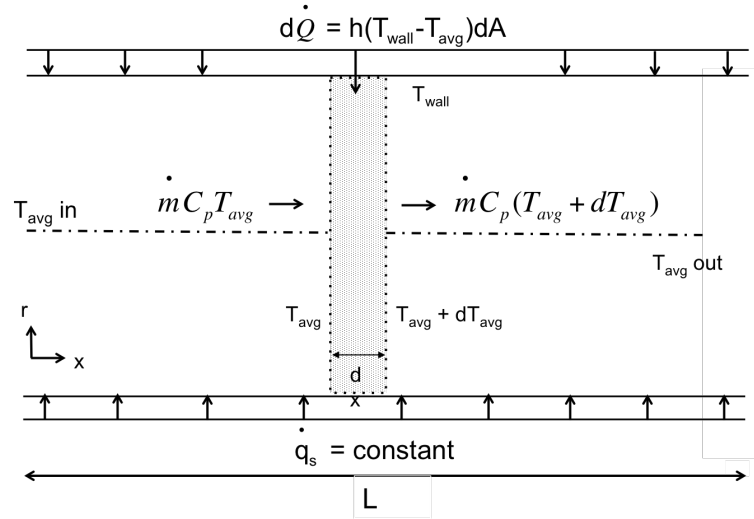


Figure 4.36: Energy balance across a differential control volume for tube flow

For the iso-flux condition, q_s does not vary with axial position, thus;

$$\frac{dT_m}{dx} = \frac{q_s \pi D}{\dot{m} C_p} = \frac{\pi D}{\dot{m} C_p} h (T_{int} - T_{avg}) \neq f(x) \quad (4.2.16)$$

Integrating from $x = 0$;

$$T_m(x) = T_{m,i} + \frac{q'_s \pi D}{\dot{m} C_p} x \quad (4.2.17)$$

Drawn tubes

Figures 4.22 - 4.23 show the wall temperature data for drawn capillaries. The profiles have been fitted with linear trendlines and the gradients are shown for reference. The profiles are consistent, and show the increase in q_s by the increase in $\frac{dT}{dx}$ with increasing current. The ratio of $\frac{T_{wavg}}{T_f}$ is between 1.2 to 1.35 for all tubes.

EDM tubes

The EDM tubes display slightly different behaviour. $\frac{dT}{dx}$ was typically lower, except for EDM 11-13, where the wall temperature profile were more similar to the drawn tubes. Tubes 1,2,5,7 and 10 show a notable decrease in $\frac{dT}{dx}$ for the highest heating power, which seems to coincide with external wall temperatures

close to or exceeding 240°C . This signals a departure from the iso flux condition to a constant surface temperature condition - indicating that the fluid may have reached the saturation temperature, T_{sat} with phase change occurring locally at nucleation sites at the wall.

The vapour pressure of heptane can be estimated using the Antoine equation;

$$\log_{10}P = A - (B/(T_f + C)) \quad (4.2.18)$$

with constants for heptane, $A = 4.028$, $B = 1268.6$, $C = -56.199$ (valid for $299 < K < 372$). The resulting saturation temperature at 20bar, is calculated to be 250°C , which is very close to the maximum external wall temperatures observed for the EDM tubes with $\frac{dT}{dx}$ trending towards zero. This effect, although not observed on all tubes is reflected in the higher ratios of $\frac{T_{wavg}}{T_f}$. The increased wall temperature shows quite clearly the reduced heat transfer capability of the smoother wall.

Nusselt number

The heat transfer coefficient is expressed in non dimensional form as the Nusselt number ($Nu = \frac{hD}{k_f}$), with k_f , the thermal conductivity of the fluid evaluated at the film temperature ($T_{film} = \frac{T_{int} + T_{avg}}{2}$). Nu is plotted against Re in figures 4.26 - 4.30 with trend lines of the form $Nu = m Re + C$. The enhancement of roughness on heat transfer is demonstrated by the increase in the gradient of the lines. Drawn capillaries 1 - 7 have $m = 0.0077$ and for R8,9 and 11 the gradient is slightly lower, $m = 0.0064$. EDM tubes 1 - 6 have $m = 0.0042$, which increases to $m = 0.0057$ for EDM 7 to 11. The gradient increases again for EDM 12 to 14 to $m = 0.0064$, which indicates similar heat transfer capability to R8 - 11. The results are compared to the data of Sheriff and Gumley [29], who tested annular heater sections with 2D wire roughness. Their results for relative roughnesses of 0.5, 0.95 and 2% are shown. The trend of increasing gradient is consistent with the wire roughness results. The fits for EDM tubes 1 to 11 compare well to the 2% roughness in [29] - in fact the value of m for EDM 7 - 11 is in exact agreement with the 2% data. EDM 1 - 6 lie somewhere in between the 0.95% and 2% lines. This would suggest that the EDM tubes have a roughness of approximately $10\mu\text{m}$, which seems large in comparison to the micrographs, but is similar to the values of sand grain roughness indicated by the pressure drop tests. The largest wire diameter ($\frac{k}{d} = 2\%$) tested by Sheriff and Gumley had a fully developed friction factor $\lambda \approx 0.02$, slightly lower than the smoothest tubes considered in this study.

The previously noted anomalous nature of EDM 3 is also displayed in the wall temperature data and values of Nusselt number.

The widely used correlation of Gnielinski [97] is also shown for comparison. The measured friction factors for representative tubes in each set were used in the calculation and the fit was extrapolated to cover a wider range of Re . The correlation consistently over predicts Nu for each set of tubes and the data of Sheriff and Gumley, although the prediction is qualitatively similar.

The data for each set was fitted to the form $Nu = C Re^m Pr^n$. Nu and Pr was evaluated at T_{film} . The values of C and the exponents m and n are tabulated in table 4.11, along with R^2 values indicating the quality of fit, which is acceptable.

Table 4.10: Correlation for Nu vs Re . Valid for $6000 < Re < 10000$

Set	C	m	n	R^2	$\lambda_{max(avg)}$
EDM 1-6	8.8E-07	1.7	1.2	0.8	0.034
EDM 7-11	1.72E-05	1.5	0.10	0.86	0.048
SA 1-7	4.04E-04	1.3	0.25	0.77	0.065

Stanton number

Profiles of Stanton number ($St = \frac{Nu}{Re Pr}$) are plotted against Reynolds number in figures 4.31 - 4.34. The data of Gowen and Smith [30] for a smooth and rough tube with water ($Pr = 5.7$) is shown for comparison. Their roughness was created by soldering a mesh screen to the internal wall. For the rough tube, the absolute relative roughness was $\frac{k}{D} = 0.027$ and the equivalent sand grain roughness of the surface was higher, $\frac{k_s}{D} = 0.05$. Unfortunately most data spans much higher Reynolds numbers than the range possible in this study. The EDM tubes compare reasonably well to the smooth tube profile of Gowen and Smith, although the rate of increase in St with Re seems more extreme. The observed increase in λ for EDM 7 - 11 and EDM 12 - 14 is displayed as a shift in the profile towards the rough tube data. The characteristic of St vs Re plots is a mild inflexion in St just before the flow becomes fully rough - which is apparent in the rough tube example data. The profiles for different relative roughnesses then reduce with Re and converge to a single line. The drawn capillaries display reasonable similarity with the profile for $\frac{k}{D} = 2.7\%$, suggesting that the tubes have an absolute roughness height of approximately $14\mu m$. When measured by microscopy, the roughness

features of the drawn capillaries were found to be between 10-20 μm .

Summary

The effect of increasing roughness on heat transfer was shown by the axial temperature rise, $\frac{dT}{dx}$, Nu and St . The dimensionless heat transfer coefficients displayed the anticipated increase with higher relative roughness. Some EDM tubes appeared to show boiling at the tube wall for the highest heat fluxes - made evident by a decrease in $\frac{dT}{dx}$. This observation highlights the improved heat transfer capability of rough walls.

The data compared favourably with data from the literature of 2D and 3D roughness on heat transfer. Values of St for the drawn capillary tubes matched the values for a tube of similar relative roughness. Gradients of Nu vs Re showed the same trend as in the literature and were quantitatively similar.

The data was fitted to the form $Nu = C Re^m Pr^n$ and a reasonable fit was achieved. The effect of roughness was shown by an increase in C and a decrease in m .

4.2.6 Deposition experiments

While the pressure drop and heat transfer measurements provide some fundamental measures of roughness, ultimately the severity of fuel deposition over the different surfaces is of primary interest. The test conditions were designed to be as close as possible to the original HiReTS method, however there were some significant differences which are outlined below.

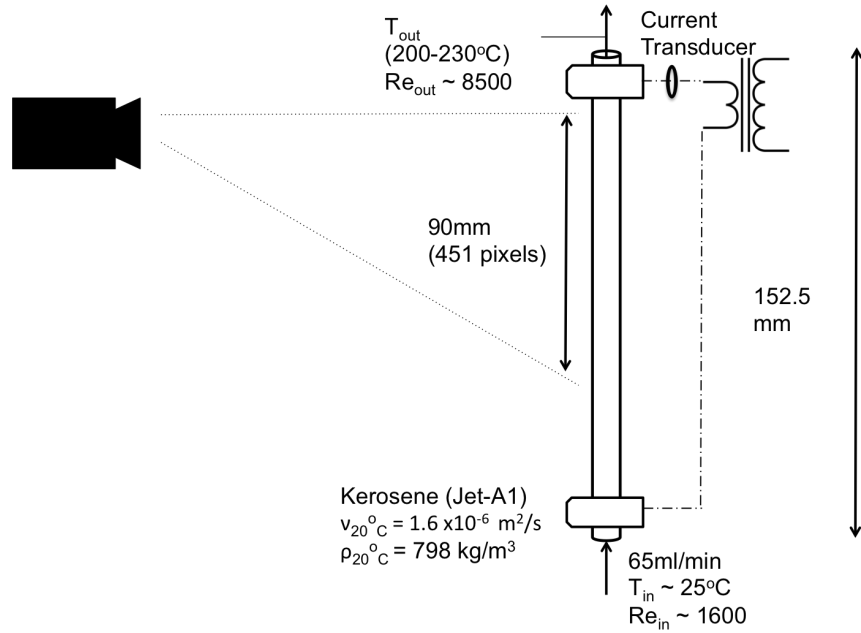


Figure 4.37: HiReTS deposition test conditions

4.2.6.1 Apparatus

The study of deposition used a modified HiReTS, as described in the preceding section. A schematic of the rig is shown with the deposition test conditions in figure 4.36. The test capillary, heated by passage of direct current is cooled by forced convection at the inner surface by the passage of fuel. The pressure of the system was 20bar for sets 1 and 2, but was increased to 25bar for set 3. The internal diameter of the test capillaries was typically around $500\mu\text{m}$, and the flow rate was increased from $35\text{ml}/\text{min}$ (for the standard method) to $65\text{ml}/\text{min}$ to produce a similar inlet Re to the standard method with $270\mu\text{m}$ tubes (≈ 1600). The power required to heat the fuel to the outlet temperature was subsequently increased according to;

$$Q = \dot{m} C_p \Delta T$$

In practice, it was found that the maximum fuel outlet temperature was limited to 230°C . The outlet Re was therefore reduced to ≈ 8500 for $530\mu\text{m}$ tubes.

The external wall temperature was measured by infra-red thermography, the fuel exit temperature was measured by a K-type thermocouple positioned in the exit reducer fitting and the fuel exit temperature was controlled to the test set point by a PID controller within LabView. Since the fuel outlet temperature is fixed, in practice the observed increase in tube external wall temperature is in fact a result of the rig demanding more power to achieve the set point, as a result of the additional thermal resistance from the deposit layer.

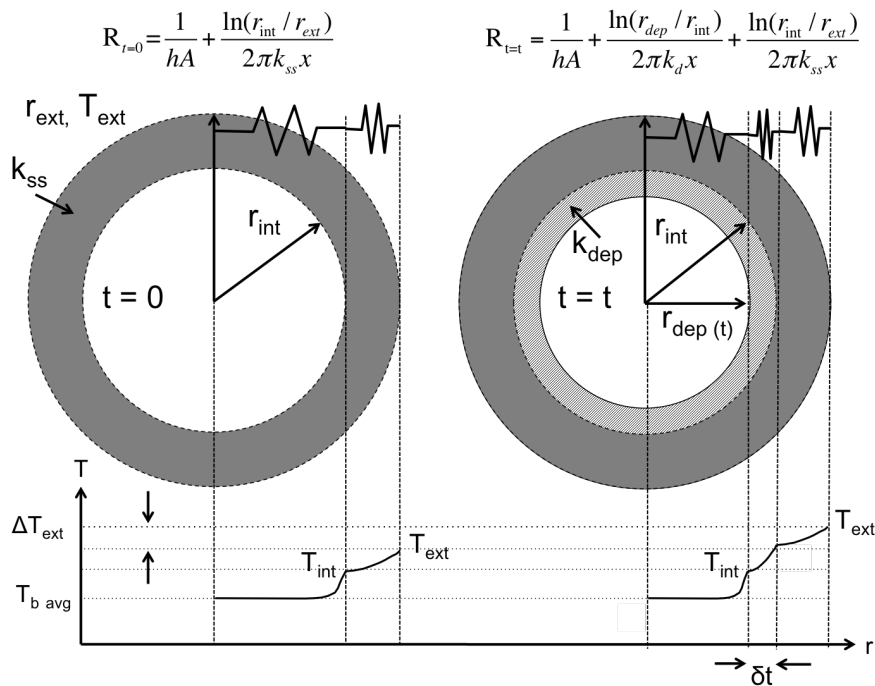


Figure 4.38: 1D thermal resistance network for deposit formation

Heat is transferred by conduction through the tube wall and subsequently to the fuel by convection at the wetted surface. This may be approximated by a 1D thermal resistance network as shown in figure 4.37. As deposit ($k_d \approx 0.15\text{W/mK}$) starts to form on the internal surface, an additional conduction resistance is created to the heat flux from the tube wall to the fluid. Since the bulk temperature rise is constant, the increase in thermal resistance can be described in terms of the external wall temperature rise according to;

$$\Delta R_{(t)} = \frac{T_{ext(t=t)} - T_{b\,avg}}{\dot{m} c_p (T_{b\,out} - T_{b\,in})} - \frac{T_{ext(t=0)} - T_{b\,avg}}{\dot{m} c_p (T_{b\,out} - T_{b\,in})} = \frac{\ln\left(\frac{r_{dep}}{r_{int}}\right)}{2\pi k_d x} \quad (4.2.19)$$

where $T_{ext\,t=0}$ is the wall temperature at an axial location at time zero, $T_{ext\,t=t}$ is

the wall temperature at time t . The deposit thickness at time t , $\delta_t = r_{dep} - r_{int}$.

4.2.6.2 Sources of uncertainty

Measurement	Instrument	Uncertainty
External wall temperature	FLIR A615 thermal cam	$\pm 2^\circ C$ or 2%
Fuel exit temperature	K type thermocouple	$\pm 2.2^\circ C$ or $\pm 0.75\%$
Fuel flow rate	graduated cylinder	$\pm 1.5\%$

Table 4.11: Sources of uncertainty - deposition experiments

4.2.6.3 Fuel selection

Fuel A

The fuel used in sets 1 and 2 of the study, hereby referred to as 'Fuel A' was a conventionally sourced Jet-A1, taken from a several thousand litre batch of fuel used for a large scale test at the Low Carbon Combustion Centre. The fuel was analysed in detail and the hydrocarbon speciation can be seen in figure 4.38. Being conventionally derived, the fuel shows a typical balance of normal and iso-alkanes, cyclo-alkanes, alkenes and aromatics.

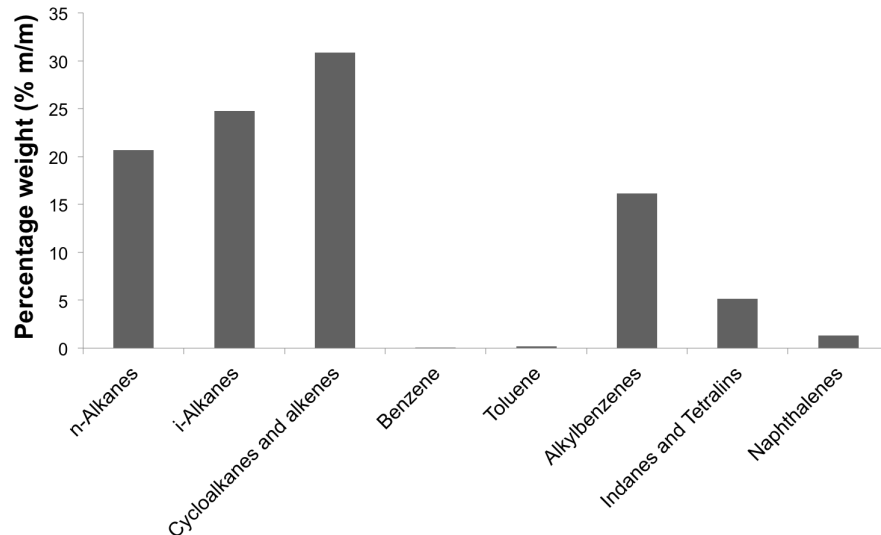


Figure 4.39: Hydrocarbon species breakdown for fuel 'A'

The fuel thermal stability was extensively tested using the standard JFTOT method (ASTM D3241) as well as the standard HiReTS method (IP482). The thermal stability specification tests showed the fuel to be generally of average to

poor thermal stability. Although the JFTOT specification test was consistently passed at 265°C , HiReTS tests - spaced several months apart - indicated a rapid deterioration of thermal stability in storage (fig 4.39).

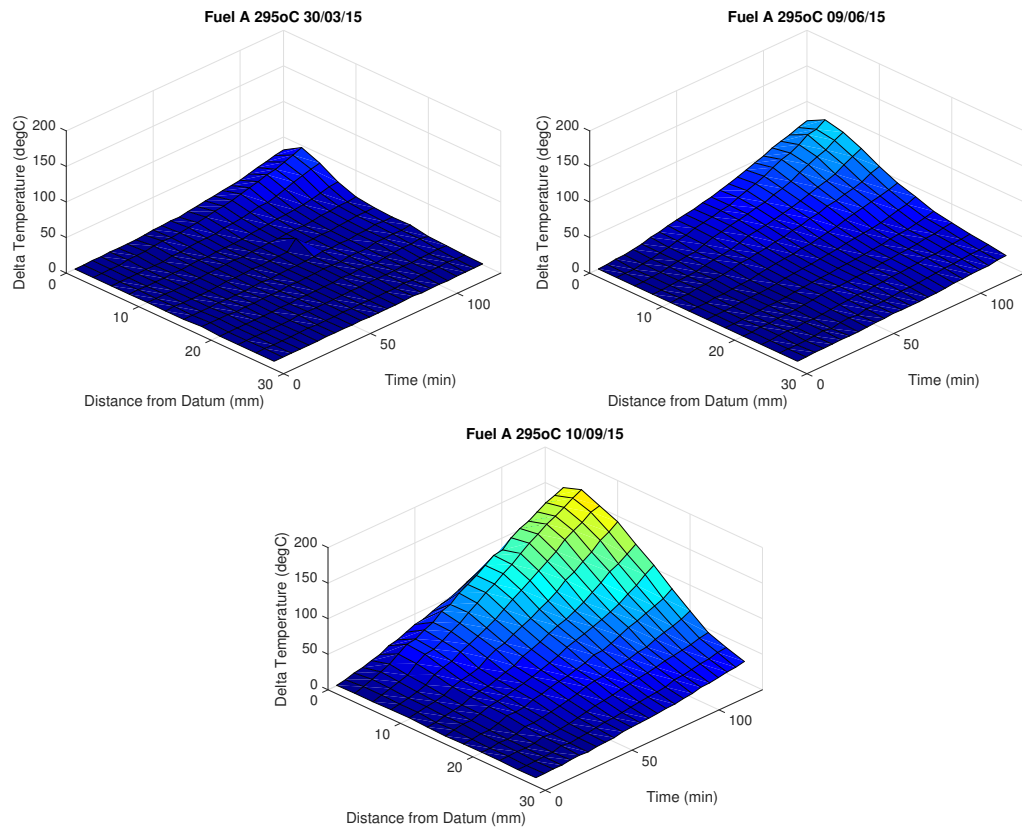


Figure 4.40: Fuel A, degradation in storage with time - standard HiReTS method. Top left; $HN_{125} = 188$. Top right; + 3 months, $HN_{125} = 546$. Bottom; + 6 months, $HN_{125} = 1193$

The fuel was considered fit for the purpose of investigating roughness effects. The poor thermal stability was quite beneficial, since the test was in effect made less extreme than the standard method due to the limitation on fuel outlet temperature. It was anticipated that the use of a relatively unstable fuel would result in sufficient progression of deposition over the course of a two hour test. Furthermore, the fuel volume required per test could be kept to a minimum.

Fuel B

Set 3 was conducted with a Jet-A1 sourced from a local regional airport. The fuel was particularly thermally stable, and was therefore blended with 10% of Fuel A in order to reduce the thermal stability and required test time. The results of the standard HiReTS method for the blend are shown in figure 4.40.

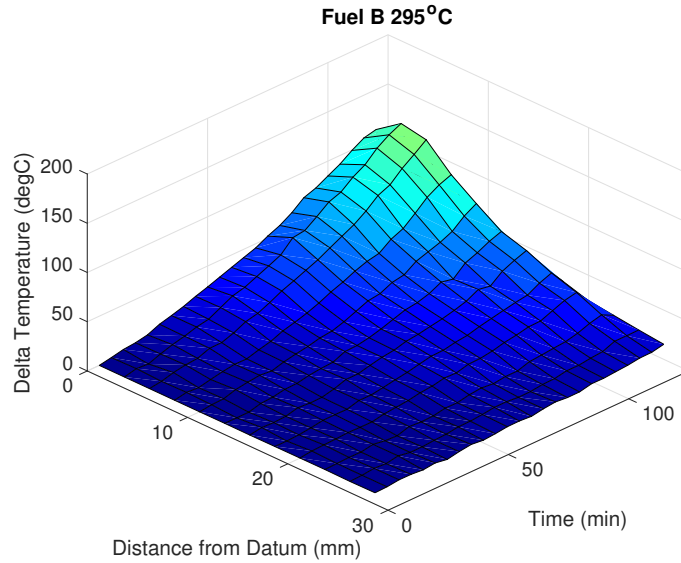


Figure 4.41: Standard HiReTS test for Fuel B. $HN_{125} = 800$

4.2.6.4 Method

Tests were performed in blocks, corresponding to the manufacture of different sets of EDM tubes, which was an iterative process. Tests within the same set were typically conducted in the same week and therefore can be directly compared. However, comparison between earlier and later experiments should be made with caution.

The standard HiReTS method was followed where possible. Immediately prior to the test, the fuel was saturated with oxygen by blowing dry air through a sparging tube for 12 minutes. Meanwhile, the fuel path was flushed with heptane. The rig was flushed with the test fuel for 1.5 minutes, during which the flow rate was verified. With the flow rate confirmed, power was applied to the tube and the rig allowed to warm up for 5 minutes, at the conclusion of which the first external wall temperature profile was recorded and the test commenced. Temperature data was recorded at 5 minute intervals and averaged over 10 seconds. At the conclusion of the test, the tube was carefully removed and the rig was flushed with heptane.

4.2.6.5 Results

Set	Tube	D (µm)	Fuel	T _{out} (°C)	Time (mins)	U _{avg} (m/s)	Re _{in}	Re _{out}	Δ Re _{out} (max)	HN ₁₂₅ *	HN ₂₅₀ *	HN Peak ₁₂₅	HN Peak ₂₅₀
1 Nov-15	R1	530	A	200	125	4.91	1602	7717	716	31827		107	
	R2	530	A	200	125	4.91	1602	7717		34069		110	
	EDM 1	485	A	200	125	5.86	1751	8433		15833		52	
	EDM 5	493	A	200	125	5.68	1722	8297		14487		42	
	R3	534	A	230	125	4.84	1590	8453	1924	49832		120	
	R4	522	A	230	125	5.06	1627	8647		49229		128	
2 Aug-16	EDM 4	438	A	230	125	7.19	1939	10305		18767		55	
	EDM 6	435	A	230	125	7.29	1952	10377		17565		54	
	R5	524	A	230	125	5.02	1621	8614		40803		195	
	EDM 7	574	A	230	125	4.19	1479	7864		16390		48	
	R6	518	A	225	125	5.14	1639	8454	930	34008		187	
	R7	538	A	225	125	4.77	1578	8140		33565		184	
3 May-17	EDM 8	564	A	225	125	4.34	1506	7765		12365		39	
	EDM 9	574	A	225	125	4.19	1479	7629		14186		70	
	EDM 10	582	A	225	250	4.07	1459	7524		15985	32945	50	86
	EDM 11	572	A	225	250	4.22	1485	7656		17122	30071	45	80
	R9	528	B	200	125	4.95	1608	7747	646	24351		100	
	EDM 11	576	B	200	125	4.16	1474	7101		17122		45	
R8 R11 EDM13 EDM12	R8	527	B	230	125	4.97	1611	8565	1395	29992		125	
	R11	539	B	230	125	4.75	1575	8374		29840		99.2	
	EDM13	495	B	230	125	5.63	1715	9119		28666		119	
	EDM12	567	B	225	125	4.29	1498	7723		32347		91	

* HiReTS numbers evaluated over top 90mm

Figure 4.42: Summary of deposition test results

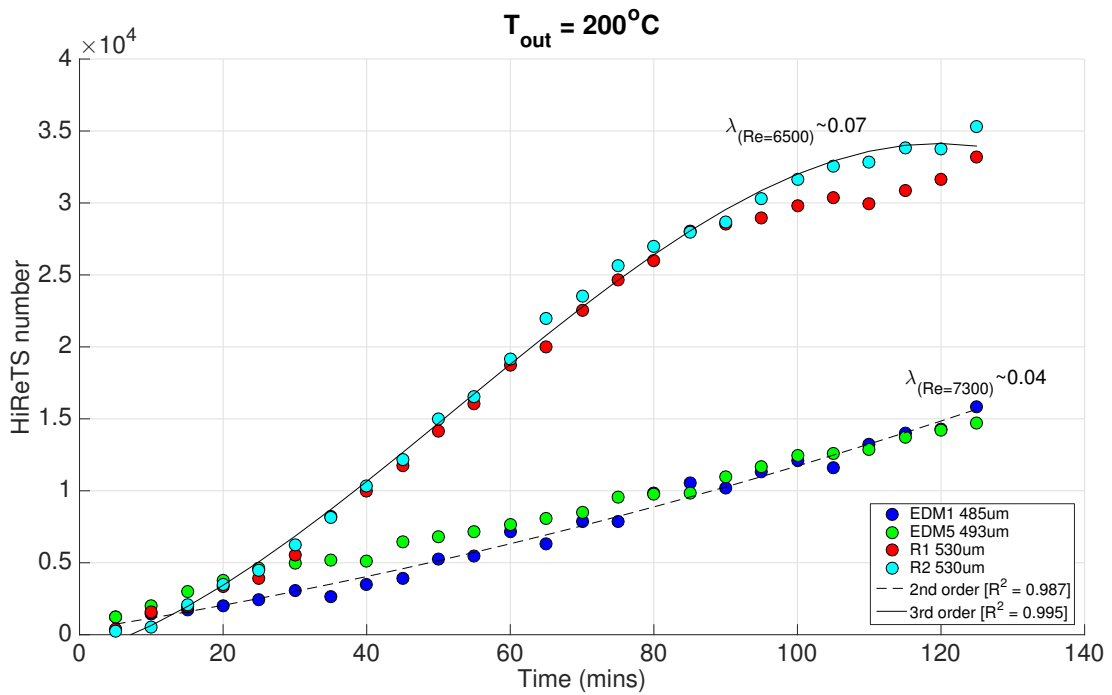


Figure 4.43: Set 1, Fuel A, 200°C. HiReTS number development with time

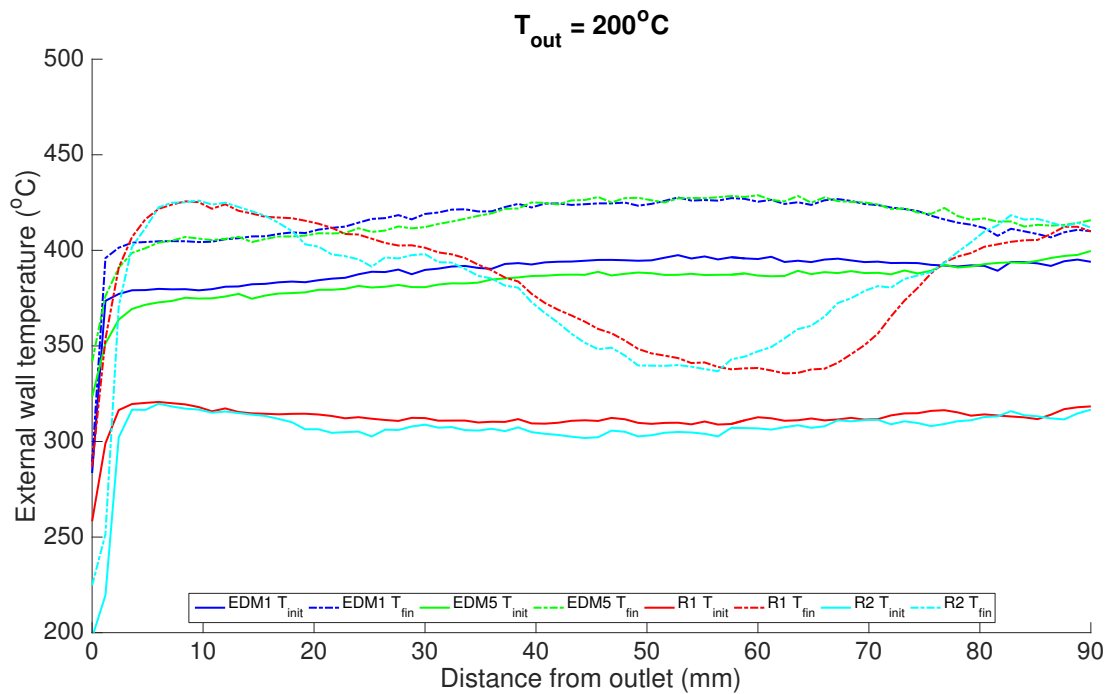


Figure 4.44: Set 1, Fuel A, 200°C. Initial and final wall temperatures

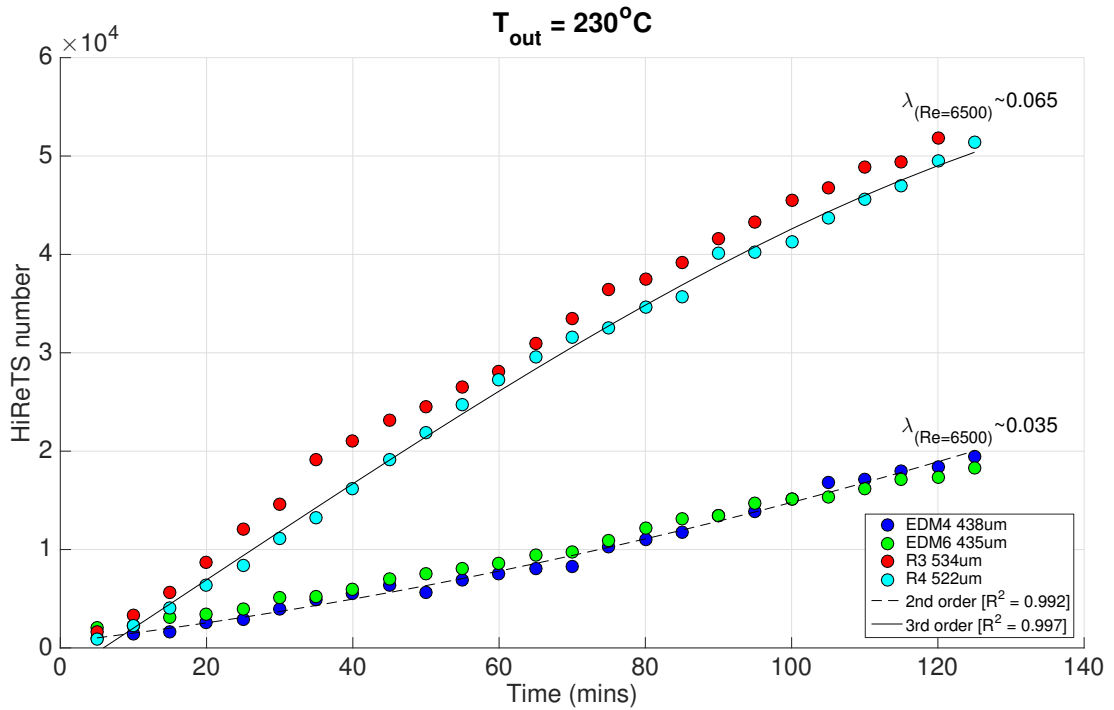


Figure 4.45: Set 1, Fuel A, 230°C. HiReTS number development with time

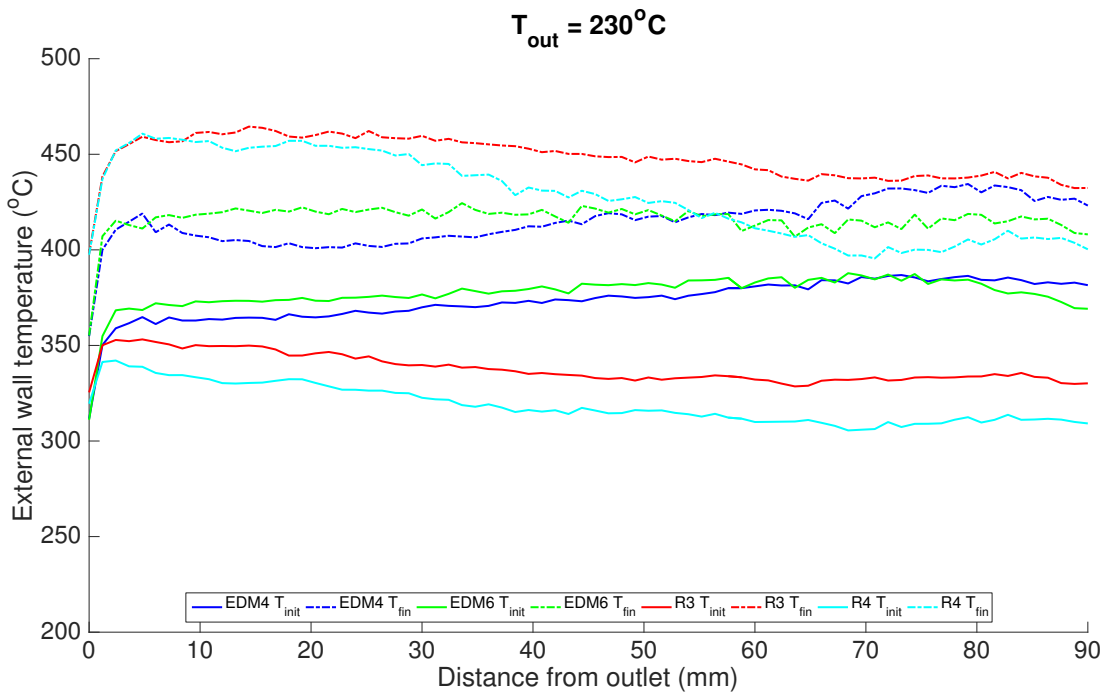


Figure 4.46: Set 1, Fuel A, 230°C. Initial and final wall temperatures

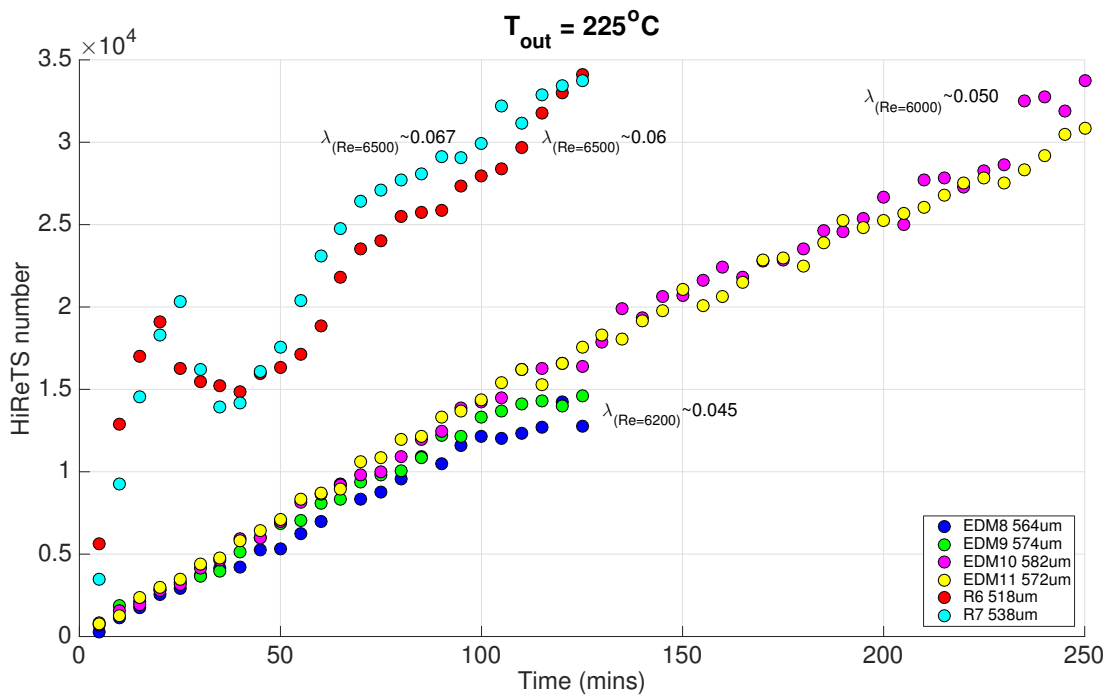


Figure 4.47: Set 2, Fuel A, 225°C. HiReTS number development with time

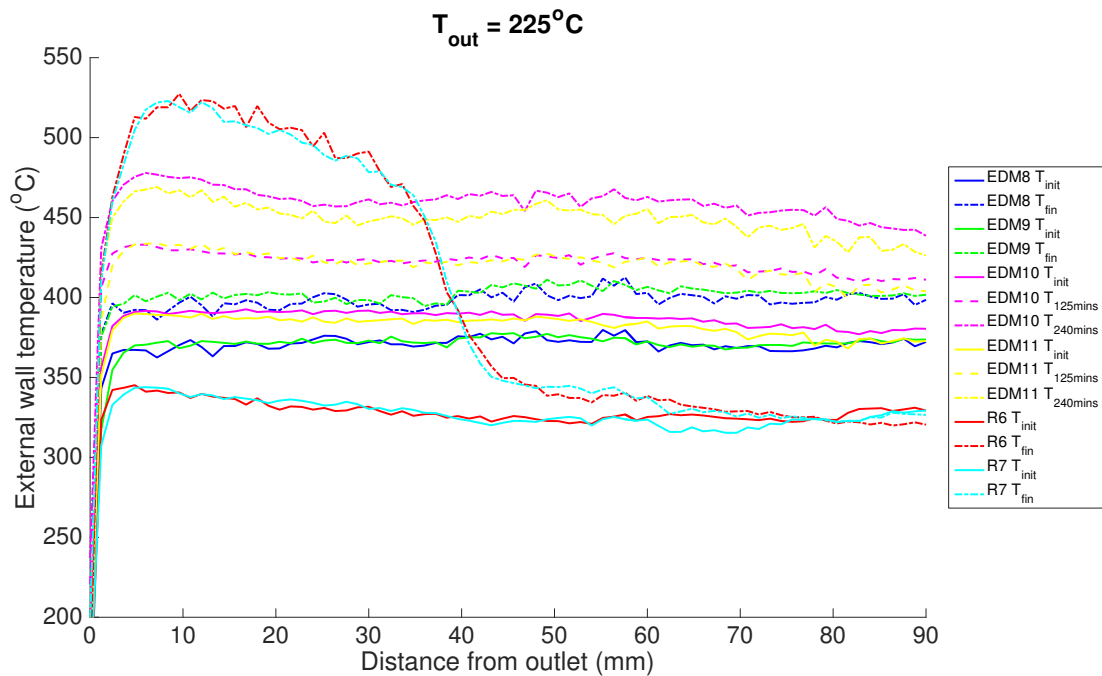


Figure 4.48: Set 2, Fuel A, 225°C. Initial and final wall temperatures

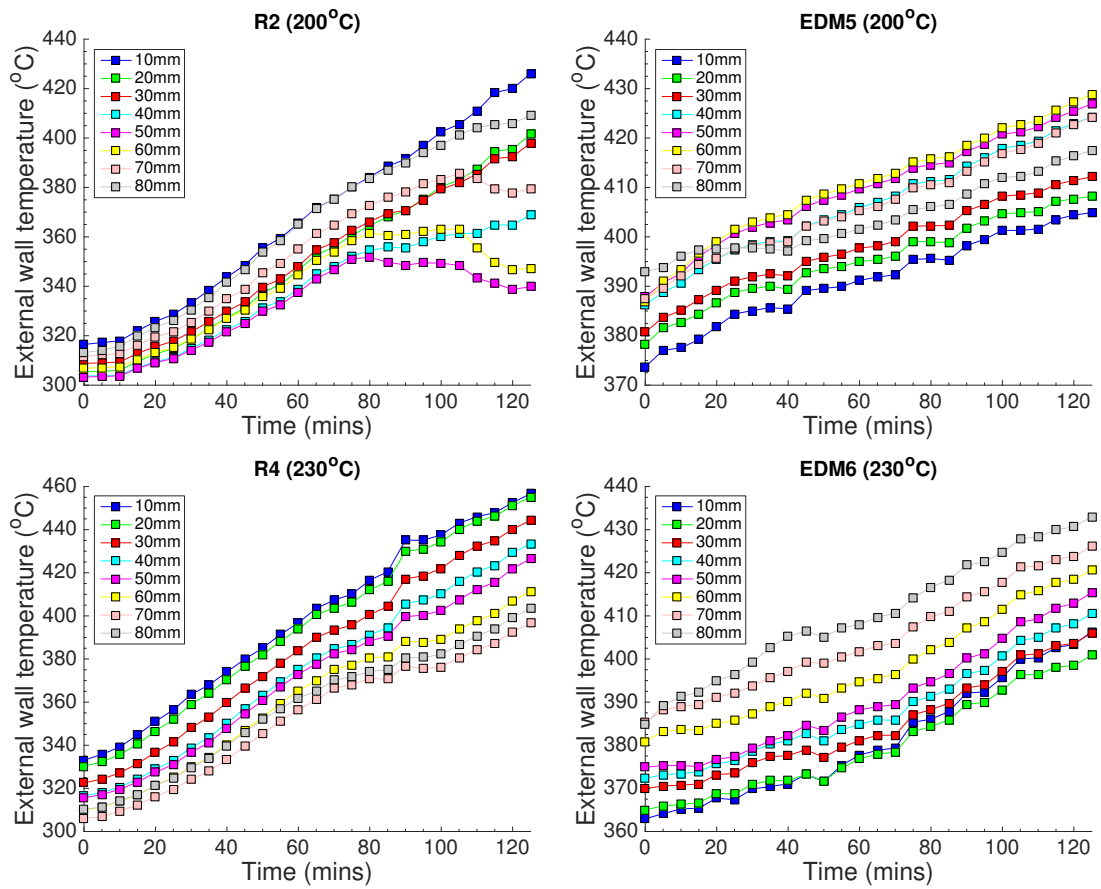


Figure 4.49: Set 1, Fuel A. Wall temperature rise with time and axial position

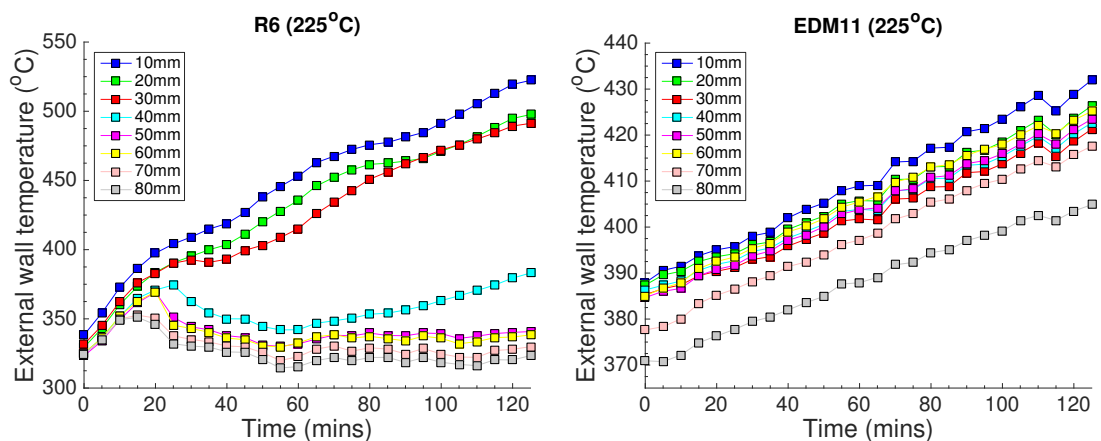


Figure 4.50: Set 2, Fuel A. Wall temperature rise with time and axial position

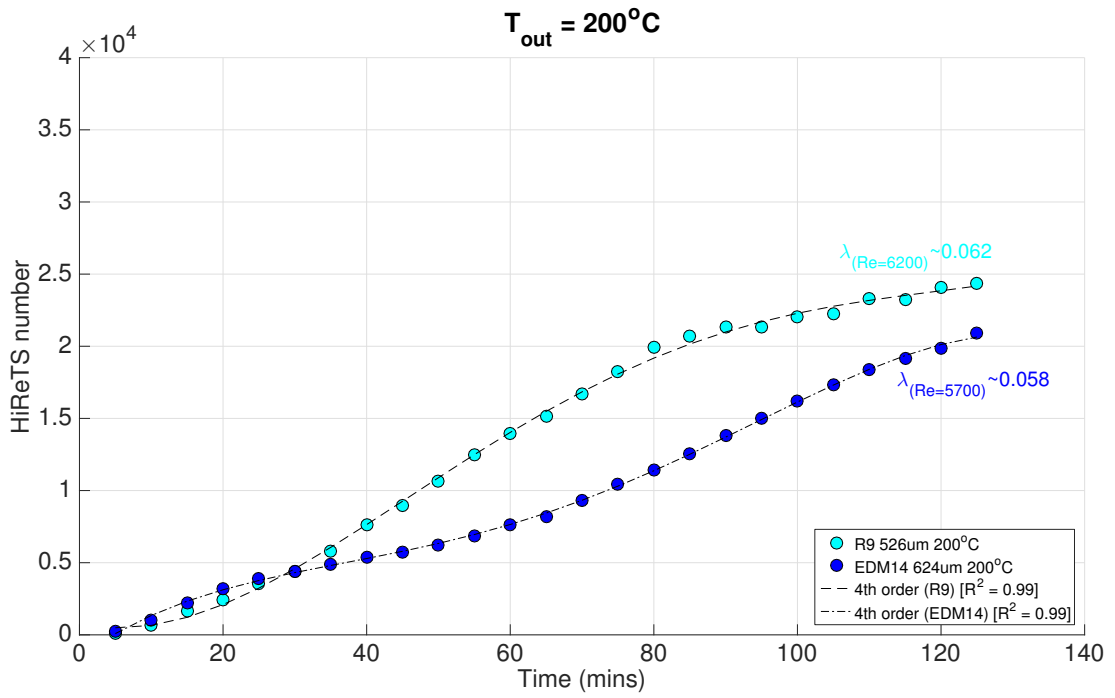


Figure 4.51: Set 3, Fuel B. 200°C. HiReTS number development with time

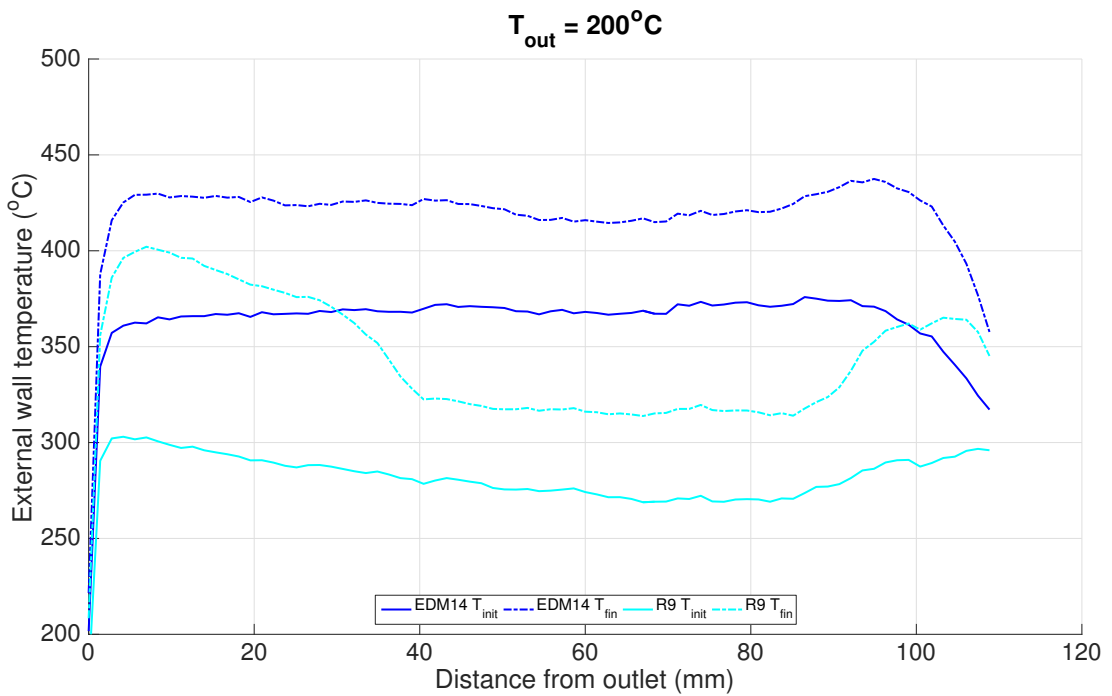


Figure 4.52: Set 3, Fuel B. 200°C. HiReTS number development with time

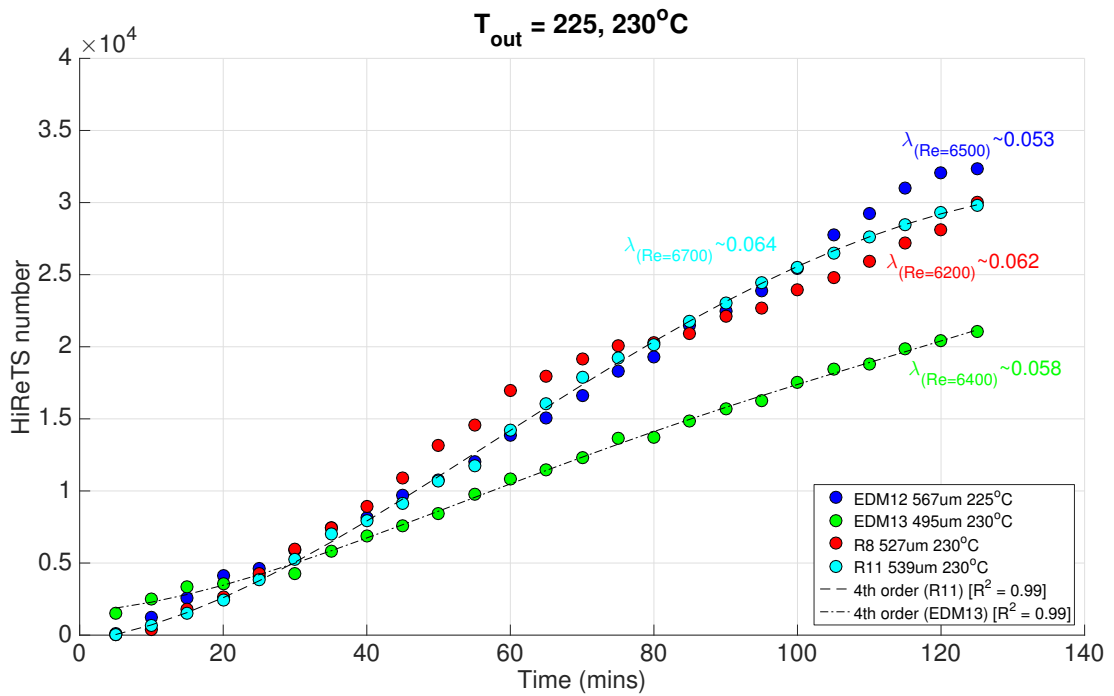


Figure 4.53: Set 3, Fuel B. 225, 230°C. HiReTS number development with time

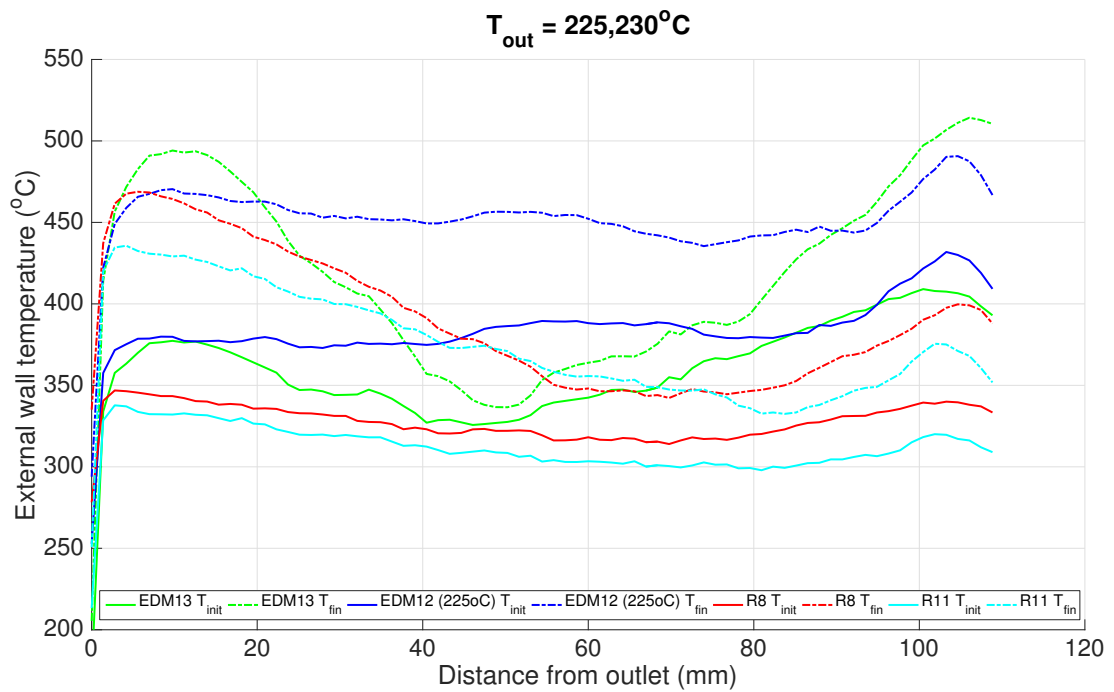


Figure 4.54: Set 3, Fuel B. 225, 230°C. Initial and final external wall temperatures

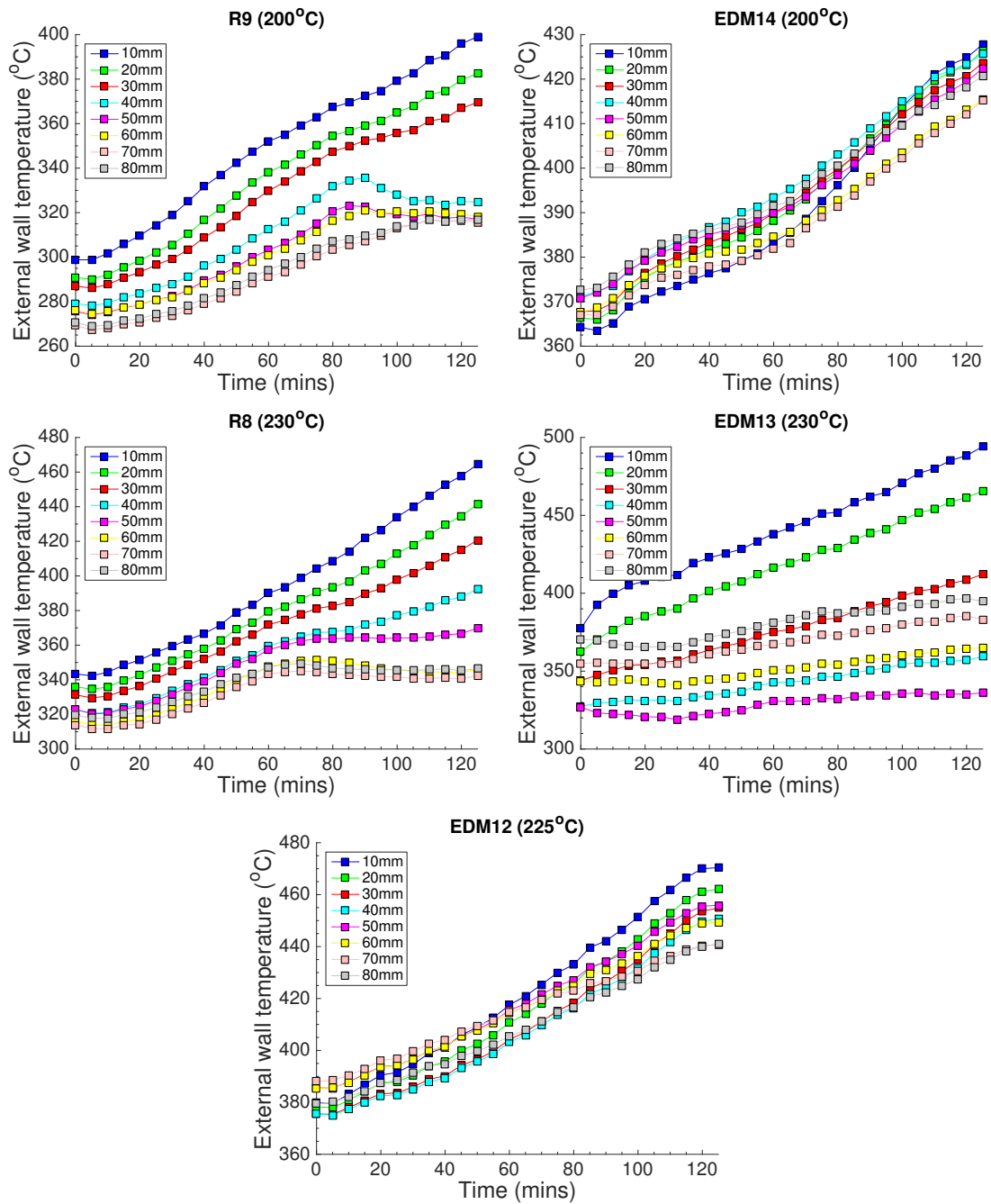


Figure 4.55: Set 3, Fuel B. Wall temperature rise with time and axial position

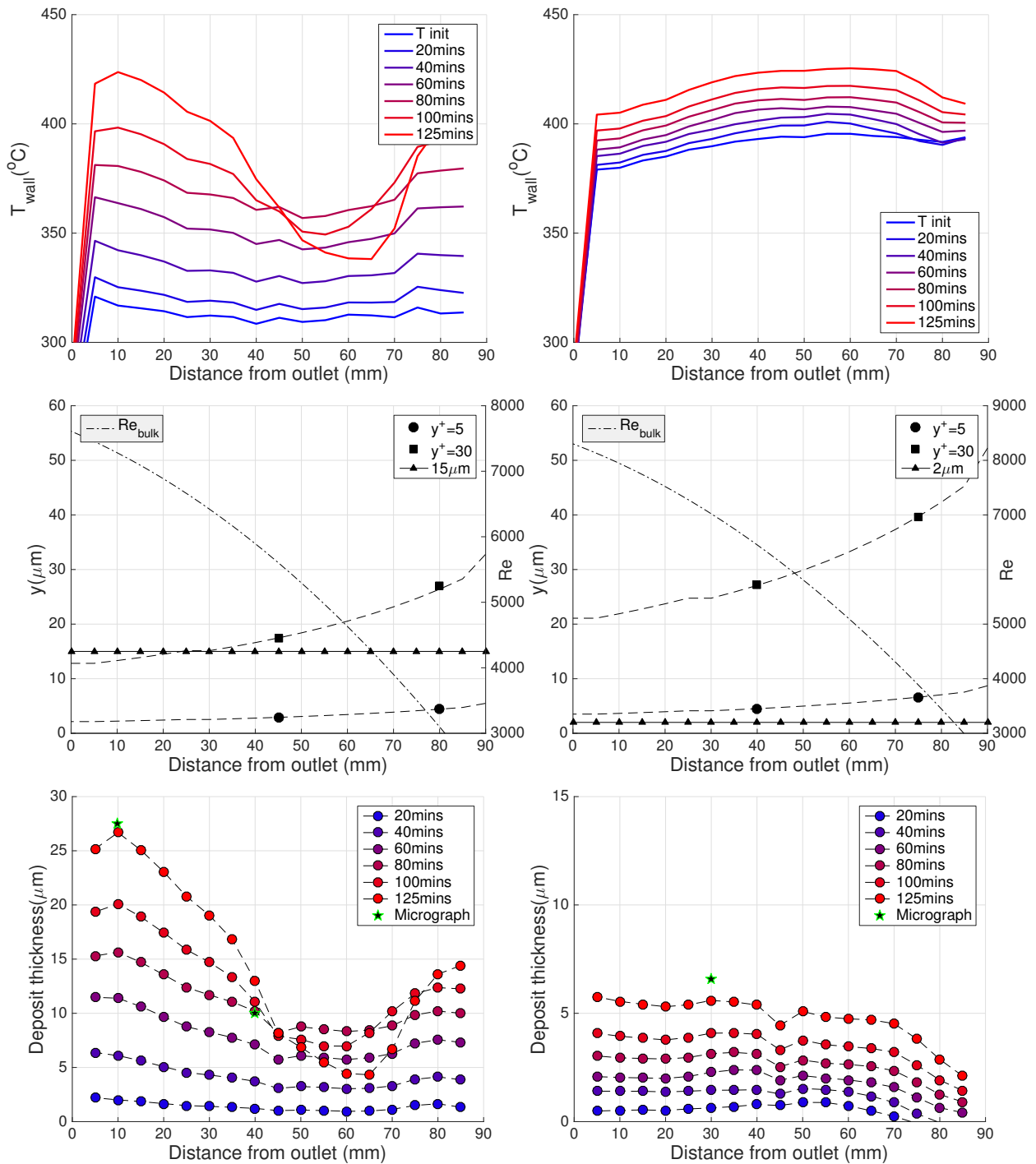


Figure 4.56: Set 1, Fuel A, 200°C. Left: R1, 530µm. Right: EDM 1, 482µm. Top: wall temperature rise with time. Middle: bulk Re , viscous and buffer layer heights. Bottom: deposit thickness

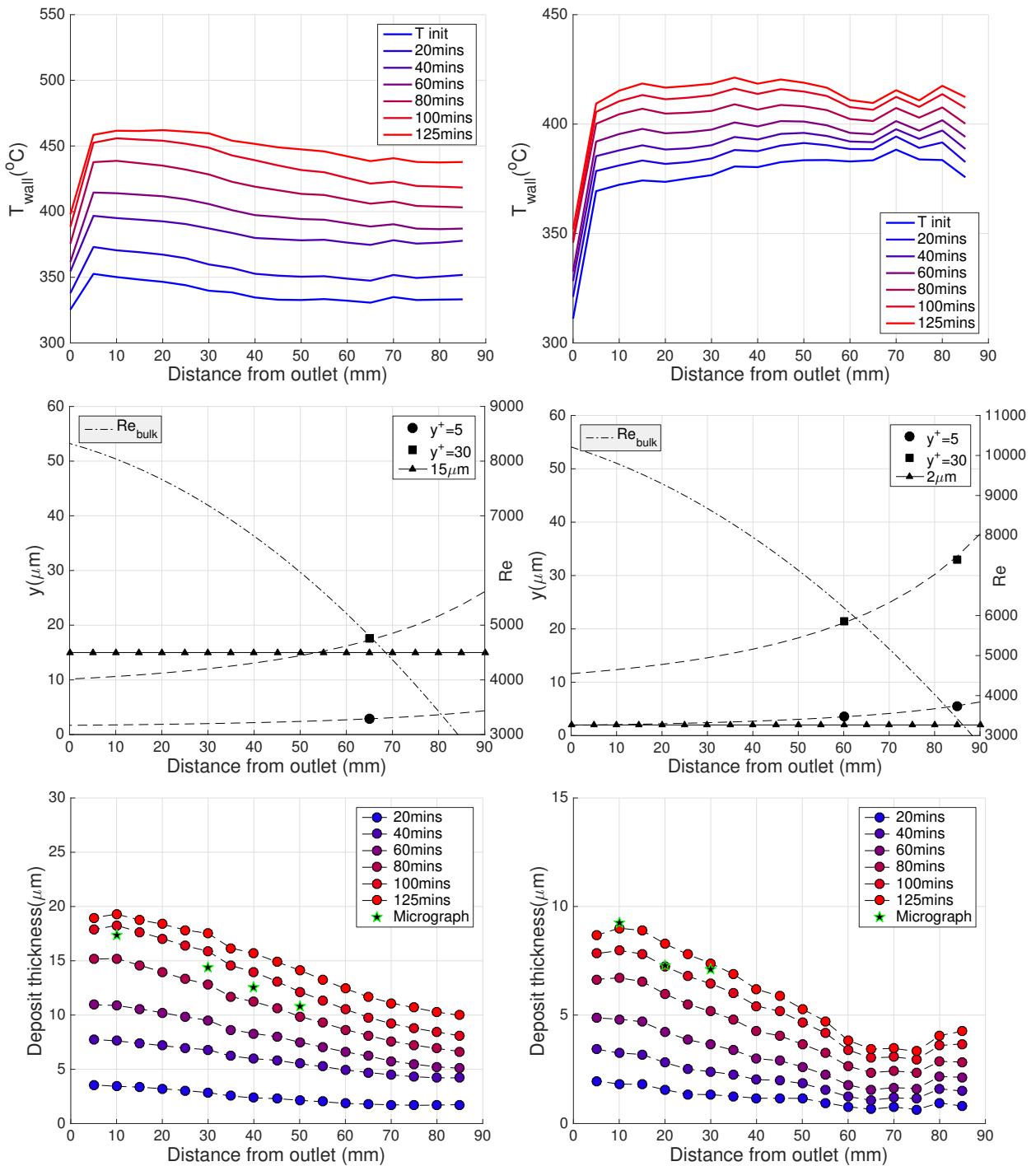


Figure 4.57: Set 1, Fuel A, 230°C. Left: R3, 537 μm. Right: EDM 6, 437 μm. Top: wall temperature rise with time. Middle: bulk Re , viscous and buffer layer heights. Bottom: deposit thickness

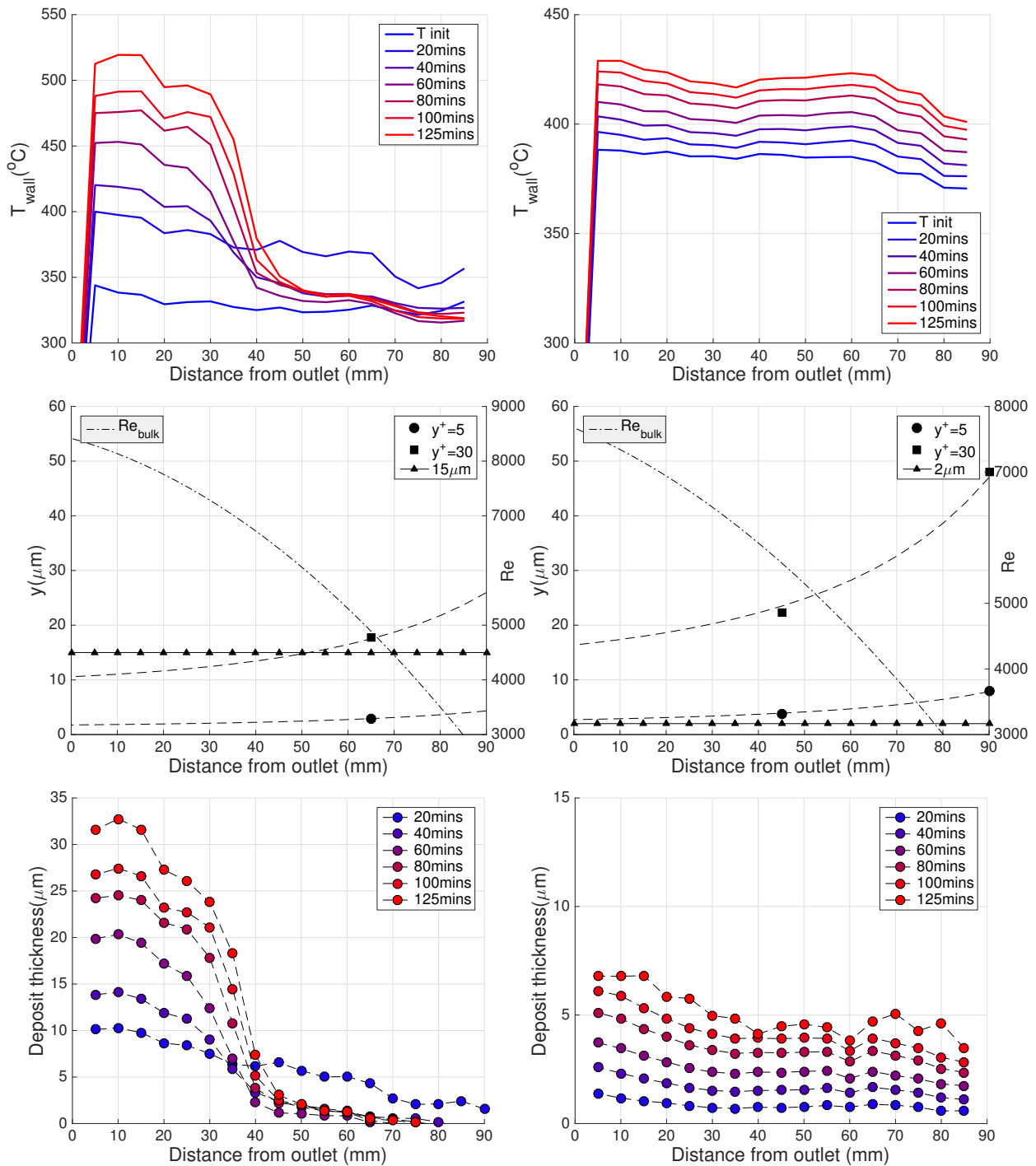


Figure 4.58: Set 2, Fuel A, 225°C. Left: R7, 530 μm. Right: EDM 11, 576 μm
 Top: wall temperature rise with time. Middle: bulk Re , viscous and buffer layer heights. Bottom: deposit thickness

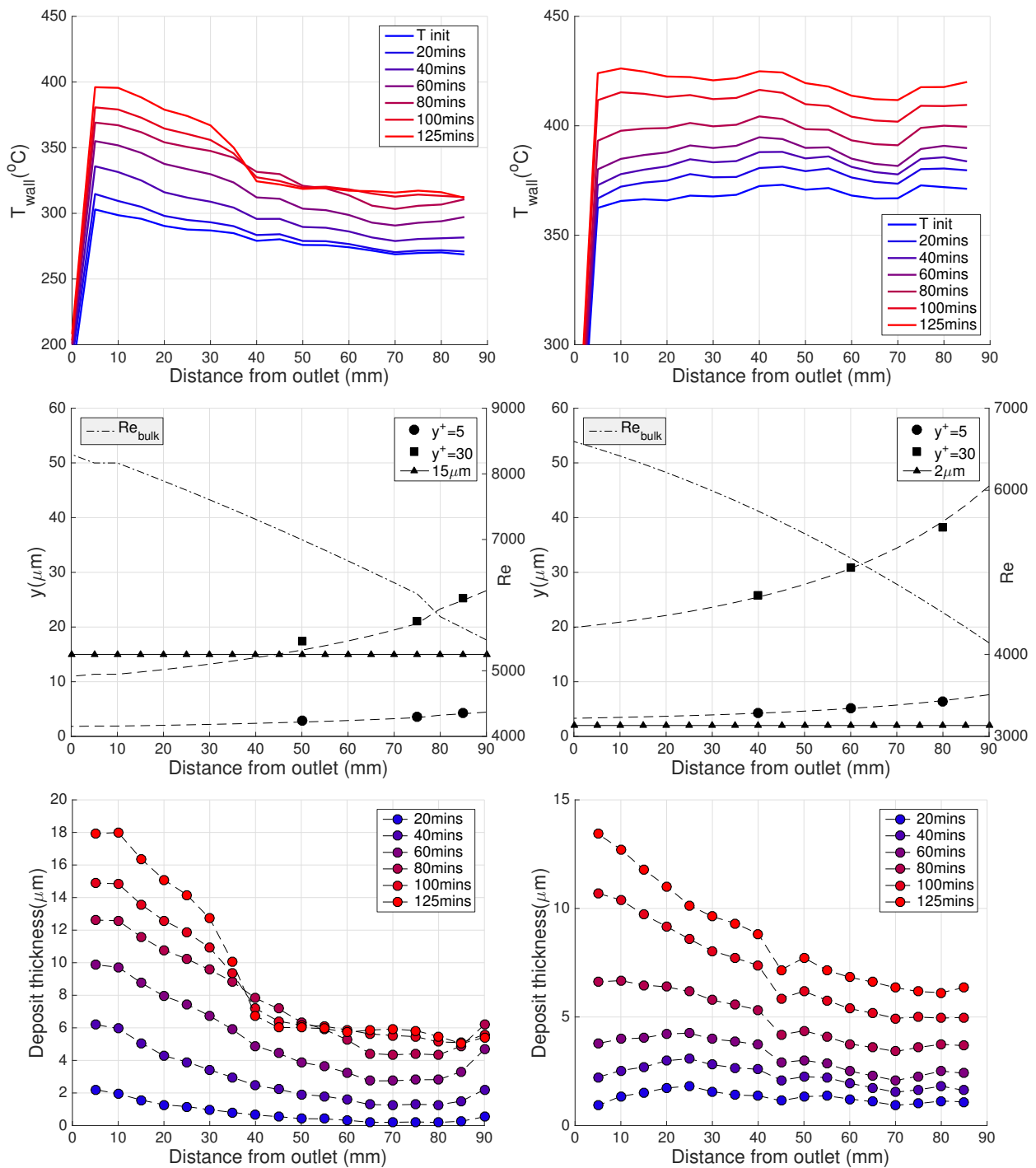


Figure 4.59: Set 3, Fuel B, 200°C. Left: R9, 528 μm. Right; EDM 14, 611 μm
 Top: wall temperature rise with time. Middle: bulk Re , viscous and buffer layer heights. Bottom: deposit thickness

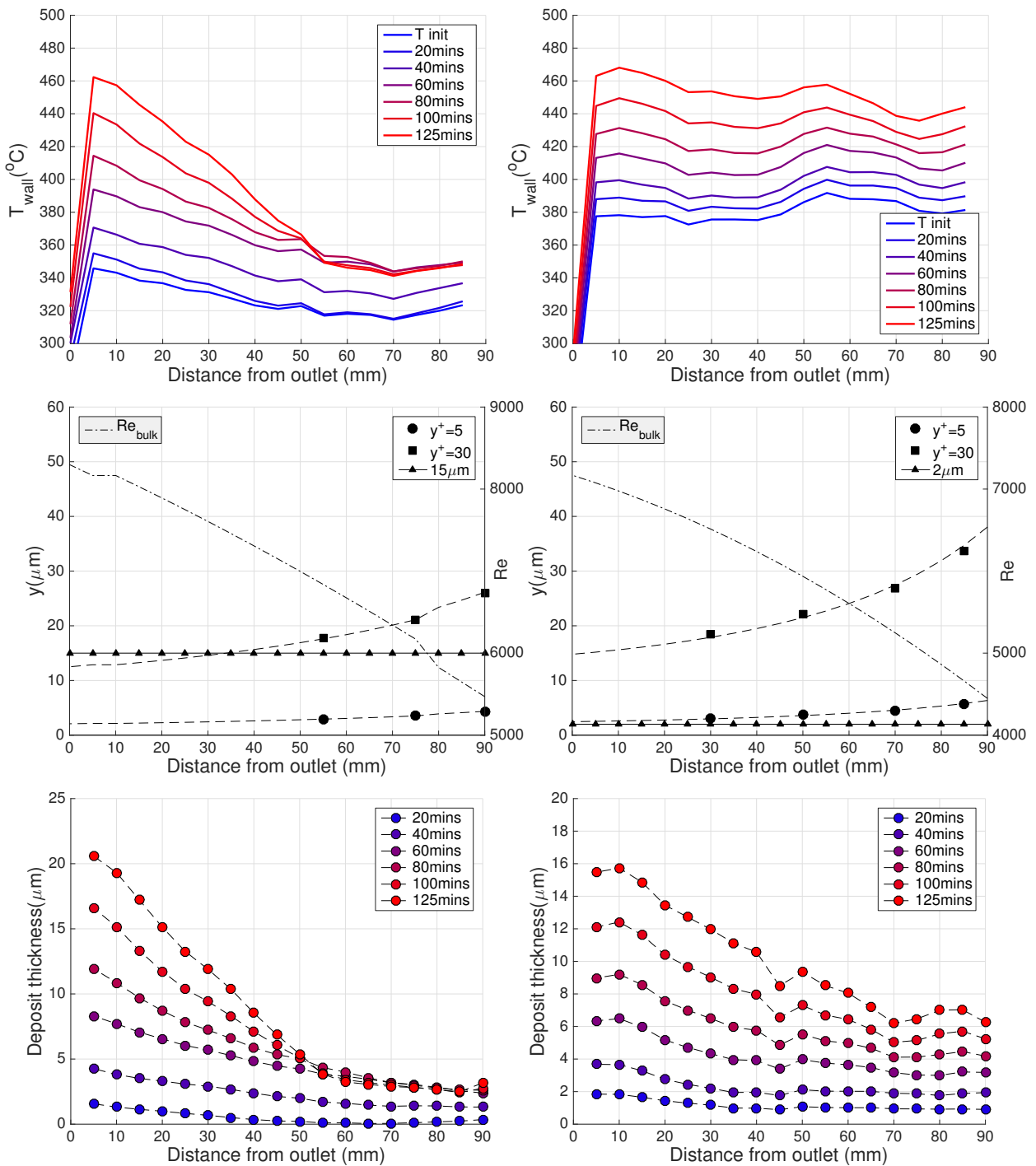


Figure 4.60: Set 3, Fuel B. Left: R8, 527 μm, 230°C. Right: EDM 12, 567 μm, 225°C

Top: wall temperature rise with time. Middle: bulk Re, viscous and buffer layer heights. Bottom: deposit thickness

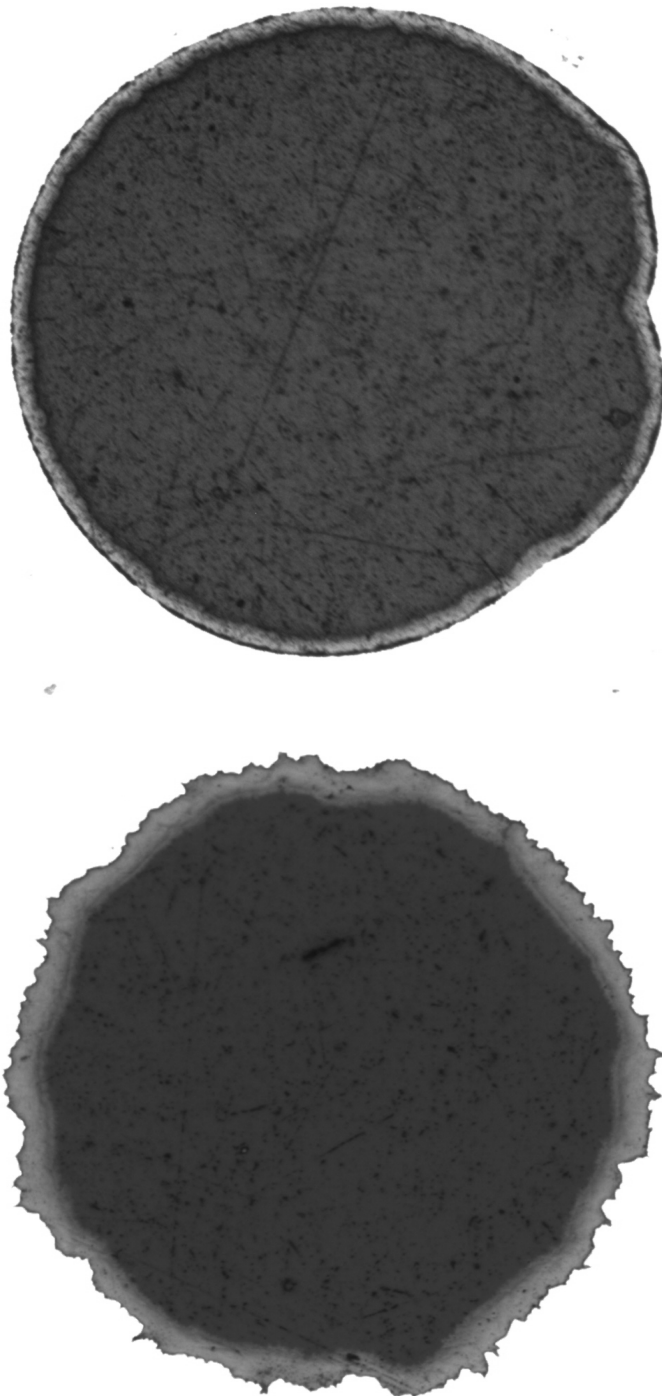


Figure 4.61: Micrographs showing deposit. Top: EDM 1. Bottom: R2

Tube	D (μm)	k_{rms} (μm)	k_s (approx) (μm)	λ ($\text{Re}=5000$)	Nu ($\text{Re}=10000$)	T_{out} ($^{\circ}\text{C}$)	HN_{peak}	HN_{125}	δ_{dep}	max (μm)	$\text{HN}_{\text{peak}}/\Delta T_{\text{bulk}}$	Fuel A		Fuel B	
												$\text{HN}_{125}/\Delta T_{\text{bulk}}$	$\text{HN}_{125}/\Delta T_{\text{bulk}}$	$\text{HN}_{\text{peak}}/\Delta T_{\text{bulk}}$	$\text{HN}_{125}/\Delta T_{\text{bulk}}$
EDM 1 ¹	482	10.53	< 8	0.0412	39	200	52	15833		5.8	0.30	90			
EDM 2	453	2.89	< 8	0.0369	36	230	TF	TF							
EDM 4 ¹	439	2.32	< 8	0.0380	46	230	55	18767			0.27	92			
EDM 5 ¹	500	4.36	< 8	0.0418	44	200	42	14487			0.24	83			
EDM 6 ¹	437	1.69		0.0320	43	230	54	17565		8.1	0.26	86			
avg	464	4.15		0.0380	42										
EDM 7 ²	575	6.27	19	0.0492	51	230	48	16390			0.23	80			
EDM 8 ²	575	4.78	< 19	0.0437	55	225	39	12365			0.20	62			
EDM 9 ²	574	6.37	19	0.0483	61	225	70	14186			0.35	71			
EDM 10 ²	581	9.33	19	0.0497	51	225	50	15985			0.25	80			
EDM 11 ²	576	6.40	19	0.0500	54	225	45	17122		6.8	0.23	86			
avg	576	6.63		0.0482	54										
EDM 12 ³	567	9.33	-	0.0558	66	225	91	32347		15.7	0.46	162			
EDM 13 ³	495	5.23	-	0.0615	58	230	119	28666			0.58	140			
EDM 14 ³	611	12.69	-	0.0579	59	200	69	20937		13.4	0.39	120			
avg	558	9.08		0.0584	61										
SA 1 ¹	530	-	> 19	0.0676	65	200	107	31827		26.7	0.61	182			
SA 2 ¹	530	-	> 19	0.0694	-	200	110	34069			0.63	195			
SA 3 ¹	537	5.36	> 19	0.0651	65	230	120	49832		19.6	0.59	243			
SA 4 ¹	527	7.48	> 19	0.0640	66	230	128	49229			0.62	240			
SA 5 ²	519	6.49	> 19	0.0649	84	230	195	40803			0.95	199			
SA 6 ²	517	5.49	> 19	0.0594	78	225	187	34008			0.94	170			
SA 7 ²	530	7.04	> 19	0.0674	76	225	184	33565		33.7	0.92	168			
avg	526	6.37		0.0654	72										
SA 8 ³	527	8.88	-	0.0616	68	230	125	29992		20.6	0.61	146			
SA 9 ³	528	8.76	-	0.0608	83	200	100	24351		18.0	0.57	139			
SA 10	531	9.72	-	0.0556	-	-	-	-							
SA 11 ³	539	9.07	-	0.0684	76	230	99.2	29840			0.48	146			
avg	531	9.11		0.0616	76										

* superscript indicates test set

TF = test failed

Figure 4.62: Summary of capillary tube tests

4.2.6.6 Discussion

Deposition test results are shown primarily by the development of HiReTS number (HN) with time, initial and final external wall temperatures and wall temperatures at discrete positions along the tube length throughout the test. The analysis is extended by calculating the growth of deposit with time through application of a 1D heat transfer analysis. Centreline O₂ measurement was not implemented at the exit since autoxidation is confined to the near wall region in testing without bulk pre-heating.

The HiReTS number (HN) is defined as;

$$HN_t = \sum_1^n \Delta T_n \quad (4.2.20)$$

where $\Delta T_n = T_{fin} - T_{init}$ at position n. In total 450 measurements were used in the calculation. The numbers quoted here must not be compared to the HiReTS number used in the HiReTS fuel specification method, which is the summation of temperatures measured at 12 locations across the top 30mm. While $HN_{(t)}$ represents the total ΔT across the tube at time t , HN_{peak} is the maximum wall temperature rise at any position.

Set 1, Fuel A

Figures 4.42 and 4.44 show HiReTS number development with time for EDM set 1 (1,4,5 and 6) and drawn capillaries 1 to 4 for 125min tests at 200°C and 230°C. For both fuel outlet temperatures, the tubes exhibit substantially different behaviour and the results for the two roughnesses show notable repeatability. For the 200°C tests, values of (HN_{125}) for the drawn tubes are within 6% and for the smooth tubes the difference is 9%. For the 230°C tests the agreement is improved further - 1% and 7% for the drawn and EDM tubes respectively. While the EDM tubes have an almost constant increase in wall temperature, the drawn tubes exhibit what appears to be a 'three piece' profile. In the initial phase, the wall temperature rise follows a power law, before reducing to a second phase of almost constant deposition rate between $40 < t < 80mins$. Beyond 80 minutes, the deposition rate then appears to reduce for R1 and R2, but for R3 and R4 at 230°C the reduction is less. The HN profiles of the drawn tubes are best represented by a third order polynomial and the R^2 values show an excellent quality of fit. An equally good fit was found with a second order polynomial for the EDM tubes.

HN curves are annotated with averaged values of λ . There is a dramatic increase in ΔT for the drawn tubes with respect to the EDM tubes. In the $200^\circ C$ test, the drawn tubes had an average $\lambda_{max} = 0.07$ and an average total HiReTS number of 32500. The EDM tubes had $\lambda_{max} = 0.04$ and $HN_{125} = 15000$. For a fuel outlet temperature of $230^\circ C$, HN for the drawn tubes ($\lambda_{max} = 0.065$) was almost 3 times higher than the EDM tubes ($\lambda_{max} = 0.035$). HN_{peak} increased with fuel outlet temperature and friction factor.

Figures 4.43 and 4.45 show the initial and final wall temperatures across the measured length, and figure 4.48 displays the wall temperature rise as a function of time at discrete points along the tubes. Since the tests show excellent repeatability, only data from one drawn and EDM is used for comparison of $\frac{dT}{dt}$. Further differences between the tubes are apparent. Principally, the initial wall temperatures are around $60^\circ C$ higher for the smooth tubes at the start of the test, which would be expected considering the difference in Nu between the tubes. Figure 4.48 shows the wall temperature rise for the smooth tubes to be very even across the measured length, in start contrast to the rough $200^\circ C$ case, for which the final wall temperature is a complicated function of axial position. For the rough tubes at $200^\circ C$, in the second half of the test, a *decrease* in wall temperature can be seen between $40mm$ and $70mm$ from the outlet, with the greatest reduction between $50-60mm$ from the outlet. Either side of this region, the wall temperature increases at reasonably consistent rate, corresponding to the conditions between $60-80mins$. This local reduction in wall temperature explains the reduction in $\frac{dHN}{dt}$ at the end of the test for R1 and R2. In contrast, the wall temperature rise is much more constant for tubes R3 and R4 at $230^\circ C$, and no reduction in wall temperature is observed, only a mild reduction in deposition rate.

Consideration must be given to the difference in Reynolds number from inlet to outlet between the tubes, which is dependent upon the tube diameter and the axial temperature difference. The fuel enters the tube at what would be considered a laminar Reynolds number and at some axial position, transitions to turbulent flow. In the first set, the tubes in the $200^\circ C$ test have ($\Delta Re_{out} = 716$) - since the difference in D was only $37\mu m$. For the $230^\circ C$ tests the difference was more considerable, $\approx 100\mu m$ resulting in $\Delta Re_{out} = 1900$.

Set 2, Fuel A

Figures 4.46, 4.47 and 4.49 show the results for tests conducted on EDM tubes 8

to 11 and drawn tubes 6 and 7 with a fuel outlet temperature of 225°C . The tests were performed at a later date to set 1 and the thermal stability of the fuel had experienced significant deterioration during the time period. The fuel was also from a different batch. Tests on EDM 10 and 11 were extended to 4 hours, but the rough tube tests could not be extended in time since the maximum allowable external wall temperature was reached shortly after 2 hours. Tubes R6 and R7 had a maximum measured λ of around 0.065 and a final $\text{HN} \approx 34000$. The EDM tubes in this set had slightly higher friction factors than in set 1, around 0.045 and 0.05 for EDM 8,9 and EDM 10,11 respectively. HN_{125} for EDM 8 and 9 was ≈ 13000 - although it should be noted that towards the end of the test (beyond 100 mins), the demand from the PID reached the maximum limit in the code, and as such the power was capped, causing the reduction in wall temperature rise beyond 100mins. The limit was subsequently increased for tests with EDM 10 and 11, and no capping in wall temperature rise was seen. The final HiReTS numbers for EDM tubes 10 and 11 at 250mins are comparable to the numbers for the drawn tubes after 125mins. In a similar fashion to the previous results, the tubes with the highest friction factor experience the greatest wall temperature rise.

From figures 4.46 and 4.49, some rather dramatic and complex behaviour is apparent between 0-50mins for R6 and R7. Initially, there is a short period of very rapid wall temperature increase ($\approx 3.5^{\circ}\text{C}/\text{min}$), followed by a sudden drop in HN between 20-40mins. Figure 4.49 shows that the decrease in HN can be attributed to a sudden local decrease in wall temperature between 40-80mm from the outlet. The wall temperatures in this region continue to decrease until around 60mins, after which the temperature at 40mm begins an upward trend and no increase is seen for the rest of the test between 50-80mm. Towards the outlet (10-30mm), the wall temperatures increase but the rate of temperature rise is not constant. The rate of change seems to oscillate - being similar between 40-60mins and 100-120mins, but between 70-90mins the rate appears to reduce. The complexity of the behaviour prohibited any curve fitting to the data for the rough tubes, but for the EDM tubes, $\frac{d\text{HN}}{dt}$ was comparable to the EDM tubes tested in set 1 - the deposition rate was almost constant but reduced slightly over the course of the test. The initial wall temperatures for all the tubes are similar to the profiles seen for set 1. The average initial wall temperatures were 327°C , 369°C and 380°C for R6 / 7, EDM 8 / 9 and EDM 10 / 11 respectively.

In contrast to set 1, the EDM tubes in set 2 were slightly wider than the rough

tubes, resulting in lower exit Reynolds numbers. The maximum difference in Re across the set was 930. Since the trends between the tests are similar for both $D_{drawn} > D_{edm}$ and $D_{edm} > D_{drawn}$, it would seem that any effect on deposition from the change in tube diameter is small compared to the effect of deposition from increased roughness.

Set 3, Fuel B

For the final tests, the system pressure was increased to $25bar$ and the camera was positioned further from the capillary so that the measured length was increased. The drawn capillaries in set 3 show the typical deposition behaviour observed in previous tests on similar tubes. HN profiles for R8 - R11 have the characteristic three-piece shape, which is most obvious in the lower temperature tests of set 1 (R1 and R2). It is interesting to compare the time at which the rate of wall temperature rise across the tube begins to decrease. For R9 at $200^{\circ}C$, the decrease appears to start at 80 minutes, however for R8 at $230^{\circ}C$, decrease occurs at around 60 minutes into the test. The reason for the reduction in the rate of HN increase is evident in the plots of external wall temperature with time along the tube (fig 4.54). Both R8 and R9 have a reduction or hold off in wall temperature from around 40-50mm from the outlet, with the reduction occurring earlier for the test at higher temperature. Similar behaviour was observed for R1,R2 and to a much greater extent for R6 and R7. The rough tubes in these tests do not show the quasi-constant wall temperature observed for sets 1 and 2, despite the temperatures being of similar magnitude. The location of deposit formation also shows strong similarity with previous tests - most notably for R1 / R2 with R8 / R11 and R9 with R6 / 7 - where the deposit forms abruptly at 40mm from the outlet.

The initial wall temperatures for EDM 12 and 14 are quasi-constant and consistent with earlier tests. HN development for EDM 14 appears to show a multi-stage deposition process, which is quite the opposite of the drawn tube. This is also evident from the profiles of wall temperature increase with time across the tube, which are quite different from any other tests. After an initial rise in wall temperature at most locations (except near the outlet where a brief reduction in wall temperature occurred), the rate of temperature rise decreased between 20 - 60mins, before increasing again at all locations beyond 60mins. At 10mm from the outlet, where the wall temperature was lowest across the tube for the initial period, the rate of temperature increase was accelerated with respect to the rest

of the tube.

For EDM 12 (tested at 225°C), the HiReTS number profile and final HiReTS number were almost identical to R11. This is a unique result and is the one case in the study where a tube with slightly lower friction factor (although similar Nu) produced a higher wall temperature rise than the drawn capillaries. The result is interesting because it is contradictory. The tube was measured to have a comparable Nu to the drawn tubes, a higher friction factor than EDM tubes in set 1 or 2 (although still lower than the drawn tubes), the severity of deposition was similar to the tubes with comparable Nu and λ , yet the initial wall temperature profile still seemed to indicate substantial differences to the heat transfer coefficient. The initial wall temperature for EDM 13 was also unique. There was similarity with the drawn tubes, but the point of minimum wall temperature was located closer to the outlet. Either side of this position, the temperature increased rapidly. At the location of minimum wall temperature, the deposition was minimal, despite the temperature being similar in magnitude to the drawn tubes, for which the deposition at the same location was more significant.

Phase change phenomena

The near constant initial wall temperatures observed for both drawn and EDM tubes warrants further discussion. Since the flow is definitely not laminar over the measured length, the observation may only be explained by localised boiling at the wall - as noted for some tubes with heptane in the previous heat transfer study at much lower wall temperatures. Further possible evidence of localised boiling was an unusual noise during the EDM tube tests, originating from either the pump, pipework or tube and synchronised with the refill stroke of the piston pump, presumably when the system pressure was a minimum. The noise might be associated with the expansion of the vapour phase and was more subtle for set 3.

The vapour pressure for kerosene was estimated by curve fitting typical vapour pressure data for Jet-A1 (between 0 to 250°C) and extrapolating. The curve is shown in figure 4.62. At the system pressure of 20bar for sets 1 and 2, the saturation temperature ($T_{sat} \approx 355^{\circ}\text{C}$, and for 25bar , $T_{sat} \approx 375^{\circ}\text{C}$ - which would appear to coincide with the initial wall temperatures of the EDM tubes, but is somewhat higher than the average initial wall temperature of tubes R1 and R2. It is unclear why the drawn tubes should have near constant wall temperatures, since the wall temperatures are lower than the calculated saturation temperature.

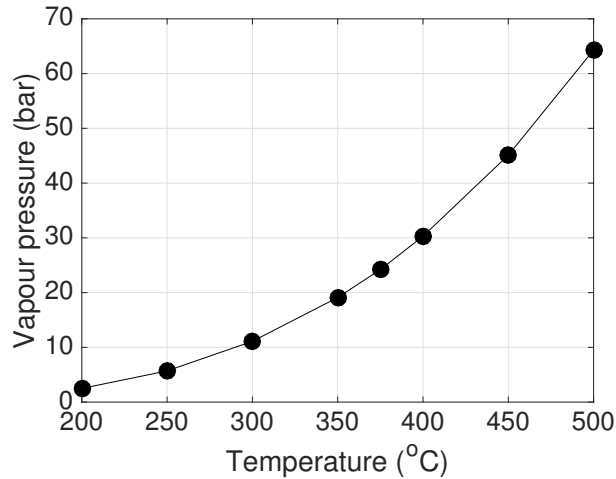


Figure 4.63: Extrapolated vapour pressure data for Jet-A1

It is also unclear as to why the temperature for tubes R3 and R4 in the 230°C tests was not constant with position, despite being higher overall.

Localised phase change at the wall further complicates the flow field, which already experiences large gradients in temperature and Reynolds number. When the formation of insoluble material is included, the flow essentially becomes three phase. Since the bulk fluid temperature is significantly below the saturation temperature, the boiling is subcooled. The excess temperature ($T_{excess} = T - T_{sat}$) is an indication of the severity of boiling - a process by which bubbles of vapour develop from nucleation sites at the wall and travel some distance towards the core flow by buoyancy forces. Boiling progresses from isolated bubble formation at low wall superheats to jets and columns of bubbles with increasing T_{excess} . With further T_{excess} , bubbles eventually coalesce in the centre of channels and confine the liquid phase to a film at the channel wall. Heat transfer is enhanced due to evaporation of the liquid film underneath a bubble during its growth, and increased convection due to bubble motion. Ultimately, the wall can completely dry at which point the wall temperature rapidly increases.

The subject of boiling in mini and micro channels was discussed recently by Karayiannis et al [119]. Surface roughness was shown to effect the uniformity of boiling. The cavities of rough walls create many more sites for bubble formation with respect to a smooth wall, for which the nucleation sites may be more non uniformly distributed - resulting in potentially large local fluctuations in heat transfer coefficient. The superheat at the onset of boiling has been found to reduce with moderate increases in roughness. In one case the wall superheat at the onset

Tube	$T_{f\ out}$	$T_{wall\ avg}$	Pressure (bar)	$\Delta T_{wall} - T_{sat}$
EDM 1	200	386	20	31
R1	200	316	20	-39
EDM 4	230	374	20	19
R3	230	337	20	-18
EDM 8	225	369	20	14
R 6	225	327	20	-28
EDM 11	225	380	20	25
EDM 12	225	384	25	9
EDM 14	200	364	25	-11

Table 4.12: Average external wall temperature compared to the extrapolated saturation temperature for Jet-A1

of boiling reduced by 50% with an increase in roughness (R_a) from 0.6 to $1\mu m$. This may explain why the drawn tubes seem to have flat temperature profiles despite having much lower average wall temperatures than the EDM tubes. The average initial external wall temperatures are compared to the estimated value of saturation temperature in table 4.13. The temperature drop through the tube wall is around $2^\circ C$.

The distance that the bubble travels in the radial direction before being condensed will be governed by the temperature distribution from the wall. Since the rough tubes have higher Nu than the smooth tubes, the radial temperature gradient will be higher and therefore it is expected that bubbles will condense more rapidly. For the smoother tubes, the vapour may persist further, and condense at greater distances from the wall.

It cannot be discounted that local boiling at the wall may have been a contributing factor to the reduced deposition over the smooth surfaces. However, the results of the $200^\circ C$ tests in set 1 may provide evidence that the boiling effect may be relatively minor in these experiments. Both drawn and EDM tubes had a constant wall temperature, yet the deposition for the drawn capillaries was still far higher. Furthermore, deposition for EDM 10 / 11 did not reduce with respect to EDM 8 / 9 despite the higher wall superheat. For set 3, where the system pressure was increased but boiling apparently still occurred for the EDM tubes, the HiReTS numbers were similar. It is not known how the presence of a vapour phase in the near wall region would effect the transport of insoluble material, but it seems unlikely that bubble formation would enhance deposition.

For tests which exhibited particularly high wall temperatures, it may also have been possible that the fuel was close to or beyond the critical point, where there is less distinction between the liquid and vapour phases and there may be significant changes to fluid density, viscosity and specific heat capacity. Edwards and Zabar-nick [120] noted that a reduction in deposition rate typically occurred around the critical point, with the critical temperature of kerosene being approximately 370°C and the critical pressure around 20bar , although the critical point was dependent on the range of hydrocarbon species present in the fuel. It was suggested that the decrease in deposition rate close to supercritical conditions may be a result of thermal decomposition of hydroperoxides (crucial intermediate reactants in the autoxidation chain) or that the solubility of the fuel may have been enhanced beyond the critical point. The authors conducted tests in a single tube heat transfer rig and found that the deposition rate was more dependent on residence time and heating rate than the critical temperature - concluding that a decrease in deposition rate at supercritical conditions was more an effect of fuel chemistry than some effect due to supercritical fluid properties.

Further analysis

Figures 4.55 - 4.59 show comparisons of wall temperature rise with time, change in initial Reynolds number across the measured length, the extent of the viscous and buffer layer across the measured length at $t=0$, and growth of deposit with time and position.

The bulk fuel temperature rise was calculated from the inlet by assuming a constant wall temperature (taken as the average initial wall temperature) according to;

$$T_{b(x)} = T_s - e^{(-\frac{\pi D L}{m c_p} h)} (T_s - T_{b,in}) \quad (4.2.21)$$

where T_b is the bulk fluid temperature, T_s is the surface temperature and h is the average value of heat transfer coefficient from inlet to outlet.

Re along the tube length was subsequently calculated using temperature dependent relations for kerosene density and viscosity from [56].

The physical extents of the viscous and buffer layers can be calculated with knowledge of the friction velocity, U^* ;

$$\text{Viscous : } y^+ = 5 = \frac{y U^*}{\nu} \quad (4.2.22)$$

$$\text{Buffer : } y^+ = 30 = \frac{y U^*}{\nu} \quad (4.2.23)$$

for which the measured values from the isothermal pressure drop experiments were used - matched as closely as possible to the Reynolds number at which they were taken. Three values for the viscous and buffer layer thickness were calculated for sets 1 and 2, and seven values for set 3 since the range of Re was increased for the pressure drop experiments on those tubes. The values were then fitted to a power law and extrapolated over the remaining length of the tube. The R^2 value of the fit was > 0.99 in all cases.

The deposit thickness was calculated in a piecewise fashion by splitting the tube length into control volumes and analysing the heat transfer in the radial direction. The analysis assumes that the temperature of the fuel wetted surface and the local convection heat transfer coefficient remain constant such that;

$$T_{w, t=0} = T_{dep, t=t} \quad (4.2.24)$$

$$h_{x, t=0} = h_{x, t=t} \quad (4.2.25)$$

At $t=0$, the radial thermal resistance is;

$$R_{(t=0)} = \frac{T_{ext(t=0)} - T_{bavg}}{\dot{m} c_p (T_{bout} - T_{bin})} = \frac{1}{\pi D L h} + \frac{\ln\left(\frac{r_{int}}{r_{ext}}\right)}{2 \pi k_{ss} x} \quad (4.2.26)$$

where k_{ss} is the thermal conductivity of 316 stainless steel and h , the local heat transfer coefficient can be calculated from;

$$h_x = -\ln \frac{T_{ext} - T_{bout}}{T_{ext} - T_{bin}} \frac{\dot{m} c_p}{\pi D x} \quad (4.2.27)$$

At $t = t$, with formation of deposit the total thermal resistance becomes;

$$R_{(t=t)} = \frac{T_{ext(t=t)} - T_{bavg}}{\dot{m} c_p (T_{bout} - T_{bin})} = \frac{1}{\pi D L h} + \frac{\ln\left(\frac{r_{int}}{r_{ext}}\right)}{2 \pi k_{ss} x} + \frac{\ln\left(\frac{r_{dep}}{r_{int}}\right)}{2 \pi k_d x} \quad (4.2.28)$$

where k_d is the thermal conductivity of the deposit ($\approx 0.15 \text{ W/mK}$) (ref).

Therefore, the change in thermal resistance at time t ;

$$\Delta R_{(t)} = \frac{T_{ext(t=t)} - T_{b\,avg}}{\dot{m} c_p (T_{b\,out} - T_{b\,in})} - \frac{T_{ext(t=0)} - T_{b\,avg}}{\dot{m} c_p (T_{b\,out} - T_{b\,in})} = \frac{\ln\left(\frac{r_{dep}}{r_{int}}\right)}{2\pi k_d x} \quad (4.2.29)$$

and the ratio of deposit radius to internal radius, $\frac{r_{dep}}{r_{int}}$ may be calculated by;

$$\frac{r_{dep}}{r_{int}} = e^{(\Delta R_{(t)} 2\pi k_d x)} \quad (4.2.30)$$

Deposit thickness

The 1D heat transfer model was verified against deposit thickness measurements taken from micrographs of axial samples of tubes from set 1. Typical micrographs of drawn and EDM tubes with deposit are shown in figure 4.60. In order to minimise the likelihood of releasing the deposit from the wall during the post test sectioning process, low viscosity epoxy resin was poured down the inside of the tube and the tube itself was set in resin. The tubes were then prepared according to the sample preparation method for SEM described previously. The technique was not entirely successful, and only some of the micrographs showed deposit in sufficient clarity to take measurements. For some of the drawn tubes cases, no deposit was visible whatsoever in the micrographs, which suggests that the deposit may have been removed in the sample preparation process. In other cases, mainly for the EDM tubes, the deposit layer seemed 'lifted' off the wall - which may have occurred perhaps due to some difference in thermal contraction between the deposit layer and the metal wall (the tube is rapidly cooled on completion of the test. Or, simply during unavoidable disturbance to the tube on removal from the rig or the sectioning and sample preparation procedure.

Figures 4.55 and 4.56 show that the calculated deposit thicknesses are in qualitative and quantitative agreement with the micrograph measurements - which were taken as the average of measurements at 4 positions around the tube. It is interesting to note the growth of deposit with respect to the height of the roughness elements. The drawn tubes have roughness peaks and roughs of approximately $15\mu m$ and according to the deposit thickness calculation, the deposit thickness exceeded $15\mu m$ at around 80-100 minutes for set 1 at $200^\circ C$ and $230^\circ C$, depending on the axial location. Thus, the deposit fills in the roughness significantly, and (as is evident in the micrograph shown in figure 4.60), after 2 hours, the roughness of the drawn tubing is completely engulfed in deposit. The deposit follows the underlying roughness shape, but it is clear that the direct effect of wall roughness diminishes with time as deposition increases. For tubes R3 and R4, the deposition

rate appears to reduce slightly beyond 60-80 minutes, as shown in figures 4.44 and 4.48. This would appear to occur around the time that the deposit thickness becomes approximately equal to the roughness height, with the effect being most noticeable at the top of the tube where the deposit thickness is at a maximum. It would seem entirely logical that the deposition rate would reduce when the roughness elements become completely embedded within deposit and cease to effect the fluid flow field - although further testing would be required to properly explore this theory.

The deposit growth not only fills in the roughness, but with small diameter tubes and high deposition rates, the deposit significantly reduces the diameter of the tube. In the case of tubes R1 and R2, the diameter was effectively reduced from $530\mu m$ to $478\mu m$ by the completion of the test. These tubes exhibited a peculiar yet repeatable reduction in deposition rate around the mid point of the tube from 80mins onwards, coinciding with a deposit thickness of approximately $10\mu m$. The profile minimum is located at $55mm$ from the outlet at $t=100mins$, and can be seen to further reduce and shift to around $60-65mm$ from the outlet at the completion of the test. If the reduction in wall temperature is indicative of transitional flow effects, then the shift towards the inlet would be consistent with an increase in Re as a result of constriction of the tube. The fact that both R1 and R2 reproduced the behaviour almost exactly would strongly suggest that the effect is firstly genuine, and secondly related to the relationship between tube diameter, change in Re from inlet to outlet and deposit growth rate.

Interaction with the turbulent boundary layer

The central plots of figures 4.55 - 4.59 show the change in thickness of the viscous and buffer regions of the turbulent boundary layer at $t=0$ along the measured length based on the increase in Re from inlet to outlet and the values of friction velocity calculated from the measured friction factors. Also included in the plot is a line corresponding to the typical roughness heights observed in the micrographs for the two types of tubes ($15\mu m$ and $2\mu m$ for drawn and EDM tubes respectively). The effect of increased Re as a result of bulk fluid temperature rise can be seen through the reduction in the extent of the viscous and buffer layers. For the rough tubes, it is clear that a viscous layer would not exist across the measured length, while for the EDM tubes, a viscous layer could remain intact over much of the tube, although it would be disturbed close to the outlet.

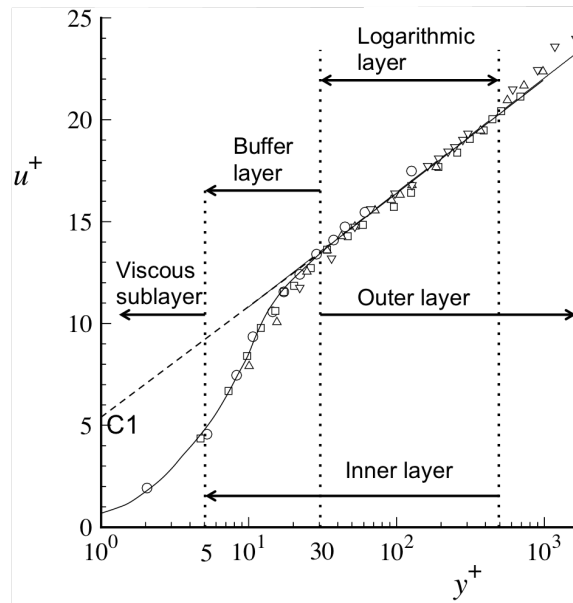


Figure 4.64: Universal mean velocity profile for the turbulent boundary layer

It is interesting to note the position of the intersection of the approximated roughness with the buffer and viscous layers with respect to the observed deposition behaviour. For example, in the case of tube R1, the roughness appears to protrude into the buffer layer at around 30-50mm from the tube outlet, beyond which the deposition is most severe. Similarly for R3, the increase in Re results in the buffer layer being pushed closer to the wall, and interacting with the roughness further from the outlet. In the R3 test, the deposit formed more broadly over the measured length, but the kick up in deposit thickness again appears around the point at which the non dimensional roughness height, k^+ would exceed 30. The most extreme behaviour was observed for R7 at $225^\circ C$, which was conducted with a much less stable fuel than the aforementioned tests. In this test, all of the deposit formed in the measured length occurred from 50mm from the outlet, which also coincides with $k^+ = 30$. Drawn tubes in set 3 also showed an abrupt rise in deposit growth for $k^+ > 30$.

There are no such abrupt changes in deposition for the EDM tubes in sets 1 and 2. However, for smoother tubes, the interaction of the roughness with the viscous layer may be observable in the data. In the case of EDM 1 at $200^\circ C$, the roughness should be contained within the viscous layer for almost all of the measured length. At around 40mm from the outlet, $k^+ \approx 3$ based on the measured friction velocity. From 40mm to the outlet, the initial wall temperature is seen to decrease, suggesting that the viscous layer may be disturbed, thus increasing heat transfer.

The thickest deposit occurred very close to the outlet, where the extent of the viscous layer was a minimum. In the case of EDM 6, the higher Reynolds number reduced the extent of the viscous layer such that $k^+ = 3$ at around $60mm$ from the outlet. In a similar fashion to EDM 1, from $60mm$ and closer to the outlet, the wall temperature decreased - suggesting improved heat transfer from interaction with more active turbulence, and the deposit thickness increased. A significant observation for EDM 6 is that although the wall temperature towards the top of the tube was lower than the mid point, the deposition was much more severe. Finally, for EDM 11, $k^+ = 3$ at $45mm$ from the outlet. Where the roughness encroached into the viscous layer closer to the inlet, the deposit thickness was higher, despite the wall temperature being near constant. For the third set, it is harder to gauge the interaction of roughness with the respective layers, because the micrographs and the friction factor results were contradictory. However there does seem agreement with the previous observations of increased deposition for upper regions of the tube where k^+ is high but the wall temperature is at or below the average wall temperature.

4.3 Tests with the JFTOT

4.3.1 Introduction

The JFTOT thermally stresses fuel in the laminar regime. As such it is not anticipated that the results from the device will demonstrate any effect on deposition due to the enhancement of momentum and heat transfer due to roughness (recalling the relation $\lambda = \frac{64}{Re}$ for laminar flow). However, since the deposit forming mechanism is thought to be metal-catalysed, an increase in the wall surface area may create more active sites for catalytic activity.

4.3.2 Establishing roughness data points

Testing was performed in collaboration with an industrial partner. For this reason certain details have been omitted. Tubes were manufactured via ALM with build angles from 0 to 90 degrees, representing the worst and best case scenarios (respectively) for surface finish. The heater tube design was modified from the standard JFTOT heater tube. The tubes were made as square sections with filleted corners, such that for each non vertical build there was an overhanging face (theoretical highest surface roughness), a top face (lowest surface roughness), and two 'control' sides which would have similar roughness. In effect, three roughnesses could be studied per test. In order to accommodate the square section, the tube had to be enlarged slightly.

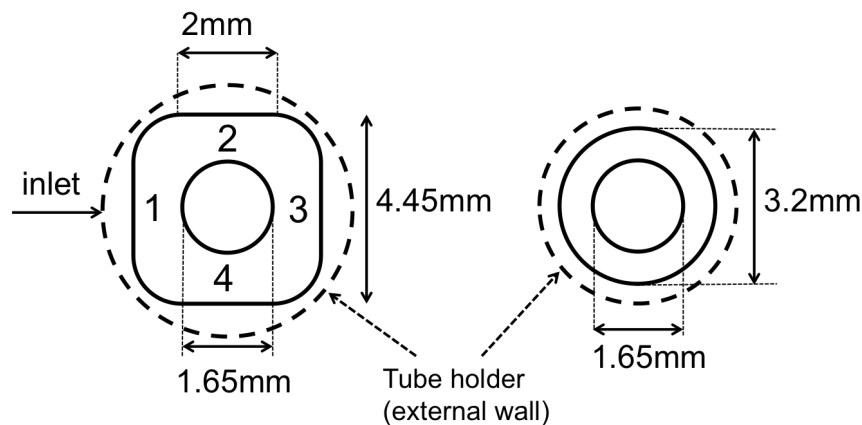


Figure 4.65: Modified JFTOT heater tube - cross section

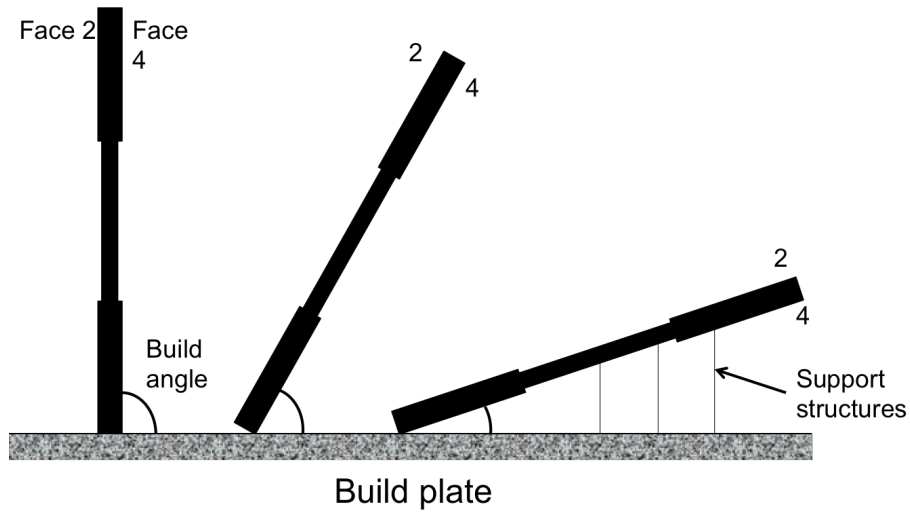


Figure 4.66: Illustration of build orientation in the ALM process

4.3.3 Roughness characterisation

As discussed previously, a particular convenience of the JFTOT is the annular test section, which allows the roughness to be measured easily by optical profilometry. The heater tube surfaces were measured by Vertical Scanning Interferometry (VSI). The areal roughness metrics quoted in this study are defined by ISO 25178 and are listed below. The data is tabulated and shown graphically in table 4.66 and figure 4.67.

S_a , the arithmetic average height;

$$S_a = \int \int_a |Z(x, y)| dx dy \quad (4.3.1)$$

S_q , the root mean squared height;

$$S_q = \sqrt{\int \int_a (Z(x, y))^2 dx dy} \quad (4.3.2)$$

S_p and S_v , the maximum peak and valley height;

$$S_p = \max_A z(x, y) \quad (4.3.3)$$

$$S_v = \min_A z(x, y) \quad (4.3.4)$$

S_{sk} , the skewness of the height distribution;

$$S_{sk} = \frac{1}{S_q^3} \int \int_a (Z(x, y))^3 dx dy \quad (4.3.5)$$

S_{ku} , the kurtosis of the height distribution;

$$S_{ku} = \frac{1}{S_q^4} \int \int_a (Z(x, y))^4 dx dy \quad (4.3.6)$$

S_{dq} , the root mean square surface slope;

$$S_{dq} = \sqrt{\frac{1}{A} \int \int_a \left[\left(\frac{\partial z(x, y)}{\partial x} \right)^2 + \left(\frac{\partial z(x, y)}{\partial y} \right)^2 \right] dx dy} \quad (4.3.7)$$

S_a and S_q are straightforward measurements of the average surface height but cannot differentiate between different surface textures and spacings. A surface with the same S_a or S_q could have substantially different surface features. S_{sk} and S_{ku} describe the distribution of roughness. A normally distributed surface roughness has $S_{sk} = 0$ and $S_{ku} = 3$. Negative skew indicates a surface with more valleys than peaks and vice versa. $S_{ku} > 3$ indicates a surface with abrupt features, while a surface with gradual changes in surface roughness will have $S_{ku} < 3$. S_{dq} evaluates the slope of the surface in all directions and is affected by roughness amplitude and spacing. For the same S_a , a surface with closed spaced features may have a higher value of S_{dq} than a surface with widely spaced roughness.

4.3.3.1 Profilometry results

Figure 4.67 shows the variation of the 3D surface metrics with build angle. The increase in surface roughness for the overhanging face (face 4) is clear to see in the values of S_a , S_q , S_p and S_v , particularly as the build angle increases beyond 45 degrees. At extreme angles, the average surface roughness is over twice that of the non-overhanging faces. For the face facing away from the powder bed, the roughness height decreases with build angle and the features appear to become more gradual - as shown by the decrease in S_{dq} . The roughness height of the side faces is unaffected by build angle. The surfaces exhibit little skew, indicating an even balance of peaks and troughs. The kurtosis for most faces changes little with build angle, although the distribution of roughness appears to focus around a tighter peak for face 2.

Build angle	Sa (µm)				Sq (µm)				Sp (µm)				Sv (µm)				Ssk				Sku				Sdq			
	1	2	3	4	1	2	3	4	1	2	3	4	1	2	3	4	1	2	3	4	1	2	3	4	1	2	3	4
90	18.4	12.8	14.2	17.0	22.6	17.0	19.0	21.0	81.3	88.6	88.0	95.0	71.9	54.1	98.6	79.8	0.4	1.4	1.3	0.4	2.8	4.8	4.9	2.8	3.3	2.8	3.0	3.1
90	20.1	13.3	12.5	17.0	24.6	17.5	16.6	21.0	95.0	77.2	85.2	81.0	66.6	61.5	53.9	71.4	0.6	1.3	1.4	0.5	2.9	4.6	4.9	2.8	3.5	2.6	2.6	3.2
90	19.0	13.2	14.2	17.4	23.5	17.5	18.1	21.5	95.5	98.6	87.5	90.0	79.8	85.5	56.3	90.6	0.6	1.4	1.2	0.4	2.9	5.0	4.0	2.9	3.6	2.6	2.5	3.1
avg	19.2	13.1	13.6	17.1	23.6	17.3	17.9	21.2	90.6	88.1	86.9	88.7	72.8	67.0	69.6	80.6	0.5	1.4	1.3	0.4	2.9	4.8	4.6	2.9	3.5	2.7	2.7	3.1
60	17.8	16.0	14.0	17.9	21.6	20.6	18.0	22.2	112.2	92.5	78.8	83.0	57.5	73.2	47.2	86.6	0.7	1.0	1.2	0.2	2.9	3.9	4.0	2.8	3.4	2.9	2.9	3.1
60	18.7	17.8	15.9	19.9	22.5	22.8	20.0	24.6	85.2	124.9	88.8	105.9	76.8	64.0	75.3	83.1	0.5	1.0	1.0	0.4	2.6	3.9	3.5	3.0	3.5	3.2	3.0	3.5
60	17.9	16.9	14.9	19.1	21.7	21.6	19.1	23.7	92.2	101.1	87.8	92.9	76.2	62.7	57.8	87.5	0.6	1.0	1.2	0.3	2.7	3.9	4.1	3.0	3.6	3.0	2.6	3.2
avg	18.2	16.9	15.0	19.0	21.9	21.7	19.0	23.5	96.5	106.2	85.1	93.9	70.2	66.6	60.1	85.8	0.6	1.0	1.1	0.3	2.7	3.9	3.9	2.9	3.5	3.0	2.8	3.3
45	18.7	16.6	19.4	22.9	22.7	21.9	23.3	28.1	78.0	115.0	76.2	102.8	73.3	63.0	81.5	106.8	0.7	1.1	0.5	0.0	2.7	4.5	2.4	2.7	3.1	2.9	3.3	3.4
45	17.7	16.4	20.2	20.6	21.8	21.6	24.6	25.7	80.0	130.5	101.0	95.9	67.7	89.5	82.2	89.0	0.9	1.1	0.7	0.1	3.2	4.8	2.9	2.8	3.1	2.7	3.5	3.1
45	15.9	15.5	20.3	23.0	20.2	20.6	24.6	28.9	93.5	109.1	95.7	117.3	52.6	63.1	72.7	103.3	1.2	1.2	0.8	0.2	4.0	4.7	2.9	3.0	2.8	2.9	3.5	3.6
avg	17.4	16.2	19.9	22.2	21.6	21.4	24.2	27.6	83.8	118.2	91.0	105.3	64.5	71.9	78.8	99.7	0.9	1.2	0.6	0.1	3.3	4.7	2.8	2.8	3.0	2.8	3.4	3.4
30	16.3	15.0	18.6	31.2	20.2	20.4	22.8	38.8	99.0	101.3	85.5	146.0	67.4	71.3	81.0	123.7	0.9	1.3	0.9	0.1	3.4	5.2	3.2	2.8	2.8	2.8	3.3	4.8
30	16.7	15.0	17.9	34.9	20.5	20.8	22.3	42.9	94.8	113.4	91.5	150.3	61.4	76.3	76.9	141.9	0.8	1.4	1.0	0.2	3.0	5.8	3.4	2.7	2.9	2.8	3.6	4.9
30	19.0	16.3	16.1	33.3	23.4	22.3	20.3	41.2	95.1	137.1	78.5	167.7	90.4	72.2	77.7	135.0	0.7	1.3	1.1	0.2	2.9	5.2	3.7	2.8	3.5	2.8	2.9	4.6
avg	17.3	15.4	17.5	33.1	21.4	21.2	21.8	41.0	96.3	117.2	85.2	154.6	73.1	73.2	78.6	133.5	0.8	1.3	1.0	0.2	3.1	5.4	3.4	2.8	3.1	2.8	3.3	4.8
15	18.6	11.5	17.9	41.4	22.6	16.0	21.6	51.3	100.2	83.2	109.1	167.9	77.5	56.9	72.7	218.3	0.1	1.4	0.6	-0.2	2.5	5.9	2.7	2.9	3.3	1.7	3.0	5.2
15	17.2	9.9	17.0	31.4	20.9	13.9	20.4	39.6	60.0	77.5	61.8	118.7	82.1	43.1	75.7	206.8	0.0	1.4	0.5	-0.4	2.5	5.9	2.6	3.2	2.8	1.3	2.6	3.7
15	19.3	11.0	17.1	38.1	23.4	15.7	21.4	47.3	80.4	85.0	80.6	177.0	80.3	54.4	58.8	214.2	0.6	1.5	1.0	0.1	2.7	6.5	3.4	3.0	3.4	1.8	3.0	4.9
avg	18.4	10.8	17.3	37.0	22.3	15.2	21.1	46.1	80.2	81.9	83.8	154.5	79.9	51.5	69.1	213.1	0.3	1.4	0.7	-0.1	2.6	6.1	2.9	3.0	3.2	1.6	2.9	4.6
0	19.4	3.2	13.5	41.2	23.5	4.3	18.1	56.1	106.9	43.4	102.6	245.8	80.6	21.9	52.7	220.3	0.5	0.5	1.5	0.2	2.8	7.6	5.6	4.1	3.4	0.3	2.7	5.5

Figure 4.67: Profilometry data - ALM JFTOT heater tubes

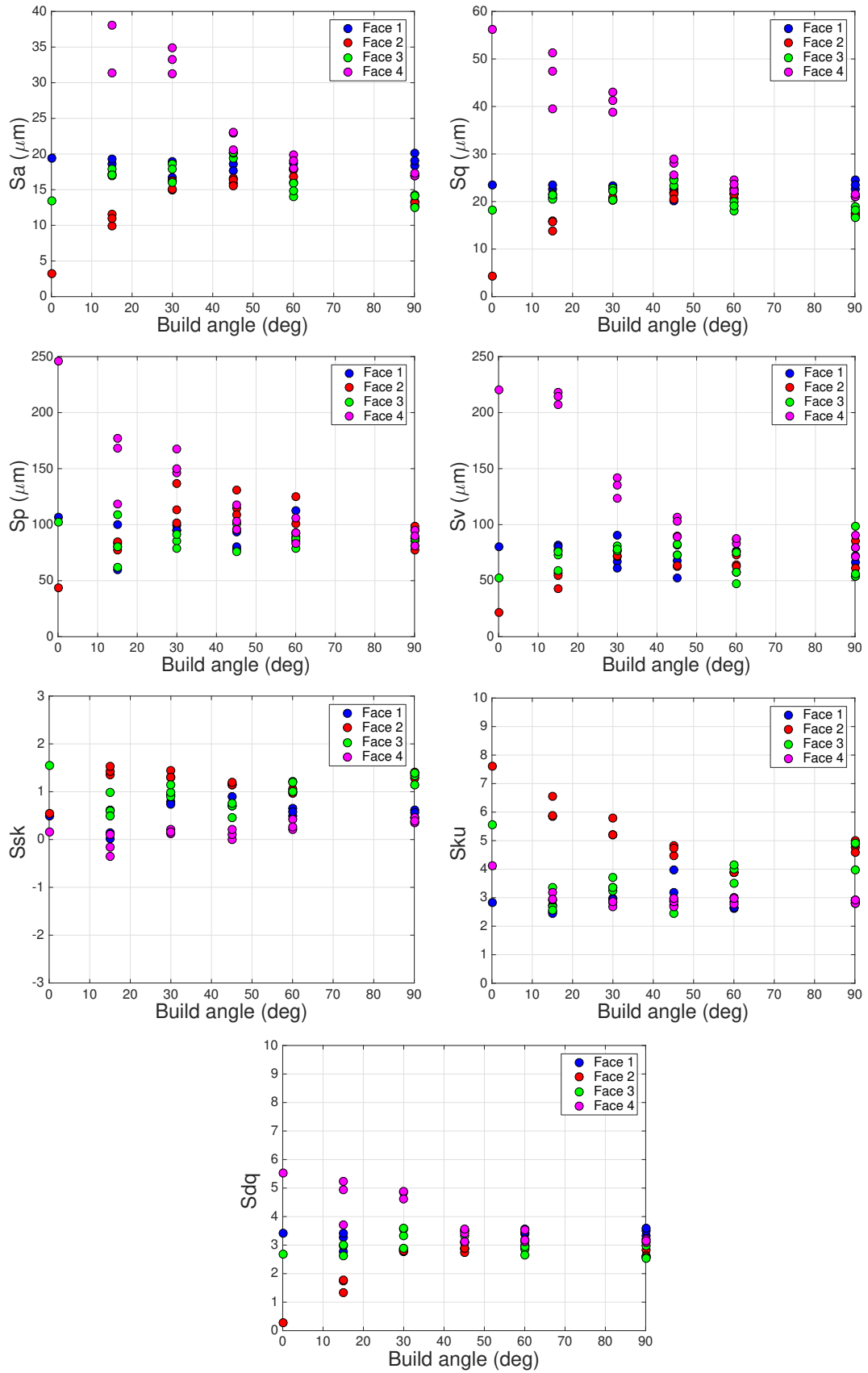


Figure 4.68: Roughness metrics for ALM surfaces by optical profilometry

4.3.4 Deposit quantification

One substantial stumbling block in the assessment of the deposit with the JFTOT is the method of deposition quantification, which has historically been by visual rating. recently, ellipsometry and interferometry have been added to the standard method as much improved techniques of deposit thickness quantification, although these methods rely on highly polished substrate surfaces and thus are not applicable to rough tubes. Similarly, the reference colour chart for grading via the standard visual rating scheme (figure 4.68) is not particularly applicable either, since the surface of rough ALM parts are not reflective. In an attempt to increase the yield of information from the testing, a method was developed to quantify the severity of deposition through image processing.

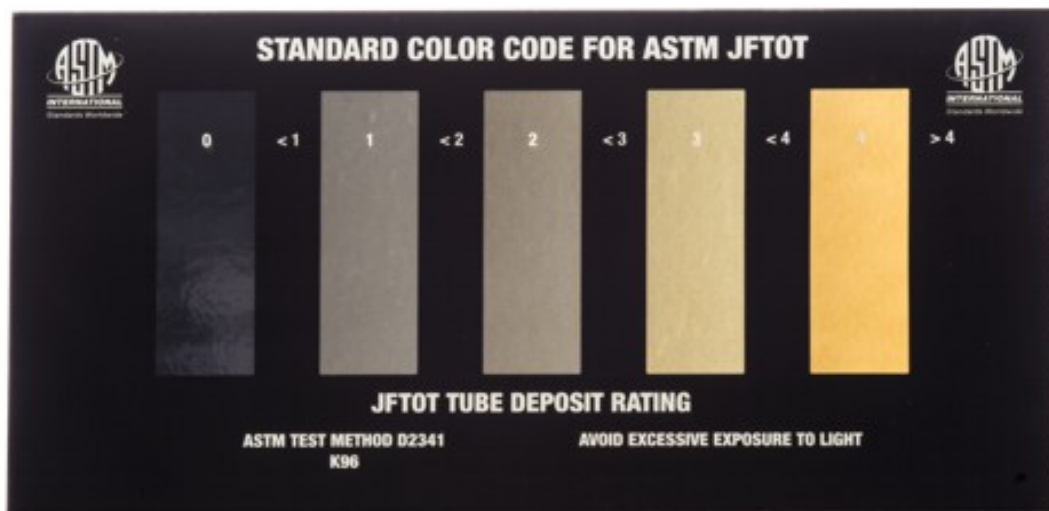


Figure 4.69: ASTM D3241 visual deposit colour reference chart

4.3.4.1 Image capture

In order to capture highly detailed images of the tubes, it was important to use a lens with high sharpness and low noise. An Asahi-Pentax 55mm, f1.8 lens was found to have suitable optical characteristics. The lens was attached to a Pentax K-30 digital single lens reflex camera, producing images with a final resolution of 4928 x 3264 pixels. Camera shutter speed, ISO and aperture were kept constant. All images were captured in uncompressed RAW format (with no further processing by the camera) and converted to uncompressed '.tiff' format. RAW conversion settings were fixed, with no further exposure compensation.

The lighting under which the photographs were taken was required to be as consistent and repeatable as possible in order to make the most valid comparison between the tested tubes. A light box (30 x 30 x 30cm) was constructed of 3mm white translucent acrylic, which served to diffuse light from the source. This diffusion box was placed inside another box, around the circumference of which were placed several equally spaced strips of high power white LEDs, with a stated colour temperature of between 4000 - 4500kelvin. There were approximately 40 LEDs per side. Best results were achieved with a spacing between the light source and diffusion screen of around 4cm. It was hoped that by using many, small, opposing point sources of light, shadows would be minimised.

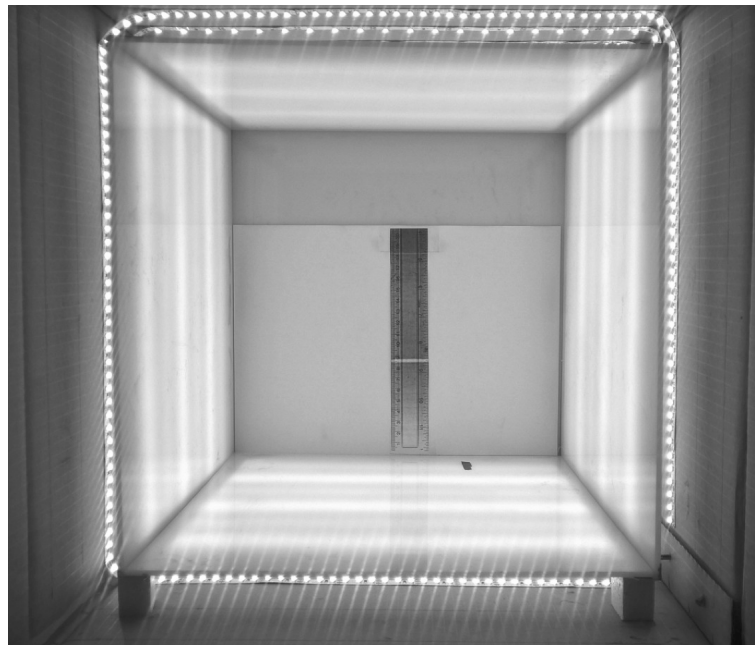


Figure 4.70: Lightbox

4.3.4.2 Image post processing

Post processing of the images was performed in Matlab. The method exploits the RGB additive colour model, which allows a unique colour to be described by a combination of three integers (with limits 0 to 255). The integers represent the intensity of red green and blue. For example, the RGB triplet for pure white is [255,255,255] and black is [0,0,0].

To begin, the colour image was converted to greyscale to reduce the three component RGB colour profile to a single profile of grayscale intensity. No difference was found in practice between the three channels, and in effect the data was

substantially reduced with no loss of information. Values of grayscale intensity were then extracted from the image along three lines along the centre of each tube face, spaced approximately 1mm apart. Data from the three lines was averaged to create a single profile of grayscale intensity. To reduce the noise, the data was passed through a locally weighted linear regression filter in Matlab. Finally, the profile values were subtracted from a 'baseline' value of grayscale intensity - taken as the average of the bottom half of the tube. The change in colour from the deposit could then be described numerically, relative to the unstained lower portion of the tube according to;

$$\Delta I_G = \left[\frac{1}{n} \sum_{n=1}^{n=1000} I_G \right] - I_G \quad (4.3.8)$$

where I_G is the filtered value of grayscale intensity and n is the number of pixels with $n=1$ at the inlet. Since the colour of the tubes was not constant, this approach effectively represented the change in tube colour with respect to the base metal colour of the tube. An example of the result from image processing is shown in figure 4.70. The image processing allowed three values to be extracted from the image; $\Delta I_{G_{max}}$ - the maximum change in grayscale intensity with respect to the base metal, $x_{\Delta I_{G_{max}}}$ - the location of maximum colour change and $x_{\Delta I=0}$ - the location where the grayscale intensity becomes equal to the averaged value from the lower portion of the tube. These values could, in theory quantify the strength and location of the maximum deposit as well as the location of the onset of deposit.

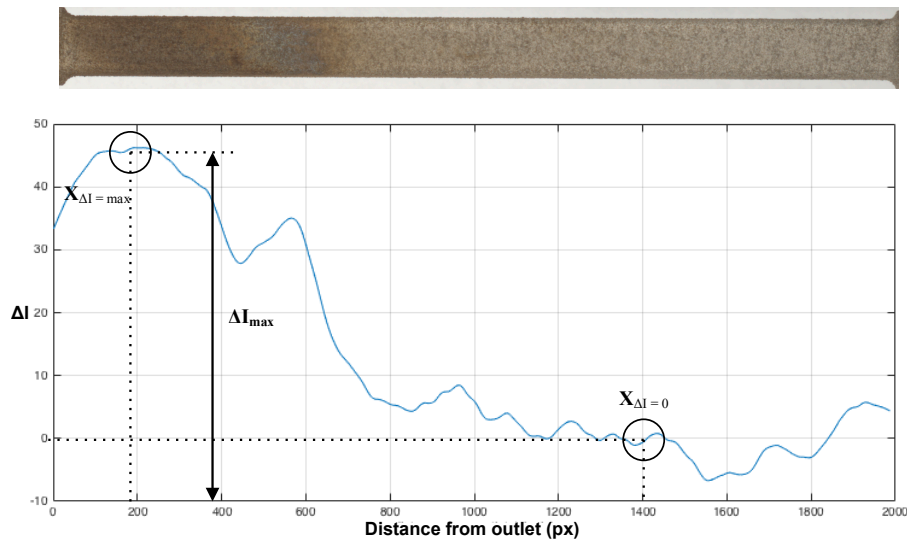


Figure 4.71: Image processing example

4.3.5 Deposition tests

4.3.5.1 Apparatus

A JFTOT mk2 was used with a modified tube holder to accommodate the custom heater tubes. A schematic of the flow path is shown in figure 4.71. It was found that further modifications were necessary in order to increase the power supplied to the tubes in order to achieve the desired test temperature. The fuel used in the testing was the same as for the HiReTS tests (Fuel A) described previously.

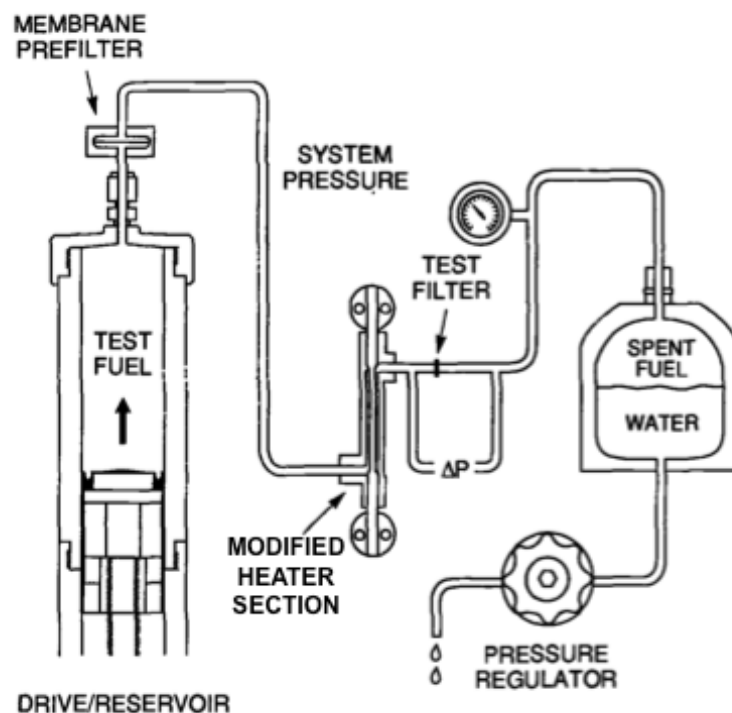


Figure 4.72: JFTOT flow path

4.3.5.2 Sources of uncertainty

The JFTOT does not have any direct measurement of deposition. Any visual comparison of the tubes must be considered to have a high degree of subjectivity.

The reproducibility of the conditions for the image capture was of paramount importance. All camera settings were recorded and kept constant to ensure consistent exposure. The images were taken in uncompressed RAW format and subsequently converted to uncompressed 'tiff' format using consistent RAW conversion settings. To achieve the correct white point, the white balance was adjusted to the midpoint of the quoted kelvin range of the LEDs. Voltage to the light box was provided

with a power supply to ensure consistent power was supplied to the LEDs. The base tube colour did vary appreciably, even for the same material which is likely to introduce some error.

To verify the reproducibility of the image capture, duplicate images were taken of the same tube with deposit on separate days. The results showed good agreement and confirmed the consistency of the lighting conditions.

4.3.5.3 Method

Tests were performed under standard conditions at 280°C (tube internal wall temperature). Aerated fuel was pumped at $3\text{ml}/\text{min}$ at 34.5bar for 150mins through an annular test section with a central resistively heated test tube. The test temperature was controlled to the maximum tube internal wall temperature, measured by a single thermocouple positioned inside the tube. The position of maximum tube wall temperature (thermocouple position) for the modified heater tubes was established prior to testing. The increased mass of some of the tubes meant that several preheating stages were required before the device was able to heat to the required tube wall temperature. Following completion of the test, the tubes were left to dry. Once dry, the tubes were photographed.

4.3.5.4 Results

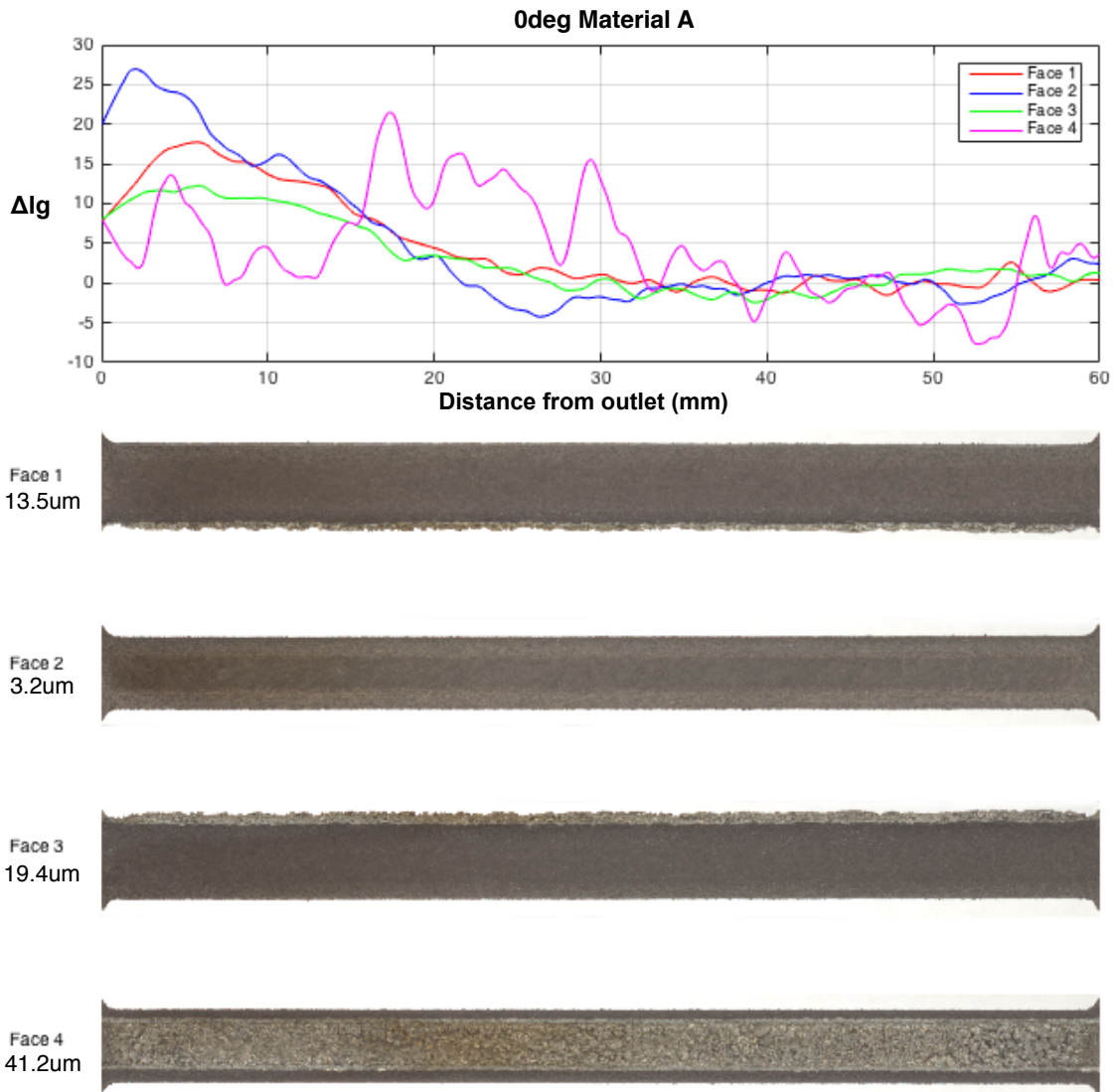


Figure 4.73: 0 degree build

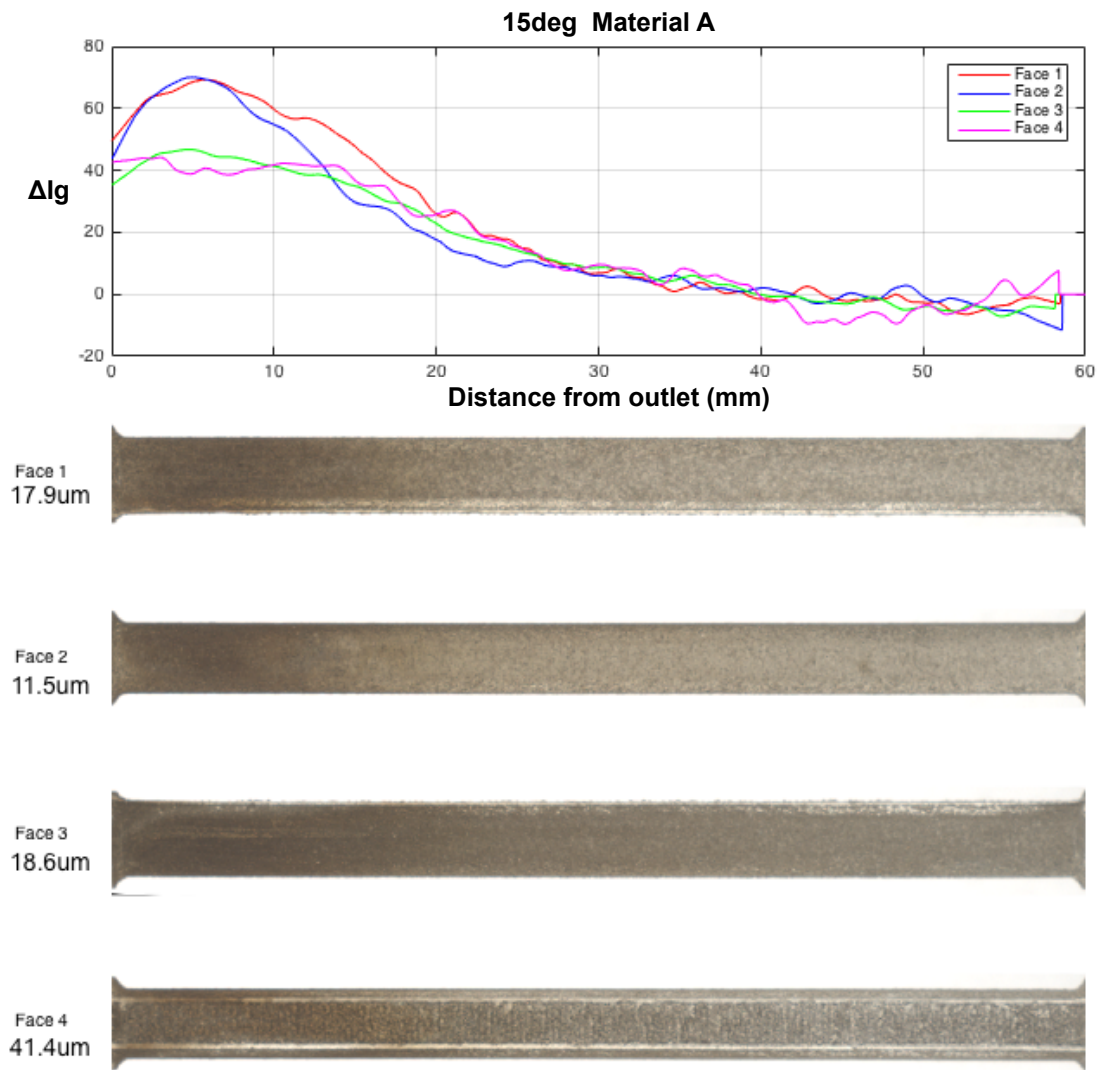


Figure 4.74: 15 degree build

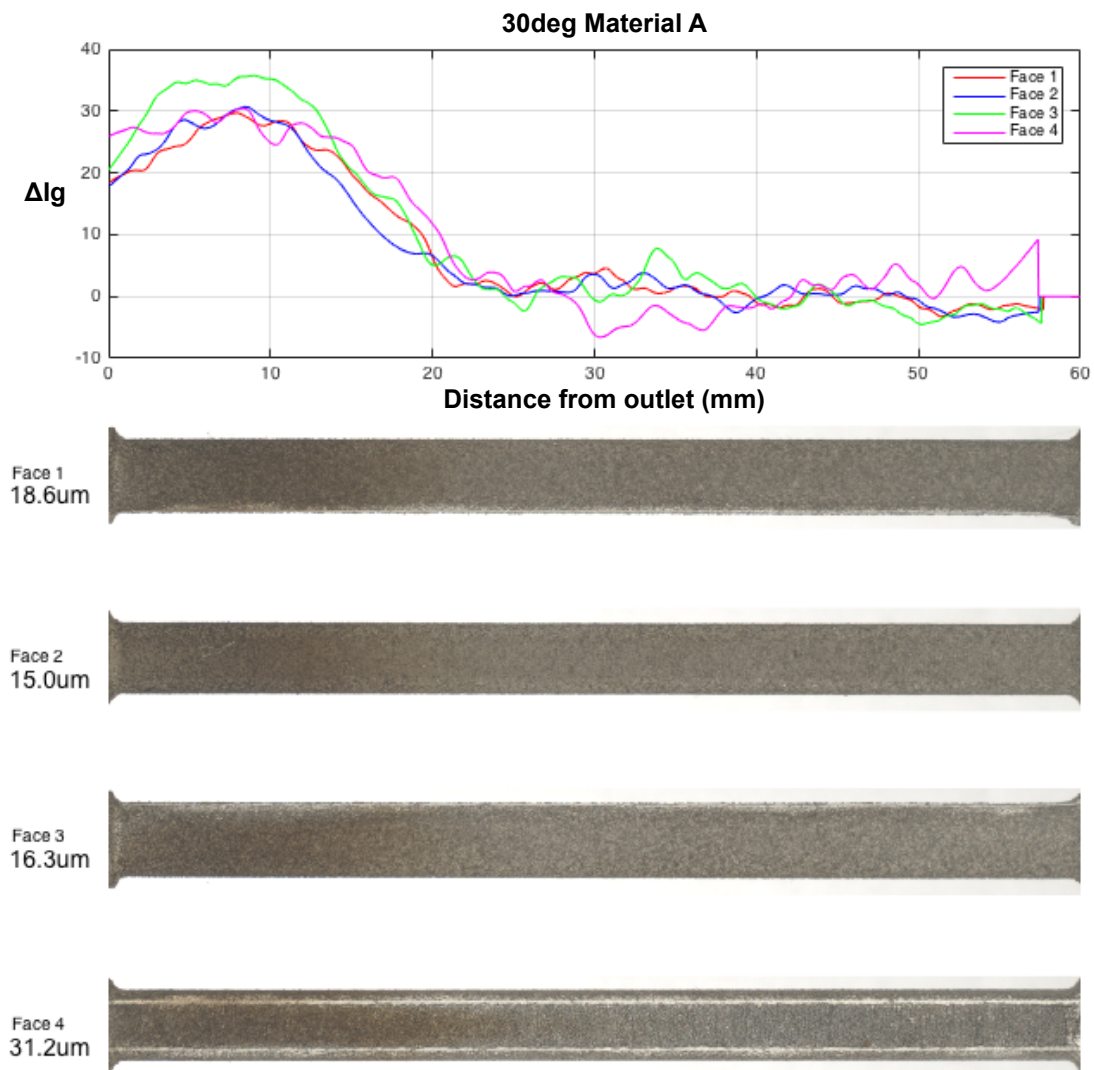


Figure 4.75: 30 degree build

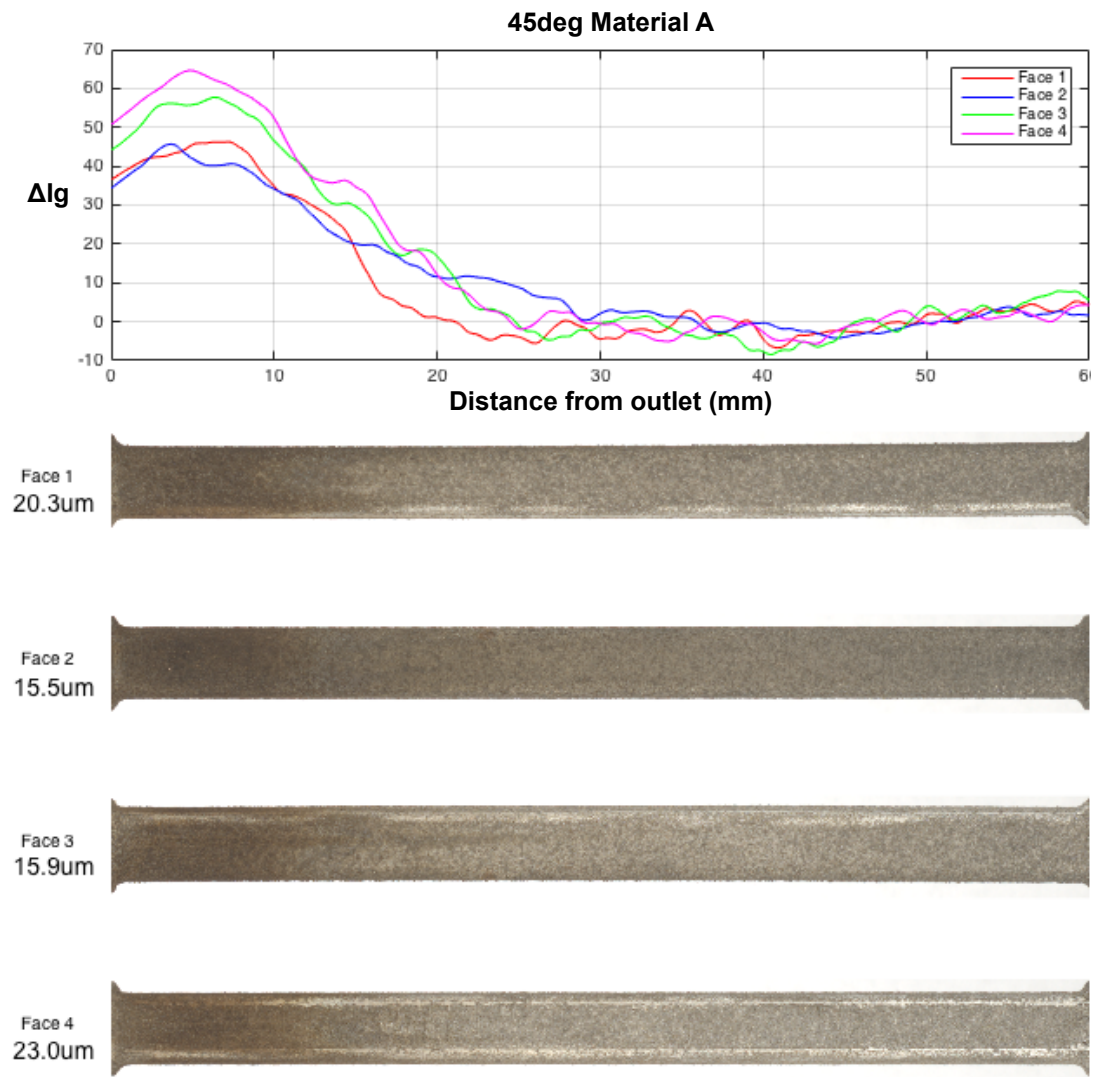


Figure 4.76: 45 degree build

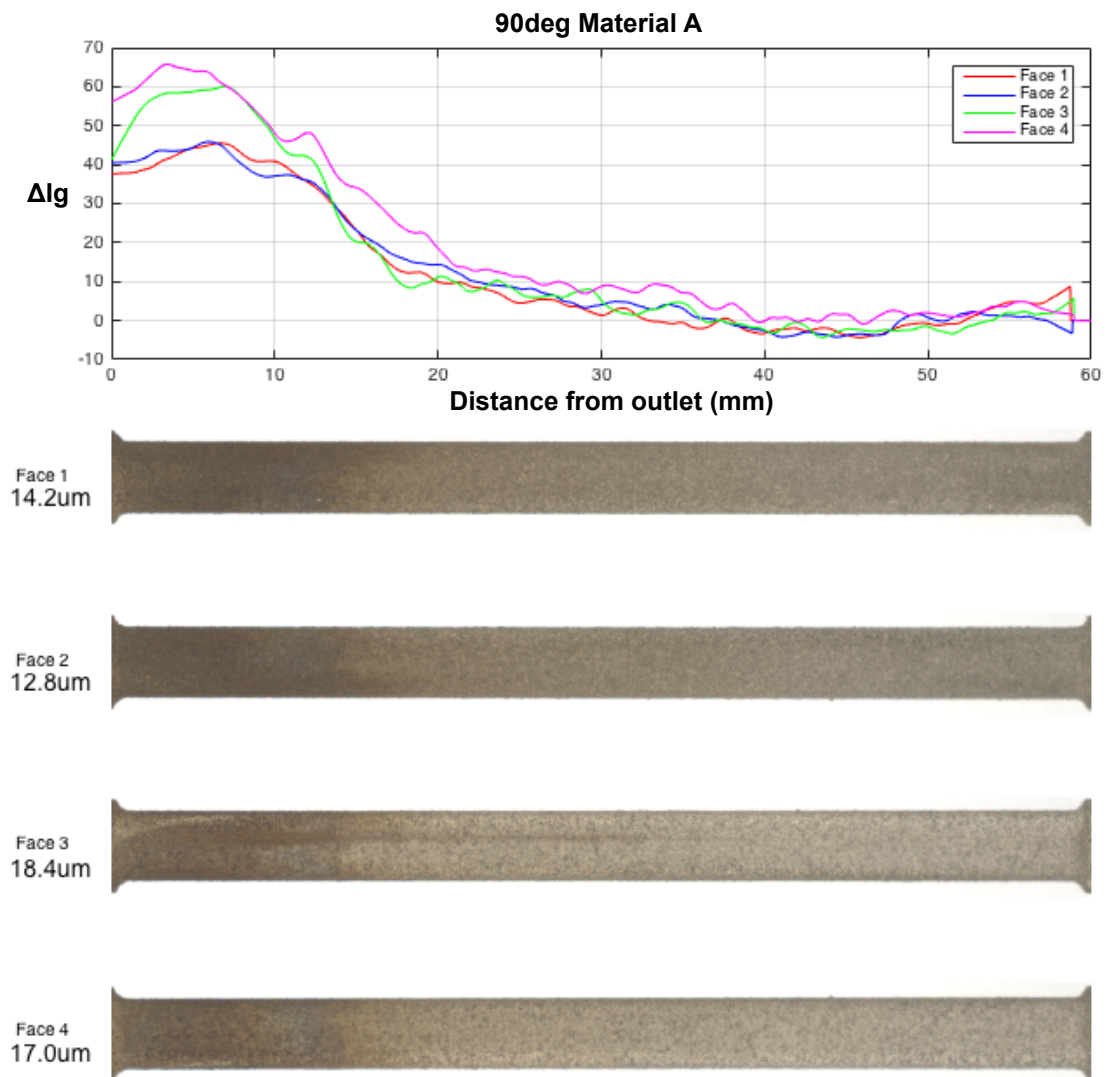


Figure 4.77: 90 degree build

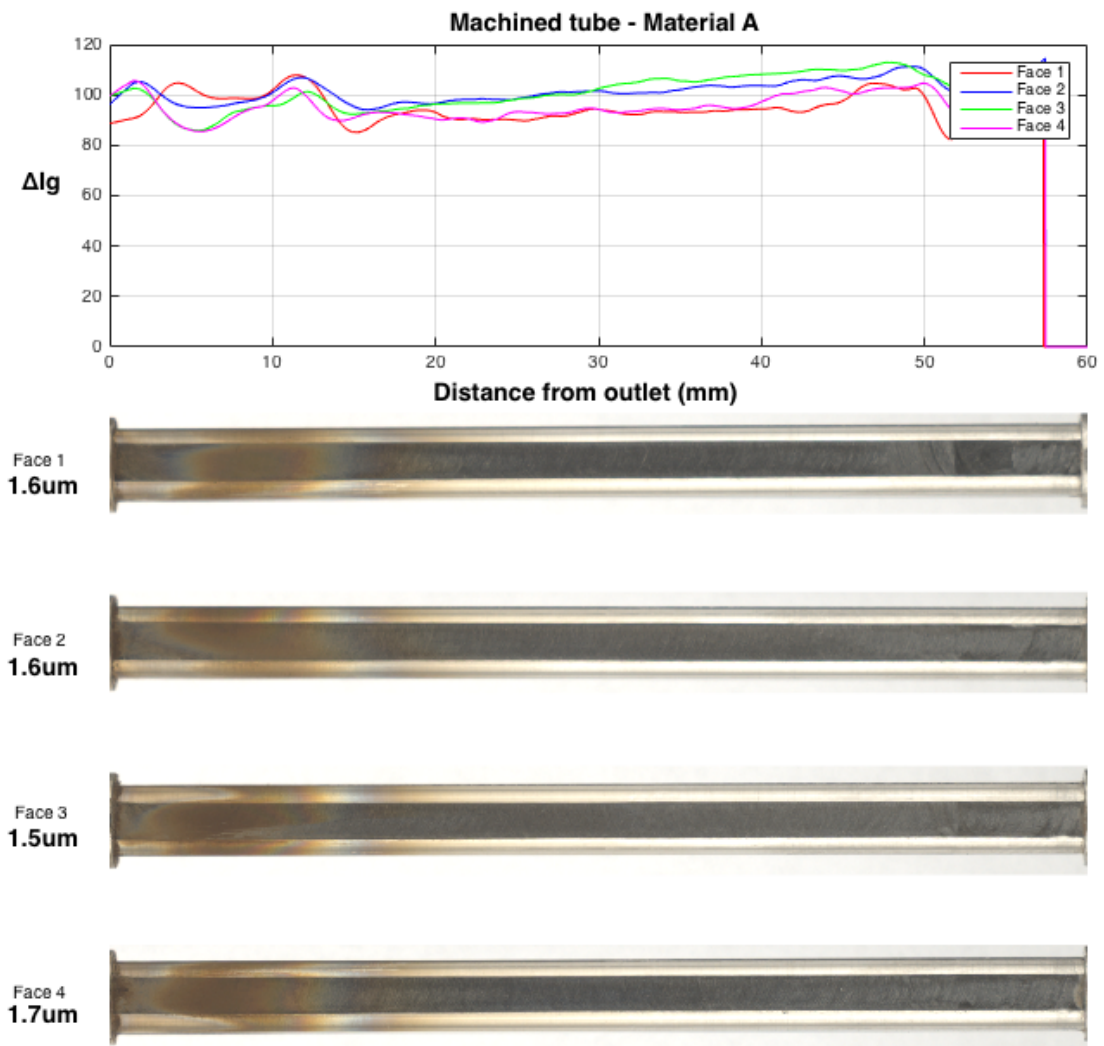


Figure 4.78: Machined tube

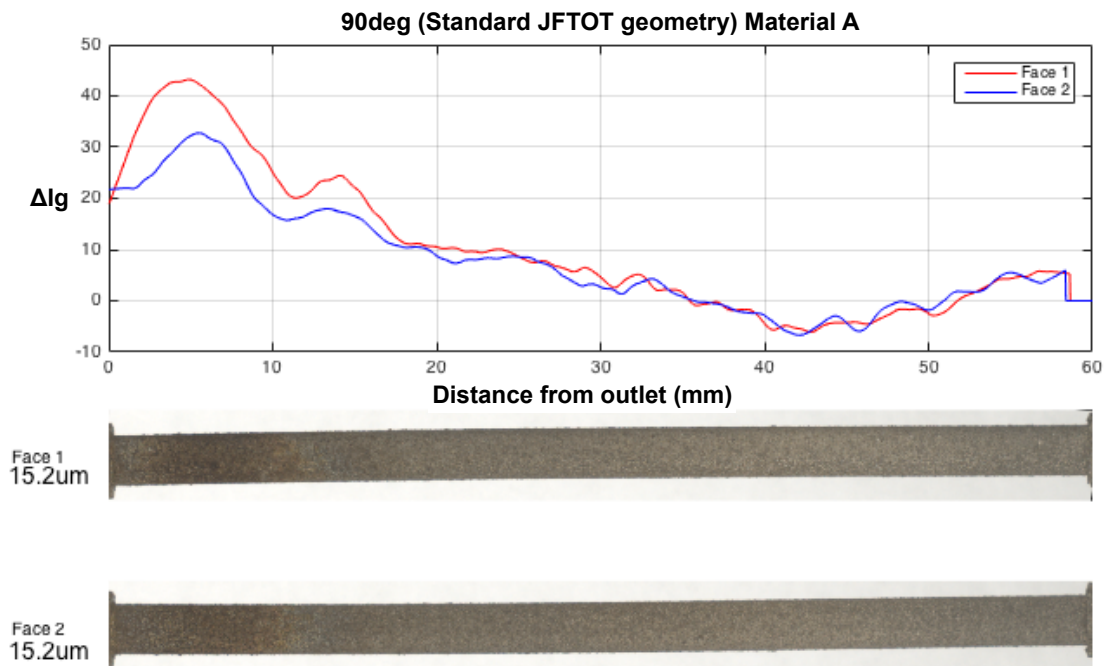


Figure 4.79: ALM tube - standard JFTOT geometry

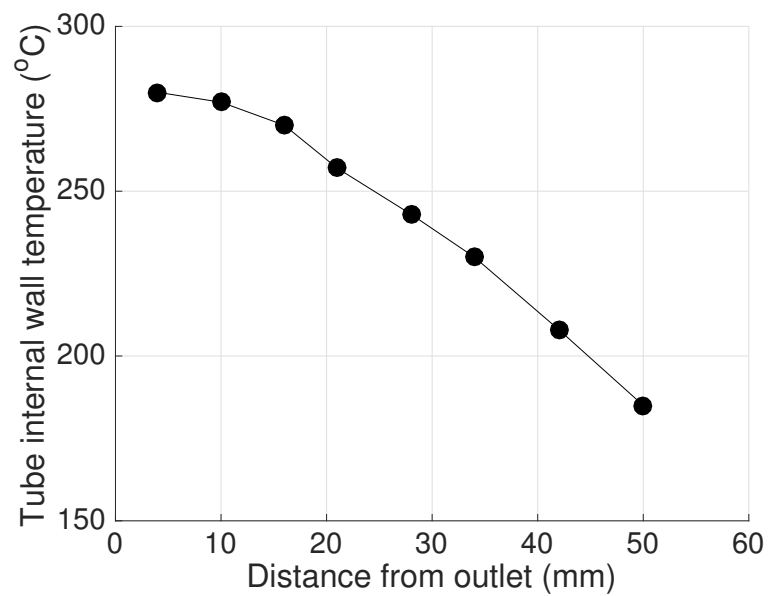


Figure 4.80: Internal wall temperature with axial position

Table 4.13: ALM tube image processing results

Build angle	Face	Sa (μm)	$\Delta I_{G \text{ max}}$	$I_{G \text{ min}}^*$	x (ΔI_{max}) from top (mm)	x (ΔI_0) from top (mm)
0	1	13.5	18	83	5.7	31.7
	2	3.2	27	78	2.0	21.6
	3	19.4	12	81	5.8	27.0
	4	41.2	22	106	17.3	7.3
15	1	17.9	69	92	5.8	39.0
	2	11.5	70	89	4.9	41.9
	3	18.6	47	83	4.7	39.8
	4	41.4	44	100	2.9	39.8
30	1	18.6	30	90	7.9	25.1
	2	15.0	31	92	8.4	37.3
	3	16.3	36	95	8.9	24.4
	4	31.2	30	95	8.3	28.2
45	1	20.3	46	92	7.1	21.1
	2	15.5	46	79	3.6	35.8
	3	15.9	58	90	6.3	24.7
	4	23.0	65	90	4.8	24.4
90	1	14.2	46	89	6.7	32.9
	2	12.8	46	89	5.9	37.3
	3	18.4	60	100	6.9	36.2
	4	17.0	66	95	3.4	39.3
90 (Ref)	1	15.2	43	81	6.7	35.4
	2	15.2	33	85	5.5	35.7

* (lower = darker)

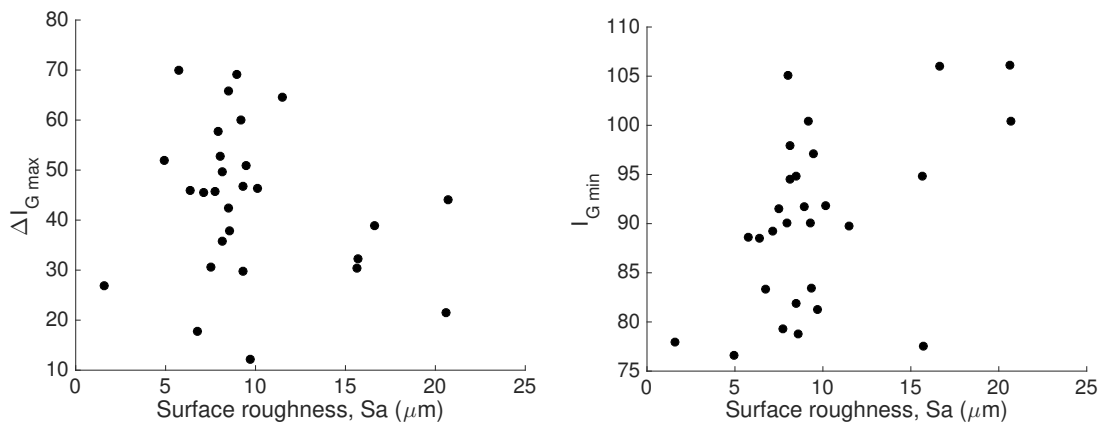


Figure 4.81: Left: maximum change in grayscale intensity. Right: absolute value of grayscale intensity (lower is darker)

4.3.5.5 Discussion

As a first step, the photographs alone will be considered for a qualitative comparison between tubes. The image analysis data will then be assessed with respect to the images themselves, and finally, the values extracted from the post processing shall be discussed. A relative increase in deposition would be likely confirmed by a more intense change in colour with respect to the base metal (increased darkening) and / or a shift in deposit starting location towards the inlet (deposition occurring lower down the tube at lower temperatures).

Qualitative comparison

Firstly, it is interesting to note the variation in the base metal colour between the tubes. The 0 degree and 15 degree tubes for instance are distinctly different, as are the 30 degree and 90 degree tubes. Since every effort was made to keep the photographic conditions constant, it seems that the variation in tube colour is either a result of some conditions during the ALM process (possibly related to the powder or the thermal environment around the part) or from heating during the JFTOT test. This presents something of a challenge for assessing the relative darkening between surfaces of different substrate colours.

The perpendicular build exhibits the smallest difference in surface roughness between the faces and similar deposition patterns are seen for each face. The deposit starts to become noticeable at around 20mm from the outlet. The deposit profiles on the 45 degree tube are also highly similar although the deposition appears more abrupt. The onset of deposit is quite clear at approximately 17mm from the outlet. At 30 degrees from horizontal, the deposit on the overhanging face with $S_a = 31.2\mu m$ would appear to extend slightly further from the outlet. The other three faces display almost identical deposition patterns. The 15 degree tube again displays comparable deposition patterns across all four faces. The deposit is distinct, and the peak of the colour change would appear to occur at the same point for all faces. There does not seem to be particularly enhanced deposit for the overhanging face, despite being considerably rougher than face 4 of the 30 degree build.

Face 4 of the horizontally build tube exhibits the highest roughness used in this study, which is plain to see in the images, when compared to faces 1 - 3. The base metal colour on faces 1 - 3 is for some reason darker than face 4, which complicates a comparison of the change in colour. It is difficult to detect any deposit by eye on faces 1 and 3. Face 4 would appear to have deposition further

from the outlet than has been seen in any other case.

A machined tube of the same material and geometry was also tested for comparison. The deposit formed in the same location as the EDM tubes. It is difficult to comment on the severity of deposition on the machined tube with respect to the EDM tubes since the substrate is highly reflective, as opposed to the matt finishes of the EDM tubes. Nevertheless, the deposit formation is clearly significant, and would probably rate at least 4 on the standard JFTOT colour rating scale.

Quantitative comparison

Two quantities were generated which could represent the 'intensity' or depth of deposit - ΔI_{max} and I_{Gmin} . Values for each face are provided in table 4.14. These two values represent two approaches that may be adopted when considering the colour change from deposition. While ΔI_{Gmax} provides a single value for the maximum amount of darkening relative to the base metal colour (or baseline value of grayscale intensity), I_{Gmin} is simply the minimum value of grayscale intensity (lower numbers are darker) recorded on the tube face and does not take into account the initial substrate colour.

In many cases, the profile of ΔI_G seems to provide a good representation of what can be seen by eye. Peaks on the charts generally match well with the deposit location and intensity. For some tubes, features of the deposit are clearly shown in the chart. For example, the 90 degree tube - where the chart picks out the just visible second band of deposit as a peak, between 10-15mm from the outlet on faces 3 and 4. The analysis seems to be most effective for the cases of lowest roughness (90 degree builds and faces 1-3 for all builds), where the base metal colour is most uniform. The analysis does not perform well in the cases of high roughness. It is clear that the enhanced contrast and optical noise of these surfaces makes analysis by colour change very difficult.

Data for the single standard geometry reference tube (figure 4.78) adds to the supporting evidence for the suitability of the post processing method for tubes of consistent base metal colour. In this case, the tube faces represent the two hemispheres of the circular section. The chart of ΔI_G bears good resemblance to the pattern of deposition that can be discerned by eye. The darkening on face 1 appears marginally more advanced than face 2, and this is shown by a difference in ΔI_{Gmax} . For this tube, the profiles of ΔI_G for both sides show a very high

degree of similitude.

With regard to ΔI_{Gmax} , it would seem that this value is strongly dependent upon the baseline metal colour. Values for Faces 3 and 4 of the 90 degree tube are significantly higher with respect to faces 1 and 2, but the base metal colour is visibly lighter, thus the colour change is greater for presumably the same thickness of deposit. Where the base metal colour is very similar between faces, the value of ΔI_{Gmax} would seem to be much more appropriate. The 30 degree tube is a good example of the analysis being more repeatable when the tube faces are more consistent in colour.

Deposit peak and onset location

The deposit peak location, $x_{\Delta I_{max}}$ derived from the image processing would appear to exhibit a good degree of accuracy. This value is not reliant upon relative colour change and can be compared to the measured wall temperature profile to provide temperature context to the final deposit profile. The location of deposit onset, $x_{\Delta I=0}$ is of greater interest; since this would provide insight into the lowest temperature that appreciable deposit is formed at. This value effectively provides an indication of the point at which the colour becomes equal to the averaged base metal colour. Due to the high degree of noise in the raw data, even after filtering there is substantial waviness which strongly effects this value. Some exceptions exist, notably the 15 and 90 degree tubes, which could provide approximate locations of the start of deposit. However, the unsuitability of this method to produce a single value for deposit onset location for surfaces with high levels of noise is clearly evident for the majority of cases.

Summary

Figure 4.80 shows the values of ΔI_{Gmax} and I_{Gmin} (lower is darker) against surface roughness measured over the area (S_a) of each face. No correlation is apparent for either value. This would be consistent with the conclusion that may be drawn from a visual assessment of the deposit. The majority of faces show no difference. One notable exception is the overhanging face on the 0 degree tube, for which the deposit seems to have shifted slightly towards the outlet. However, the stain is faint, and the substantially different colours on the tube and the complexity of the roughness (in texture and colour) prevent conclusions being drawn from the test with any real confidence. The machined tube, with very low roughness seemed to deposit no less than the ALM tubes. For the material and roughnesses considered

here, an increase in surface area did not significantly enhance deposition.

4.4 Tests with the AFTSTU

4.4.1 Introduction

The AFTSTU is the largest scale thermal stability rig at the Low Carbon Combustion Centre and most representative of an aircraft fuel system, with the highest 'technology readiness Level' (TRL). A description of the early incarnations of the rig can be found in appendix A. The present version follows the same design philosophy, featuring low and high pressure sections, low and high temperature regions with the option of fuel preheating, spill loops for recirculation, metering valves, orifices, screens and filters of various gradings and ultimately, simulated injector feed arms. The typical fuel flow rate is 23l/hr , resulting in turbulent flow throughout and tests may consume thousands of litres of fuel - thus studies with the AFTSTU are rather more costly than the aforementioned specification devices.

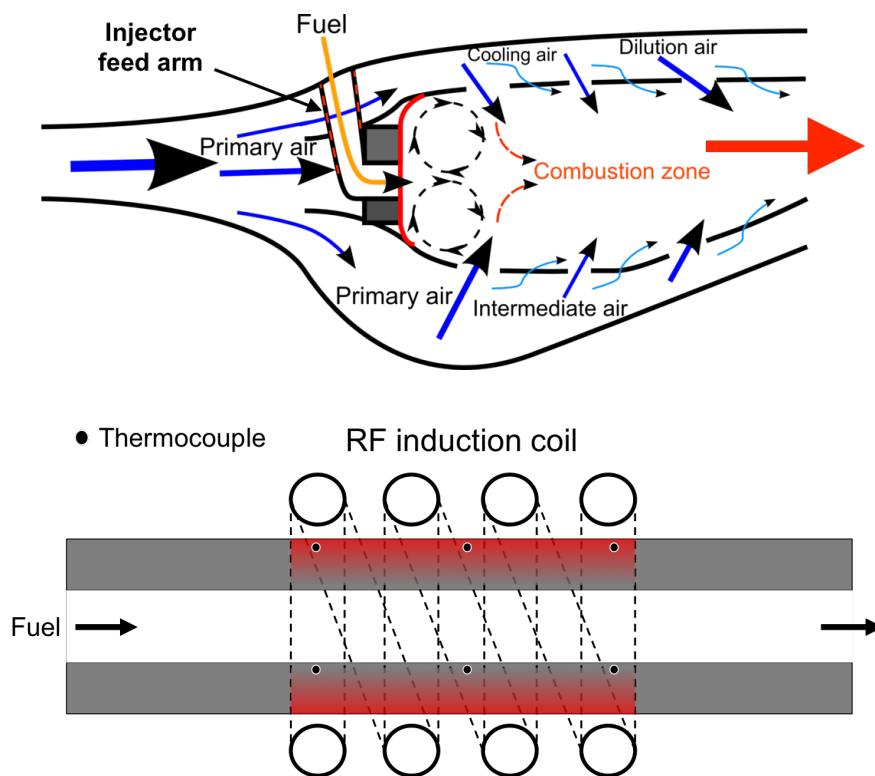


Figure 4.82: Top: Combustor schematic. Bottom: AFTSTU simulated injector feed arm

The section of the rig with highest relevance to this work is the injector feed arm section, which is intended to simulate the high thermal loading provided by compressor discharge air to the stem of an injector. The simulated feed arm is

simply a length of 6mm OD, 2mm ID SS316 tube, placed within an induction coil. The total heated length is 110mm. Future injectors will undoubtedly be made by additive manufacturing, which presents a new and unique challenge for injector design. As will be shown in the work that follows, additively manufactured parts have inherent roughness and fuel injectors have small hydraulic diameter internal channels (of the order of 1mm), which may not be able to be smoothed with abrasive flow techniques. Maximum fuel flow rates through the injector are typically around 1000l/hr and wetted wall temperatures may be as high as 300°C. Therefore, high relative surface roughness may be introduced to a engine component critical to combustion efficiency and turbine life, which typically has high Reynolds number flow and experiences the highest thermal loading in thermal stability problems. Furthermore, insoluble material or precursors may already be present in the bulk fuel due to upstream thermal stressing. In some ways, this represents the 'perfect storm' of thermal stability.

The objective of the work in this section was to study the effect of roughness on deposition using highly representative surfaces and flow conditions. First, the additive manufacture of the injector feed arms is discussed, followed by a description of the characterisation of the roughness by optical metrology and fluid dynamics experiments. Ultimately, the deposition test is outlined.

4.4.2 Establishing roughness data points

4.4.2.1 ALM SLM build considerations

There are two main contributing factors that can affect the roughness of components produced by Selective Laser Melting (SLM). One is build angle of the part (as discussed in the JFTOT section). The other is related to certain parameters of the build that may be adjusted. For instance; the laser scanning speed, power, focus offset and spot size which control the amount of energy applied to the powder, layer thickness which controls 'stepping' of curved parts, and the hatch spacing (or spacing between adjacent laser passes). The parts used in this study were built in collaboration with the Centre for Advanced Additive Manufacturing (AdAM) at the University of Sheffield.

4.4.2.2 SLM build parameter study

Since the simulated injector feed arms are straight lengths of tube, it seemed inappropriate to modify the roughness by altering the build angle, since this would likely have resulted in an uneven distribution of roughness around the inner surface. An initial study was performed to assess the effect of altering various build parameters that were anticipated to have a direct effect on the surface finish of the part; namely the laser power, point distance and exposure time of the border zone, and the laser power in the offset zone. Small sample cubes with flat sides were built using a Renishaw SLM125 in 316 stainless steel and the surface roughness was measured using an optical profilometer in Vertical Scanning Interferometry (VSI) mode. A summary of the parameters and the resulting surface roughnesses are shown below. Statistical roughness data was taken from both sides of each sample, and the average was taken.

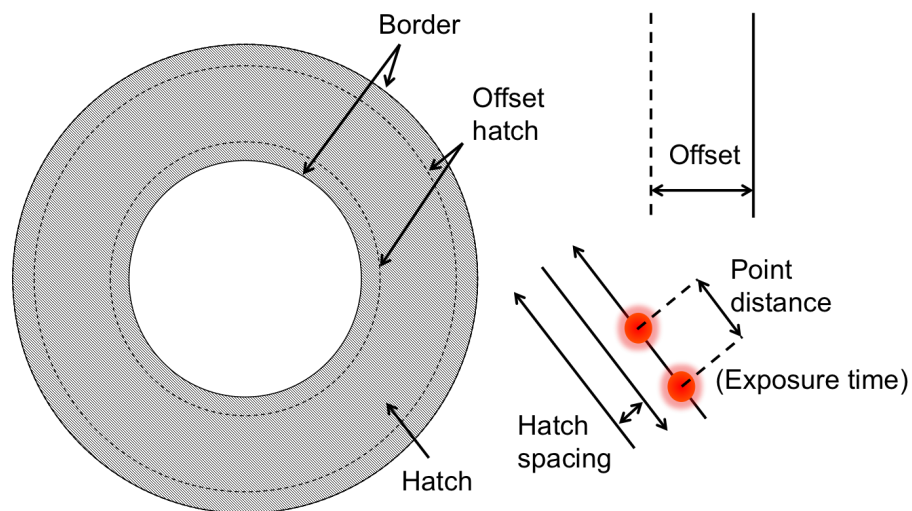


Figure 4.83: SLM part edge parameters

Figure 4.83 shows a 3D profilometry map of a typical ALM surface. The texture is comprised primarily of small circular raised areas ($D \approx 0.03\mu m$) which are evenly distributed across the surface and are almost certainly the remains of partially melted powder particles. occasionally the particles appear to be fused together to create larger raised areas. A second notable quality of the surface is the repeated pattern of parallel streaks - probably a result of the stepwise nature of the build process. In some samples the streaks were evenly spaced and were measured to have a width of approximately $0.1\mu m$. The streak spacing could be related to the step height of the build, the hatch spacing or the laser spot diameter. The tallest peaks in the surface seem to be coincident with groups of fused powder particles

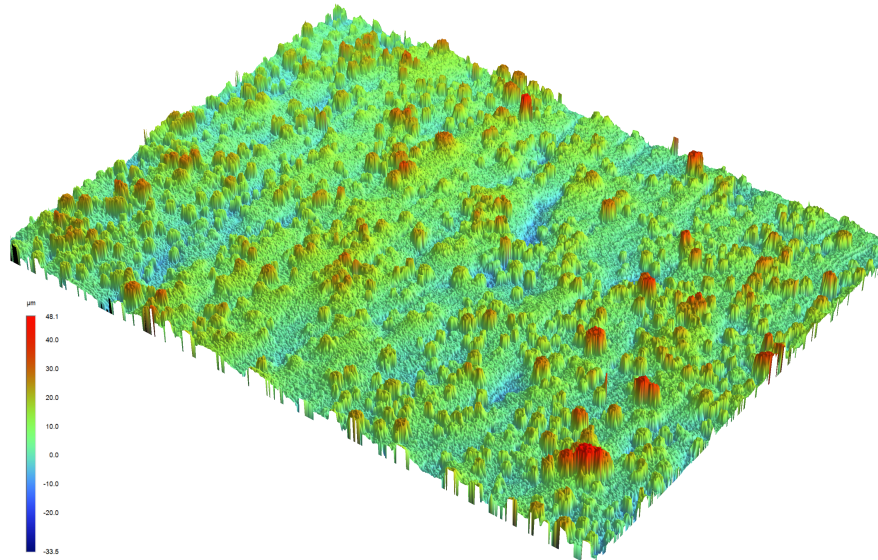


Figure 4.84: 3D optical profilometry contour plot of an ALM surface (0.94 x 1.26mm area)

being present on top of a raised streak.

Analysis of the samples confirms that the build parameters can have a reasonably strong effect on the final surface roughness. The range in S_a across the samples was $15\mu m$. As seen for the ALM JFTOT tubes, the skew and kurtosis of the height distribution indicated that the roughness was normally distributed. The lowest roughness was achieved with 'standard' parameters (sample A, $8\mu m$). The roughnesses of the other cubes with 'non standard' parameters are mostly of similar magnitude. For the cases with the highest laser power applied to the border and offset zones, increasing the point distance doubled the average roughness height and halving the exposure time to the border had a similar effect. The variation in the build parameters does not appear to have a particularly consistent effect - for example, tube G - for which the laser power was zero in both the border and offset regions, did not exhibit the highest roughness as may have been expected. The effect of border and offset laser parameters in ALM is clearly complicated, but is not the main focus of this study. Crucially, the samples showed that ALM parts may be produced with a wide range of roughnesses.

Table 4.14: SLM part edge parameters

Sample	S_a (μm)	S_q (μm)	S_p (μm)	S_v (μm)	S_{ku}	S_{sk}	Power (W)	Border		Offset
								Point distance (μm)	Point exposure time (μs)	Power (W)
A	8.16	10.18	52.10	-35.85	3.30	0.68	200	30	100	200
B	16.83	21.30	89.85	-74.31	3.81	0.91	200	30	50	200
C	17.55	22.19	104.94	-66.50	3.86	0.75	200	100	100	200
D	23.29	27.69	89.31	-90.14	2.43	0.43	100	30	100	200
E	19.16	23.12	88.62	-75.78	2.75	0.60	100	30	100	100
F	22.19	26.48	77.39	-96.56	2.36	0.03	0	30	100	100
G	18.94	23.60	74.11	-92.47	2.92	-0.25	0	30	100	0
H	13.47	16.92	73.92	-71.44	3.21	0.26	0	30	50	200

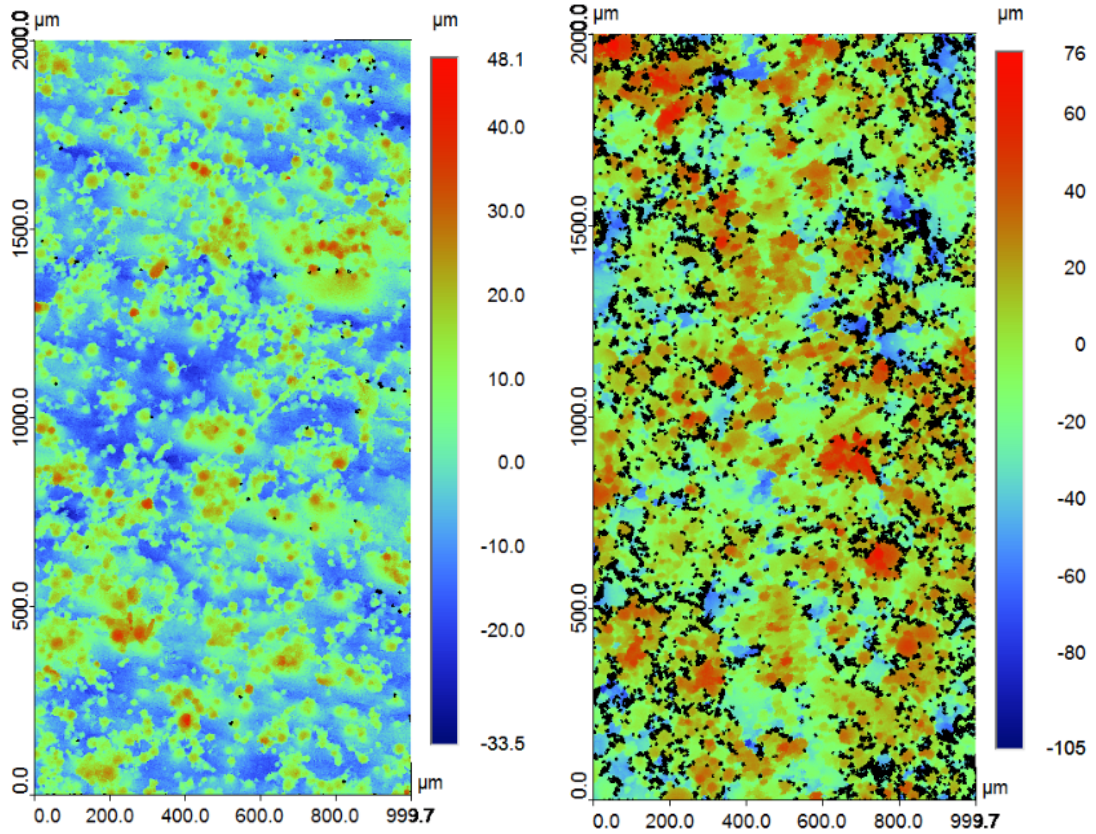


Figure 4.85: Left; Full laser power on border and offset parameters, $S_a \approx 8\mu\text{m}$. Right; no border and offset, $S_a \approx 17\mu\text{m}$

4.4.2.3 Tube builds

Informed by the parameter study, 10 tubes were built vertically with build parameters outlined in table 4.16 using a Renishaw SLM125. The tube length was limited by the capacity of the powder hopper in the machine to 110mm and since the tubes had to be wire cut from the build plate, the final tube length was 100mm. Lengths of drawn tube were subsequently welded to each end of the ALM piece, to form a total length of 250mm.

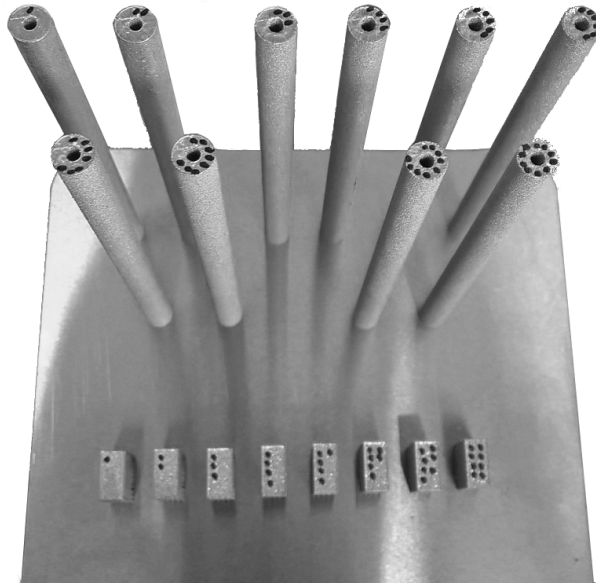


Figure 4.86: ALM tubes as removed from the machine (dots are ID)

4.4.3 Roughness characterisation

4.4.3.1 Optical profilometry

Since the same laser parameters are applied to external and internal boundaries, it was assumed that the external surface would be representative of the internal surface roughness. VSI was used to quantify the external surface roughness. Best results were achieved with narrow band green wavelength light, using a backward and forward scanning length of $95\mu m$ ($190\mu m$ total vertical scan). The threshold for noise was 2% and the light intensity was 80%. At 10x magnification, the spot area was $0.24mm^2$. Single measurements were taken at 3 locations along the tube in addition to a $4 \times 1mm$ axial stitch at an arbitrarily chosen location along the tube length. The values quoted in table 4.16 are averaged over the 3 discrete measurements and the stitch.

For some reason, the tubes exhibit a smaller range of roughness height than the cube samples. With the exception of tubes 1 and 2 (built with standard parameters, $S_a \approx 7\mu m$), the other tubes are near enough identical, with roughnesses around $11 - 12\mu m$. The reason for the difference between the cube and tube samples is not clear, but may be related to the curvature of the part. Somehow it would seem that the roughness created on a vertical surface with curvature is less sensitive to a change in the laser parameters than a flat vertical surface.

Table 4.15: ALM tubes - average and RMS roughness height data

Tube ID	S_a (μm)	S_q (μm)	Power out (W)	Volume border		Volume offset	
				Point distance (μm)	Point exposure time (μs)	Power out (W)	
1	6.13	10.45	200	30	100	200	
2	7.63	13.17	200	30	100	200	
3	12.83	17.48	200	100	100	200	
4	10.94	15.40	200	100	100	200	
5	11.22	15.27	0	100	100	100	
6	11.63	16.12	0	100	100	100	
7	10.59	14.50	100	30	100	100	
8	9.99	13.20	100	30	100	100	
9	12.30	17.35	0	30	100	0	
10	14.60	20.10	0	30	100	0	

4.4.3.2 Isothermal pressure drop experiments

Following the previously described method with the HiReTS capillary tubes, the pressure drop was measured to calculate the fully rough friction factor.

4.4.3.3 Apparatus

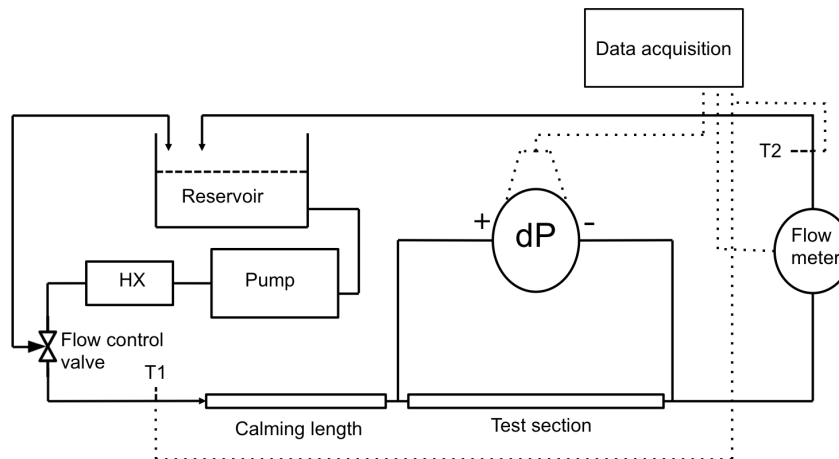


Figure 4.87: Pressure drop measurement apparatus

The measurement apparatus was largely unchanged. A larger three phase fuel pump capable of delivering 600 l/hr was used and the pipe network was replaced with tubing (6.35 mm OD , 2 mm ID) to match the test section dimensions as closely as possible. An upstream calming length of $125D$ was used. Positive and negative pressure tappings were created with 6.35 mm T unions. Fuel flow control was achieved with a bypass line with coarse and fine control. An Omega FPD3000 positive displacement flowmeter was used to measure the flow rate, the output of which was recorded in LabView. Fluid temperature was recorded by k-type thermocouples at two locations. To manage the heat input to the fluid

from the pump, a tube in shell heat exchanger was used. The pressure measuring equipment was unchanged, but the range of the output signal was increased and the instrument re-calibrated.

4.4.3.4 Sources of uncertainty

Table 4.16: Sources of uncertainty - pressure drop experiments

Measurement	Instrument	Uncertainty
Flow rate	Omega FPD3000	$\pm 1\%$
dP	ABB pressure transducer	$\pm 0.1\%$
Fuel temperature	K type thermocouple	$\pm 2.2^\circ C$

4.4.3.5 Method

Differential pressure across the tubes was measured from $30l/hr$ to until the pressure transducer reached its maximum limit (around $300-400l/hr$) depending on the roughness. The typical range of Re was 2000 to 40000. The flow rate was set with the flow control valve and allowed to stabilise for 1 minute, after which the pressure, flow rate and temperature data was recorded for a further minute at $4Hz$. The working fluid was kerosene, and since the heat input from the pump to the fuel was significant, temperature dependent material properties were used ([56]) in the calculations of λ and Re .

4.4.3.6 Results

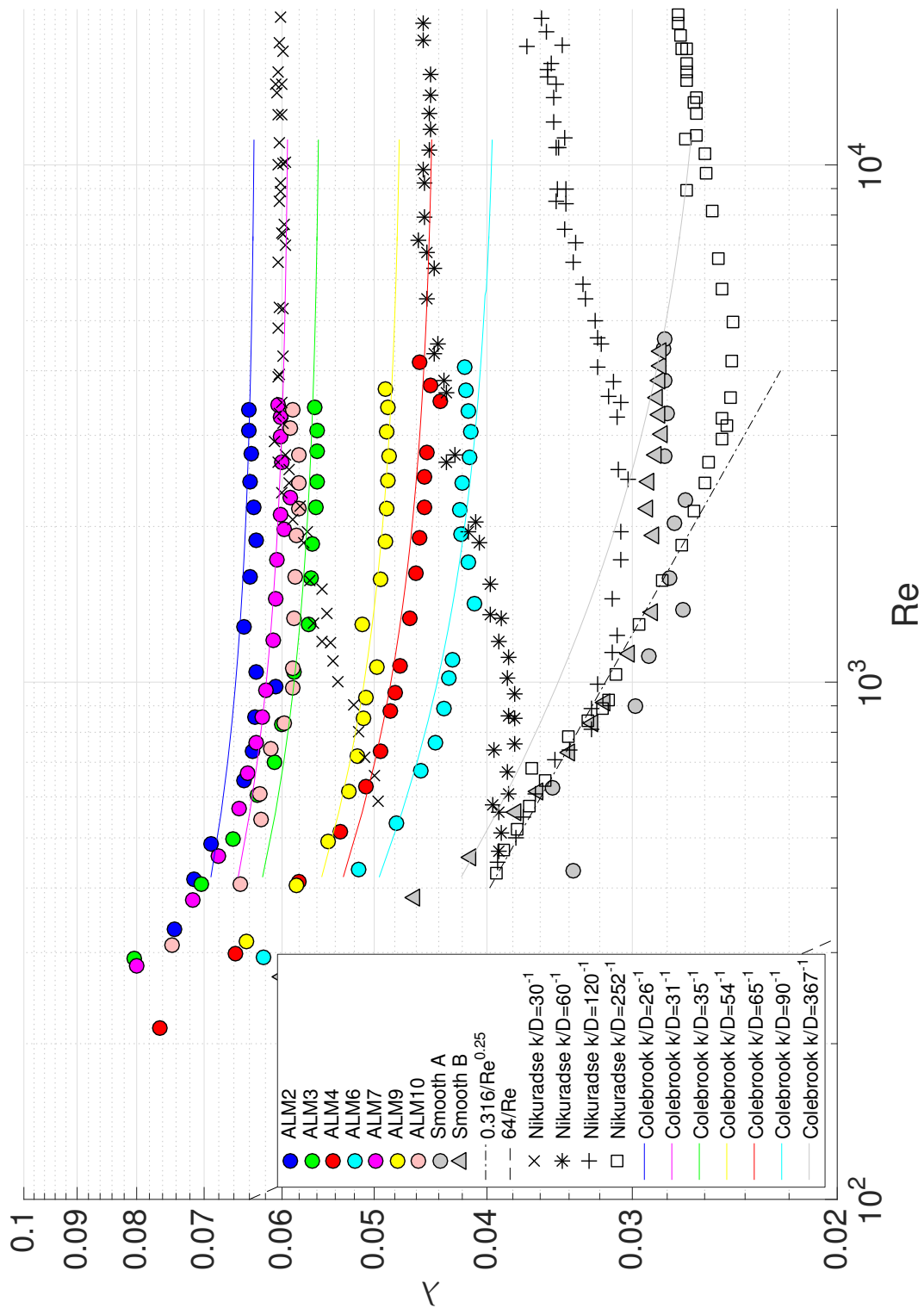


Figure 4.88: Friction factor data for ALM tubes

Table 4.17: Friction factor data for tubes used in deposition tests

Tube ID	D (mm)	A (m ²)	k _s (μm)	Qdot (l/hr)	Qdot (m ³ /s)	U _{avg} (m/s)	dP (bar)	T _{avg} (°C)	τ _w (kg/ms ²)	u* (m/s)	Re	λ	δ Re	δ λ
ALM2	2	3.14E-06	76.0	32.6	7.13E-05	2.88	0.31	17.05	62	0.278	3328	0.0742	37	0.0015
				41.7	7.58E-05	3.68	0.49	16.84	97	0.348	4167	0.0714	47	0.0015
				48.6	8.04E-05	4.30	0.64	16.77	128	0.399	4866	0.0690	54	0.0014
				63.3	8.50E-05	5.60	1.01	17.51	203	0.504	6461	0.0647	72	0.0013
				71.9	8.95E-05	6.36	1.28	17.97	257	0.567	7335	0.0635	82	0.0013
				82.2	9.41E-05	7.26	1.67	18.31	334	0.647	8550	0.0634	96	0.0013
				94.4	9.86E-05	8.34	2.11	18.55	423	0.727	9819	0.0608	110	0.0013
				100.6	1.03E-04	8.89	2.50	18.61	499	0.790	10466	0.0631	117	0.0013
				122.8	1.08E-04	10.86	3.81	18.97	762	0.976	12780	0.0646	143	0.0013
				150.6	1.12E-04	13.31	5.66	19.30	1131	1.190	15982	0.0639	179	0.0013
				176.8	1.17E-04	15.63	7.70	19.76	1540	1.389	18765	0.0631	210	0.0013
				201.7	1.21E-04	17.83	10.07	20.09	2014	1.589	21827	0.0635	244	0.0013
				225.9	1.26E-04	19.97	12.72	20.61	2544	1.786	24448	0.0640	273	0.0013
				250.5	1.31E-04	22.15	15.60	21.20	3120	1.978	27648	0.0638	309	0.0013
277.4	1.35E-04	24.52	19.18	21.97	3836	2.194	30610	0.0640	342	0.0013				
298.8	1.40E-04	26.42	22.28	22.63	4456	2.366	33622	0.0641	376	0.0013				
Smooth A	2	3.14E-06	5.5	25.5	7.08E-06	2.25	0.07	17.95	14	0.131	2288	0.0272	26	0.0006
				29.2	8.12E-06	2.58	0.11	18.96	21	0.162	2625	0.0316	29	0.0007
				40.2	1.12E-05	3.55	0.20	19.22	41	0.225	3608	0.0320	40	0.0007
				48.3	1.34E-05	4.27	0.30	17.98	60	0.273	4334	0.0326	48	0.0007
				60.1	1.67E-05	5.32	0.44	21.22	88	0.331	6547	0.0311	73	0.0006
				70.6	1.96E-05	6.24	0.59	20.83	118	0.385	7686	0.0305	86	0.0006
				74.4	2.07E-05	6.58	0.66	18.85	133	0.405	6678	0.0304	75	0.0006
				91.2	2.53E-05	8.06	0.96	20.81	191	0.490	9927	0.0295	111	0.0006
				100.6	2.79E-05	8.90	1.16	18.71	233	0.537	9036	0.0292	101	0.0006
				125.2	3.48E-05	11.07	1.75	20.24	350	0.663	13628	0.0287	152	0.0006
				152.7	4.24E-05	13.50	2.57	20.54	514	0.802	16624	0.0283	186	0.0006
				179.1	4.98E-05	15.84	3.41	20.95	681	0.924	19501	0.0272	218	0.0006
				203.3	5.65E-05	17.98	4.48	21.95	896	1.060	22135	0.0278	247	0.0006
				227.4	6.32E-05	20.10	5.67	22.40	1134	1.192	24754	0.0281	277	0.0006
252.9	7.02E-05	22.36	6.91	23.04	1382	1.316	27529	0.0277	308	0.0006				
303.8	8.44E-05	26.86	10.01	24.55	2002	1.584	33074	0.0278	370	0.0006				
353.8	9.83E-05	31.29	13.70	25.63	2740	1.853	38520	0.0281	431	0.0006				
400.3	1.11E-04	35.40	17.62	27.05	3523	2.101	43580	0.0282	487	0.0006				

4.4.3.7 Discussion

The profiles of friction factor show a clear distinction between drawn and ALM tubes. They also indicate that the fully rough condition was achieved for all but the smoothest tubes, permitting the equivalent sand grain roughness to be evaluated with relative certainty. The two drawn tubes showed good similarity ($\lambda = 0.028$, $k_s = 5.5\mu m$). The ALM profiles are spread over a considerable range, which is surprising considering the profilometry data from the external wall - which showed little difference between the tubes. Of the ALM tubes, tube 6 had the lowest friction factor ($\lambda = 0.042$, $k_s = 22\mu m$) and tube 2 the highest ($\lambda = 0.064$, $k_s = 76\mu m$), contrary to the S_a and S_q roughness metrics from the external wall. The assumption that the external surface is representative of the internal surface may not be valid, or the number of measurements along the tube may not have been sufficient. The spread may also be due to slight misalignments in the tube at the weld locations.

The ALM surfaces are reasonably well represented by the Colebrook-White formula (shown as lines in figure 4.87), which suggests that the surfaces themselves are not particularly uniform. This is quite evident from inspection of the profilometry maps.

4.4.4 Deposition experiments

4.4.4.1 Method / Apparatus

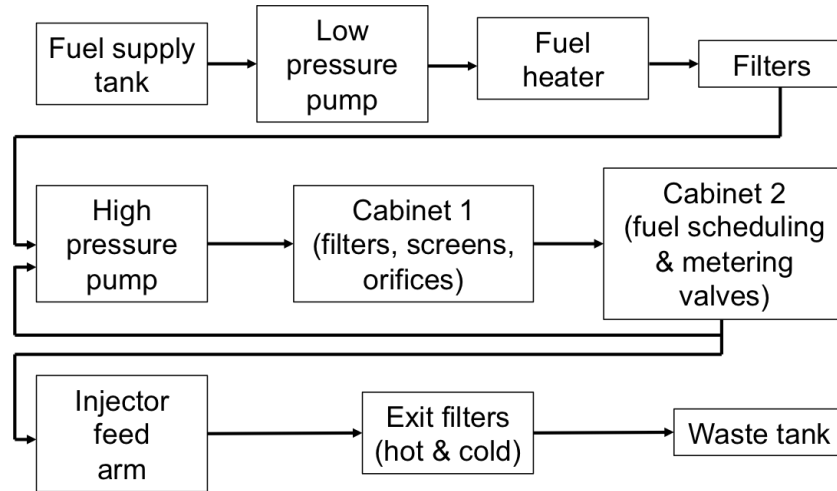


Figure 4.89: AFTSTU flow diagram

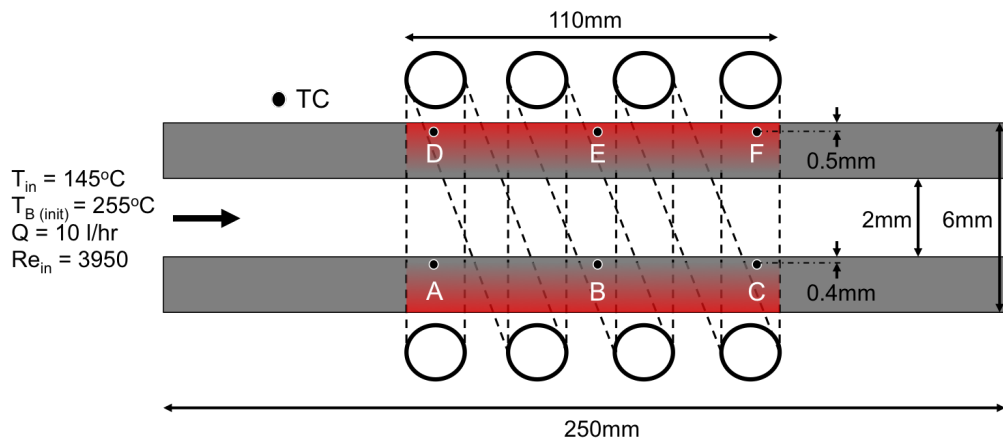


Figure 4.90: Injector feed arm deposition test conditions

'ALM2' and 'Drawn B' (having the highest and lowest measured friction factors respectively) were selected for inclusion into a programme of ongoing testing on the AFTSTU with an industrial partner. To record the internal and external wall temperature along the heated length, the tubes were instrumented with 6 k-type thermocouples, silver soldered to the positions shown in figure 4.89. The rig configuration in its current form is shown in figure 4.88. Fuel, preheated to 140°C was pumped at 10 l/hr at 34 bar through a series of filters, screens, orifices and valves which were periodically cycled. Fuel was recirculated and the residence time in the high temperature section was dependent upon the spill ratio and fuel flow

rate. Towards the end of the fuel path, heat flux from the compressor discharge air was simulated by induction heating of the instrumented feed arm tubes, which were placed inside a radio frequency induction coil. The total heated length was 110mm and the tubes were positioned such that the central thermocouples were located in the middle of the induction coil. Fuel inlet and outlet temperatures for the injector feed arm section were recorded with k-type thermocouples and flow rates around the rig were recorded with coriolis flow meters.

The flow conditions for the injector feed arm section are shown in figure 4.89. In practice it was found that for the same heater power, the wall temperature of the drawn tubes was substantially higher than the ALM tubes - demonstrating the general increase in Nu for rougher surfaces. Although a constant power for both tubes would have been more representative of real engine conditions, to produce a more direct comparison of the surfaces, the heater power was reduced for the drawn tube in order to achieve the same initial wetted wall temperature (255°C) for both surfaces. The total test duration was in excess of 100 hours, but was discontinuous due to the blockage of filters. Injector feed arms were installed after a shutdown for filter replacement. The feed arm test and valve cycles were initiated after a 4 hour warm up period to establish steady state conditions. 10 hours of continuous data was recorded for both feed arm tests.

4.4.4.2 Results

Table 4.18: AFTSTU deposition test results

	T in ($^\circ\text{C}$)	T out ($^\circ\text{C}$)	Q (l/hr)	Q_{heat} (W)	T B _{init} ($^\circ\text{C}$)	T B _{fin} ($^\circ\text{C}$)	dT ($^\circ\text{C}$)	Re avg	k_s (μm)	k_s^+
Drawn B	141	155	10	67.4	252	257	5	4058	5.0	5.5
ALM 2	145	174	10	140.4	255	298	43	4283	76	64

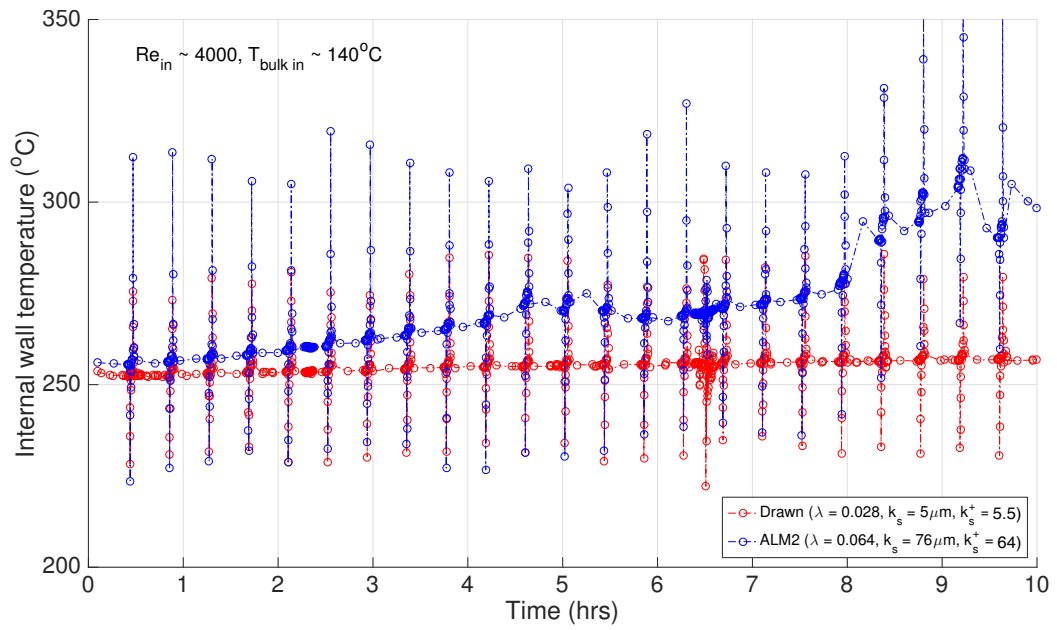


Figure 4.91: Wall temperature rise (thermocouple B) over 10 hours for drawn and ALM tubes

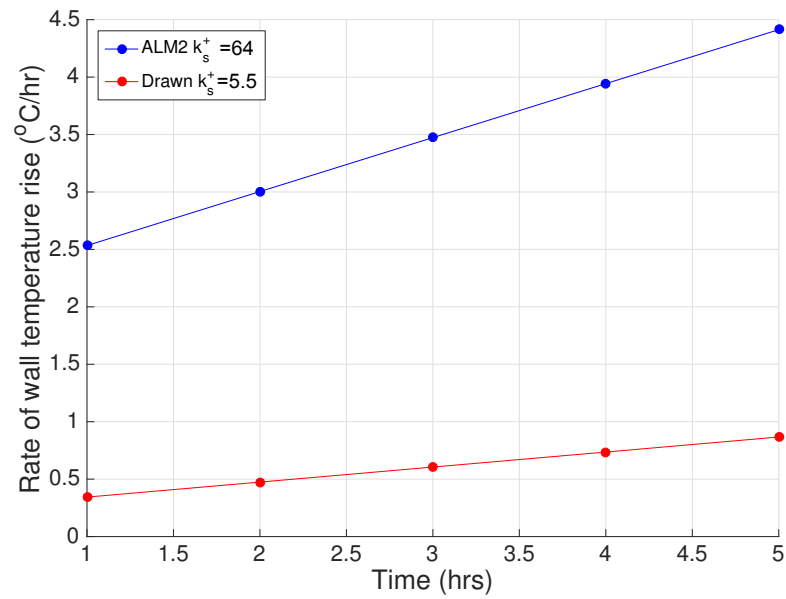


Figure 4.92: Rate of wall temperature rise for drawn and ALM tubes

4.4.4.3 Discussion

Figure 4.90 shows data from the central internal wall thermocouple for both tubes. The data from the adjacent thermocouples has been omitted for clarity. The regular sharp spikes in wall temperature are related to fluctuations in the flow caused by the cycling of valves upstream of the injector feed arm section. Since the feed arms shown here were inserted into the rig reasonably late in the overall test, the metering and flow control valves were already significantly fouled. Sticking of valves due to deposit formation is most likely the cause of the fluctuations beyond 8 hours for the ALM tube data. After ten hours, the difference in severity of deposition for the two surfaces is plain to see. The wall temperature of the ALM tube increased by 43°C , while the drawn tube showed a very slight increase of 5°C . The noise in the data is somewhat prohibitive of a more detailed analysis, but nevertheless the difference in severity of deposition between the two surfaces is distinct. Rate of wall temperature rise for the first five hours (pre valve cycle noise) is also plotted in figure 4.91.

Table 4.19 shows the values of k_s^+ for the two surfaces based on the pressure drop data, calculated based on the average Reynolds number across the tube. Since the flow is preheated, the axial gradients of temperature and Re are much less extreme than for the HiReTS device - therefore the values of k_s^+ change little across the heated length. The relatively low Re through the section (it was unfortunate that the flow rate was predetermined and could not be increased) resulted in a thick viscous sublayer which is reflected in the low values of k_s^+ . Based on Nikuradse's classification - for the drawn tube, the flow was transitionally rough ($k_s^+ = 5.5$) indicating some moderate disruption to the viscous sublayer. The ALM tube was close to the fully rough condition, ($k_s^+ = 64$), indicating severe disturbance to the viscous layer.

The results presented here are limited and repeat testing must be performed to confirm the observed behaviour. However, the data suggests that at typical in-service wetted wall temperatures, the deposition over rough ALM surfaces may be significantly enhanced, even for relatively low roughness Reynolds numbers.

Chapter 5

General Discussion

This chapter will provide a more general discussion of the experiments described in the preceding chapter, with reference to the objectives of the study;

- Identify most viable test method/s.
- Establish data points for roughness.
- Characterise roughnesses as thoroughly as possible.
- Experimentally determine the effect of roughness on isothermal flow and heat transfer.
- Experimentally determine whether a trend exists between surface roughness and deposit formation rate.

5.1 Laminar flow

Deposition over rough and smooth surfaces in the laminar regime was assessed through testing conducted with the JFTOT. Conventionally machined tubes with average roughness height $\approx 1.5\mu m$ were compared against tubes made by additive layer manufacturing. The roughness of the tubes was characterised with optical profilometry. The highest roughness of the additive manufactured tubes was $40\mu m$, which occurred for tube faces which were overhanging the powder bed during the build process. Tests were conducted with a maximum heater tube temperature of $280^{\circ}C$ for 150 minutes using a straight run kerosene ('Fuel A') of poor thermal stability (but which passed ASTM D3241). In the absence of better methods of deposit quantification, the tube deposit was assessed visually using digital photography under consistent lighting conditions. Image processing

was used in an effort to compare the change in tube colour as a result of deposit formation numerically using the RGB colour scale.

Differences in deposition patterns across the range of roughness were slight for the majority of cases, although there were two possible exceptions. For the 31 μ m face on the 30 degree build, and the 41 μ m face on the horizontally built tube, deposit seemed to become noticeable on the surface at marginally lower tube wall temperatures. It should be noted however that the texture and colour of the surfaces greatly complicated the judgement of very subtle colour changes and the comparison with the machined tube. It is difficult to say with any certainty from a purely visual comparison whether the thickness of deposit on the rough surfaces is greater than the smooth surface. Numerical values were derived by image processing. Although profiles of ΔI_g (change in grayscale intensity with respect to the base metal colour) across the tube appeared to be representative of the deposit pattern discernible by eye, the magnitude of the value was strongly influenced by the base metal colour, which was not constant. Furthermore, the inherent noise of the data prevented a meaningful assessment of the deposit onset location to be performed.

If deposit does indeed form at lower temperatures over a very rough tube and laminar flow, it is unlikely to be as a result of any enhancement to momentum or heat transfer - recalling that $\lambda = 64/Re$ and $Nu = \text{constant}$ in this flow regime. Since the auto oxidation mechanism of deposit formation is metal catalysed - as has been shown with the JFTOT for various tube materials, it could be that a large increase in roughness presents more active sites for catalysis than a machined surface. As a result, the rate of reaction may be increased at lower temperatures, although the experiments presented here suggest any effect to be minor.

5.2 Turbulent flow experiments

5.2.1 HiReTS

For turbulent flow, which is most relevant to aircraft fuel systems, the effect of wall roughness on deposition was studied with the HiReTS device using $\approx 500\mu\text{m}$ capillary tubes. Cold drawn technical grade HPLC tubing was appropriated for the rough data points, while Electro Discharge Machining was used to create tubes with lower surface roughness. The roughness was quantified by microscopy and

image analysis in combination with experiments to characterise the roughness by observing the differences in momentum and heat transfer. A summary of results for the pressure drop, heat transfer and deposition tests is shown in table 4.61. To begin, the various factors that complicate the ultimate assessment of the effect of roughness on deposition will be outlined. The range of roughness that was achieved will be considered, before a further discussion of the observations for the deposition experiments.

5.2.1.1 Critical review of experiments

Roughness quantification

Various means were used to try and quantify the roughness geometry. Through sectioning, microscopy and image analysis, circumferential roughness profiles were extracted from micrographs and statistical 2D roughness metrics were calculated. While the analysis improved on the usefulness of a simple micrograph, the samples themselves were only truly representative of a single cross section, and to say that the roughness metrics were representative of the whole tube would be a large assumption. Furthermore, since the roughness height was calculated from the deviation of the wall-centroid distance from the average radius, the values calculated by this method were sensitive to non uniformities in the tube cross section. For example, in the case of EDM 12 and 14, which would appear from the micrographs alone to be substantially smoother than the drawn tubes yet have values of R_a and R_q determined by image processing which are higher than the drawn tubes. EDM 13, which is more uniform, appears to have slightly more obvious roughness features than EDM 12 and 14, yet the rms roughness height is similar to the 2nd set of EDM tubes, which were generally more regular in shape. The ratio $P/\pi D$ seems to be a better representation of what can be seen by eye from the micrographs. The drawn tubes, which are clearly much rougher, have an average value of 1.3, while EDM set 1 has an average value of 1.12 and the other EDM tubes are slightly higher at 1.18. EDM 13 has a higher value of $P/\pi D$ than EDM 12 and 14, yet has lower values of R_a and R_q . While the image processing was useful in many respects for highlighting general differences between the different sets of tubes, the most useful physical values of average roughness height (R_a and R_q) could not really be relied upon for the reasons described above.

To extend the assessment of roughness to the entire tube, experiments were conducted to measure the frictional resistance of the wall to fluid flow - following the classical work of Nikuradse. The typical approach is to measure the pressure drop

across the tube with increasing Reynolds number until λ becomes independent of Re and only dependent on the relative roughness. Unfortunately, even with a relatively low viscosity fluid such as heptane, it was not possible to produce the fluid velocity required to achieve the fully rough condition. At most, the tubes were measured to the transitionally rough regime. Further tests were conducted with a higher capacity pump with kerosene, but the maximum range of the pressure transducer was exceeded before the dataset could be extended to higher Re . Some profiles showed resemblance to the start of Nikuradse's data, and for these cases it is possible that the data could be extrapolated with reasonable accuracy. For the other tubes, only estimations can be made.

By formulating heat transfer results in terms of dimensionless variables Nu and St , it was possible to compare the values to results available in the literature at similar Reynolds numbers for which the roughnesses were characterised. The calculated values of Nu and St were in good agreement with correlations and values in the literature, providing valuable context with other, well characterised roughnesses.

Reynolds number effects - transition

For the tube diameters and flow rates considered, the fluid entered the tube at a high laminar Reynolds number and transitioned to fully turbulent flow at some point along the tube, as a result of the reduction in fluid viscosity and density via bulk heating. The location of transition (which by its nature is a region of higher uncertainty than fully laminar or turbulent flow) is governed by tube diameter and roughness, both of which varied quite significantly over the range of tests. For narrower, rougher tubes, the transition would be expected to occur much closer to the inlet and effect a shorter axial length than a wider, smoother tube. The transitional Reynolds number for mini and micro channels was discussed in Kandlikar [121]. For smooth tubes, some investigators reported earlier transition at around 2000, but other studies showed that transition occurred at typical Reynolds numbers for larger scale tubes and channels (2300). For tubes of high relative roughness, transition has been noted to occur much earlier than 2300. For $k/D \leq 0.08$, Kandlikar provided the following empirical expression for the transitional Reynolds number based on experimental data;

$$Re_{t,cf} = 2300 - 18750 \frac{k}{D_{cf}} \quad (5.2.1)$$

where D_{cf} is the 'constricted hydraulic diameter', $D_{cf} = D - 2k$. If k is taken

to be the typical rms roughness height R_q measured by microscopy, then for the drawn capillaries with $R_q \approx 8\mu\text{m}$, the transitional Re based on the above expression for tubes with diameter $530\mu\text{m}$ would be ≈ 2008 , while for the EDM tubes with $R_q \approx 4$, Re_t may be slightly higher at 2150. This expression would suggest that transitional effects would be confined to a region close to the inlet and outside of the measured length for the deposition tests. Furthermore, since the local fluid viscosity would be a minimum close the wall, flow instabilities caused by the roughness elements would probably be less effectively damped by viscosity in this region, and transition may be expected to occur sooner than for isothermal flow.

The higher resolution pressure drop experiments on R8 - R11 and EDM 12 - 14 do show an early departure from the laminar relation $f = 64/Re$ (around $Re = 1000$) although the data is scarce in this region. Unlike the tubes of Ghajar [41], which had a very abrupt inflection in the transition region, the data from the tubes in this study shows the transition to occur over a much broader range of Re . At $Re = 3100$, based on the change in friction factor profile, the flow appears to still be in the process of transition, and the profiles become parallel to the turbulent smooth asymptote at a Reynolds number of around 4000. The differences between the results may be due to some aspect of the experimental setup. The use of a piston pump for instance, which created periodic fluctuations in the flow, the use of a rough tube for the upstream length or the use of pipe fittings as pressure ports rather than more carefully designed ports.

The worst case scenario for transition introducing complications to the deposition experiments would be for a smooth tube of large diameter with low bulk fuel temperature increase. The tests on EDM tubes 10 and 11 may be suitable test cases since they had the largest diameters of the smoothed tubes. Based on a logarithmic bulk temperature increase (assuming a constant wall temperature), the Reynolds number would exceed 4000 upstream of the measured length. R1 and R2, which experienced a bizarre reduction in wall temperature around the mid point of the tube (which was initially thought to be indicative of some transitional effect) would have Reynolds numbers in this region in excess of 5000, so it seems unlikely that the reversal in wall temperature for those cases was a result of transition.

Roughness Reynolds number effects - k^+

The change in Reynolds number from inlet to outlet also further complicates the

study. As Re increases, the extent of the viscous and buffer layers of the boundary layer are reduced and since the roughness height remains constant, the roughness Reynolds number $k^+ = \frac{kU^*}{\nu}$ increases. Nikuradse expressed the roughness Reynolds number in terms of the sand grain roughness height, $k_s^+ = \frac{k_s U^*}{\nu}$ and found that the limit of hydraulically smooth flow was $k_s^+ < 3$, and the limit of the fully rough regime was $k_s^+ > 60$.

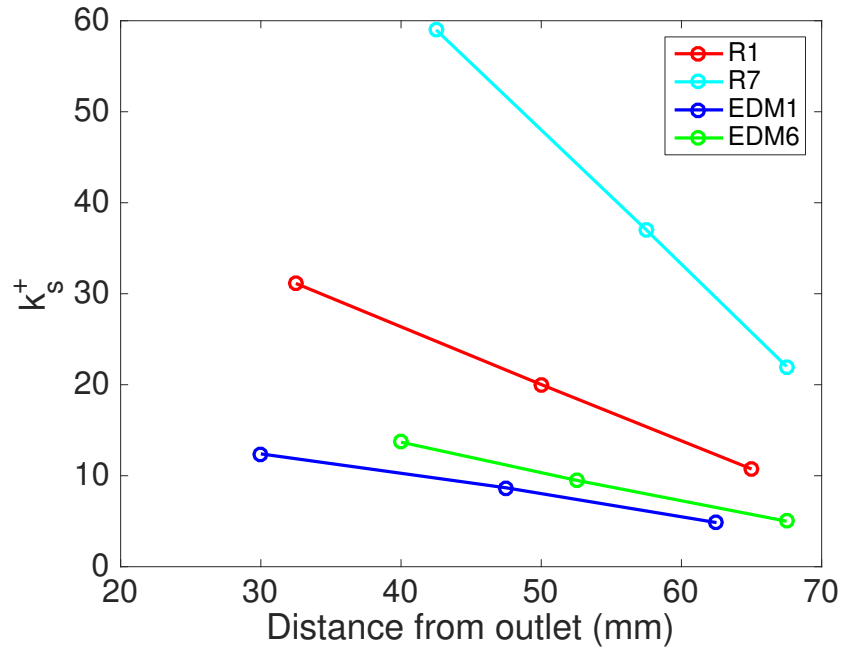


Figure 5.1: Change in k^+ with axial distance - HiReTS geometry

By comparing the friction factor results to those of Nikuradse, values of k_s^+ can be estimated and the roughness regime for the tests can be placed into context. For example, drawn tubes R1-7 were in excess of Nikuradse's maximum relative roughness, but taking the relative roughness to be $k_s/D = 1/30$, the equivalent sand grain roughness for a $530\mu m$ tube would be $\approx 18\mu m$.

Taking the measured values of U^* for R1 from the pressure drop experiments and matching to the equivalent Re based on the bulk fuel temperature in the deposition test, $k_s^+ \approx 20$ at $80mm$ from the outlet ($Re = 5200$), and increases to $k_s^+ \approx 31$ at $45mm$ from the outlet ($Re = 6500$). For R3, which was tested with a fuel outlet temperature of $230^\circ C$ and therefore has a higher gradient in Re across the tube, $k_s^+ \approx 19$ at $95mm$ from the outlet ($Re = 5100$) and $k_s^+ \approx 31$ at $65mm$ from the outlet ($Re = 6500$). For the first set of EDM tubes, which appeared to have friction factors lower than Nikuradse's data for $k_s/D = 1/60$, $k_s^+ \approx 8$ at

75mm from the outlet ($Re = 5900$) and $k_s^+ \approx 12$ at 40mm from the outlet ($Re = 7200$).

These values (although approximate), demonstrate how the roughness regime changes with axial position. The test is therefore far removed from an isothermal mass transfer experiment for instance, where k^+ would remain constant. In effect, each HiReTS test was a study of the dependence of fuel deposition rate on k^+ , Re and temperature - although in the cases of near constant wall temperature, this reduces to k^+ and Re . If the friction factor data could have been extended to the fully rough regime and the sand grain roughness calculated with more confidence, then the wall temperature rise (or deposition rate of carbon) could have been plotted as a function of k_s^+ , and thereby be directly related to the roughness regime.

Figure 5.2 demonstrates the kind of relationship between deposition rate of carbon and roughness that would be possible to derive if k_s was calculated with certainty. To generate the plot, the measured values of U^* were extrapolated to the outlet. The calculated deposit thickness was converted into a volume by subtracting the initial tube volume from the final tube volume according to;

$$V_{dep} = \sum_1^n (\pi r_i^2 x - \frac{1}{3} \pi x (r_1^2 + r_1 r_2 + r_2^2)) \quad (5.2.2)$$

where n is the number of temperature measurement positions, x is the axial distance between temperature measurements, r_i is the initial tube radius, r_1 is the deposit radius at position n and r_2 is the deposit radius at position $n + 1$. The mass of deposit was calculated using a density of 1000 kg/m^3 [6]. As mentioned above, the analysis is only valid for near-constant wall temperatures where the dependence of deposition on temperature is minimised but k_s^+ still varies due to the change in Re due to the bulk fuel temperature rise. The effect of wall temperature may be negated by only comparing k_s^+ against deposition rate for locations with the same initial wetted wall temperature. Furthermore, non-dimensionalising the deposition rate with the total fuel mass flow rate ($\frac{m_{dep}}{t} \times \frac{1}{\dot{m}_f}$), may aid a comparison between other test devices of different scales, although the usual complexities associated with cross comparison of results from different stressing regimes and differences in fuel chemistry would remain.

Comments on roughness measurements and the range of roughness

The limitations of the methods of roughness measurement have been discussed, but by combing the various sources of information, it is not impossible to compare

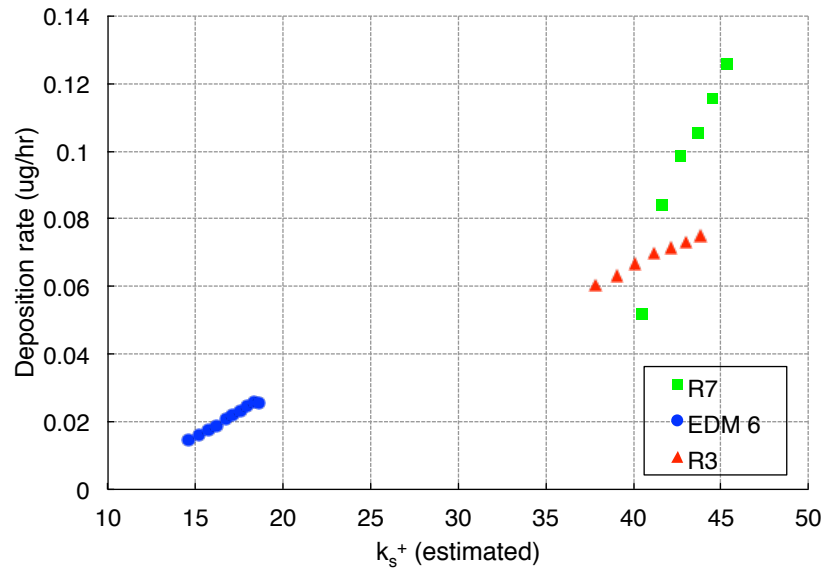


Figure 5.2: Estimated dependence of carbon deposition rate with k_s^+ - HiReTS geometry

the general trends between the tubes.

The first set of EDM tubes (1-6) were measured by microscopy to have the lowest values of k_{rms} ($2-4\mu m$, $k/D \approx 0.9\%$), the lowest average friction factor ($\lambda \approx 0.04$) and the lowest average Nusselt number ($Nu \approx 42$) in the study. A comparison against the work of Nikuradse [8] for the set suggested a relative roughness (k_s/D) below 1.7%, or an approximate equivalent sand grain roughness height of less than $8\mu m$. Profiles of Nu vs Re showed good similarity with the 2D wire roughness data of Sheriff and Gumley [29] for relative roughnesses of 0.95% and 2%, which would also suggest a roughness height of around $8\mu m$. Stanton number profiles for these EDM tubes compared well to the 'smooth' tube data of Gowen and Smith [30] (for which a roughness height was not provided), but fall below their data for a tube with $k/D = 2.7\%$. From the comparison of measured values to results in the literature, the relative roughness of EDM tubes 1-6 may be taken as $\approx 1.5\%$.

The second set of EDM tubes (7-11) were apparently rougher than the first. The average rms roughness height measured by microscopy was around $6.6\mu m$ ($k/D \approx 1.1\%$), the average friction factor showed a corresponding increase to ≈ 0.05 , and Nu increased on average to ≈ 54 . The relative roughness of the second set of EDM tubes was more similar to Nikuradse's data for $k_s/D = 1/30$ (3%), suggesting an equivalent sand grain roughness height, $k_s \approx 19\mu m$. Comparison of Nu vs Re against the data of Sheriff and Gumley suggested a relative roughness

greater than 2%, and the St vs Re profiles fell slightly below the data of Gowen and Smith for $k_s/D = 5.1\%$. From the comparison of measured values to results in the literature, the relative roughness for EDM tubes 7-11 may be taken as $\approx 3\%$.

The EDM process for the final set of tubes (12-14) seemed to be far less effective, which is reflected in the average values of λ and Nu (0.058 and 62 respectively). Although there is some spread in the microscopy analysis for these tubes, the average value of k_{rms}/D is similar to the drawn capillary tubing. The shape of the friction factor profile prohibited an estimation of equivalent sand grain roughness by comparison with Nikuradse's data.

For the drawn capillaries, microscopy measured the typical relative roughness to be $k_{rms}/D = 1.4\%$. The friction factors were higher than the roughest case studied by Nikuradse ($k_s > 19\mu m$, $k_s/D > 3.6\%$) and the Stanton number profiles were similar to Gowen and Smith's [30] data for $k_s/D = 5.1\%$. The average maximum Nu for the tubes was typically around 70, and the profiles of Nu suggested a relative roughness greater than 2% based on data of Sheriff and Gumley [29]. The relative roughness of the drawn capillaries may be estimated as $k/D \approx 5\%$.

Comments on the observed deposition

For all (bar one) of the tests conducted, tubes with higher friction factors and Nusselt numbers experienced the lowest average wall temperatures and the highest rates of deposition. Smoother tubes with lower heat transfer coefficients experienced consistently higher initial wall temperatures, yet the deposition rate was far less. Overall correlation between λ and Nu and λ and HN (made dimensionless by dividing by ΔT_{bulk}) is reasonable and shown in figure 5.3. It is clear that the rougher walls significantly enhance heat transfer, and by association mass transfer but it is not completely clear through what mechanism the deposition rate is reduced for the smoother tubes. Furthermore, for most rough tubes, the deposition was highly non uniform across the length of the tube. Minima in deposit was often seen around the mid point, and in several cases the wall temperature actually reduced after deposit had been formed - suggesting a change to the heat transfer resistance either by removal of deposit or a sudden increase in heat transfer coefficient. Very abrupt changes in deposition rate were observed towards the tops of rougher tubes, corresponding to higher Re and k^+ . For smoother tubes, the deposition rate was usually more even across the length of the tube.

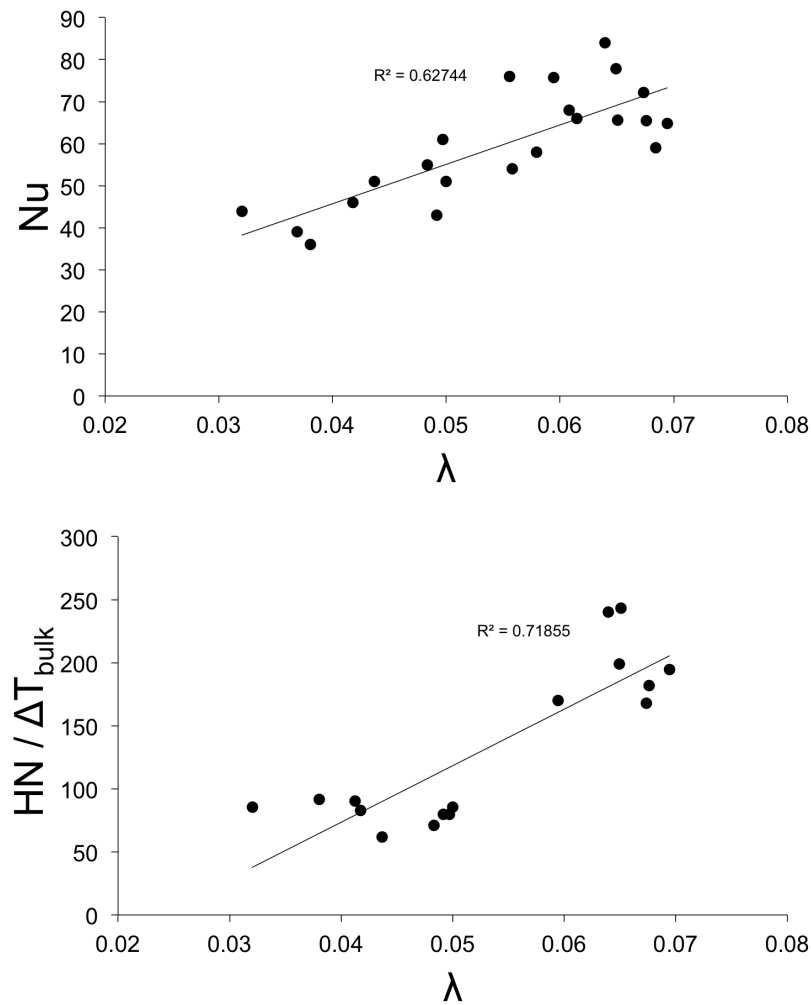


Figure 5.3: Top: correlation of λ_{max} and Nu_{max} . Bottom: correlation of λ_{max} and $HN / \Delta T_{bulk}$

Chemical aspects

While the fluid flow field determines the temperature, residence time and species transport to the wall region, the formation of insoluble material is governed by liquid phase autoxidation. In the experiments conducted in this study with the HiReTS, it is believed that phase change occurred locally at the wall, and that the vaporisation was exacerbated by the reduced heat transfer coefficients of smoother tubes. Studies on the effect of boiling on hydrocarbon deposition are rather limited in number. Crittenden and Khater [122] studied fouling rates from vaporising kerosene in laminar flow using a horizontal tube in a tubular furnace. It was found that with partial vaporisation of the fuel, the highest fouling rates occurred at the bottom of the tube, where the fuel remained in the liquid phase. When the surface temperature was raised further so that complete

vaporisation occurred, there was a substantial reduction in fouling rate, which was suggested to be due to rapid degassing of the oxygen from the liquid phase and / or a vapour blanket being formed at the wall which hindered deposition by the liquid phase mechanism. Vranos [123] studied the effect of film boiling on the thermal decomposition of vaporising n-Hexadecane ($C_{16}H_{34}$). A reduction in fuel decomposition was observed around the transition from nucleate to film boiling, but in the film boiling regime, a rapid increase in fuel decomposition was observed with increasing temperature - attributed to film boiling induced decomposition of hydroperoxides. Since kerosene is comprised of many hydrocarbon species with a range of molecular weights, the lightest and most volatile hydrocarbon components will be the first to vaporise. The lightest hydrocarbons also generate radicals more quickly in liquid phase autoxidation (see figure 3.5), and so the reaction rate may also be reduced through exclusion of these hydrocarbons from the liquid phase autoxidation mechanism.

Improvements to the method

In the HiReTS, the question remains whether the reduction in deposition rate for the smoother tubes was due to fluid dynamic effects, changes to the mechanism of deposition through local vaporisation of the fuel - or a combination. The following recommendations are proposed to improve the HiReTS method in order to gain a clearer understanding of the phenomena and isolate roughness effects.

1. Tube diameter tolerance

In some cases the difference in diameter between the smooth and rough cases created undesirable differences to the change in Reynolds number across the tube. To minimise Reynolds number effects, the tube diameters should ideally be as similar as possible.

2. Roughness quantification via dP measurement

The effectiveness of the study was reduced due to limitations on the quantification of roughness. This could be resolved by using alternative pumping equipment to extend the dP measurement to the fully rough regime - permitting evaluation of the equivalent sand grain roughnesses.

3. Roughness quantification via microscopy

The accuracy of the image processing analysis may be improved by considering more axial sections.

4. Testing with unstable fuels

The comparison between sets of tests was limited due to the continual degradation of the fuel in storage. Ideally future tests should be conducted within a shorter time period where the fuel chemistry does not change appreciably.

5. Boiling effects

The effect of localised boiling on the deposition mechanism is something of an unknown and should be avoided. Boiling may be minimised by increasing the system pressure of the HiReTS. The device would require modification from the current configuration.

6. Reynolds number

The flow velocity should be increased such that the fluid enters the tube in the turbulent regime. Ideally the fuel outlet temperature should be reduced such that the axial gradient in temperature and Reynolds number is less extreme. The pumping equipment would have to be upgraded and the rig would have to be modified to supply more power.

5.2.2 AFTSTU

Opportunity for testing was limited with the AFTSTU but nevertheless, two injector feed arm tests were conducted with tubes having very different roughnesses. The external surfaces of the ALM tubes were measured by optical profilometry and found to have typical roughness heights of $10\mu m$ (S_a). Pressure drop experiments showed a spread in friction factor for the ALM tubes ($0.04 < \lambda < 0.06$), while drawn tubing used as the smooth reference had $\lambda = 0.028$. Comparison with Nikuradse's data showed the drawn and ALM tube to have an equivalent sand grain roughness of $5.5\mu m$ and $k_s = 76\mu m$ respectively. 10 hour tests in the AFTSTU showed the deposition to be more severe over the ALM surface - the final wall temperature rise was almost an order of magnitude higher than the drawn tube. The tests were conducted at a relatively low Reynolds number but the range of roughness Reynolds number (based on the sand grain roughness height) spanned the transitional regime ($k_s^+ \approx 5$ for the drawn tubing and $k_s^+ \approx 65$ for the ALM surface). Considering Nikuradse's classification of roughness regimes, where the departure from hydraulically smooth conditions occurs for $k_s^+ > 3$, the AFTSTU testing indicates that modest disruption to the viscous layer can severely increase the rate of deposition.

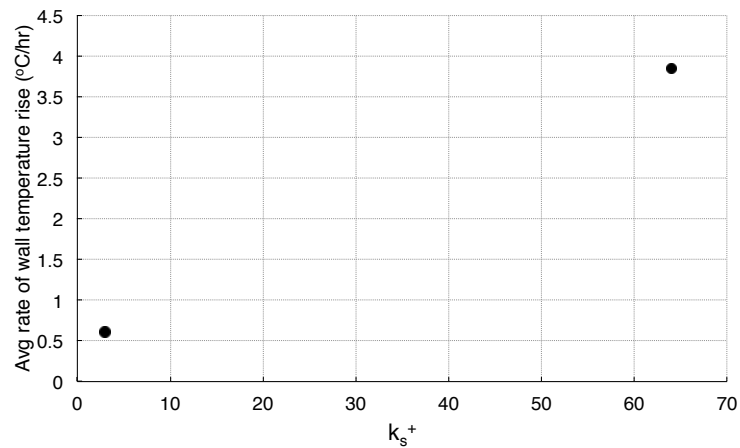


Figure 5.4: Deposition rate with k_s^+ - AFTSTU

The larger scale results are consistent with the observations made for the smaller scale turbulent flow tests. The AFTSTU data (recorded at higher pressure and lower temperature than the HiReTS) provides evidence that the reduced deposition for the smoother capillaries was more a result of fluid mechanics effects than a departure from liquid phase autoxidation.

Further testing is required to confirm the initial observations, and construct a more complete dataset for the dependence of deposition rate with k_s^+ in order to populate figure 5.4

5.3 Proposed mechanism for deposition of insoluble fuel degradation products

Based on the works discussed in the literature review and the observations from the testing described in previous chapters, some conclusions may be formulated for the mechanism of deposition enhancement for rough walled flow.

Several investigators have noted momentum exchange in and out of roughness cavities - associated with the 'scouring' of the wall by turbulence structures ([19], [21], [22]) and increases in turbulence intensity and Reynolds normal and shear stresses in the near wall region and the outer layer with increasing k^+ ([24], [15], [22], [25], [26], [27]). Furthermore, with increasing k^+ , the turbulence sweep-ejection cycle may be altered, with enhancement of sweeps to the wall and suppression of ejections away from the wall ([89], [87], [25]). Roughness has been shown to increase the rate of turbulence production and dissipation and to modify the transport of turbulent kinetic energy ([24]), to increase the absolute vorticity in the vicinity of roughness and reduce the anisotropy of near wall turbulence by breaking up the characteristic quasi-streamwise vortices fundamental to the turbulent boundary layer ([27]). The enhancement of convection near the wall by roughness has also been demonstrated by increases in the values of Nusselt number and Stanton number ([101], [28], [29], [30], [105]). In addition, large increases in particle deposition rate have been observed for fairly moderate increases in k^+ in mass transfer experiments and numerical particle tracking simulations ([37], [34], [38], [39]), and the coherent turbulence structures have been shown to play a crucial role in the transport of particles from the viscous layer to the wall.

Based on a particle density of $1000\text{kg}/\text{m}^3$ ([6]) and diameter of $0.1\mu\text{m}$ ([77]), the relaxation time of an insoluble fuel particle can be estimated by;

$$\tau_p = \frac{\rho_p d_p^2}{18\mu} \quad (5.3.1)$$

$$\tau_p^+ = \frac{\tau_p U^{*2}}{\nu} \quad (5.3.2)$$

resulting in $\tau_p = 0.003$, although agglomeration of insoluble particles would increase this value. Brownian and eddy diffusion would be the relevant mass transfer mechanisms, although it has been shown that diffusion may become less significant over rough walls compared to the inertia-interception mechanism ([37]).

A theory on the role of roughness is outlined as follows;

Hydraulically smooth walls:

- Insoluble oxidation products are generated within the thermal boundary layer according to an arrhenius relationship.
- Particles may form directly on the wall and off the wall at a rate governed by the temperature profile and fuel chemistry.
- Initial deposit formation serves to roughen the wall and small enhancements to heat transfer may occur.
- The temperature gradient across the boundary layer is a minimum.
- Wall shear stress is a minimum.
- Within the viscous layer, particles are deposited by brownian diffusion, or by the passage of particularly intense turbulent motions which are able to penetrate through the buffer layer and impart momentum to fluid and particles in the otherwise quiescent viscous layer.
- Viscous dissipation of turbulent kinetic energy is a maximum.
- Residence time in the near wall region is high.

Transitionally rough walls:

- The roughness elements begin to protrude through the viscous layer and vortex shedding occurs from the elements, introducing turbulence to the near wall region.
- Deposit forms initially in roughness cavities where the temperature is high and the residence time is long.
- Heat transfer is enhanced as previously stagnant areas around roughness elements are disturbed.
- The wall-normal temperature gradient is increased due to enhanced convection.
- Wall shear stress is increased.

- The volume of fluid at the highest temperatures is reduced.
- The wall is exposed to more intense turbulence as k^+ increases.
- Viscous dissipation of turbulent kinetic energy is reduced.
- Strong sweeps from quasi-streamwise vortices replenish the wall region with oxygenated fuel and deposit precursor.
- Supply of oxidation products is increased according to the frequency and intensity of near wall vortices.
- Insoluble particles formed off the wall but with insufficient momentum to reach the wall are provided with inertia with which to deposit.

Fully rough walls:

- Roughness elements are exposed to intense turbulence.
- Near wall vortices are made less anisotropic by roughness and the turbulence intensity is increased.
- Radial temperature and velocity gradients are most extreme.
- Wall shear stress is a maximum.
- Viscous dissipation becomes negligible.
- The extent of the deposit forming region is a minimum.
- Resupply of oxidation products to the wall region is rapid.
- Residence time close to the wall is a minimum, except for in roughness cavities.
- The roughness is reduced with time as deposit fills the roughness cavities.

Chapter 6

Summary and Conclusions

6.1 Summary

To summarise the work described in preceding chapters, it is useful to refer to the aims and objectives outlined previously.

Objectives:

- Identify most viable test method/s:

Three thermal stability rigs were critically examined for suitability and ranked against a set of criteria.

- Establish data points for roughness:

EDM was used to smooth commercially available drawn capillary tubes for use in the HiReTS. Drawn capillaries provided a consistent rough data point. The EDM process varied in its effectiveness, producing some variation in the roughness for the 'smooth' data points. It was difficult to achieve a designed range of roughness.

ALM components were used in the JFTOT and AFTSTU rigs. The process produced the most controlled variation in surface roughness, depending on the build angle and laser parameters.

- Characterise roughnesses as thoroughly as possible:

Optical profilometry was used to measure the roughness of ALM components in detail. Microscopy in conjunction with image processing was employed to characterise features of the capillary tubing. Profilometry produced more useful data than the 2D sections.

Non dimensional pressure drop and heat transfer data was compared against data available in the literature.

- Experimentally determine the effect of roughness on isothermal flow and heat transfer:

Experiments were designed to measure the drop in pressure over the test sections to calculate the friction factor. The method was not completely successful for the capillary tubes but the ALM AFTSTU tubes were measured across all roughness regimes. Increasing surface roughness resulted in higher wall shear stress and increased loss of mean flow momentum.

The HiReTS was used to measure heat transfer coefficients of the capillary tubes. The data showed good similarity with data from the literature. Roughness considerably enhanced heat transfer.

- Experimentally determine whether a trend exists between surface roughness and deposit formation rate:

Deposition tests were conducted in the laminar and turbulent regimes. No significant correlation was observed between surface roughness and severity of deposition for laminar flow.

For both turbulent flow devices, there was a clear relationship between severity of deposition and surface roughness (expressed as the friction factor or roughness Reynolds number). With one exception, deposition was universally more severe for the rougher case.

Aims:

- Establish whether a correlation exists between surface roughness and the deposition rate of thermally stressed aviation fuel:

The data produced from this study indicates that fuel deposition is more severe over rough surfaces than smooth surfaces in the turbulent flow regime. However, insufficient roughness data points were achieved to construct an empirical correlation for the dependence of deposition rate with roughness.

- Provide more detailed information than is available in the current literature about the roughness geometry associated with any observed trend:

Roughnesses were quantified optically by profilometry and microscopy and experimentally through momentum and heat transfer experiments. No such measurements were performed in the available literature for fuel thermal stability.

- Build a dataset for roughness geometry and deposition:

The investigation only considered two types of roughness - ALM surfaces and drawn tubing. As a result, the dataset produced in this study is not particularly dense. A greater range of roughness heights and types of roughness would be desirable.

6.2 Recommendations and future work

Surface quality recommendations for aircraft fuel system components:

- For fuel pathways where wetted wall temperatures are low and heat transfer is not of critical importance, the surface roughness should be minimised.
- For fuel pathways where heat transfer is critical, a rough surface would provide maximum initial heat transfer performance. Transitionally rough surfaces operating at the peak of the Stanton number curve offer the optimum ratio of heat transfer performance to pressure drop. Deposition rates in these sections would likely be high and the heat transfer performance would deteriorate according to the deposition rate.
- Roughness should be minimised in sections of the fuel system which have high Re and / or are very sensitive to fuel deposition products. Significant acceleration of deposition may occur for moderate increases in roughness Reynolds number.
- For ALM (SLM) components which are subject to high heat flux, the number of surfaces overhanging the powder bed should be minimised.

Future work:

- Perform static tests with smooth and rough coupons on the Petroxy device to study in further detail non-flowing catalytic effect of roughness
- Improve the HiReTS dP measurement method to measure the tubes to the fully rough condition.
- Improve the HiReTS deposition method to eliminate Reynolds number and boiling effects.
- Conduct further HiReTS testing with constant surface heat flux as opposed to fixed fuel outlet temperature condition.

- Conduct further injector feed arm tests with the AFTSTU. The tests should be performed when the valves are clean to achieve the highest quality data. Re should be increased.
- Continue to build the dataset on k^+ against deposition rate for different types of roughness (eg. flexible fuel lines).
- Establish a general experimental correlation based on dimensionless variables.
- Improve numerical models of the HiReTS. CFD models were developed but did not include phase change and could not recreate the external wall temperature. The nucleate boiling model should be implemented.
- Establish methods for accurate inclusion of irregular roughness effects (mean and fluctuating quantities) into numerical simulations.
- Develop numerical modelling techniques to simulate insoluble particle formation, transport and growth on the wall. Lagrangian particle tracking could be combined with RANS / LES simulations of the fluid flow field and chemical kinetics mechanisms.
- Develop experimental apparatus to quantify higher order turbulence statistics (profiles of Reynolds stresses) over ALM surfaces. The results could be used to produce a roughness sublayer model for numerical simulations.

Bibliography

- [1] D. R. Kendall, R. H. Clark, and P. Wolveridge, “Fuels for Jet Engines : The Importance of Thermal Stability,” *Aircraft Engineering*, vol. 59, no. 12, pp. 2–7, 1987.
- [2] B. J. Kim, P. Moin, and R. Moser, “Turbulence Statistics in Fully Developed Channel Flow at Low Reynolds Number,” *Journal of Fluid Mechanics*, vol. 177, pp. 133–166, 1987.
- [3] W. F. Taylor, “Deposit Formation from Deoxygenated Hydrocarbons. I. General Features,” *Industrial & Engineering Chemistry Product Research and Development*, vol. 13, no. 2, pp. 133–138, 1974.
- [4] W. F. Taylor, “Kinetics of Deposit Formation from Hydrocarbons,” *Industrial & Engineering Chemistry Product Research and Development*, vol. 8, no. 4, pp. 375–380, 1969.
- [5] C. Moses, “Effect of Reynolds Number on Deposition in Fuels Flowing Over Heated Surfaces,” *Journal of Engineering for Gas Turbines and Power*, vol. 135, no. 12, 2013.
- [6] J. A. TeVelde and M. R. Glickstein, “Heat Transfer and Thermal Stability of Alternative Aircraft Fuels,” tech. rep., Naval Air Propulsion Centre, Trenton, New Jersey, 1983.
- [7] R. Bradley, R. Bankhead, and W. E. Bucher, “High Temperature Hydrocarbon Fuels Research in an Advanced Aircraft Fuel System Simulator,” tech. rep., Air Force Aero Propulsion Laboratory, 1974.
- [8] J. Nikuradse, “Laws of Flow in Rough Pipes,” *NACA Tech. Mem.*, no. 1292, pp. 1–62, 1950.
- [9] H. Schlichting, “Experimental Investigation of the Problem of Surface Roughness,” *NACA Tech. Mem.*, no. 823, pp. 1–60, 1937.

- [10] C. F. Colebrook and C. M. White, "Experiments with Fluid Friction in Roughened Pipes," *Proceedings of the Royal Society A: Mathematical, Physical and Engineering Sciences*, vol. 161, no. 906, pp. 367–381, 1937.
- [11] F. Clauser, "Turbulent Boundary Layers in Adverse Pressure Gradients," *Journal of the Aeronautical Sciences*, vol. 21, pp. 91–108, 1954.
- [12] M. A. Shockling, J. J. Allen, and A. J. Smits, "Roughness Effects in Turbulent Pipe Flow," *Journal of Fluid Mechanics*, vol. 564, pp. 267–285, 2006.
- [13] F. A. Dvorak, "Calculation of Turbulent Boundary Layers on Rough Surfaces in Pressure Gradient," *AIAA Journal*, vol. 7, no. 9, pp. 1752–1759, 1969.
- [14] J. Jimenez, "Turbulent Flows Over Rough Walls," *Annual Review of Fluid Mechanics*, vol. 36, no. 1, pp. 173–196, 2004.
- [15] D. H. Wood and R. A. Antonia, "Measurements in a Turbulent Boundary Layer Over a D-Type Surface Roughness," *Journal of Applied Mechanics*, no. September 1975, pp. 591–597, 1975.
- [16] A. E. Perry, W. H. Schofield, and P. N. Joubert, "Rough Wall Turbulent Boundary Layers," *Journal of Fluid Mechanics*, vol. 37, no. 02, p. 383, 1969.
- [17] P. R. Bandyopadhyay, "Rough-wall Turbulent Boundary Layers in the Transition Regime," *Journal of Fluid Mechanics*, vol. 180, p. 231, 1987.
- [18] R. L. Simpson, "A Generalized Correlation of Roughness Density Effects on the Turbulent Boundary Layer.," *AIAA Journal*, vol. 11, no. 2, pp. 242–244, 1973.
- [19] H. Townes and R. Sabersky, "Experiments on the Flow over a Rough Surface," *International Journal of Heat and Mass Transfer*, vol. 9, no. 8, pp. 729–738, 1966.
- [20] S. J. Kline, W. C. Reynolds, F. A. Schraub, and P. W. Runstadler, "The Structure of Turbulent Boundary Layers," *Journal of Fluid Mechanics*, vol. 30, no. 04, pp. 741–773, 1967.
- [21] C. K. Liu, S. J. Kline, and J. P. Johnston, "An Experimental Study of Turbulent Boundary Layer on Rough Walls," tech. rep., Stanford University, Stanford, California, 1966.

- [22] L. Djenidi, F. Anselmet, and R. A. Antonia, "LDA Measurements in a Turbulent Boundary Layer over a D-Type Rough wall," *Experiments in Fluids*, vol. 16, pp. 323–329, 1994.
- [23] L. Djenidi, R. Elavarasan, and R. A. Antonia, "The Turbulent Boundary Layer over Transverse Square Cavities," *Journal of Fluid Mechanics*, vol. 395, pp. 271–294, 1999.
- [24] P. M. Ligrani and R. J. Moffat, "Structure of Transitionally Rough and Fully Rough Turbulent Boundary Layers," *Journal of Fluid Mechanics*, vol. 162, pp. 69–98, 1986.
- [25] M. P. Schultz and K. A. Flack, "The Rough Wall Turbulent Boundary Layer from the Hydraulically Smooth to the Fully Rough Regime," *Journal of Fluid Mechanics*, vol. 580, p. 381, 2007.
- [26] R. A. Antonia and P. A. Krogstad, "Turbulence Structure in Boundary Layers over Different Types of Surface Roughness," *Fluid Dynamics Research*, vol. 28, pp. 139–157, 2001.
- [27] K. Bhaganagar, J. Kim, and G. Coleman, "Effect of Roughness on Wall-Bounded Turbulence," *Flow, Turbulence and Combustion*, vol. 72, pp. 463–492, 2004.
- [28] D. F. Dipprey and R. H. Sabersky, "Heat and Momentum Transfer in Smooth and Rough Tubes at Various Prandtl Numbers," *International Journal of Heat and Mass Transfer*, vol. 6, pp. 329–353, 1962.
- [29] N. Sheriff and P. Gumley, "Heat Transfer and Friction Properties of Surfaces with Discrete Roughness," *International Journal of Heat and Mass Transfer*, vol. 9, pp. 1297–1320, 1965.
- [30] R. Gowen and J. Smith, "Turbulent Heat Transfer from Smooth and Rough Surfaces," *International Journal of Heat and Mass Transfer*, vol. 11, no. 11, pp. 1657–1674, 1968.
- [31] M. H. Hosni, H. W. Coleman, J. W. Garner, and R. P. Taylor, "Roughness Element Shape Effects on Heat Transfer and Skin Friction in Rough-wall Turbulent Boundary Layers," *International Journal of Heat and Mass Transfer*, vol. 36, no. 1, pp. 147–153, 1993.

- [32] N. B. Wood, "A Simple Method for the Calculation of Turbulent Deposition to Smooth and Rough Surfaces," *Journal of Aerosol Science*, vol. 12, no. 3, pp. 275–290, 1981.
- [33] J. W. Cleaver and B. Yates, "A Sublayer Model for the Deposition of Particles from a Turbulent flow," *Chemical Engineering Science*, vol. 30, no. 8, pp. 983–992, 1975.
- [34] A. C. Wells and A. C. Chamberlain, "Transport of Small Particles to Vertical Surfaces," *British Journal of Applied Physics*, vol. 18, pp. 1793–1799, 1967.
- [35] B. Y. H. Liu and J. K. Agarwal, "Experimental Observation of Aerosol Deposition in Turbulent Flow," *Journal of Aerosol Science*, vol. 5, no. 206, pp. 145–155, 1974.
- [36] G. Kallio and M. Reeks, "A Numerical Simulation of Particle Deposition in Turbulent Boundary Layers," *International Journal of Multiphase Flow*, vol. 15, no. 3, pp. 433–446, 1989.
- [37] F. G. Fan and G. Ahmadi, "A Sublayer Model for Turbulent Deposition of Particles in Vertical Ducts with Smooth and Rough Surfaces," *Journal of Aerosol Science*, vol. 24, no. 1, pp. 45–64, 1993.
- [38] C. Marchioli and A. Soldati, "Mechanisms for Particle Rransfer and Segregation in a Turbulent Boundary Layer," *Journal of Fluid Mechanics*, vol. 468, pp. 283–315, 2002.
- [39] C. Marchioli, A. Giusti, M. V. Salvetti, and A. Soldati, "Direct Numerical Simulation of Particle Wall Transfer and Deposition in Upward Turbulent Pipe Flow," *International Journal of Multiphase Flow*, vol. 29, no. 6, pp. 1017–1038, 2003.
- [40] S. K. Robinson, "Coherent Motions in the Turbulent Boundary Layer," *Annual Review of Fluid Mechanics*, vol. 23, pp. 601–639, 1991.
- [41] A. J. Ghajar, C. C. Tang, and W. L. Cook, "Experimental Investigation of Friction Factor in the Transition Region for Water Flow in Minitubes and Microtubes," *Heat Transfer Engineering*, vol. 31, no. 8, pp. 646–657, 2010.
- [42] K. H. Strauss, "Thermal Stability of Aviation Turbine Fuel - a History," in *Aviation Fuel Thermal Stability Requirements* (P. W. Kirklin and P. David, eds.), pp. 8–17, 1992.

- [43] CRC, "Development of Research Techniques for Determining the Oxidative Stability of Aircraft Gas Turbine Fuels," Tech. Rep. 450, CRC, 1972.
- [44] J. Bauldreay, R. Heins, G. Houlbrook, and J. Smith, "Hi Reynolds Number Thermal Stability Rig for Realistic Rapid Evaluation of Distillate Fuel Thermal Oxidation Stability," in *6th International Conference on Stability and Handling of Liquid Fuels*, (Vancouver), pp. 295–314, 1997.
- [45] S. P. Brown, J. M. Emens, R. A. Frederick, H. Number, and A. H. Number, "RP-1 and JP-8 Thermal Stability Experiments," tech. rep., UAH Propulsion Research Centre, Huntsville, 2005.
- [46] R. H. Clark and P. A. Stevenson, "The Thermal Degredation of Aviation Fuels in Jet Engine Injector Feed Arms: Results From a Half Scale Rig," *Symposium on the Stability and Oxidation Chemistry of Middle Distillate Fuels*, no. August, pp. 1302–134, 1990.
- [47] D. L. Daggett, A. Veninger, C. Lewis, S. Bullock, and R. Kamin, "The development of an aviation fuel thermal stability test unit," 1995.
- [48] W. F. Taylor, "Jet Fuel Thermal Stability," in *Nasa Technical Memorandum 79231* (W. F. Taylor, ed.), (Cleveland), 1979.
- [49] R. N. Hazlett, *Thermal Oxidation Stability of Aviation Turbine Fuels*. Philadelphia: ASTM, 1991.
- [50] CRC, "CRC Literature Survey on the Thermal Oxidation Stability of Jet Fuel," tech. rep., CRC, Atlanta, 1979.
- [51] L. Hibbert, "Adding Beats Subtraction," *Professional Engineering*, pp. 44–45, 2014.
- [52] L. Prandtl, *Prandtl's Essentials of Fluid Mechanics*. Springer (Applied Mathematical Sciences), 2 ed., 2004.
- [53] H. Schlichting, *Boundary Layer Theory*. Springer, 8 ed., 2001.
- [54] A. S. Monin and A. M. Yaglom, *Statistical Fluid Mechanics - Mechanics of Turbulence Volume 1*. Dover, 1 ed., 2007.
- [55] W. F. Taylor, "The Effect of Manufacturing Processes on Aviation Turbine Fuel Thermal Stability," in *Aviation Fuel Thermal Stability Requirements* (P. Kirklin and P. David, eds.), pp. 81–89, Philadelphia: ASTM, 1992.

- [56] C. R. Council, *Handbook of Aviation Fuel Properties*. No. 663, 2014.
- [57] R. N. Hazlett, "The Physicochemical Aspects of Thermal Stability," in *Aviation Fuel Thermal Stability Requirements* (P. Kirklin and P. David, eds.), pp. 18–33, Philadelphia: ASTM, 1992.
- [58] J. S. Ervin, S. P. Heneghan, C. R. Martel, and T. F. Williams, "Surface Effects on Deposits From Jet Fuels," *Journal of Engineering for Gas Turbines and Power*, vol. 118, no. 2, p. 278, 1996.
- [59] E. L. Wong and D. A. Bittker, "Effect of Hydrocarbon Fuel Type on Fuel Thermal Stability," tech. rep., Lewis Research Centre, Cleveland, 1982.
- [60] E. Baker, A. Bittker, M. Cohen, and G. T. Seng, "Research on Aviation Fuel Instability," tech. rep., Lewis Research Centre, Cleveland, 1983.
- [61] W. F. Taylor, "Deposit Formation from Deoxygenated Hydrocarbons. II. Effect of Trace Sulfur Compounds," *Industrial & Engineering Chemistry Product Research and Development*, vol. 15, no. 1, pp. 64–68, 1976.
- [62] J. S. Mills and D. R. Kendall, "The Quantification and Improvement of the Thermal Stability of Aviation Turbine Fuel," *Journal of Engineering for Gas Turbines and Power*, vol. 108, no. 85, pp. 381–386, 1986.
- [63] W. F. Taylor and J. W. Frankenfeld, "Deposit Formation from Deoxygenated Hydrocarbons. 3. Effects of Trace Nitrogen and Oxygen Compounds," *Industrial & Engineering Chemistry Product Research and Development*, vol. 17, no. 1, pp. 86–90, 1978.
- [64] W. F. Taylor, "Kinetics of Deposit Formation from Hydrocarbons - III Heterogeneous and Homogenous Metal Effects," *Journal of Applied Chemistry*, vol. 18, pp. 251–254, 1968.
- [65] J. Colbert and C. J. Nowack, "US Navy Evaluation of the High Reynolds Number Thermal Stability (HiReTS) Test Unit," tech. rep., Naval Air Systems Command, 2003.
- [66] J. D. Smith, "The Effect of Metals and Alloys on the Thermal Stability of Avtur 50," *Aircraft Engineering and Aerospace Technology*, vol. 39, no. 4, pp. 19–26, 1967.

- [67] R. Hazlett, J. Hall, and M. Matson, "Reactions of Aerated N-Dodecane Liquid Flowing Over Heated Metal Tubes," *Industrial & Engineering Chemistry Product Research and Development*, vol. 16, no. 2, pp. 171–177, 1977.
- [68] R. H. Clark and L. Thomas, "An Investigation of the Physical and Chemical Parameters Affecting the Performance of the JFTOT," *SAE technical paper series*, 1988.
- [69] I. L. Stavinoha, D. W. Naegeli, and L. McInnis, "The Role of Surface Composition in Fuel Deposition," *American Chemical Society, Division of Fuel Chemistry*, vol. 35, pp. 1315–1323, 1990.
- [70] J. S. Ervin, T. A. Ward, T. F. Williams, and J. Bento, "Surface Deposition Within Treated and Untreated Stainless Steel Tubes Resulting from Thermal-oxidative and Pyrolytic Degradation of Jet Fuel," *Energy and Fuels*, vol. 17, no. 3, pp. 577–586, 2003.
- [71] J. D. Smith, "Effects of Deposits on Heat Transfer to Aviation Kerosine," *Industrial & Engineering Chemistry Process Design and Development*, vol. 8, no. July, pp. 299–308, 1969.
- [72] P. J. Marteney and L. J. Spadaccini, "Thermal Decomposition of Aircraft Fuel," *Journal of Engineering for Gas Turbines and Power*, vol. 108, pp. 648–653, 1986.
- [73] S. Siouris, S. Blakey, and C. W. Wilson, "Investigation of Deposition in Aviation Gas Turbine Fuel Nozzles by Coupling of Experimental Data and Heat Transfer Calculations," *Fuel*, vol. 106, pp. 79–87, 2013.
- [74] J. S. Chin and A. H. Lefebvre, "Influence of Flow Conditions on Deposits From Heated Hydrocarbon Fuels," *Journal of Engineering for Gas Turbines and Power*, vol. 115, no. 3, p. 433, 1993.
- [75] D. W. Naegeli, "Thermal Stability of Jet Fuels: Kinetics of Forming Deposit Precursors," tech. rep., Southwest Research Institute, San Antonio, 1997.
- [76] E. J. Szetela, A. J. Giovanetti, and S. Cohen, "Fuel Deposit Characteristics at Low Velocity," *Journal of Engineering for Gas Turbines and Power*, vol. 108, no. 85, pp. 460–464, 1986.
- [77] R. M. Schirmer, "Morphology of Deposits in Aircraft and Engine Fuel Systems," in *Society of Automotive Engineers National Air Transportation Meeting*, (New York), 1970.

- [78] J. S. Ervin and T. F. Williams, "Global Kinetic Modeling of Aviation Fuel Fouling in Cooled Regions in a Flowing System," *Industrial & Engineering Chemistry Research*, vol. 35, no. 11, pp. 4028–4036, 1996.
- [79] F. Hopf, "Die Messung der Hydraulischen Rauigkeit," *Zs. angew. Math, und Mech.*, vol. 3, pp. 329–339, 1923.
- [80] L. Fromm, "Stromungswiderstand in Rauhen Rohren," *Zs. angew. Math, und Mech.*, vol. 3, pp. 339–358, 1923.
- [81] H. Coleman, B. K. Hodge, and R. P. Taylor, "A Re-Evaluation of Schlichting's Surface Roughness Experiment," *Transactions of the ASME*, vol. 106, pp. 60–65, 1984.
- [82] C. F. Colebrook, "Turbulent Flow in Pipes, With Particular Reference To the Transition Region Between the Smooth and Rough Pipe Laws," *Journal of the Institution of Civil Engineers*, vol. 11, no. 4, pp. 133–156, 1939.
- [83] L. F. Moody, "Friction Factors for Pipe Flow," *Transactions of the ASME*, pp. 671–684, 1944.
- [84] F. R. Hama, "Boundary- Layer Characteristics for Smooth and Rough Surfaces," *Transactions of the Society of Naval Architects and Marine Engineers*, vol. 62, pp. 333–358, 1954.
- [85] W. F. Scaggs, R. P. Taylor, and H. W. Coleman, "Measurement and Prediction of Rough Wall Effects on Friction Factor - Uniform Roughness Results," *Journal of Fluids Engineering*, vol. 110, pp. 385–391, 1988.
- [86] R. P. Taylor, H. W. Coleman, and B. K. Hodge, "Prediction of Turbulent Rough-Wall Skin Friction Using a Discrete Element Approach," *Journal of Fluids Engineering*, vol. 107, no. 2, pp. 251–257, 1985.
- [87] P. A. Krogstad, R. A. Antonia, and L. W. B. Browne, "Comparison Between Rough and Smooth Wall Turbulent Boundary Layers," *Journal of Fluid Mechanics*, vol. 245, pp. 599–617, 1992.
- [88] P. A. Antonia, R. A. Krogstad, "Surface Roughness Effects in Turbulent Boundary Layers," *Experiments in Fluids*, vol. 27, no. 4, pp. 450–460, 1999.
- [89] K. A. Flack, M. P. Schultz, and T. A. Shapiro, "Experimental Support for Townsend's Reynolds Number Similarity Hypothesis on Rough Walls," *Physics of Fluids*, vol. 17, no. 2005, pp. 1–9, 2005.

- [90] A. A. Townsend, *The Structure of Shear Flows*. Cambridge: Cambridge University Press, 2 ed., 1976.
- [91] M. R. Raupach, R. A. Antonia, and S. Rojagopalan, "Rough Wall Turbulent Boundary Layers," *Applied Mechanics Review*, vol. 44, no. 1, pp. 1–25, 1991.
- [92] V. Streeter, "Stromungswiderstand in Rauhen Rohren," *Trans. Amer. Soc. Civ. Eng.*, vol. 101, pp. 681–704, 1936.
- [93] J. W. Johnson, "Rectangular Artificial Roughness in Open Channels," *Transactions of the American Geophysical Union*, pp. 906–914, 1944.
- [94] D. Bettermann, "Contribution a L'Etude de la Convection Forcee Turbulente le Long de Plaques Rugueuses," *International Journal of Heat and Mass Transfer*, vol. 9, pp. 153–164, 1965.
- [95] A. E. Perry and P. N. Joubert, "Rough-wall Boundary Layers in Adverse Pressure Gradients," *Journal of Fluid Mechanics*, vol. 17, no. 2, pp. 193–211, 1963.
- [96] P. R. Spalart, "Direct Simulation of a Turbulent Boundary Layer up to $R\theta = 1410$," *Journal of Fluid Mechanics*, vol. 187, pp. 61–98, 1988.
- [97] V. Gnielinski, "New Equation for Heat and Mass Transfer in Turbulent Pipe and Channel flow," *Int. Chem. Eng.*, vol. 16, pp. 359–367, 1976.
- [98] F. P. Incropera and D. P. DeWitt, *Fundamentals of Heat and Mass Transfer*. Wiley, 4 ed., 1996.
- [99] A. Bhattacharyya, "Heat Transfer and Pressure Drop with Rough Surfaces, a Literature Survey," tech. rep., Aktiebolaget Atomenergi, Stockholm, 1964.
- [100] M. M. Pimenta, R. J. Moffat, and W. M. Kays, "The Turbulent Boundary Layer: an Experimental Study of the Transport of Momentum and Heat with the Effect of Roughness," Tech. Rep. AD-A014 29, Stanford University, Stanford, 1975.
- [101] W. Nunner, "Heat Transfer and Pressure Drop in Rough Tubes," *AERE Lib/Trans. 786*, 1956.
- [102] R. Martinelli, "Heat Transfer to Molten Metals," *Trans. ASME*, vol. 69, p. 947, 1947.

- [103] J. W. Smith and N. Epstein, "Effect of Wall Roughness on Convective Heat Transfer in Commercial Pipes," *A.I.Ch.E Journal*, vol. 3, no. 2, pp. 242–248, 1957.
- [104] P. Owen and W. Thomson, "Heat Transfer across Rough Surfaces," *Journal of Fluid Mechanics*, vol. 15, no. 3, pp. 321–334, 1963.
- [105] M. H. Hosni, H. W. Coleman, and R. P. Taylor, "Heat Transfer Measurements and Calculations in Transitionally Rough Flow," in *Gas Turbine and Aeroengine Congress and Exposition*, (Brussels), pp. 1–9, ASME, 1990.
- [106] P. G. Papavergos and A. B. Hedley, "Particle Deposition Behaviour from Turbulent Flows," *Chemical Engineering Research and Design*, vol. 62, pp. 275–295, 1984.
- [107] S. K. Friedlander and H. F. Johnstone, "Deposition of Suspended Particles from Turbulent," *Industrial and Engineering Chemistry*, vol. 49, no. 7, pp. 1151–1156, 1957.
- [108] C. N. Davies, "The Rate of Deposition of Aerosol Particles from Turbulent Flow Through Ducts," *Annals of Occupational Hygiene*, vol. 8, pp. 239–245, 1965.
- [109] P. Hutchinson, G. F. Hewitt, and A. E. Dukler, "Deposition of Liquid or Solid Dispersions from Turbulent Gas Streams : a Stochastic Model," *Chemical Engineering Science*, vol. 26, pp. 419–439, 1971.
- [110] A. J. Grass, "Structural Features of Turbulent Flow over Smooth and Rough Boundaries," *Journal of Fluid Mechanics*, vol. 50, no. 2, pp. 233–254, 1971.
- [111] S. Beal, "Deposition of particles in turbulent flow on channel or pipe walls," *Nuclear Science and Engineering*, vol. 40, no. 1, pp. 1–11, 1970.
- [112] B. Y. H. Liu and T. A. Ilori, "Aerosol Deposition in Turbulent Pipe Flow," *Environmental Science & Technology*, vol. 8, no. 4, pp. 351–356, 1963.
- [113] S. Goren and D. Erhart, "Particle Velocities Normal to a Wall for Turbulent Shear Flow," *Journal of Fluid Mechanics*, vol. 187, 1989.
- [114] J. B. McLaughlin, "Aerosol Particle Deposition in Numerically Simulated Channel Flow," *Physics of Fluids A: Fluid Dynamics*, vol. 1, no. 7, pp. 1211–1224, 1989.

- [115] T. L. Montgomery and M. Corn, "Aerosol Deposition in a Pipe with Turbulent Airflow," *Aerosol Science*, vol. 1, pp. 185–213, 1970.
- [116] N. Epstein, "Particulate Fouling of Heat Transfer Surfaces, Mechanisms and Models," in *Fouling Science and Technology*, pp. 143–164, Kluwer Academic Publishers, 1988.
- [117] I. Owen, A. A. El-Kady, and J. W. Cleaver, "Deposition of sub-micrometre particles onto a heated surface with widely spaced roughness elements," *Journal of Aerosol Science*, vol. 20, no. 6, pp. 671–681, 1989.
- [118] J. S. Ervin, S. Zabarnick, and T. F. Williams, "One-Dimensional Simulations of Jet Fuel Thermal-Oxidative Degradation and Deposit Formation Within Cylindrical," *Journal of Energy Resources Technology*, vol. 122, no. December, pp. 229–238, 2000.
- [119] T. G. Karayiannis and M. M. Mahmoud, "Flow boiling in microchannels : Fundamentals and applications," *Applied Thermal Engineering*, vol. 115, pp. 1372–1397, 2017.
- [120] T. Edwards and S. Zabarnick, "Supercritical Fuel Deposition Mechanisms," *Industrial & Engineering Chemistry Research*, vol. 32, no. 1986, pp. 3117–3122, 1993.
- [121] S. G. Kandlikar, S. Garimella, D. Li, S. Colin, and M. R. King, *Heat Transfer and Fluid Flow in Minichannels and Microchannels*. Elsevier Butterworth-Heinemann, 2 ed.
- [122] B. D. Crittenden and E. M. H. Khater, "Fouling From Vaporizing Kerosine," *Journal of Heat Transfer*, vol. 109, no. August 1987, pp. 583–589, 1987.
- [123] A. Vranos and E. Section, "Influence of Film Boiling on the Thermal Decomposition of n-Hexadecane," *Industrial & Engineering Chemistry Product Research and Development*, vol. 20, pp. 167–169, 1981.
- [124] M. Sherratt, J. Wood, J. Bauldreay, and R. Heins, "Factors Influencing the Results Obtained by the High Reynolds Number Thermal Stability Test Instrument (HiReTS)," in *IASH 2000, the 7th International Conference on Stability and Handling of Liquid Fuels*, (Graz), 2000.
- [125] S. G. Pande and D. R. Hardy, "Quest for a Reliable Method for Determining Aviation Fuel Thermal Stability: Comparison of Turbulent and Laminar Flow Test Devices," *Energy and Fuels*, vol. 15, pp. 224–235, 2001.

- [126] E. Alborzi, S. Blakey, H. Ghadebigi, C. Pinna, and C. Wilson, "Microscopy and Elemental Analysis of Surface Deposits Formed in a Simulated Jet Engine Feed Arm Injector under Representative Conditions," 2011.

Appendices

Appendix A

Literature Review of Fuel Testing Devices

Quantifying the thermal stability of a fuel and predicting fuel performance in a real aircraft fuel system is not straightforward. Testing on full-scale fuel system simulators undoubtedly provides the most accurate demonstration of how a fuel will behave under aircraft operating conditions. However it is also prohibitively impractical, since full scale systems consume thousands of litres of fuel per hour, and instability effects typically occur over hundreds of hours. Conversely, small scale specification devices must provide a result within a few hours to be practical and ideally must use as small a quantity of fuel as possible. These dynamic tests typically pass fuel through single heated tubes (akin to those found in fuel/oil heat exchangers) and must stress the fuel at non-representative temperatures to initiate a faster rate of deposit formation for a reduced test duration. Although the rate of deposition has been found to be strongly dependent on initial wall temperature according to the Arrhenius relationship, the results of specification tests cannot be directly applied to aircraft, and the relationship remains largely empirical. Development of a correlation between laboratory scale devices and engines was highlighted in [50] as a key area for future research and the subject of test rig suitability for thermal stability assessment is discussed at length in the literature. In the middle ground, sit test rigs that are neither complete simulators nor specification devices. Such rigs are usually designed to recreate as best as possible the flow path (condition the fuel) up to a critical component of interest (eg. a fuel injector feed arm) or include several components of interest over a range of temperature regimes. Temperatures are representative, not exaggerated as with laboratory devices - although usually compare to the most extreme conditions seen in flight (ie. at the start of descent, where engine temperatures are high

and fuel flow rates are low). The level of instrumentation provides a wealth of temperature and deposition data - key to the understanding of the heat transfer and chemistry in the deposition process. The downside of running large scale rigs at representative temperatures is that the testing requires a great deal of time and fuel, although successful efforts have been made to generate meaningful data from scaled systems with a much reduced appetite. Data from such devices is the primary source of validation for the smaller scale devices.

A.1 Laboratory scale test devices

A.1.1 CRC Coker (ASTM D1660)

Table A.1: CRC Coker operating conditions

Preheater outlet temperature ($^{\circ}C$)	150
Filter temperature ($^{\circ}C$)	204
Fuel flow rate (ml/min)	60
Test time (h)	5
System pressure (bar)	10

It was in the fuel manifold of the J57 engine where fuel instability problems were first observed, and the Coker test was designed to simulate such an environment [61]. The operating conditions are summarised in table A1. Over the course of the test, around 19l of fuel is passed through the pre-heater assembly (representing hot fuel lines in an engine) - an annulus with an inner aluminium tube, heated internally with an electric cartridge heater [49] and an outer tube with external diameter 12.7mm. The length of the fuel-contacted surface is 330mm. The temperature of the fuel is controlled through a thermocouple measuring the bulk fuel outlet temperature, controlling the heating power applied to the inner surface. Flow through the preheater assembly is laminar. The stainless steel, 25 μm test filter (intended to represent injector nozzles or small flow passages prone to blockage) is heated separately from the preheater assembly through heating of the filter housing and instrumented to measure pressure drop over the filter.

Table A.2: Coker tube colour rating scale [49]

0	No visible deposit
1	Haze or dulling, no colour
2	Barely visible discolouration
3	Light tan
4	Heavier than 3

In ASTM D1660, thermal stability of the fuel is assessed through a visual rating of the preheater tube deposit against an arbitrary colour rating scale (table A2) and the filter pressure drop at the end of the test. Specification limits were selected to correlate with flight test results and were applied on a pass/fail basis. A fuel failed the specification test with a visual rating of 3 or more, and a filter pressure drop of $10kPa$.

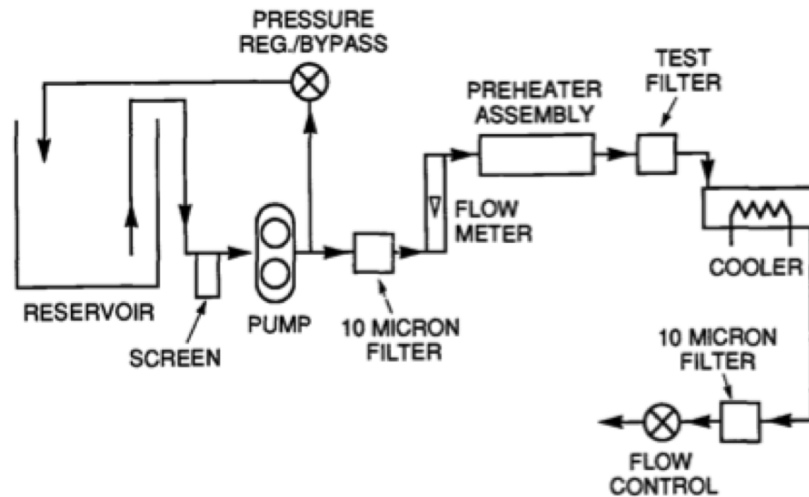


Figure A.1: CRC coker flow path (taken from [42])

It became apparent through use that the Coker and associated test method exhibited a number of flaws. Principally, the large sample requirement and test duration, wear and pressure limitations of the pump, nature of temperature control (bulk fuel outlet not fuel wetted surface temperature), precision of temperature control, method of tube heating and method of deposit assessment [57], [42].

A.1.2 JFTOT (ASTM D3241)

An extensive review of two proposed JFTOT devices was conducted in 1972. Specifications for the proposed JFTOT were drawn from prior Coker experience ([43]). The JFTOT designs were compared against each other and the Coker in a program of testing on 5 fuels, which was complemented with additional data on the same fuels from a full scale engine simulator and a selection of other dynamic and static testing devices. The review investigated the repeatability and reproducibility of the devices (including between operators and laboratories), the ability of each device to distinguish fuels, the effect of varying control temperatures, drift of results with time and measurement precision compared to the Coker.

It was found from analysis of the standard deviations of visual deposit ratings that no significant improvement was observed with either device when compared to a repeatability study of the Coker - highlighting the variance created through operator interpretation of the deposit. Both JFTOT designs were found to be generally more precise (in pressure drop measurement and temperature required to produce a given deposit rating) and both designs ranked fuels in agreement with data from other devices - although the Alcor unit provided results in closer agreement to simulator data [7]. The Alcor JFTOT was ultimately selected as the Coker replacement - since it was more compact and used a much smaller sample size.

The JFTOT operating conditions are listed in table A3. In the JFTOT test (ASTM D3241), a 600ml fuel sample is filtered through a 0.5 μ m membrane filter and passed through the heater section - an annulus with an inner aluminium tube, heated via resistive heating. The fuel-contacted surface is reduced from the Coker test to 60mm. The test temperature is controlled by a thermocouple measuring the internal wall temperature at the hottest point along the heated tube, adjusting the heating power applied to the tube to ensure a maximum wall temperature of 260°C. System pressure is controlled independently of the pump and is raised from the Coker test to 34bar - to permit testing at higher temperatures while maintaining single-phase flow. Flow through the preheater assembly remains laminar ($Re \approx 101$). The 17 μ m test filter is located at the exit of the preheater assembly and is heated only through the passage of hot fuel.

In ASTM D3421, the rating criteria remain as preheater deposit colour rating and filter pressure drop. A fuel meets the specification if it gives a preheater colour

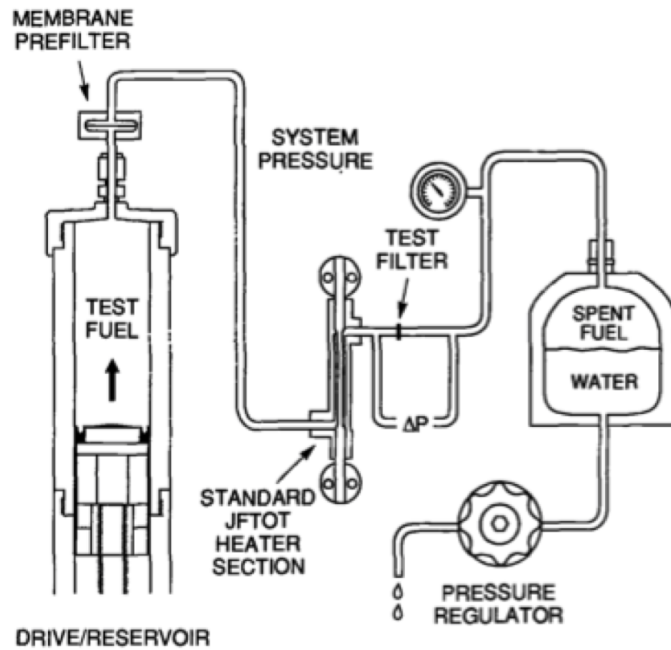


Figure A.2: JFTOT flow path (taken from [43])

rating of less than 3 and a filter pressure drop of no more than $3.3kPa$. Since the pass/fail nature of the specification test provides little insight into the potential of fuels that pass the test, the JFTOT can also be used in a 'breakpoint' evaluation to provide a more quantitative assessment - where the preheater temperature is increased with each test until the fuel no longer meets the specification criteria.

Despite the improvements over the Coker test, the JFTOT is still widely considered to have shortcomings, most notably the visual rating method of deposit and the laminar flow nature of the device - which is not representative of fuel / oil heat exchangers in real aircraft.

Table A.3: JFTOT operating conditions

Heater outlet temperature ($^{\circ}C$)	260
Fuel flow rate (ml/min)	3
Test time (hrs)	2.5
System pressure (bar)	34.5

A.1.3 HiReTS (EI482 / ASTM D6811)

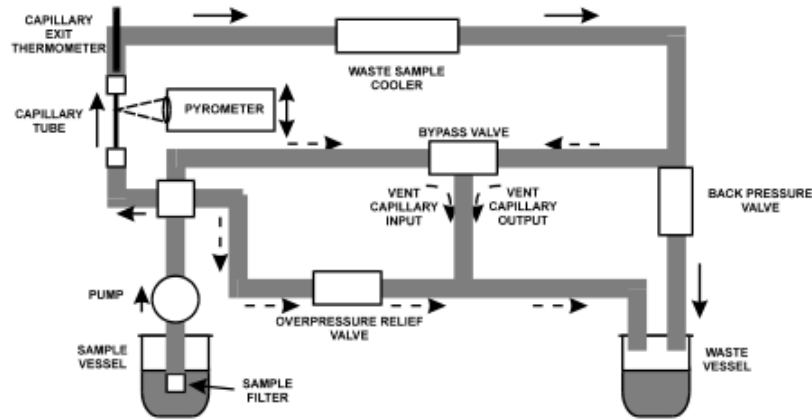


Figure A.3: HiReTS flow path

The High Reynolds Number Thermal Stability rig was developed by Shell in the 1990s, to satisfy the requirement for a small scale thermal stability tester that operated under flow conditions more representative of those found in aircraft fuel systems. Other rigs that operated in the turbulent regime at the time of HiReTS development were large scale rigs testing full scale or scaled down components (eg. injector feed arms, fuel/oil heat exchanger tubes) with large appetites for fuel - unsuitable for fuel specification tests.

Table A.4: HiReTS operating conditions

Fuel outlet temperature ($^{\circ}C$)	290
Fuel flow rate (ml/min)	35
Test time ($mins$)	125
System pressure (bar)	20

The HiReTS operating conditions are shown in table A4. 5l of fuel is aerated, filtered with a $20\mu m$ stainless steel sample filter and pumped with an HPLC pump through the test section at 20bar. Turbulent flow and a small sample size are achieved through use of a 150mm long capillary tube (stainless steel) with $300\mu m$ internal diameter and fuel flow rate of $35ml/min$. The Reynolds number at the exit of the tube is at least 5000, based on a bulk fuel exit temperature of $280^{\circ}C$. The capillary is heated electrically via resistive heating, with heating power controlled via a PID controller and a thermocouple measuring bulk fuel temperature at the exit of the capillary. The device provides a quantitative measure of thermal

stability through measurement of the capillary outer wall temperature rise over time (total HiReTS number), which occurs as insulating deposits form on the inner surface of the tube and the heating power is increased to maintain the constant fuel outlet temperature. The capillary outer wall temperature is measured at 12 locations, spaced at 2.5mm intervals by an infrared scanning pyrometer. For accuracy of temperature measurement, the outer surface of the tube is blackened with high emissivity reference paint. The calculation of the total HiReTS number - the sum of the differences between the minimum and final temperatures at each measurement location and measure of fuel stability is shown below:

$$\text{HN total} = \sum_1^n \Delta T(x) \quad (\text{A.1.1})$$

where $\Delta T(x) = T_{fin,x} - T_{min,x}$.

Correlation between thermal stability measurements

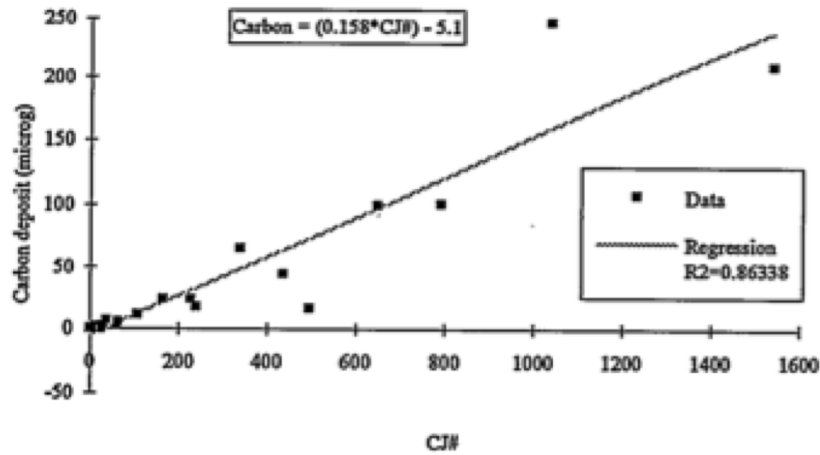


Figure A.4: HiReTS correlation (taken from [44])

Correlation between the HiReTS result and other devices was investigated in [44]. Initially, HiReTS Carbon Burn Off (CBO) values were compared against JFTOT CBO / breakpoint, Single Tube Heat Transfer Rig (STHTR) loss in heat transfer coefficient (ΔHTC), Mini-Injector Feed Arm Rig (MIFAR) deposition rate and radical initiation rate from the Thornton Flask Oxidation Test for 14 fuels. Good correlation was observed between HiReTS CBO and MIFAR / Flask Oxidation Tests - the latter supporting a HiReTS result driven by fuel chemistry rather than mass transport effects. Correlation was observed between the HiReTS CBO and

STHTR results, although it was no better than the JFTOT. It was suggested that the lack of fuel preheating in the HiReTS may have affected the correlation with the STHTR although no improvement was observed when pre-heating was included. The moderate correlation between STHTR and JFTOT was attributed to the very slow flow having some similar effect to pre-heating in the test section.

The HiReTS number was compared to post test carbon burn off (CBO) data (fig. A4). Sufficient agreement was found to allow the HiReTS number alone to be used for comparison against other test devices - thus negating the lengthy and relatively technical carbon burn off procedure. However, it was noted that the repeatability of the test seemed to decrease with fuel quality and the data for comparison was sparse for poor fuels.

In a further phase of assessment, the HiReTS test was compared to other devices using the HiReTS number alone. A non linear trend was observed between HiReTS number and JFTOT breakpoint. A good correlation between the two devices was not anticipated due to the difference in flow regime and heater tube metallurgy, however the comparison was deemed necessary due to the success of the JFTOT in preventing thermal stability problems since the specification was created. The JFTOT 260°C breakpoint was found to equate to a HiReTS number of 1000.

The HiReTS was shown to correlate well with large scale rigs. Close agreement was observed between HiReTS number and deposition rate in the MIFAR. Correlation was also good between the HiReTS number and STHTR Δ HTC and was improved on the earlier comparison with HiReTS CBO. Preheating in the STHTR was suggested as a probable cause for the weaker trend with the STHTR than the MIFAR.

The US Navy conducted a very thorough review of the HiReTS in [65]. Testing was performed on an extensive range of fuels, split into refinery fuels (straight from the refinery without handling) and field samples (exposed to transport and storage environments) at standard and non-standard operating conditions.

While a direct comparison of HN and breakpoint temperature (BPT) showed no correlation, a pass/fail approach (a pass being $HN > 1000$, BPT > 260) awarded 86% agreement between the devices with refinery samples and 70% with field samples. The lack of correlation was attributed to the dramatically different methods of fuel stressing between the devices.

The correlation between HN and post test CBO was also studied. For the refinery samples, there was excellent agreement, although there was a greater spread in the results for good fuels ($HN < 50$). Field samples were much more scattered however. It was suggested in [65] and [44] that the spread of results was due to the variation in deposit structure between fuels with differing chemistry and the resulting levels of carbon in the deposit - thus creating different insulating effects for a given mass of carbon.

HiReTS number was compared to carbon burn off with 6 fuels in [124]. An outlier result was present in the data, which when removed increased the correlation to 0.98.

Repeatability and reproducibility

The repeatability of the device was examined in [65]. Both CBO and HN were considered on 7 field sample fuels. For the fuel with most tests (16), HN was found to be more repeatable (within 10%). While 5 of the seven fuels gave consistently repeatable pass/fail results, two fuels did not, with results for one fuel varying from 410 to 1190.

Repeatability and reproducibility of the HiReTS was also reported in [45]. Multiple tests were performed on two compositions of JP-8, one aged and one stable and blends of the stable fuel with 20 and 40% of the aged fuel. A standard RP-1 rocket fuel, low sulphur RP-1, and 5ppm sulphur RP were also tested. Tests were repeated at a different location using an alternate HiReTS.

The average result from each fuel tested was compared against the precision function for the total HN for a 125 minute test - defined in ASTM D6811 as:

$$r = 1.322x^{0.9} \tag{A.1.2}$$

where r is the acceptable difference in test results obtained by the same operator and machine. Results for jet fuel are shown in fig. A5. The stable fuel (JP-8-00 in the figure) lies outside of the accepted repeatability range - however being a very stable fuel was considered within the noise range of the machine and thus not particularly notable. On the contrary this does perhaps highlight an inadequacy in the device to accurately differentiate between very stable fuels. The 100% aged fuel test did not complete due to the wall temperature rise exceeding the safety

cutoff. Repeatability for the blended fuel tests (six 20% tests and seven 40% tests) was well within the defined limit, although a small difference can be observed between 20% blend tests conducted at different locations. The rocket fuel tests also showed good repeatability for high HN s and poor repeatability for low HN s ($HN < 150$).

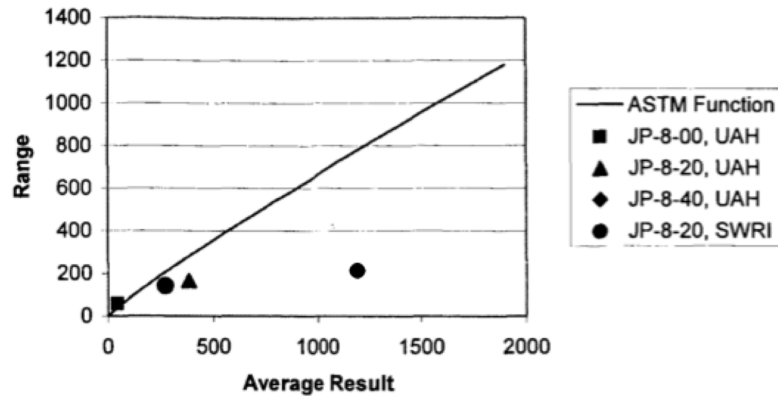


Figure A.5: HiReTS repeatability (taken from [45])

A similar analysis was conducted for machines between locations. Both devices were found to be operating within the ASTM reproducibility function for the jet fuel tests, although one machine (UOH in fig. A6) was found to give consistently higher results. For the rocket fuels, the reproducibility barely met the ASTM requirement and in fact the low sulphur blends fell outside of the defined limit.

A direct comparison of tube temperature profiles from JP-8 tests with the lowest variance revealed one HiReTS had significantly higher initial and final wall temperatures for almost the same HN (fig. A6). In addition, temperature increase did not appear to occur at the same rate along the length of the tube for the two devices. Following the rocket fuel tests, a $90^{\circ}C$ difference was found between the average top bus bar temperatures at the start of tests. However it is unclear whether this demonstrates a noteworthy difference in heating input between the devices or simply an effect caused by heat transfer via the bus bars (ie. the first test of the day having lower temperatures than subsequent tests).

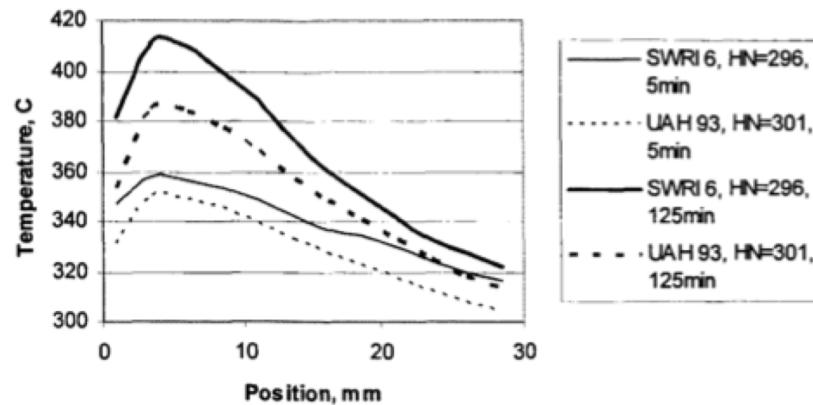


Figure A.6: HiReTS wall temperature reproducibility (taken from [45])

Differences in initial outer wall temperature have been observed between two HiReTS devices during testing by the author (fig. A7). Temperatures were measured using a thermal imaging camera. One device shows a temperature profile roughly 30°C higher than the other for the same fuel. Both tests were the first test performed of the day on each device. No major difference was observed between total HN s since the fuel was particularly stable. However, it is hard to imagine the variation in initial wall temperatures between devices not being a source of reduced reproducibility.

Repeatability of one HiReTS device at the University of Sheffield was determined from data available from two fuel testing campaigns. The 'A.Baseline' fuel averaged $HN = 775$ from 9 tests and the 'drum 320' fuel $HN = 104$ from 8 tests. Both fell within the ASTM limit for repeatability. These results are not dissimilar to those in [45] and add to the evidence for worsening repeatability when fuel quality increases.

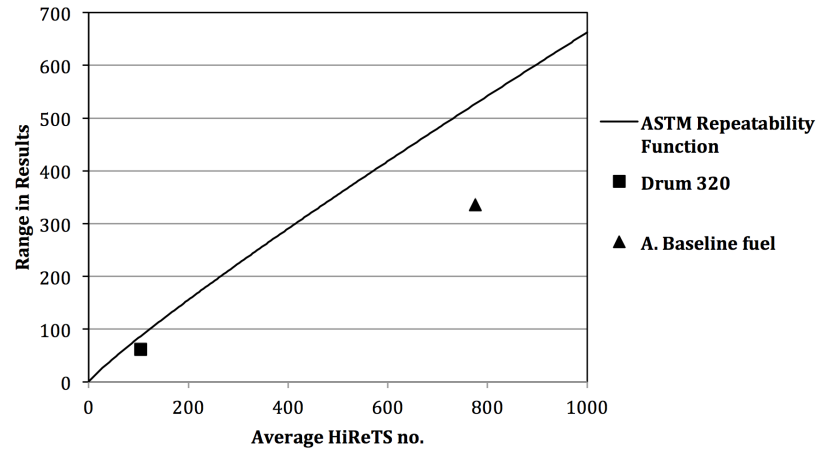


Figure A.7: HiReTS repeatability assessed by the author

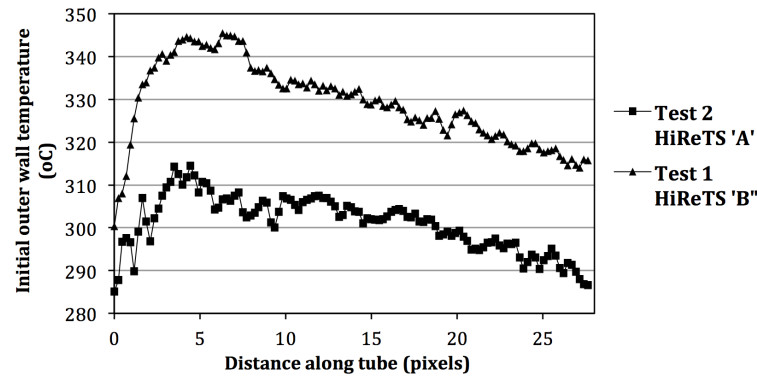


Figure A.8: HiReTS wall temperature variation observed by the author

A.2 Large scale rigs / simulators

Laboratory scale devices like the aforementioned have demonstrated their suitability for characterisation of fuel thermal stability and investigation of the physico-chemical aspects of thermal instability in fuels at low cost. However, extrapolating their results to predict the response of real fuel system components to fouling is rather presumptuous. Complete simulators naturally offer the best insight into thermal instability effects in real aircraft fuel systems, since assumptions made about the physics and component geometry are kept to a minimum. Rigs are usually designed to recreate as best as possible the flow path up to a critical component of interest (eg. a fuel injector feed arm) or include several components of interest over a range of temperature regimes. Temperatures are representative, not exaggerated as with laboratory devices - although usually compare to the most

extreme conditions seen in flight (ie. at the start of descent, where engine temperatures are high and fuel flow rates are low). The level of instrumentation provides a wealth of temperature and deposition data - key to the understanding of the heat transfer and chemistry in the deposition process. The downside of running large scale rigs at representative temperatures is that the testing requires a great deal of time and fuel, although successful efforts have been made to generate meaningful data from scaled systems with a much reduced appetite. Data from such devices is the primary source for validation of the smaller devices discussed previously.

A.2.1 (Mini) Injector Feed Arm Rig ((M)IFAR)

Feed arms, which pass fuel into the combustor, provide the most hostile environment for fuel. Not only are compressor discharge temperatures around the feed arm typically around 500°C ($\approx 300^{\circ}\text{C}$ inner wall temperature), but also the fuel passing through the feed arm has already been preheated. Deposits can form quickly in these passages - deposition rates that would result in complete blockage of the feed arm within 1000 hours have been recorded in some tests [48]. Deposit that flakes off may foul atomisers, disrupting the spray pattern and causing engine malfunction.

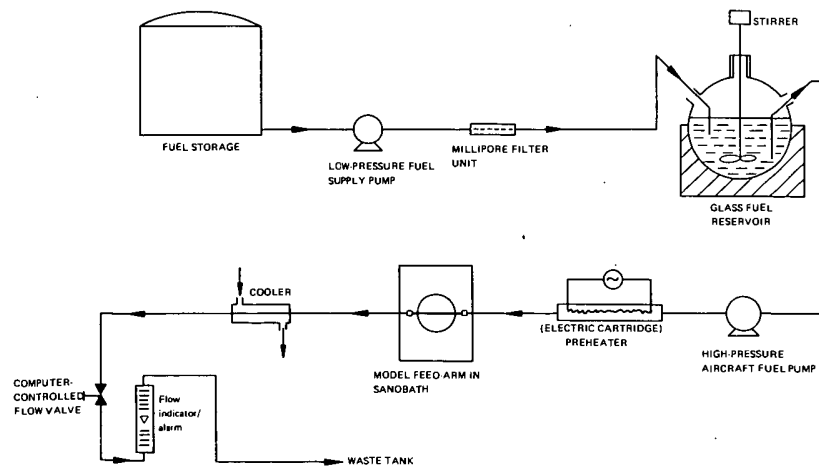


Figure A.9: MIFAR flow path (taken from [46])

Developed by Shell, the IFAR was a full scale simulator which included 4 feed arms in a fluidized bed heated to 540°C (resulting in an inner wall temperature of 300°C). The fuel temperature at the inlet to the feed arms was 165°C . The test lasted 80 hours and consumed 50,000l of fuel. Practically, this resulted in a limited

usefulness for in depth investigation of heat transfer and chemistry during the test. As a result, a half scale rig was developed- the Mini Injector Feed Arm Rig - which operates at identical temperatures but consumes only 2000l of fuel per test.

A schematic of the rig is shown in figure A9. The glass fuel reservoir simulates a subsonic wing fuel tank without aerodynamic heating or fuel recirculation, while the cartridge heater simulates heat addition to the fuel from cooling systems for avionic and engine components. The injector feed arm is modelled as a half scale burner stem - a steel tube (6mm OD, 2mm ID). The heated length is 10cm. Thermocouples measure the temperature of the inner wall along the heated length. On-line deposition monitoring is achieved through the observed rise in inner wall temperature as insulating deposits reduce the amount of heat transferred from the tube to the fuel. Post test carbon burn off provides additional deposition data.

Detailed results from MIFAR testing are presented in [46]. Ten fuels of varying sulphur content / thermal stability / processing method were tested. The results were compared to the JFTOT (breakpoint and carbon deposition data), STHTR, radical initiation rate (Ri), fuel sulphur content and total acid content (TAC). The best correlation was observed with the analytically derived fuel chemistry tests - TAC, Ri and sulphur (in order of decreasing correlation). There was a lack of significant correlation between the MIFAR and the STHTR, thought likely to be due to the extended preheating time prior to the test section complicating the chemistry of the process in the STHTR and moving it away from the simpler oxidation reaction in the MIFAR predicted with TAC, Ri and sulphur. Neither JFTOT result correlated well with the MIFAR, deemed likely to be due to the dramatic difference in flow regimes between the devices.

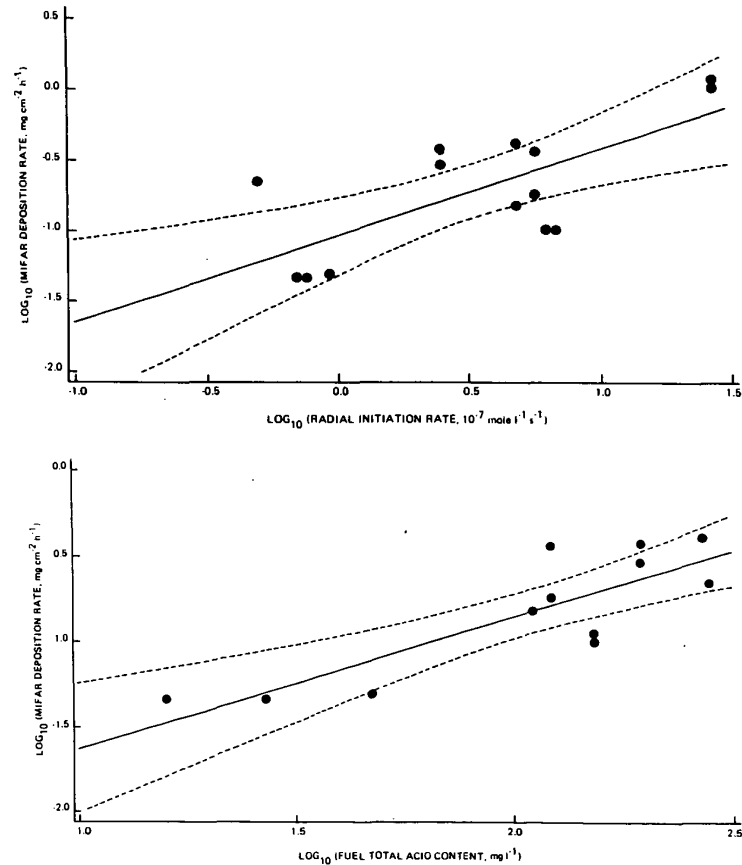


Figure A.10: MIFAR correlation (taken from [46])

A.2.2 Aviation Fuel Thermal Stability Test Unit (AFT-STU)

The AFTSTU rig was designed in the mid 1990s by Rolls-Royce in collaboration with the US Navy. The design philosophy behind the rig was to include multiple fuel system components sensitive to fuel thermal instability and to condition the fuel as accurately as possible from low to high temperature environments. The temperature regimes and components within each regime can be seen in fig. A11.

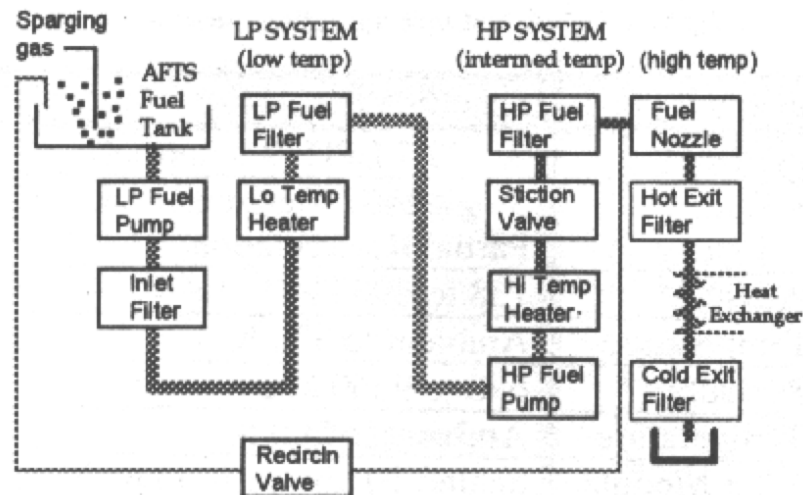


Figure A.11: AFTSTU flow path (taken from [47])

Low temperature regime (fuel tank to high pressure pump)

A low pressure pump feeds fuel from the tank, through a $10\mu\text{m}$ inlet filter which represents an airframe or ground vehicle filter. This filter also serves to remove any debris generated by the pump, ensuring the fuel is properly conditioned before reaching the heated sections. Fuel is heated to 80°C and passed through a scaled $10\mu\text{m}$, resin impregnated low pressure aircraft filter.

Intermediate temperature regime (high pressure pump to fuel nozzle)

In the next stage, the pressure of the system is increased and the fuel is heated (according to the operating conditions shown in table A5). Fuel then passes through a hydraulic differential pressure sensing spool valve, used to assess the propensity for deposit to alter the mechanical operation of devices with small tolerances (ie. metering valves). Deposition problems are observed as hysteresis in the pressure as the valve cycles from open to closed. The final component is a $70\mu\text{m}$ stainless steel woven mesh screen simulating the high pressure fuel filter prior to the injectors. Differential pressure across the filter provides an online measure of filter plugging as well as pre/post test weighing.

High temperature regime (fuel nozzle)

The high temperature section simulates the extreme environment of fuel injection nozzles. The test section is a modelled thick walled injector feed arm, 387mm in length and 6.35mm in diameter, with a bore of 0.76mm . Tube dimensions were chosen to ensure the fluid flow and heat transfer characteristics closely match conditions in service. The central 100mm of the tube is manufactured by Electro

Discharge Machining (EDM) from 316 stainless steel in order to recreate the surface roughness and metallurgy of a feed arm. Constant heat flux is applied to the central section via a radio frequency induction coil. The heated section is instrumented with 6 thermocouples, spaced 50mm apart measuring the external and internal wall temperature. Similarly to the MIFAR, test output is primarily wall temperature measurement, with additional pressure data and destructive analysis such as post test carbon burn off and microscopy.

Table A.5: AFTSTU operating conditions

Flow rate (<i>l/hr</i>)	10-23
Flow path	single / recirculation
LP pressure (<i>bar</i>)	13
LP temperature ($^{\circ}C$)	150
HP pressure (<i>bar</i>)	34
HP temperature ($^{\circ}C$)	220

Preliminary testing of the AFTSTU was reported in [47]. Deposition rate data from 500-800K showed good agreement with the data from [6]. Results from the AFTSTU were compared to two other test devices (a laminar rig and the HiReTS) in [125]. Poor correlation was found between the total mass of tube deposits and rise in wall temperature at the central location. However, it was noted that tube deposits may be non uniformly distributed within the tube and that the relationship between deposit mass and wall temperature is likely nonlinear. Correlation improved significantly when the total mass of hot deposits (including filters) was compared with initial wall temperature. Deposit thicknesses calculated from wall temperature data and measured deposit thicknesses measured via SEM were compared in [126]. Reasonable agreement was found between the two methods. The calculated deposit thickness closely matched the measured thickness at the third thermocouple location (location of highest deposition).

Appendix C

Fluid Properties

Heptane					
Temperature (°C)	Dyn Viscosity (kg/ms)	Density (kg/m ³)	Cp (J/kg K)	Thermal cond. (W/m K)	Kinematic viscosity (m ² /s)
20	4.22E-04	685.61	2218.70	0.1333	6.16E-07
30	3.77E-04	677.28	2255.90	0.1308	5.57E-07
40	3.39E-04	668.89	2294.80	0.1283	5.07E-07
50	3.07E-04	660.40	2335.20	0.1258	4.65E-07
60	2.79E-04	651.81	2377.00	0.1233	4.28E-07
70	2.55E-04	643.10	2420.00	0.1209	3.97E-07
80	2.33E-04	634.25	2464.20	0.1185	3.67E-07
90	2.15E-04	625.23	2509.50	0.1161	3.44E-07
100	1.98E-04	616.03	2555.90	0.1138	3.21E-07
110	1.83E-04	606.60	2603.40	0.1115	3.02E-07
120	1.69E-04	596.93	2652.00	0.1092	2.83E-07
130	1.57E-04	586.96	2701.90	0.1069	2.67E-07
140	1.46E-04	576.66	2753.40	0.1047	2.53E-07
150	1.36E-04	565.97	2806.70	0.1024	2.40E-07
160	1.26E-04	554.80	2862.40	0.1002	2.27E-07
170	1.17E-04	543.08	2921.30	0.0979	2.15E-07
180	1.09E-04	530.67	2984.40	0.0956	2.05E-07
190	1.01E-04	517.40	3053.60	0.0932	1.95E-07
200	9.30E-05	503.02	3132.00	0.0908	1.85E-07
210	8.60E-05	487.17	3225.10	0.0881	1.77E-07
220	7.80E-05	469.22	3343.90	0.0853	1.66E-07
230	7.10E-05	447.97	3515.90	0.0820	1.58E-07
240	6.20E-05	420.55	3835.30	0.0779	1.47E-07
245	5.70E-05	401.59	4190.00	0.0751	1.42E-07
245	1.41E-05	87.09	4166.40	0.0396	1.62E-07
250	1.39E-05	80.36	3721.20	0.0397	1.73E-07
260	1.36E-05	71.75	3367.70	0.0402	1.90E-07
270	1.36E-05	66.06	3222.60	0.0410	2.06E-07
280	1.36E-05	61.82	3149.80	0.0418	2.20E-07
290	1.36E-05	58.44	3111.40	0.0428	2.33E-07
300	1.36E-05	55.64	3092.40	0.0437	2.44E-07

Figure C.1: Thermophysical properties of n-Heptane

Kerosene						
T (°C)	dynamic viscosity, μ (kg/ms)	kinematic viscosity, ν (m ² /s)	Density, ρ (kg/m ³)	Thermal conductivity, k (W/mK)	Specific Heat, cp (J/Kg K)	Thermal Diffusivity, α (m ² /s)
0	1.9913E-03	2.4460E-06	814.1	0.1283	1866	8.4457E-08
10	1.5872E-03	1.9692E-06	805.989	0.126562	1909.38	8.2240E-08
20	1.2961E-03	1.6244E-06	797.878	0.124824	1952.76	8.0115E-08
30	1.0800E-03	1.3675E-06	789.767	0.123086	1996.14	7.8076E-08
40	9.1559E-04	1.1713E-06	781.656	0.121348	2039.52	7.6118E-08
50	7.8776E-04	1.0184E-06	773.545	0.11961	2082.9	7.4236E-08
60	6.8654E-04	8.9693E-07	765.434	0.117872	2126.28	7.2424E-08
70	6.0512E-04	7.9902E-07	757.323	0.116134	2169.66	7.0678E-08
80	5.3871E-04	7.1903E-07	749.212	0.114396	2213.04	6.8995E-08
90	4.8387E-04	6.5291E-07	741.101	0.112658	2256.42	6.7370E-08
100	4.3811E-04	5.9770E-07	732.99	0.11092	2299.8	6.5799E-08
110	3.9953E-04	5.5117E-07	724.879	0.109182	2343.18	6.4281E-08
120	3.6674E-04	5.1165E-07	716.768	0.107444	2386.56	6.2810E-08
130	3.3862E-04	4.7783E-07	708.657	0.105706	2429.94	6.1386E-08
140	3.1434E-04	4.4871E-07	700.546	0.103968	2473.32	6.0004E-08
150	2.9323E-04	4.2348E-07	692.435	0.10223	2516.7	5.8663E-08
160	2.7476E-04	4.0151E-07	684.324	0.100492	2560.08	5.7361E-08
170	2.5850E-04	3.8228E-07	676.213	0.098754	2603.46	5.6094E-08
180	2.4411E-04	3.6538E-07	668.102	0.097016	2646.84	5.4862E-08
190	2.3130E-04	3.5045E-07	659.991	0.095278	2690.22	5.3662E-08
200	2.1983E-04	3.3723E-07	651.88	0.09354	2733.6	5.2492E-08
210	2.0953E-04	3.2547E-07	643.769	0.091802	2776.98	5.1351E-08
220	2.0022E-04	3.1497E-07	635.658	0.090064	2820.36	5.0237E-08
230	1.9177E-04	3.0558E-07	627.547	0.088326	2863.74	4.9148E-08
240	1.8407E-04	2.9715E-07	619.436	0.086588	2907.12	4.8084E-08
250	1.7702E-04	2.8957E-07	611.325	0.08485	2950.5	4.7042E-08
260	1.7054E-04	2.8272E-07	603.214	0.083112	2993.88	4.6021E-08
270	1.6456E-04	2.7653E-07	595.103	0.081374	3037.26	4.5021E-08
280	1.5903E-04	2.7092E-07	586.992	0.079636	3080.64	4.4039E-08
290	1.5388E-04	2.6582E-07	578.881	0.077898	3124.02	4.3075E-08

Figure C.2: Thermophysical properties of kerosene

Appendix D

Calibration data

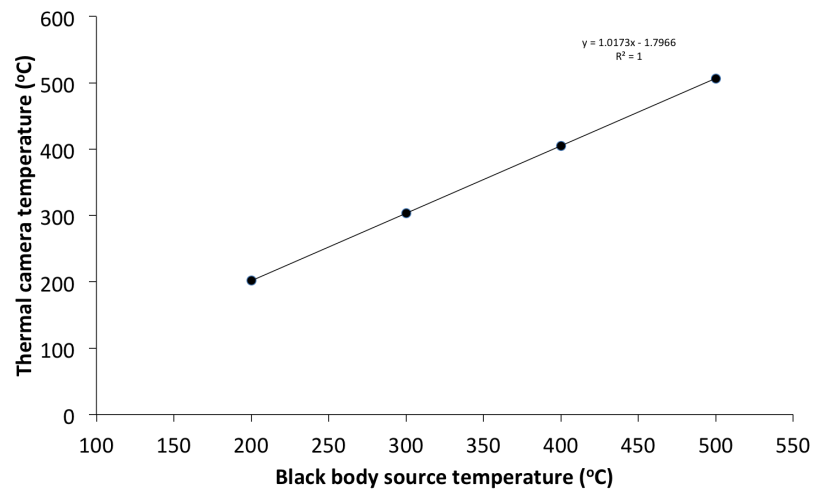


Figure D.1: Thermal camera black body source calibration data

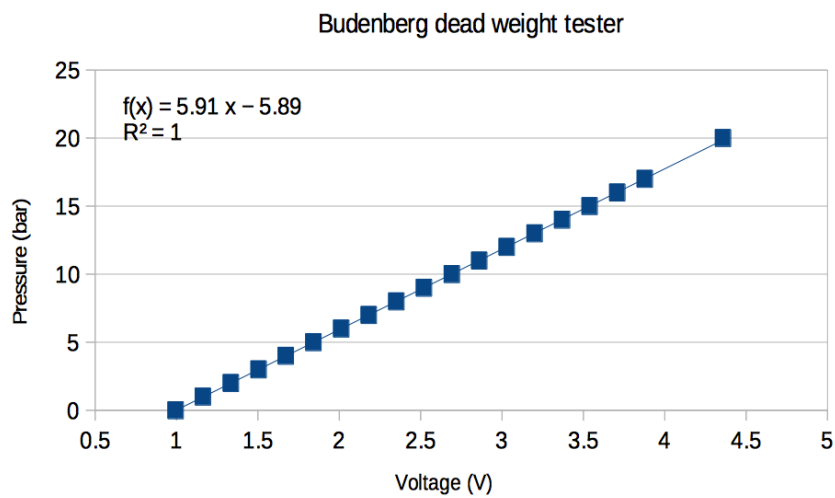


Figure D.2: Differential pressure transducer calibration data

Appendix E

Heat transfer data

Tube	D (µm)	Current (A)	Q _{heat} (W)	Q _{heat} (dT) (W)	U _{heat} (ms)	T _{exit} (°C)	ΔT	T _{w,max} (°C)	T _{w,min} (°C)	T _{w,avg} (°C)	T _{w,wall-T_{ex}}	dT/dx	T _{surf} (W/m ²)	h (W/m ² K)	Nu	δNu	Re _{exit}	δRe	Pr	St	ES _T
EDM 1	482	40	97	84	5.9	72.4	50.4	125.3	115.6	1.60	0.21	52.93	3.61E+05	6815	28.5	2.1	7172	276	4.65	8.54E-04	7.03E-05
		50	152	138	5.9	104.0	82.0	180.6	169.2	1.63	0.23	76.62	5.92E+05	7731	35.8	2.2	8848	340	3.84	1.05E-03	7.66E-05
		60	219	203	5.9	141.8	119.8	256.9	249.7	1.76	0.06	115.08	8.73E+05	7586	39.5	2.2	11233	432	3.31	1.06E-03	7.14E-05
EDM 2	453	40	96	82	7.0	71.3	49.3	122.9	112.7	1.58	0.20	51.65	3.84E+05	7439	28.5	2.2	7817	311	4.65	7.85E-04	6.70E-05
		50	150	136	7.0	102.7	80.7	177.6	164.7	1.60	0.25	74.86	6.36E+05	8492	36.1	2.3	9644	383	3.84	9.75E-04	7.37E-05
		60	215	200	7.0	140.1	118.1	240.7	227.2	1.62	0.21	100.58	9.38E+05	9328	44.5	2.6	12243	486	3.31	1.10E-03	7.84E-05
EDM 3	472	40	97	85	6.4	73.1	51.1	103.9	89.8	1.23	0.22	30.76	3.81E+05	12372	48.7	5.1	7465	291	4.85	1.35E-03	1.51E-04
		50	152	134	6.4	101.9	79.9	145.6	123.5	1.21	0.35	43.71	6.01E+05	13747	58.7	4.8	9209	359	4.10	1.55E-03	1.41E-04
		60	218	194	6.4	136.9	114.9	190.3	158.0	1.15	0.49	53.42	8.68E+05	16244	75.5	5.5	11066	432	3.60	1.90E-03	1.57E-04
EDM 4	439	40	97	78	7.2	69.1	47.1	108.8	99.9	1.44	0.21	39.62	3.74E+05	9428	34.8	3.1	7357	294	4.85	9.78E-04	9.51E-05
		50	151	133	7.2	101.0	79.0	155.7	143.6	1.42	0.28	54.70	6.32E+05	11550	46.3	3.4	9798	392	4.10	1.15E-03	9.67E-05
		60	218	193	7.2	136.4	114.4	207.4	194.3	1.42	0.30	71.07	9.19E+05	12928	57.8	3.8	11774	471	3.49	1.41E-03	1.09E-04
EDM 5	500	40	97	82	5.7	71.3	49.3	122.7	114.8	1.61	0.17	51.39	3.47E+05	6748	28.7	2.1	7056	270	4.65	8.74E-04	7.29E-05
		50	152	134	5.7	101.9	79.9	178.9	170.1	1.67	0.18	76.96	5.68E+05	7380	34.8	2.1	8705	333	3.84	1.04E-03	7.50E-05
		60	218	199	5.7	139.7	117.7	238.8	235.4	1.69	0.01	99.08	8.44E+05	8516	43.9	2.5	10460	400	3.40	1.23E-03	8.43E-05
EDM 6	437	40	97	84	7.3	72.5	50.5	114.3	102.3	1.41	0.27	41.76	4.03E+05	9656	36.2	3.1	7987	321	4.65	9.73E-04	9.23E-05
		50	151	137	7.3	103.8	81.8	165.3	148.6	1.43	0.38	61.54	6.59E+05	10703	43.6	3.1	9866	396	3.97	1.11E-03	8.98E-05
		60	217	205	7.3	143.1	121.1	228.5	204.6	1.43	0.43	85.41	9.84E+05	11518	52.4	3.3	12524	502	3.40	1.23E-03	9.12E-05
EDM 7	575	40	103	91	4.2	77.0	55.0	178.4	116.7	1.52	0.24	101.47	3.32E+05	3275	17.2	0.9	6060	221	4.10	6.92E-04	4.44E-05
		50	161	149	4.2	111.0	89.0	215.2	168.7	1.52	0.33	104.23	5.43E+05	5210	29.8	1.6	7965	290	3.60	1.04E-03	6.64E-05
		60	231	218	4.2	150.6	128.6	245.3	231.1	1.54	0.23	94.72	7.91E+05	8356	51.5	2.8	10000	364	3.31	1.56E-03	1.01E-04
EDM 8	575	40	102	92	4.3	77.6	55.6	122.7	110.8	1.43	0.24	45.11	3.42E+05	7578	37.6	2.9	6168	226	4.45	1.37E-03	1.17E-04
		50	160	146	4.3	109.1	87.1	174.2	157.8	1.45	0.31	65.04	5.41E+05	8320	44.8	2.8	7609	279	3.84	1.53E-03	1.11E-04
		60	230	213	4.3	147.6	125.6	232.9	218.7	1.48	0.29	85.31	7.87E+05	9227	55.8	3.1	9660	354	3.31	1.75E-03	1.17E-04
EDM 9	574	40	97	102	4.2	82.8	60.8	125.6	115.7	1.40	0.17	42.77	3.70E+05	8639	43.6	3.5	6541	238	4.45	1.50E-03	1.32E-04
		50	152	156	4.2	114.9	92.9	180.2	167.2	1.46	0.21	65.29	5.67E+05	8682	47.6	3.0	7965	290	3.84	1.56E-03	1.12E-04
		60	219	224	4.2	154.5	132.5	236.7	228.4	1.48	0.04	82.24	8.16E+05	9920	61.1	3.5	10000	364	3.31	1.85E-03	1.24E-04
EDM 10	581	40	103	99	4.1	81.3	59.3	130.9	117.6	1.45	0.26	49.59	3.55E+05	7168	36.7	2.7	6451	234	4.45	1.28E-03	1.03E-04
		50	161	153	4.1	113.1	91.1	187.5	170.6	1.51	0.32	74.41	5.48E+05	7368	41.9	2.5	7856	285	3.73	1.43E-03	9.85E-05
		60	232	219	4.1	151.6	129.6	247.9	234.3	1.54	0.21	96.30	7.87E+05	8174	51.0	2.7	9863	358	3.31	1.56E-03	1.01E-04
EDM 11	576	40	103	96	4.2	79.3	57.3	124.9	110.4	1.39	0.32	45.57	3.49E+05	7669	38.5	3.0	6082	222	4.45	1.43E-03	1.21E-04
		50	160	151	4.2	112.2	90.2	180.9	157.9	1.41	0.47	68.72	5.52E+05	8034	43.9	2.7	7993	291	3.84	1.43E-03	1.02E-04
		60	231	216	4.2	149.4	127.4	238.4	214.0	1.43	0.59	89.01	7.87E+05	8845	54.3	3.0	9525	347	3.31	1.72E-03	1.14E-04
EDM 12	567	40	102	96	4.3	79.2	57.2	119.5	101.5	1.28	0.37	40.3135	3.52E+05	8726	42.6	3.55	6135	224	4.65	1.49E-03	1.36E-04
		50	160	146	4.3	109.1	87.1	164.6	141.2	1.29	0.48	55.5166	5.38E+05	9694	51.4	3.5	7569	277	3.97	1.71E-03	1.32E-04
		60	230	210	4.3	146.0	124.0	214.8	186.5	1.28	0.55	68.8256	7.73E+05	11230	66.6	4.06	9609	351	3.40	2.04E-03	1.45E-04
EDM 13	495	40	99	90	5.6	76.1	54.1	140.2	99.6	1.31	0.28	64.0877	3.79E+05	5919	25.7	1.69	7028	268	4.45	8.24E-04	6.26E-05
		50	155	142	5.6	106.6	84.6	165.1	142.8	1.34	0.38	58.4562	5.99E+05	10243	47.4	3.26	8670	331	3.97	1.38E-03	1.08E-04
		60	223	204	5.6	142.3	120.3	218.8	189.7	1.33	0.44	76.525	8.59E+05	11224	58.1	3.55	11006	420	3.40	1.58E-03	1.12E-04
EDM 14	611	40	105	99	3.7	81.5	59.5	138.9	117.5	1.44	0.41	57.4202	3.40E+05	5914	32.4	2.13	6145	220	4.27	1.23E-03	9.23E-05
		50	164	156	3.7	114.9	92.9	197.0	169.2	1.47	0.56	82.1361	5.33E+05	6485	38.7	2.14	7483	268	3.73	1.39E-03	9.15E-05
		60	236	224	3.7	154.4	132.4	238.7	220.1	1.43	0.38	84.2883	7.66E+05	9086	59.6	3.27	9395	336	3.31	1.92E-03	1.26E-04

Table E.1: Heat transfer data - EDM tubes

Tube	D (µm)	Current (A)	Q _{heat} (W)	Q _{heat} (dT) (W)	U _{avg} (ms)	T _{exit} (°C)	ΔT	T _{w,max} (°C)	T _{w,avg} (°C)	T _{w,avg} /T _r	dT/dx	T _{wall} -T _{ax}	q _{surf} (W/m ²)	h (W/m ² K)	Nu	δNu	Re exit	δRe	Pr	St	δSt
1	530	40	100	81	4.9	70.8	48.8	105.5	95.4	1.35	0.21	34.71	3.20E+05	9208	41.2	5.8	6563	437.1	4.56	1.37E-03	2.16E-04
		50	156	134	4.9	102.0	80.0	150.5	135.8	1.33	0.29	48.51	5.29E+05	10901	52.9	6.9	8097	539.3	3.70	1.77E-03	2.58E-04
		60	225	194	4.9	137.2	115.2	199.0	179.8	1.31	0.37	61.81	7.65E+05	12376	65.5	8.2	9730	648.0	3.10	2.17E-03	3.07E-04
3	537	40	97	77	4.8	68.5	46.5	109.3	91.4	1.33	0.25	40.78	3.03E+05	7418	33.4	4.5	6035	399.5	4.56	1.21E-03	1.82E-04
		50	152	130	4.8	99.5	77.5	149.2	129.2	1.30	0.35	49.74	5.08E+05	10221	50.0	6.4	7512	497.3	3.70	1.80E-03	2.60E-04
		60	219	190	4.8	134.6	112.6	195.6	169.3	1.26	0.46	61.04	7.42E+05	12154	64.8	8.1	9657	639.4	3.10	2.16E-03	3.05E-04
4	527	40	100	84	5.1	72.7	50.7	111.2	92.5	1.27	0.28	38.54	3.37E+05	8739	39.3	5.5	6664	449.2	4.93	1.19E-03	1.84E-04
		50	157	139	5.1	104.7	82.7	162.6	129.2	1.23	0.41	57.92	5.55E+05	9586	46.8	6.0	8221	554.1	4.18	1.36E-03	1.96E-04
		60	225	200	5.1	140.3	118.3	205.5	172.7	1.23	0.54	65.13	8.01E+05	12301	65.6	8.2	10437	703.5	3.67	1.71E-03	2.44E-04
5	519	40	100	96	5.0	79.6	57.6	108.8	97.0	1.22	0.26	29.13	3.83E+05	13164	59.4	9.1	6639	446.1	4.93	1.81E-03	3.02E-04
		50	157	149	5.0	110.6	88.6	153.5	132.9	1.20	0.39	42.93	5.82E+05	13800	67.6	9.1	8726	586.4	4.18	1.85E-03	2.79E-04
		60	226	212	5.0	147.1	125.1	200.7	174.5	1.19	0.50	53.66	8.44E+05	15719	84.1	10.8	10397	698.7	3.49	2.32E-03	3.37E-04
6	517	40	100	89	5.1	75.3	53.3	105.8	92.6	1.23	0.26	30.48	3.57E+05	11718	52.3	7.9	6716	455.4	4.65	1.68E-03	2.77E-04
		50	156	140	5.1	105.5	83.5	150.6	130.5	1.24	0.37	45.07	5.65E+05	12531	59.4	8.0	8285	561.8	3.70	1.94E-03	2.92E-04
		60	225	203	5.1	141.8	119.8	196.0	170.5	1.20	0.47	54.23	8.17E+05	15065	77.9	10.1	10517	713.3	3.26	2.27E-03	3.32E-04
7	530	40	101	87	4.8	74.4	52.4	107.5	95.0	1.28	0.25	33.16	3.38E+05	10190	47.2	6.7	6466	425.6	4.65	1.57E-03	2.47E-04
		50	158	141	4.8	106.2	84.2	151.3	132.8	1.25	0.38	45.05	5.48E+05	12174	60.0	7.8	7977	525.0	3.89	1.93E-03	2.82E-04
		60	227	202	4.8	141.6	119.6	198.6	173.7	1.23	0.48	56.99	7.85E+05	13783	75.7	9.5	10126	666.5	3.33	2.25E-03	3.17E-04
8	527	40	100	96	5.0	79.5	57.5	115.1	98.5	1.24	0.29	35.56	3.80E+05	10701	48.6	6.9	6601	441.6	3.88	1.89E-03	2.96E-04
		50	157	149	5.0	110.8	88.8	159.2	135.7	1.22	0.40	48.41	5.90E+05	12194	60.1	7.9	8676	580.4	3.40	2.04E-03	2.99E-04
		60	226	208	5.0	144.6	122.6	209.2	179.0	1.24	0.53	64.63	8.22E+05	12722	68.5	8.5	10338	691.6	3.17	2.09E-03	2.96E-04
9	528	40	100	101	4.9	82.2	60.2	112.3	93.7	1.14	0.33	30.11	3.96E+05	13206	60.1	9.0	7111	475.0	4.37	1.93E-03	3.17E-04
		50	157	153	4.9	113.2	91.2	161.4	134.0	1.18	0.48	48.20	6.05E+05	12553	62.0	8.1	8659	578.4	3.77	1.90E-03	2.79E-04
		60	226	215	4.9	148.8	126.8	203.9	169.1	1.14	0.61	55.13	8.49E+05	15395	83.0	10.6	10318	689.2	3.17	2.54E-03	3.66E-04
11	539	40	101	96	4.7	79.2	57.2	112.5	92.2	1.16	0.28	33.31	3.70E+05	11111	51.6	7.3	6454	424.2	4.37	1.83E-03	2.87E-04
		50	158	148	4.7	110.2	88.2	155.2	128.5	1.17	0.42	44.98	5.73E+05	12745	64.3	8.4	8483	557.5	3.59	2.11E-03	3.09E-04
		60	227	208	4.7	145.1	123.1	203.1	168.2	1.16	0.54	58.05	8.07E+05	13905	76.6	9.5	10108	664.3	3.17	2.39E-03	3.37E-04

Figure E.1: Heat transfer data - Drawn tubes

Appendix F

Publications from this work

1. P. Gadsby and S. G Blakey, "Wall Roughness Effects on Deposition of Thermally Stressed Aviation Fuel," in *15th International Conference on Stability and Handling of Liquid Fuels*, (Rome), 2017.